

# Measurement of the Cross Section of the reactions $e^+e^- \rightarrow \pi^+\pi^-2\pi^0$ and $e^+e^- \rightarrow \pi^+\pi^-3\pi^0$ at BESIII

Dissertation  
zur Erlangung des Grades  
„Doktor der Naturwissenschaften“  
am Fachbereich Physik, Mathematik und Informatik  
der Johannes Gutenberg-Universität  
in Mainz



JOHANNES GUTENBERG  
UNIVERSITÄT MAINZ

Martin Ripka  
geb. in Bad-Kreuznach  
Mainz, den 10.10.2017



## Zusammenfassung

Die Frage nach der Existenz von Physik jenseits des Standardmodells der Teilchenphysik ist eine der wichtigsten Fragestellungen der Physik. Physik jenseits des Standardmodells wird in zwei Forschungsrichtungen gesucht. Die eine ist die direkte Suche nach neuen schweren Teilchen im Bereich der Hochenergie-Physik auf der TeV Skala. Die zweite ist die Suche nach neuen Resonanzen oder Abweichungen zwischen Experiment und Theorie auf dem Gebiet der Niederenergie-Präzisionsphysik. Diese Arbeit leistet einen Beitrag in letzterem Bereich und beschäftigt sich mit der Standardmodellvorhersage des anomalen magnetischen Moments des Myons  $a_\mu$ . Diese physikalische Größe beschreibt die Wechselwirkung eines Myons mit einem externen elektromagnetischen Feld. Sie wurde experimentell mit einer relativen Genauigkeit von  $0,5 \cdot 10^{-6}$  bestimmt. Allerdings weicht der gemessene Wert um mehr als drei Standardabweichungen von der theoretischen Vorhersage ab.

In der Berechnung von  $a_\mu$  treten neben den Beiträgen der Quantenelektrodynamik auch Korrekturbeiträge der schwachen Wechselwirkung und der Quantenchromodynamik (QCD) auf. Im Gegensatz zu den beiden anderen Beiträgen kann der QCD-Beitrag nicht störungstheoretisch berechnet werden. Er besteht aus dem hadronischen Vakuumpolarisations-Beitrag und dem hadronischen Lichtan-Licht-Streuungs-Beitrag. Letzterer kann mittels des Optischen Theorems auf hadronische Wirkungsquerschnitte zurückgeführt werden. Diese wiederum können in Elektron-Positron Vernichtungsreaktionen experimentell gemessen werden. In dieser Arbeit wird der Wirkungsquerschnitt des Prozesses  $e^+e^- \rightarrow \pi^+\pi^-2\pi^0$  experimentell bestimmt, welcher einen großen Beitrag zur Unsicherheit des Vakuumpolarisations-Beitrages von  $a_\mu$  liefert. Der Vakuumpolarisationsanteil von  $a_\mu$  wird vom Wirkungsquerschnitt unterhalb von 1,8 GeV dominiert. Das Ziel ist es, diese Unsicherheit durch eine Präzisionsmessung zu reduzieren.

Diese Messung wird mit Daten des BESIII-Experiments am BEPCII- Beschleunigerzentrum in Peking, China, durchgeführt. Es werden Daten verwendet, deren Schwerpunktsenergie der Elektron-Positron-Kollision von 3,773 GeV entsprechen. Daher wird die Methode der Abstrahlung eines Photons im Anfangszustand angewendet. Diese Methode ermöglicht es, den Wirkungsquerschnitt als kontinuierliches Spektrum unterhalb einer Energie der Schwerpunktsenergie zu messen. Um die für  $a_\mu$  notwendige Präzision zu erreichen, sind neben der Messung des Wirkungsquerschnitts des Prozesses  $e^+e^- \rightarrow \pi^+\pi^-2\pi^0$  Effizienzstudien der  $\pi^0$  Rekonstruktion, sowie genaue Messungen der Wirkungsquerschnitte der Prozesse  $e^+e^- \rightarrow \pi^+\pi^-3\pi^0$  und  $e^+e^- \rightarrow \pi^+\pi^-3\pi^0\gamma_{ISR}$  erforderlich. Diese treten als Untergrundbeiträge zu  $e^+e^- \rightarrow \pi^+\pi^-2\pi^0$  auf. Dadurch ist es gelungen den systematischen Fehler der Messung auf etwa 3% in dem für  $a_\mu$  wichtigen Bereich des  $e^+e^- \rightarrow \pi^+\pi^-2\pi^0$  Wirkungsquerschnitts zu minimieren. Auch der Wirkungsquerschnitt des Prozesses  $e^+e^- \rightarrow \pi^+\pi^-3\pi^0$  wird in dieser Arbeit behandelt.



## Summary

The search for physics beyond the Standard Model of particle physics is one of the most challenging topics of modern particle physics. Physics beyond the Standard Model has two frontiers. The first one is the search for new heavy particles in the field of high energy physics at energies above the TeV scale. The second is the search of weakly coupled new forces at the low energy precision frontier. This thesis is placed in the field of low energy precision physics and deals with the Standard Model prediction of the anomalous magnetic moment of the muon  $a_\mu$ . This observable describes the interaction of a muon with an external electromagnetic field. It has been measured experimentally to a relative precision of  $0.5 \cdot 10^{-6}$ . However, there is a discrepancy of more than three standard deviations between the experimentally measured value and the Standard Model prediction.

Besides the contribution from quantum electrodynamics, the calculation also involves higher order quantum corrections from the weak interaction and quantum chromodynamics (QCD). The QCD contribution cannot be calculated in terms of perturbation theory as the other contributions. It further decomposes into a hadronic light-by-light contribution and a hadronic vacuum polarization contribution. The latter one can be related to hadronic cross sections via the optical theorem. The hadronic cross sections can be measured in electron positron annihilation processes. This thesis presents a measurement of the processes  $e^+e^- \rightarrow \pi^+\pi^-2\pi^0$ , which contribute with a large uncertainty to the vacuum polarization contribution of  $a_\mu$ . The dispersion integral used to calculate the vacuum polarization correction is dominated by the hadronic cross sections in the region below 1.8 GeV. The goal of this thesis is to reduce this uncertainty by a new precise measurement.

This measurement uses data taken with the BESIII detector located at the BEPCII accelerator facility in Beijing, China. The initial state radiation method is used to measure the cross section as a continuous spectrum in the interesting region below the center of mass energy, though the center of mass energy of the used data is 3.773 GeV. In order to reach the desired precision, it is not sufficient to measure only the processes  $e^+e^- \rightarrow \pi^+\pi^-2\pi^0$ . New precise efficiency studies of the  $\pi^0$  reconstruction as well as detailed measurements of the background processes  $e^+e^- \rightarrow \pi^+\pi^-3\pi^0$  and  $e^+e^- \rightarrow \pi^+\pi^-3\pi^0\gamma_{ISR}$  are necessary. With these efforts it was possible to optimize the systematic uncertainty of the measurement to about 3% in the energy region that is important for  $a_\mu$ . Moreover, the cross section of the process  $e^+e^- \rightarrow \pi^+\pi^-3\pi^0$  is measured in this thesis.



# Contents

|   |           |
|---|-----------|
| <b>1. Introduction</b>  | <b>1</b>  |
| 1.1. The Standard Model of Particle Physics . . . . .                                   | 2         |
| 1.2. The Anomalous Magnetic Moment of the Muon . . . . .                                | 4         |
| 1.3. Experimental Measurement of the Anomalous Magnetic Moment of<br>the Muon . . . . . | 5         |
| 1.4. Standard Model Prediction . . . . .  | 11        |
| 1.4.1. Higher Order QED and Weak Contributions . . . . .                                | 11        |
| 1.4.2. Hadronic Contributions . . . . .   | 12        |
| 1.5. Composition of the Vacuum Polarization Contribution . . . . .                      | 16        |
| <b>2. The BESIII experiment</b>   | <b>19</b> |
| 2.1. The BEPCII Collider . . . . .  | 20        |
| 2.2. The BESIII Detector . . . . .  | 20        |
| 2.2.1. Interaction Region and Beam Pipe . . . . .                                       | 22        |
| 2.2.2. Multilayer Drift Chamber . . . . .   | 22        |
| 2.2.3. Time-of-Flight System . . . . .  | 24        |
| 2.2.4. Electromagnetic Calorimeter . . . . .  | 27        |
| 2.2.5. Superconducting Solenoid Coil . . . . .  | 30        |
| 2.2.6. Muon Chamber . . . . .   | 30        |
| 2.2.7. Trigger System . . . . .   | 30        |
| 2.3. Software Framework . . . . .   | 32        |
| 2.3.1. Geant4 . . . . .   | 32        |
| 2.3.2. CERN ROOT . . . . .  | 33        |
| 2.3.3. BESIII Offline Software System . . . . .   | 33        |
| 2.4. BESIII Data Sets . . . . .   | 34        |
| 2.5. Monte Carlo Simulations . . . . .  | 37        |
| <b>3. Physics of Initial State Radiation</b>  | <b>41</b> |
| 3.1. Leading Order Initial State Radiation . . . . .                                    | 42        |
| 3.2. Next-to-Leading Order Initial State Radiation . . . . .                            | 46        |
| 3.3. Final State Radiation . . . . .  | 47        |
| <b>4. Event Selection</b>   | <b>49</b> |
| 4.1. Event Selection for $e^+e^- \rightarrow \pi^+\pi^-2\pi^0\gamma_{ISR}$ . . . . .    | 52        |

|           |  |            |
|-----------|--|------------|
| 4.2.      | Event Selection for $e^+e^- \rightarrow \omega\pi^0\gamma_{ISR}$ . . . . .   | 60         |
| 4.3.      | Event Selection for the Background . . . . .   | 61         |
| 4.3.1.    | Event Selection for $e^+e^- \rightarrow \pi^+\pi^-3\pi^0\gamma_{ISR}$ . . . . .  | 61         |
| 4.3.2.    | Event Selection for $e^+e^- \rightarrow \omega2\pi^0\gamma_{ISR}$ . . . . .  | 65         |
| 4.3.3.    | Event Selection for $e^+e^- \rightarrow 5\pi\gamma_{ISR}$ excluding $\eta$ , and $e^+e^- \rightarrow \eta\pi^+\pi^-\gamma_{ISR}$ . . . . . | 66         |
| 4.3.4.    | Event Selection for $e^+e^- \rightarrow \pi^+\pi^-3\pi^0$ . . . . .  | 67         |
| 4.3.5.    | Event Selection for $e^+e^- \rightarrow \omega2\pi^0$ . . . . .  | 69         |
| 4.3.6.    | Event Selection for $e^+e^- \rightarrow \eta\pi^+\pi^-$ . . . . .  | 70         |
| 4.4.      | Mass Resolution of the $\pi^+\pi^-2\pi^0$ Mass Spectrum . . . . .  | 71         |
| <b>5.</b> | <b>Background of <math>e^+e^- \rightarrow \pi^+\pi^-2\pi^0\gamma_{ISR}</math></b>  | <b>73</b>  |
| 5.1.      | Correction of the $e^+e^- \rightarrow \pi^+\pi^-3\pi^0$ Background . . . . .   | 76         |
| 5.2.      | Correction of the $e^+e^- \rightarrow \pi^+\pi^-3\pi^0\gamma_{ISR}$ Background . . . . .   | 78         |
| 5.3.      | Normalization of the Remaining $q\bar{q}$ Contribution . . . . .   | 81         |
| 5.4.      | Background Subtraction Crosscheck with the Sideband Subtraction . . . . .  | 85         |
| 5.5.      | Mass Spectrum of $\pi^+\pi^-2\pi^0$ after Background Corrections . . . . .   | 88         |
| <b>6.</b> | <b><math>\pi^0</math> Reconstruction Efficiency</b>  | <b>89</b>  |
| 6.1.      | $\pi^0$ Efficiency in the $J/\psi\pi^0\pi^0$ Channel . . . . .   | 90         |
| 6.1.1.    | Event Selection . . . . .  | 91         |
| 6.1.2.    | Determination of the Efficiency . . . . .  | 94         |
| 6.1.3.    | Systematic Uncertainty . . . . .   | 99         |
| 6.2.      | $\pi^0$ Efficiency in the $\omega\pi^0$ Channel . . . . .  | 99         |
| 6.2.1.    | Event Selection . . . . .  | 100        |
| 6.2.2.    | Determination of the Efficiency . . . . .  | 104        |
| 6.2.3.    | Systematic Uncertainty . . . . .   | 108        |
| 6.3.      | Combined $\pi^0$ Efficiency . . . . .  | 109        |
| 6.3.1.    | Cross Checks and Combination Study . . . . .   | 109        |
| 6.3.2.    | Combining the Results and Combined Fit . . . . .   | 113        |
| <b>7.</b> | <b>Determination of the Cross Sections</b>   | <b>115</b> |
| 7.1.      | Determination of the $e^+e^- \rightarrow \pi^+\pi^-2\pi^0$ Cross Section . . . . .   | 116        |
| 7.1.1.    | Reconstruction Efficiency of $e^+e^- \rightarrow \pi^+\pi^-2\pi^0\gamma_{ISR}$ . . . . .   | 116        |
| 7.1.2.    | Efficiency Correction for $\pi^0$ Reconstruction . . . . .   | 118        |
| 7.1.3.    | Final State Radiation Correction . . . . .   | 119        |
| 7.1.4.    | Vacuum Polarization Correction . . . . .   | 121        |
| 7.1.5.    | Calculation of the ISR Cross Section . . . . .   | 123        |
| 7.1.6.    | Cross Section of $e^+e^- \rightarrow \pi^+\pi^-2\pi^0$ . . . . .   | 124        |
| 7.2.      | Determination of the $e^+e^- \rightarrow \omega\pi^0$ Cross Section . . . . .  | 126        |
| 7.2.1.    | Mass Spectrum of $e^+e^- \rightarrow \omega\pi^0$ . . . . .  | 126        |

|            |  |            |
|------------|--|------------|
| 7.2.2.     | Cross Section of $e^+e^- \rightarrow \omega\pi^0$ . . . . .  | 128        |
| 7.3.       | Determination of the $e^+e^- \rightarrow \pi^+\pi^-3\pi^0$ Cross Section via ISR . . .                               | 129        |
| 7.3.1.     | Mass Spectra of $e^+e^- \rightarrow \omega 2\pi^0\gamma_{ISR}$ and $e^+e^- \rightarrow \eta\pi^+\pi^-\gamma_{ISR}$ . | 129        |
| 7.3.2.     | Reconstruction Efficiency of $e^+e^- \rightarrow \pi^+\pi^-3\pi^0\gamma_{ISR}$ . . . . .                             | 130        |
| 7.3.3.     | Cross Section of $e^+e^- \rightarrow \pi^+\pi^-3\pi^0$ and Sub-Processes via ISR                                     | 131        |
| 7.4.       | Determination of the $e^+e^- \rightarrow \pi^+\pi^-3\pi^0$ Cross Section without ISR .                               | 133        |
| 7.4.1.     | Reconstruction Efficiency of $e^+e^- \rightarrow \pi^+\pi^-3\pi^0$ . . . . .   | 133        |
| 7.4.2.     | Cross Section of $e^+e^- \rightarrow \pi^+\pi^-3\pi^0$ at $\sqrt{s} = 3.773 \text{ GeV}/c^2$ . .                     | 133        |
| <b>8.</b>  | <b>Intermediate Resonances</b>   | <b>135</b> |
| 8.1.       | Intermediate Resonances in $e^+e^- \rightarrow \pi^+\pi^-2\pi^0\gamma_{ISR}$ . . . . .                               | 136        |
| 8.2.       | Intermediate Resonances in $e^+e^- \rightarrow \pi^+\pi^-3\pi^0$ . . . . .   | 139        |
| 8.3.       | Intermediate Resonances in $e^+e^- \rightarrow \pi^+\pi^-3\pi^0\gamma_{ISR}$ . . . . .                               | 139        |
| <b>9.</b>  | <b>Contribution to <math>a_\mu</math></b>  | <b>141</b> |
| 9.1.       | Contribution of $e^+e^- \rightarrow \pi^+\pi^-2\pi^0$ to $a_\mu$ . . . . .   | 142        |
| 9.2.       | Contribution of $e^+e^- \rightarrow \pi^+\pi^-3\pi^0$ to $a_\mu$ . . . . .   | 144        |
| <b>10.</b> | <b>Branching Fractions</b>   | <b>147</b> |
| 10.1.      | Calculation of the Branching Fractions . . . . .   | 148        |
| <b>11.</b> | <b>Systematic Uncertainty Estimations</b>  | <b>151</b> |
| 11.1.      | Signal Efficiencies . . . . .  | 152        |
| 11.1.1.    | $\pi^0$ Reconstruction . . . . .   | 152        |
| 11.1.2.    | Intermediate States . . . . .  | 153        |
| 11.1.3.    | Signal Selection . . . . .   | 156        |
| 11.2.      | Background Subtraction . . . . .   | 157        |
| 11.2.1.    | Systematic Uncertainty Estimation for $e^+e^- \rightarrow \pi^+\pi^-3\pi^0\gamma_{ISR}$                              | 157        |
| 11.2.2.    | Systematic Uncertainty Estimation for $e^+e^- \rightarrow \pi^+\pi^-3\pi^0$ . .                                      | 161        |
| 11.2.3.    | Subtraction of the Dominating Backgrounds . . . . .  | 162        |
| 11.2.4.    | Subtraction of the Remaining Backgrounds . . . . .   | 163        |
| 11.3.      | Summary of the Systematic Uncertainties for $e^+e^- \rightarrow \pi^+\pi^-2\pi^0\gamma_{ISR}$                        | 164        |
| 11.4.      | Systematic Uncertainties for $e^+e^- \rightarrow \omega\pi^0\gamma_{ISR}$ . . . . .                                  | 165        |
| 11.5.      | Systematic Uncertainties for $e^+e^- \rightarrow \omega\pi^0$ . . . . .  | 165        |
| 11.6.      | Systematic Uncertainties for the Branching Fractions . . . . .   | 167        |
| <b>A.</b>  | <b>Data-MC Comparison of Kinematic Variables</b>   | <b>169</b> |
| <b>B.</b>  | <b>Cross Section Tables</b>  | <b>173</b> |



# Chapter 1.

## Introduction

---

*This chapter presents the scientific context of this thesis. First, the Standard Model of particle physics is introduced. The experimental measurement and the theoretical prediction by the Standard Model of the muon's anomalous magnetic moment,  $a_\mu$ , is explained in the following sections. Then it is discussed, how hadronic cross section measurements, performed at  $e^+e^-$  colliders, are used in the calculation of the hadronic vacuum polarization contribution to  $a_\mu$ . Last, an overview of the current experimental and theoretical situation is given.*

---

## 1.1. The Standard Model of Particle Physics

Since the ancient Greek times philosophers tried to model the world with theories in order to find some deeper understanding of nature. Galilei and Newton gave birth to the scientific field of physics in the 16th century by introducing the methods of repeatable experimental measurements and with the theory about the equations of motion. In the late 19th century Maxwell showed with his theory of electrodynamics that completely distinct phenomena, like electric and magnetic interactions, can be explained and described within only one theory of electromagnetism. Albert Einstein revolutionized the understanding of space and time with his theories about special and general relativity. After the birth of quantum mechanics in 1905, triggered by Max Planck, it is the goal of modern physics to explain all observed interactions within only one theory.

The Standard Model (SM) of elementary particle physics represents the theory which incorporates the current knowledge of known matter and its interactions [1], except Gravity. The SM was first proposed by Weinberg, Glashow and Salam. T'Hooft's prove of its renormalizability [2] and the discovery of the asymptotic freedom of the strong interaction by Gross, Wilczek and Politzer [3, 4] confirmed the reliability of the SM. It successfully describes all phenomena of quantum electrodynamics, the weak force, and the strong force in terms of a quantum field theory.

The SM divides all known elementary particles into two groups. The first group consists of the bosonic gauge bosons that act as force carriers. The second group contains the fermionic matter fields. The massless photon,  $\gamma$ , mediates electrodynamic interactions, the  $W^\pm$  and  $Z^0$  bosons carry the weak force. Finally there are 8 gluons,  $g$ , that carry the strong force. The fermionic matter is further divided into quarks ( $u, d, s, c, b, t$ ) and leptons ( $e, \nu_e, \mu, \nu_\mu, \tau, \nu_\tau$ ). All particles couple to the gauge bosons of the weak interaction and all except the three neutrinos,  $\nu$ , interact with the photon. The six quarks couple to the gluons additionally. All fundamental particles of the SM are shown in Fig. 1.1.

For energies above a few GeV, all SM predictions are confirmed by experiment with a very good precision. All the gauge bosons and fermions that were predicted by the SM have indeed been found in several experiments. In particular the prediction of the existence of the  $W^\pm$  and  $Z^0$  bosons [5, 6], as well as the top-quark [7] and the  $\tau$  lepton [8] were milestone achievements of the SM that were granted with Nobel Prizes in physics in 1984, 1990, and 1995, respectively. The most recent and important prediction of the SM was the Higgs boson, which is responsible for the masses of the SM particles via the Higgs-mechanism [9, 10, 11, 12]. The discovery of the Higgs boson in 2012 at the LHC at CERN [13, 14] was a major success of the SM and proved its correctness.

However, the precision of SM predictions is limited in the low energy range.

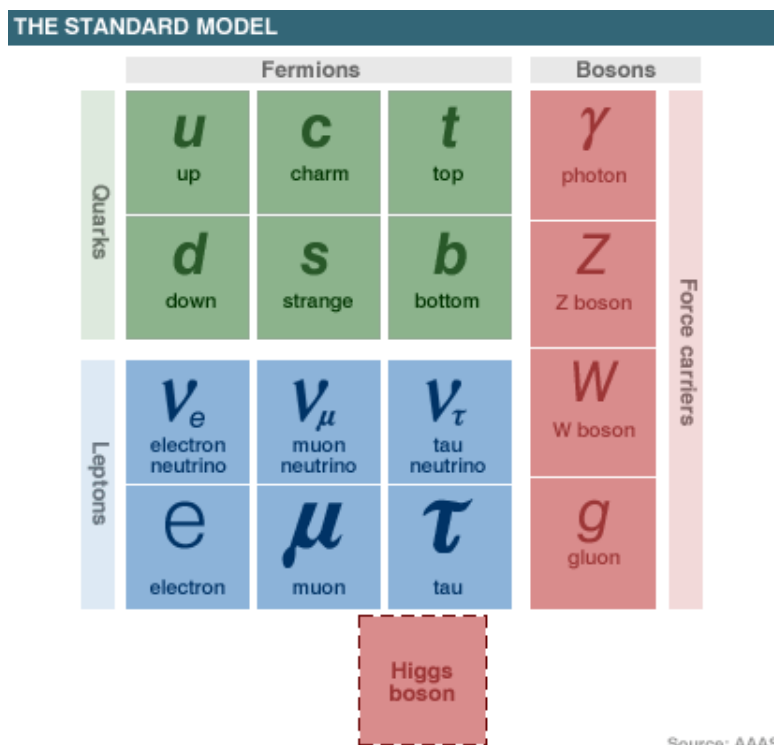


**Figure 1.1.:** Particles of the standard model and their classification.  
[http://www.daviddarling.info/encyclopedia/S/standard\\_model.html](http://www.daviddarling.info/encyclopedia/S/standard_model.html)

Quarks and gluons cannot be observed separately, but only in color neutral bound states, the hadrons. This phenomenon is called confinement. The hadronic bound states cannot be described in the perturbative approach of quantum chromodynamics. Astrophysical observations of galaxy rotations and the accelerated expansion of the universe suggest the existence of dark matter and dark energy, which are not included in the SM. The matter-antimatter asymmetry found in the universe is much stronger than expected from the CP-violation in the CKM [15] mechanism provided by the SM. Moreover, the SM completely ignores gravity. Below the electroweak scale, gravity is so weak, that it can be safely neglected. However, a grand unified theory should explain all phenomena in the universe at all energy scales. The goal of modern physics is to find this grand unified theory. The SM is expected to be the low energy limit of such a theory. Physics beyond the SM does not necessarily need to occur at energy scales above the TeV scale. In fact, there may be unobserved particles with very light masses that have a tiny coupling to the SM particles, even at low energies.

Testing the SM at energy scales below the TeV scale requires observables that can be measured with very high precision. Such quantities are for instance the

running electromagnetic coupling at the scale of the  $Z^0$  mass, and the anomalous magnetic moment of the muon [17],  $a_\mu$ . In fact, a deviation between experiment and the SM prediction of the anomalous magnetic moment of the muon is observed. At present, the significance of this deviation is about three to four standard deviations, which is not yet significant to claim the existence of physics beyond the SM. However, it is regarded as a strong evidence for physics beyond the SM and therefore triggered numerous efforts to clarify whether the deviation is really significant.

The aim of this thesis is to contribute to these efforts by increasing the precision of the SM prediction of  $a_\mu$ , which would shed light on the deviation between experiment and theory. The following sections explain the latest  $(g - 2)_\mu$  experiment and how new high precision measurements of exclusive hadronic reactions in  $e^+e^-$  annihilations can reduce the uncertainty of the SM prediction.

## 1.2. The Anomalous Magnetic Moment of the Muon

All electrically charged leptons have a magnetic moment defined as

$$\vec{\mu} = g_\ell \frac{e}{2m_\ell} \vec{S} \quad , \quad \ell = e, \mu, \tau ,$$

where  $e$  denotes the elementary charge,  $g_\ell$  is the gyro-magnetic factor,  $m_\ell$  is the mass and  $\vec{S}$  the spin of the lepton. This quantity is well suited to perform precision tests of the Standard Model, since it can be measured very precisely in experiments for the electron and muon flavors and it also can be calculated theoretically. In case of the muon with accuracy equal to the experimental precision. Dirac theory predicts  $g_\ell = 2$  for all charged lepton flavors. It describes relativistically a charged spin 1/2 particle in a fixed exterior electromagnetic field [18]. However, Dirac theory neglects that the charged particle influences the exterior electromagnetic field in return. These rebound actions are considered in the SM as quantum corrections and will be explained later. Dirac theory is identical to the leading order contribution of the Standard Model shown in the left panel of Fig. 1.2. Experiments [19] indeed revealed a deviation from  $g_\ell = 2$ . Therefore, the anomalous magnetic moment is defined as the relative deviation from the Dirac solution

$$a_\ell = \frac{1}{2} (g_\ell - 2) \quad , \quad \ell = e, \mu, \tau .$$

Schwinger was the first who derived the first order correction to the anomalous

magnetic moment using quantum electrodynamics (QED) [20]. His result was

$$\begin{aligned} a_\ell^{QED} &= \frac{\alpha}{\pi} K(0) \\ &= \frac{\alpha}{2\pi} \quad , \quad \ell = e, \mu, \tau , \end{aligned} \quad (1.2.1)$$

which is lepton flavor independent. The expression  $K(s) = \int_0^1 dx \frac{x^2(1-x)}{x^2 + \frac{s}{m_\ell^2}(1-x^2)}$  is the kernel-function. The Feynman diagram corresponding to Schwinger's correction is shown in the right panel of Fig. 1.2.

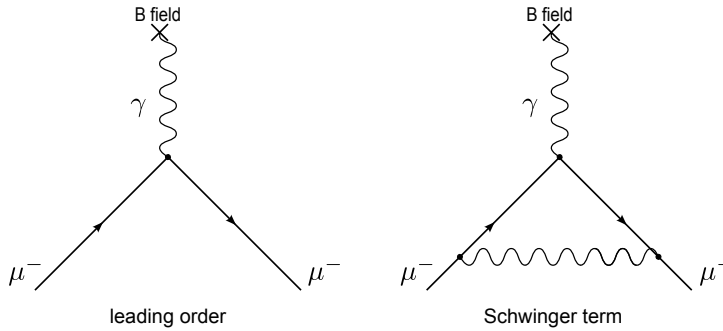


**Figure 1.2.:** Feynman diagrams of  $a_\mu$  for leading order (left) and the Schwinger correction (right).

### 1.3. Experimental Measurement of the Anomalous Magnetic Moment of the Muon

The first measurements of  $(g - 2)_\mu$  were performed in Columbia in 1960 [21] and at CERN between 1961 and 1979 [22, 23, 24]. The last CERN measurement reached an accuracy of a few parts per million. Between 1998 and 2001 the E821 experiment at the Brookhaven National Laboratory (BNL), USA, was measuring  $(g - 2)_\mu$  [25, 26, 27, 28, 29, 30]. The latest result from the BNL experiment is the most precise result on  $(g - 2)_\mu$  up to the time of writing. Its accuracy is 0.54 ppm. The experimental approach of this  $(g - 2)_\mu$  experiment shall be described in more detail.

The Alternating Gradient Synchrotron at BNL provides a proton beam with an energy of 24 GeV. The protons, impinging on a fixed target, produce a secondary charged pion beam. Pions with an energy of 3.1 GeV are filtered out and injected into a storage ring, as depicted in Fig. 1.3. The charged pions,  $\pi^\pm$ , decay via the weak interaction dominantly into polarized muons,  $\mu^\pm$ , and neutrinos,  $\nu$ , as shown

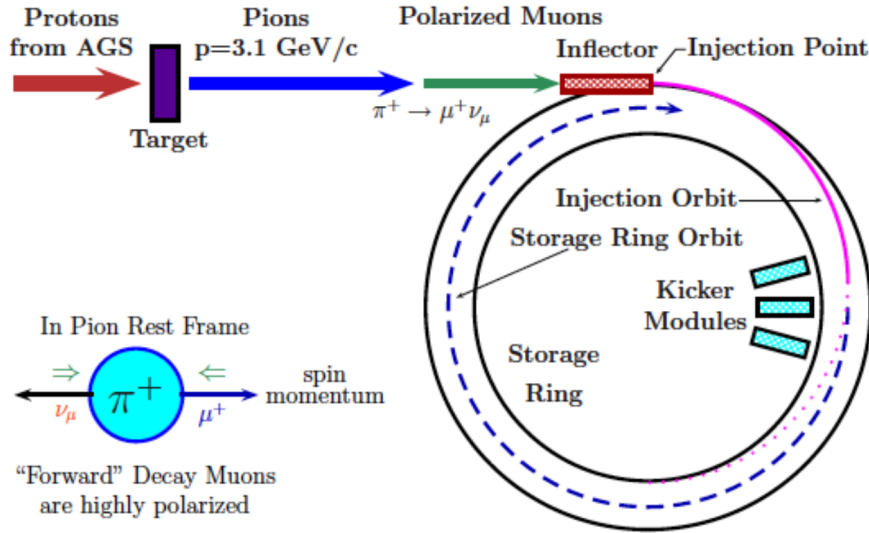


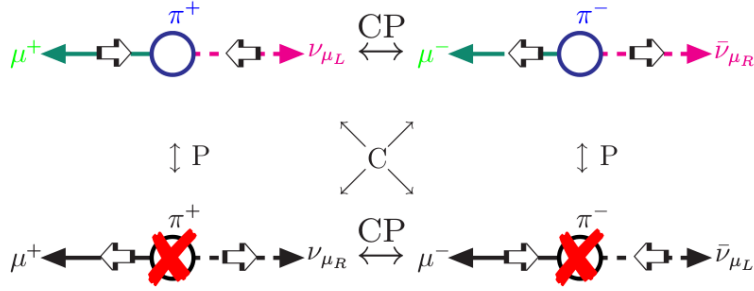
**Figure 1.3.:** Sketch of the experimental setup of the BNL experiment (Figure from [17]).

here for the  $\pi^-$  decay

$$\begin{aligned}\pi^- &\rightarrow \mu^- + \bar{\nu}_\mu \\ \mu^- &\rightarrow e^- + \bar{\nu}_e + \nu_\mu.\end{aligned}$$

The appearance of neutrinos ensures lepton number conservation. The branching fraction of the decay  $\pi^- \rightarrow e^- + \bar{\nu}_e$  is  $1.2 \cdot 10^{-4}$  times smaller than the branching fraction of the decay  $\pi^- \rightarrow \mu^- + \bar{\nu}_\mu$  [31], although the decay involving the electron, which is about 200 times lighter than the muon, is strongly favored by the phase space of the reaction. Due to the parity violation of the weak (vector-axialvector) interaction, only leptons with left-handed chirality and anti-leptons with right-handed chirality couple to the  $W^\pm$  bosons. The spin orientations of the pion decay are illustrated in Fig. 1.4. This decay would be forbidden by spin conservation, since the muon and the (anti-) neutrino can not be left- and right-handed as required by the weak interaction, such that the sum of their helicities add up to the spin of the pion, which is zero. However, helicity is not Lorentz-invariant and there is a probability of  $1 - \beta$  to observe a particle in a rest frame where it has an inverted helicity. The decay width of the pion decay is proportional to  $1 - \beta$ . One obtains  $1 - \beta_e = 2.6 \cdot 10^{-5}$ , if the pion decays into an electron plus an electron anti-neutrino and  $1 - \beta_\mu = 0.72$  for the decay involving a muon. For this reason, the branching fraction of the  $\pi \rightarrow e + \nu_e$  decay is so much smaller than the branching fraction of the  $\pi \rightarrow \mu + \nu_\mu$  decay. This fact is instrumented for the BNL experiment, as it provides a muon yield of nearly 100% from the pion

□  $\mu$ 's produced in pion decays are polarized



□ polarized  $\mu$ 's decay producing electrons carrying the  $\mu$  spin direction

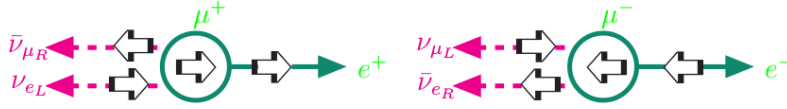


**Figure 1.4.:** Spin transfer properties in the production and the decay of the muons (Figure from [17]).

beam. Moreover, the helicity suppression fixes the polarization of the muons to be oriented into the pion's direction of flight.

Those polarized muons are injected into a storage ring with a diameter of 14 m and a constant magnetic field  $|\vec{B}|$  of 1.45 Tesla. There are electric quadrupoles to focus the beam, which create an additional electric field,  $\vec{E}$ , in the ring. As illustrated in Fig. 1.5, the muon spins precesses with the Lamor frequency

$$\vec{\omega}_L = -\frac{ge\vec{B}}{2m_\mu} - (1 - \gamma) \frac{e\vec{B}}{\gamma m_\mu} + \frac{e}{m_\mu c} \left( \frac{g}{2} - \frac{\gamma^2}{\gamma^2 - 1} \right) \vec{\beta} \times \vec{E} \quad (1.3.1)$$

around their flight direction. The quantity  $e$  is the electric charge of the muon,  $c$  is the speed of light,  $m_\mu$  is the muon mass,  $\vec{\beta}$  is the velocity of the muons in the storage ring and  $\gamma = 1/\sqrt{1 - \beta^2}$  is the relativistic Lorentz factor.

At the same time, inside the storage ring, the muon spin rotates with the cyclotron frequency

$$\vec{\omega}_C = -\frac{ge\vec{B}}{\gamma m_\mu} + \frac{e}{\gamma m_\mu c} \vec{\beta} \times \vec{E}. \quad (1.3.2)$$

Using Eq. 1.3.1 and Eq. 1.3.2, the observed anomalous frequency  $\vec{\omega}_a$  is given by [17]

$$\vec{\omega}_a = \vec{\omega}_L - \vec{\omega}_C = \frac{e}{m_\mu} \left[ a_\mu \vec{B} - \left( a_\mu - \frac{1}{\gamma^2 - 1} \right) \vec{\beta} \times \vec{E} \right]. \quad (1.3.3)$$

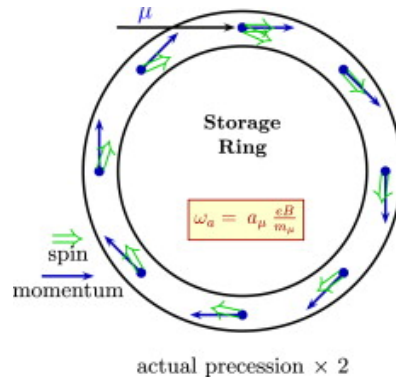


**Figure 1.5.:** Directions of the spin-precession of the BNL experiment (Figure from [17]).

At the so called magic momentum of  $3.098 \text{ GeV}/c$ , which corresponds to  $\gamma = 29.378$ , the expression for the anomalous frequency in Eq. 1.3.3 simplifies to

$$\vec{\omega}_a \simeq \frac{e}{m_\mu} a_\mu \vec{B} \Big|_{p=3.1 \text{ GeV}/c}, \quad (1.3.4)$$

since for this value of  $\gamma$  the electric field term cancels. The magnetic field strength of  $|\vec{B}| = 1.45 \text{ T}$  used at the BNL experiment requires the diameter of the storage ring to be 14 m. The lifetime of the muons in the laboratory frame corresponding to this boost is  $64.54 \mu\text{s}$ , which is long enough to perform a precise experiment. The magnetic field, which is proportional to  $\omega_a$  needs to be measured with high precision. Therefore, the Larmor frequency of the free proton  $\omega_p = \frac{eB}{m_p}$  is measured with a probe of  $\text{H}_2\text{O}$  inside the same magnetic field instrumenting the nuclear-magnetic-resonance (NMR) method. A precision of a 0.05 ppm is achieved using 375 fixed sensors and a mobile device measuring the field at 6000 different positions. The muons will finally decay into electrons or positrons, according to the charge of the muon. Also a neutrino and an anti-neutrino are produced in the decay. The electrons or positrons produced in the muon decay are emitted in the direction of the muon spin. The storage ring is equipped with 24 calorimeters on the inner side. Electrons or positrons with a minimum energy of  $E_{\min} = 1.8 \text{ GeV}$ , that fly to the inner side of the storage ring are detected by the calorimeters, as shown in Fig. 1.6. The number of positrons with a minimum energy of  $E_{\min}$  in the storage ring is exponentially decreasing according to

$$N(t) = N_0(E_{\min}) e^{-\frac{t}{\tau_\mu}} [1 + A(E_{\min}) \sin(\omega_a t + \varphi(E_{\min}))],$$

where  $N_0(E_{\min})$  is a normalization factor,  $\tau_\mu$  is the muon lifetime,  $A(E_{\min})$  is the asymmetry factor reflecting parity violation in the muon decay, and  $\varphi(E_{\min})$  is a phase. A typical count rate as a function of time is depicted in Fig. 1.7. The decay shows a modulation with the anomalous frequency  $\omega_a$ , as expected.

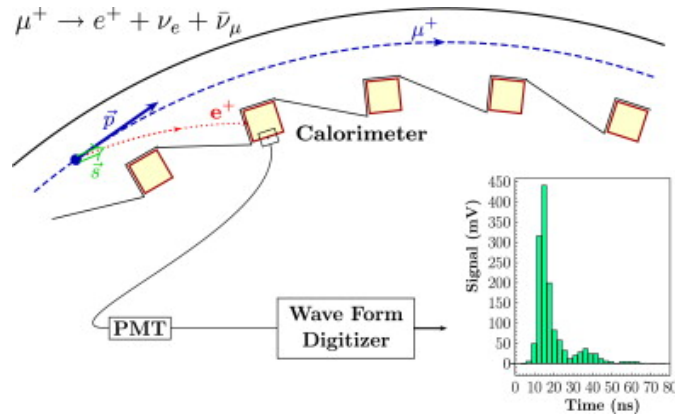


**Figure 1.6.:** Measurement of  $g-2$  of the muon via the decay to an electron (Figure from [17]).

The anomalous magnetic moment of the muon can then be determined via

$$a_\mu = \frac{1}{2} (g_\mu - 2) = \frac{\omega_a}{\omega_p |\mu_\mu / \mu_p| - \omega_a}.$$

The ratio  $|\mu_\mu / \mu_p|$  is given from high precision measurements of the muonium hyperfine structure. Results of some of the  $(g-2)_\mu$  experiments are shown in Tab. 1.1. The world average value of  $a_\mu$  [30], which is completely dominated by the latest

**Table 1.1.:** Results of the Cern and BNL muon  $g-2$  experiments.

| Experiment        | $a_\mu \times 10^{11}$ | $\frac{\Delta a_\mu}{a_\mu}$ [ppm] | ref. |
|-------------------|------------------------|------------------------------------|------|
| CERN $\mu^+$ 1961 | 114500000(2200000)     | 4300                               | [21] |
| CERN $\mu^+$ 1972 | 116616000(31000)       | 270                                | [23] |
| CERN $\mu^+$ 1979 | 116591000(1100)        | 10                                 | [24] |
| CERN $\mu^-$ 1979 | 116593600(1200)        | 10                                 | [24] |
| BNL $\mu^+$ 1997  | 116592510(1500)        | 13                                 | [25] |
| BNL $\mu^+$ 1998  | 116591910(590)         | 5                                  | [26] |
| BNL $\mu^-$ 1999  | 116592020(150)         | 1.3                                | [27] |
| BNL $\mu^+$ 2000  | 116592040(90)          | 0.73                               | [28] |
| BNL $\mu^-$ 2001  | 116592140(90)          | 0.72                               | [29] |

BNL experiments, reads

$$a_\mu^{exp} = 116592080(54)(33) \times 10^{-11} \quad [0.54\text{ppm}] .$$

The anomalous magnetic moment of the muon is one of the most precisely measured quantities of the Standard Model. There are two new experiments in progress

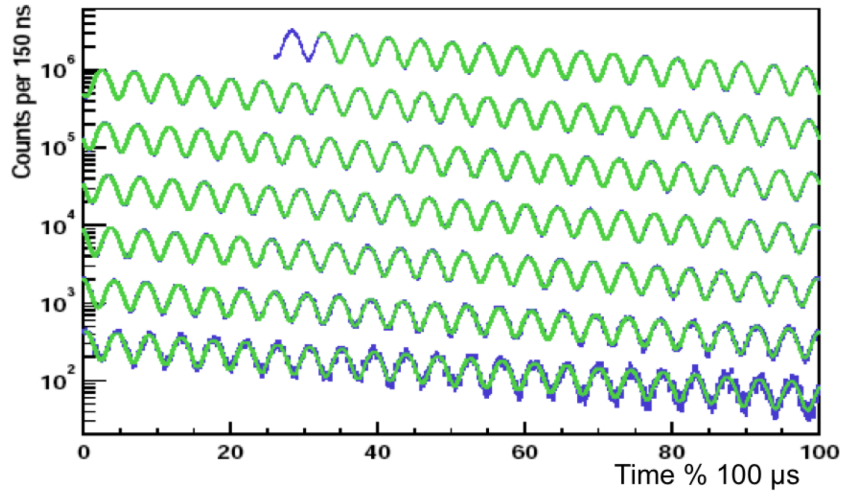


**Figure 1.7.:** Counts of positrons with  $E_{min} > 1.8$  GeV versus the time modulo  $100 \mu\text{s}$  since muon injection. The modulation is at the anomalous precession frequency (Figure from [30]).

to measure  $a_{\mu}^{exp}$  with even higher precision. The storage ring used at BNL was shipped to Fermilab in Chicago, USA, where the accelerator facility can provide higher beam currents, which lead to higher statistics for the  $a_{\mu}^{exp}$  measurement [32]. The experimental setup is also improved in order to reduce the systematic uncertainties. For this reason the knowledge of NMR trolley location and its temperature changes is improved. More NMR probes are installed and a new temperature control stabilizes the heat in the experimental hall. Moreover, the full probe waveforms are stored to measure at higher gradients in the magnetic field. The calorimeters are segmented to achieve temporal separation of the signals. This reduces the systematic uncertainties due to the calorimeter pile-up. A laser based calibration system is instrumented to improve the intra-fill gain stability of the calorimeters.

The magnet is ready since September 2015. The calibration of the passive shimming tools was completed in October 2015. In August 2016, the shimming procedure was completed and a highly uniform magnetic field is achieved. A first run of data taking for commissioning started in July 2017. The commissioning phase is planned to finish in November 2017. First results are expected in the end of 2018 or 2019.

The other experiment is located at the Japan Proton Accelerator Research Complex (J-PARC) in Tokai, Japan [33]. A new method using an ultra-cold muon beam will be instrumented, which provides a completely independent approach to measure  $a_{\mu}^{exp}$ . Both experiments aim for a precision in the order of 0.1 ppm, which reduces the error of the existing results by a factor of four.

## 1.4. Standard Model Prediction

In this section, the theoretical calculation of the muon anomalous magnetic moment within the SM is explained. The description of Ref. [17] is followed.

Schwinger's calculation on the anomalous magnetic moment given in Eq. 1.2.1, which was introduced in section 1.2 is independent of the lepton flavor and provides the most sizable correction to  $(g-2)_\mu$ . This correction is equal to the leading order correction obtained with the SM. In order to obtain a more precise value of the anomalous magnetic moment of the muon,  $a_\mu$ , higher order corrections have to be taken into account. These higher order corrections depend on the lepton mass. The anomalous magnetic moment of the muon can be additively decomposed in terms of the three forces contained in the SM

$$a_\mu = a_\mu^{\text{QED}} + a_\mu^{\text{weak}} + a_\mu^{\text{had}}. \quad (1.4.1)$$

### 1.4.1. Higher Order QED and Weak Contributions

The quantum electrodynamic (QED) part  $a_\mu^{\text{QED}}$  in Eq. 1.4.1 has been calculated up to tenth order in perturbation theory, which corresponds to five the loop correction [34]. It only contains radiative corrections involving photons and leptons as illustrated in Fig. 1.8. Up to the third order the contributions are known ana-

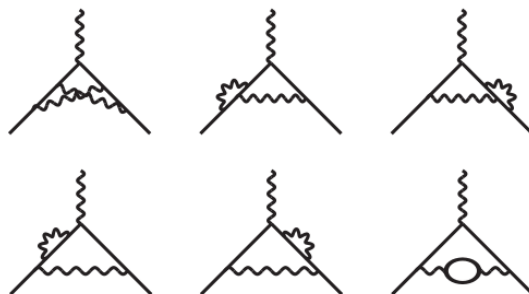


**Figure 1.8.:** Some diagrams of the second order QED corrections (Figure from [17]).

lytically, whereas the fourth and the fifth order have been calculated numerically. Recently, the parts of the four loop corrections containing only electron loops or electron and tau loops have been calculated analytically [35] to cross check the numeric results.

Also the weak part  $a_\mu^{\text{weak}}$  in Eq. 1.4.1 has been evolved to a high precision. After the discovery of the Higgs boson, the electroweak contributions involving the W and Z bosons as well as the Higgs boson itself were recalculated using the correct Higgs mass [36]. The most important electroweak Feynman diagrams are shown in Fig. 1.9. The QED and weak contributions are

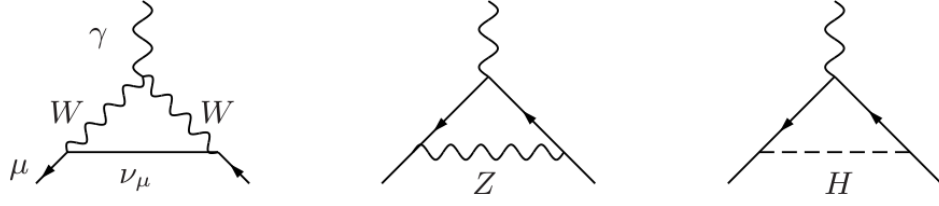


**Figure 1.9.:** Leading order contributions to  $a_\mu^{\text{weak}}$  of the weak interaction. (Figure from [17].)

$$a_\mu^{\text{QED}} = (116584718.104 \pm 0.148) \times 10^{-11} [34] \quad \text{and}$$

$$a_\mu^{\text{weak}} = (153.6 \pm 1.0) \times 10^{-11} [36].$$

### 1.4.2. Hadronic Contributions

The hadronic contribution  $a_\mu^{\text{had}}$  in Eq. 1.4.1 cannot be calculated using perturbative quantum chromodynamics (QCD), since this theory is not valid at low energies due to confinement. The running coupling  $\alpha_S(E)$  of the non-Abelian  $SU(3)_c$  gauge theory, which is the basis of QCD, has a pole at  $E = 0$ . The hadronic contribution can be decomposed into three parts

$$a_\mu^{\text{had}} = a_\mu^{\text{HVP,LO}} + a_\mu^{\text{HVP,HO}} + a_\mu^{\text{LbL}},$$

as is illustrated in Fig. 1.10.

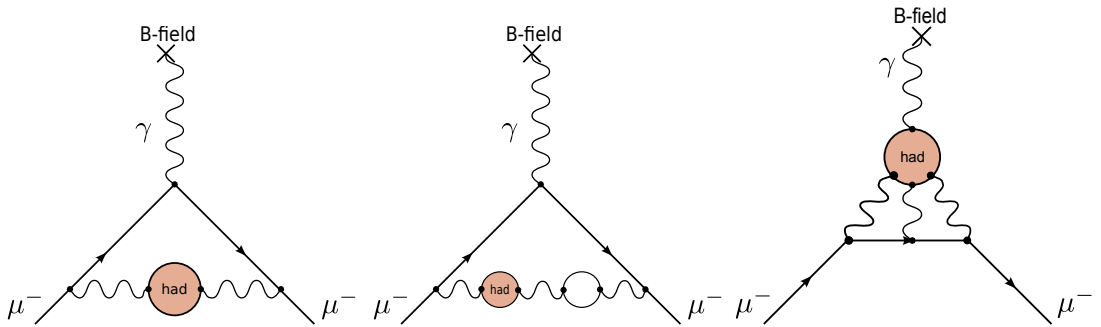


**Figure 1.10.:** Leading-order (LO) hadronic vacuum polarization (HVP) corrections (left), higher-order HVP corrections (middle) and hadronic light-by-light scattering corrections (right) to  $a_\mu^{\text{had}}$ .

The hadronic light-by-light scattering corrections (HLbL) are not subject of this thesis. These contributions can not be determined in a model-independent way.

Experimental input of space-like as well as time-like transition form-factors of processes of the type  $\gamma^*\gamma^{(*)} \rightarrow \pi^0, \eta, \eta', \pi^+\pi^-, \pi^0\pi^0$  and  $e^+e^- \rightarrow \gamma\pi^0, \gamma\eta, \gamma\eta'$  or  $\pi^0, \eta, \eta' \rightarrow \gamma^*\gamma^{(*)}$  are used to validate the hadronic models used in the calculations. A calculation of the HLbL contribution to  $a_\mu^{\text{had}}$ , which is very often used, was calculated by Knecht and Nyffeler [37] and reads

$$a_\mu^{\text{HLbL}} = (116 \pm 39) \times 10^{-11}. \quad (1.4.2)$$

The leading order hadronic vacuum polarization (HVP) correction  $a_\mu^{\text{HVP,LO}}$  is closely related to the topic of this thesis and will now be investigated in more detail. The first step in the calculation of  $a_\mu^{\text{HVP,LO}}$  is to dress the photon propagator according to

$$\frac{1}{q^2} \longrightarrow \int_0^\infty \frac{ds}{s\pi} \frac{\text{Im} \Pi_\gamma(s)}{q^2 - s}, \quad (1.4.3)$$

where  $\Pi_\gamma(s)$  is the photon self-energy-function. Fig. 1.11 illustrates the dressing of the photon propagator.

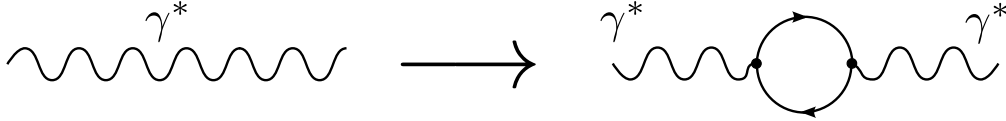


**Figure 1.11.:** Next-to-leading order correction to the photon self-energy

The photon self-energy-function can be calculated analytically for leptons, where the result is  $\text{Im} \Pi_\gamma(s) = \sqrt{1 - \frac{4m_\ell}{s}} \left(1 + \frac{2m_\ell}{s}\right)$ , which is a part of the NLO QED contribution.

In the case of quarks in the loop, an analytic calculation is not possible anymore due to the non-perturbative nature of QCD. However, the loop can be calculated using experimental data. The optical theorem,

$$\sigma(s)_{e^+e^- \rightarrow \text{hadrons}} = \frac{4\pi\alpha}{s} \text{Im} \Pi_\gamma(s), \quad (1.4.4)$$

which is illustrated in Fig. 1.12, relates the total hadronic cross section  $\sigma(s)_{e^+e^- \rightarrow \text{hadrons}}$  to the desired photon self-energy-function.

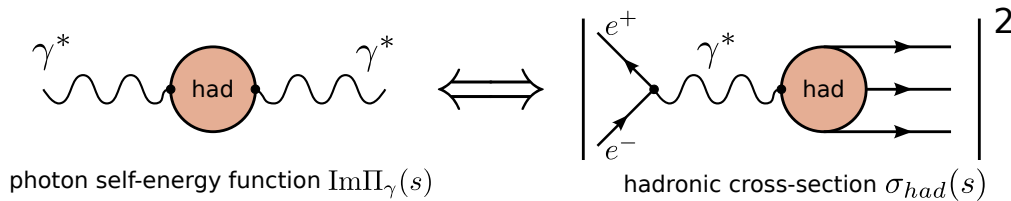


**Figure 1.12.:** Relation between the photon self-energy-function and the hadronic cross sections.

Extending Schwinger's result from Eq. 1.2.1 by involving the dressed photon propagator from Eq. 1.4.3 and applying the optical theorem from Eq. 1.4.4, the anomalous magnetic moment can be determined via the dispersion integral [17]

$$\begin{aligned}
a_\mu^{\text{HVP,LO}} &= \frac{\alpha}{\pi} \int_0^\infty \frac{ds}{s\pi} K(s) \text{Im} \Pi_\gamma(s) \\
&= \frac{1}{4\pi^3} \int_0^\infty ds K(s) \sigma(s)_{e^+e^- \rightarrow \text{hadrons}} \\
&= \left( \frac{\alpha m_\mu}{3\pi} \right)^2 \int_0^\infty ds \frac{\hat{K}(s) R_\gamma(s)}{s^2}.
\end{aligned} \tag{1.4.5}$$

Again,  $K(s) = \frac{m_\mu^2}{3s} \hat{K}(s) = \int_0^1 dx \frac{x^2(1-x)}{x^2 + \frac{s}{m_\mu^2}(1-x^2)}$  is the analytically known kernel function as used before in Eq. 1.2.1, and  $R_\gamma(s) = \frac{3s}{4\pi\alpha^2} \sigma(e^+e^- \rightarrow \text{hadrons})$  is the hadronic  $R$ -ratio. The integral to determine  $a_\mu^{\text{HVP,LO}}$  can be split up into a region where perturbative QCD fails and another where it can be applied. In the low energy region  $m_\pi < \sqrt{s} < 1.8 \text{ GeV}$ , experimental data from  $e^+e^-$ -colliders are needed as input using the optical theorem. The composition of the quantity  $a_\mu^{\text{VP}}$  is explained in further detail in the following section 1.5. In the region  $1.8 < \sqrt{s} < 5.0 \text{ GeV}$  inclusive R-scan measurements from PLUTO [38], Crystal Ball [39] and BES [40] are used for the calculation of the integral. In the remaining region  $\sqrt{s} > 5.0 \text{ GeV}$  perturbative QCD can be used safely [17]. The latest results obtained by two independent theory groups are in good agreement with each other

$$\begin{aligned}
a_\mu^{\text{HVP,LO}} &= (6922 \pm 25) \times 10^{-11} [41], \\
a_\mu^{\text{HVP,LO}} &= (6926 \pm 33) \times 10^{-11} [42].
\end{aligned} \tag{1.4.6}$$

Among the QCD contributions shown in Fig. 1.10, this contribution is the largest, both in terms of the absolute value and the uncertainty. The higher order vacuum polarization corrections  $a_\mu^{\text{HVP,HO}}$  involve multiple blobs, as shown in the middle panel of Fig. 1.10, but their contribution is much smaller than the leading order one. They have been calculated to be [17]

$$a_\mu^{\text{VP,HO}} = (-97.9 \pm 0.9) \times 10^{-11}. \tag{1.4.7}$$

Combining all contributions from Eq. 1.4.2, Eq. 1.4.6 and Eq. 1.4.7, the total value for the SM prediction of the anomalous magnetic moment of the muon results in

$$a_\mu^{\text{theo}} = (116595802 \pm 42 \pm 26 \pm 2) \times 10^{-11}.$$

The difference between the experimental result from Eq. 1.3 in section 1.2 and the theoretical calculation is

$$a_\mu^{exp} - a_\mu^{theo} = (268 \pm 76) \times 10^{-11}.$$

This deviation between experiment and theory corresponds to a statistical significance of  $3.6\sigma$ . Several theory groups have published SM predictions of  $a_\mu$ . Some older ones are based on the  $\tau$  spectral functions instead of the  $e^+e^-$ -collider data for the hadronic cross section data to be used in the HVP contribution to  $(g-2)_\mu$ , or have modified ranges of the dispersion integral from Eq. 1.4.5. The deviations between the BNL measurement and several SM predictions are displayed in Fig. 1.13. All SM predictions confirm the difference of more than two standard deviations. A significance of  $5\sigma$  would be a good hint at physics beyond the Stan-

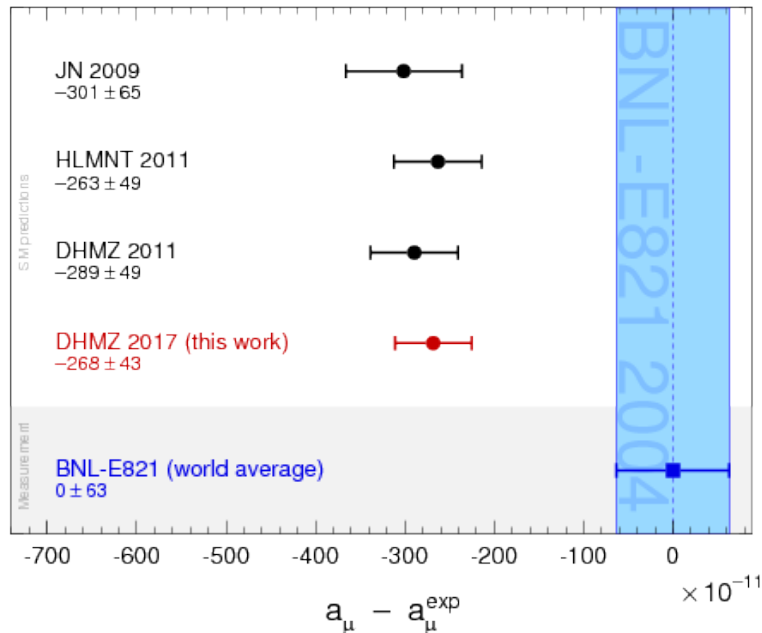


**Figure 1.13.:** Deviation between theoretical predictions and the experimental value of  $a_\mu$  (Figure from [42]).

standard Model to cause the deviation. The objective of this thesis is to perform a new precise measurement of the  $e^+e^- \rightarrow \pi^+\pi^-2\pi^0$  cross section in order to reduce the uncertainty of the vacuum polarization contribution  $a_\mu^{\text{HVP,LO}}$ .

## 1.5. Composition of the Vacuum Polarization Contribution

The dispersion integral shown in Eq. 1.4.5 is used to relate the vacuum polarization contribution  $a_\mu^{\text{HVP,LO}}$  to hadronic cross sections measured in  $e^+e^-$  annihilations [43]. The integrand of Eq. 1.4.5 is proportional to  $s^{-2}$ . This implies, that cross sections at low energies for example in the  $\rho$  resonance region dominate  $a_\mu^{\text{HVP,LO}}$ . Nevertheless, all hadronic cross sections up to 1.8 GeV are needed to gain the desired precision. The left-hand chart of Fig. 1.14 shows the relative contribution of different energy regions to the dispersion integral from Eq. 1.4.5. The (squared) errors are presented in the right-hand chart of Fig. 1.14. The en-

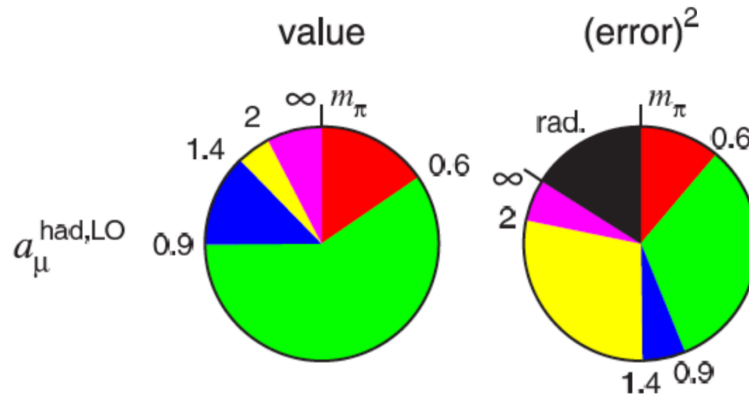


**Figure 1.14.:** Distribution of the contribution (left) and uncertainties (right) to  $a_\mu^{\text{HVP,LO}}$  (Figure from [43]).

ergy region between the pion mass threshold and 900 MeV is dominated by the  $\rho$  and  $\omega$  resonances, which subsequently can be observed in the hadronic channels  $e^+e^- \rightarrow \pi^+\pi^-$  and  $e^+e^- \rightarrow \pi^+\pi^-\pi^0$ . 73% of the contribution stems from the  $e^+e^- \rightarrow \pi^+\pi^-$  process, containing the  $\rho$  and  $\omega$  resonances and in their interference. This hadronic cross section has been measured in the  $e^+e^-$  collision experiments TOF [44], OLYA [45], CMD [46], CMD-2 [47, 48, 49, 50, 51], SND [52], DM1 [53], DM2 [54], KLOE [55, 56, 57, 58], BABAR [59] and BESIII [60]. The cross section is shown in Fig. 1.15. The BABAR, KLOE and BESIII measurements claim an uncertainty below 1%. However, there is a discrepancy of about  $2\sigma$  between the BABAR and KLOE measurements. The newest BESIII measurement [60] rather favors the KLOE results. Many hadronic processes contribute in the energy region between 900 MeV and 1.8 GeV, such as  $e^+e^- \rightarrow \pi^+\pi^-\pi^0$ ,  $\pi^+\pi^-\pi^+\pi^-$ ,  $\pi^+\pi^-2\pi^0$ ,  $\pi^+\pi^-\eta$ ,  $\pi^+\pi^-3\pi^0$ ,  $K\bar{K}$ ,  $K\bar{K}\pi$ .

The channel  $e^+e^- \rightarrow \pi^+\pi^-2\pi^0$ , which is topic of this thesis, has been measured previously by ACO [61], M3N [62], MEA [63], GG2 [64], OLYA [65], DM2 [66], ND [67], CMD-2 [68], SND [69]. A new result from BABAR was released in September 2017 [70] just before finalizing this thesis. The cross sections determined

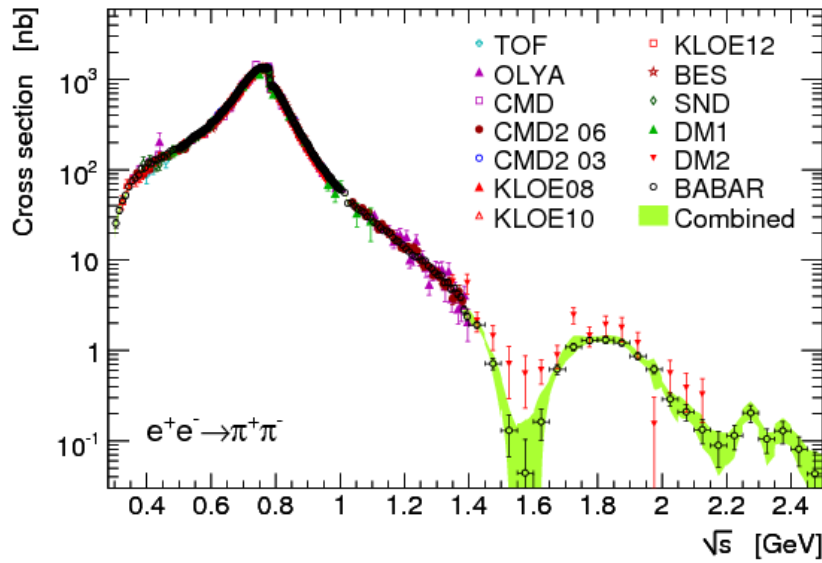


**Figure 1.15.:**  $e^+e^- \rightarrow \pi^+\pi^-$  cross section as function of center of mass energy (Figure from [42]).

by these experiments are shown in Fig. 1.16. The error bars show statistical errors only. The uncertainty of the  $e^+e^- \rightarrow \pi^+\pi^-2\pi^0$  channel has a large contribution to the uncertainty of  $a_\mu^{\text{HVP,LO}}$ . Hence, it needs further investigations to improve it. This is the main goal of this thesis.

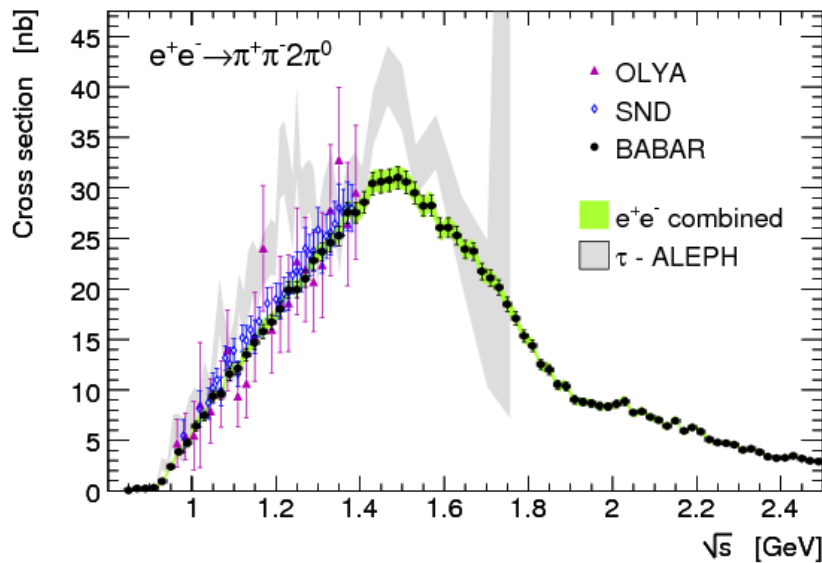


**Figure 1.16.:** Measurements of the cross section  $e^+e^- \rightarrow \pi^+\pi^-2\pi^0$  (Figure from [42]).



## Chapter 2.

# The BESIII experiment

---

*This thesis is based on experimental data taken by the BESIII detector operated at the BEPCII accelerator ring facility located at the Institute for High Energy Physics in Beijing, China. This chapter gives an overview of the BEPCII accelerator and storage ring, as well as the BESIII detector. In addition to all detector components, the software frameworks used for this thesis are described.*

---

## 2.1. The BEPCII Collider

The BESIII experiment is located at the BEPCII (Beijing Electron Positron Collider II) accelerator in Beijing, China, shown in the left panel of Fig. 2.1. The

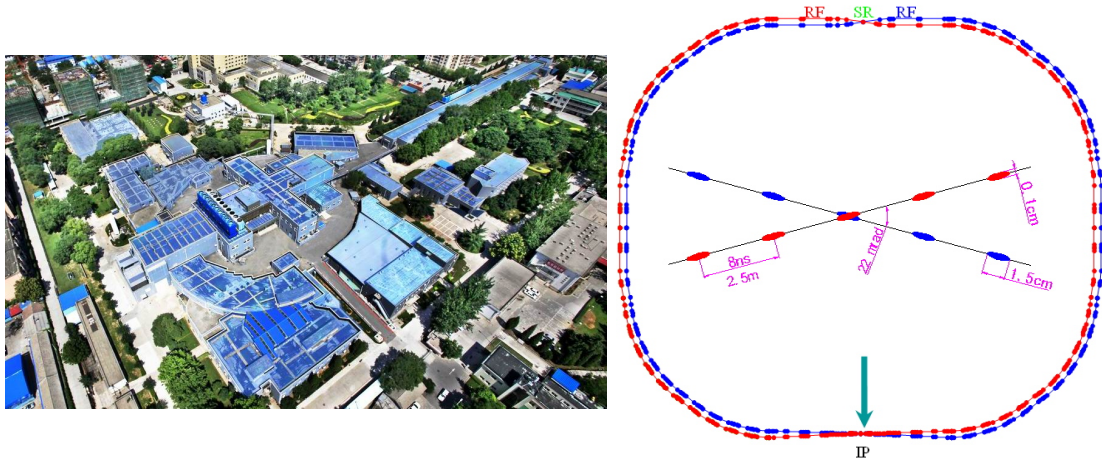


**Figure 2.1.:** BEPCII accelerator facility (left) and the storage rings (right) [71].

accelerator facility BEPCII, which was built in 2008, consists of an electron gun, a positron source, a linear accelerator (linac) and two storage rings. The left panel of Fig. 2.1 shows an aerial view of the BEPCII accelerator facility. The electron gun and the positron source produce pulsed bunches of electrons or positrons every 8 ns. The bunch length is 1.5 cm and the beam current is 0.91 A per beam. These bunches are inserted to the linac and accelerated by synchronized radio-frequency electromagnetic pulses. The beam energy can be set between 1 – 2.3 GeV. At the end of the linac, the electrons and positrons are injected to the two independent storage rings, as shown in the right panel of Fig. 2.1. 93 bunches can be stored in each ring with a beam current of up to 0.91 A. The two beams can be collided with a horizontal crossing angle of 11 mrad at the interaction point, where the Beijing Spectrometer III (BESIII) detector is located. All the design parameters are summarized in Table 2.1. The center of mass energy of the colliding beams is in the range between 2 – 4.6 GeV. The peak instantaneous luminosity is  $10^{33} \text{ cm}^{-2} \text{ s}^{-1}$  at beam energies of 1.89 GeV. The design luminosity of  $10^{33} \text{ cm}^{-2} \text{ s}^{-1}$  was reached in 2016, but data taking is still in progress.

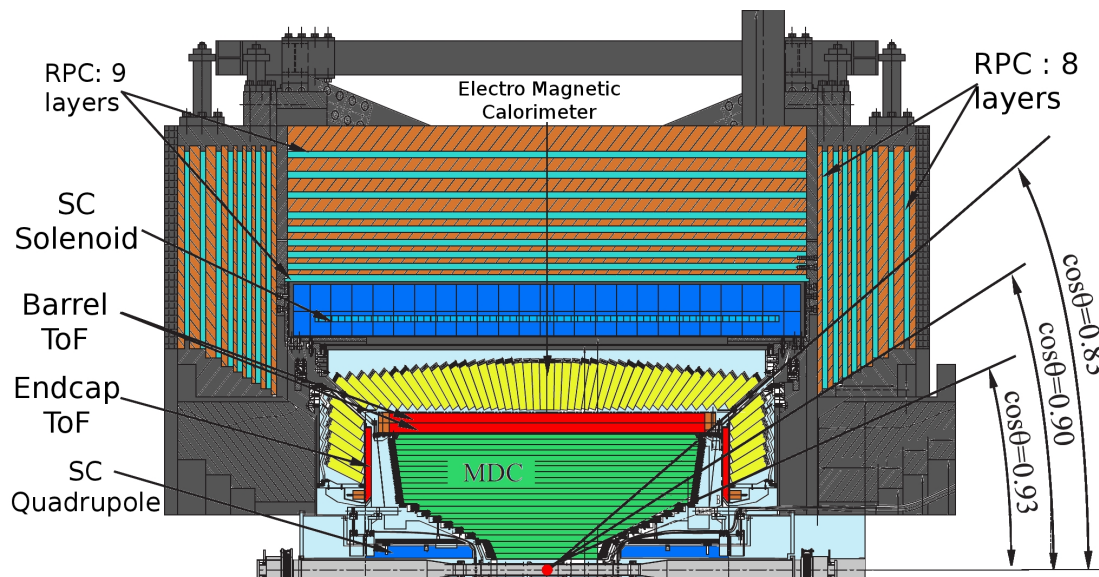
## 2.2. The BESIII Detector

The BESIII detector is described in full detail in Ref. [72]. A cross section of the detector is shown in Fig. 2.2. It is a cylindrical shaped multi purpose detector

**Table 2.1.:** Parameters of the BEPCII accelerator

|  |   |
|--|---|
| Center-of-mass-energy                          | 2 - 4.6 GeV                                 |
| Designed Peak luminosity at $2 \cdot 1.89$ GeV | $\sim 10^{33} \text{cm}^{-2} \text{s}^{-1}$ |
| Number of bunches                              | $2 \cdot 93$                                |
| Beam current                                   | $2 \cdot 0.91$ A                            |
| Bunch spacing                                  | 2.4 m / 8 ns                                |
| Bunch length                                   | 1.5 cm                                      |
| Relative energy spread                         | $5 \cdot 10^{-4}$                           |
| Crossing angle                                 | $\pm 11$ mrad                               |

providing systems to detect and reconstruct charged and neutral particles. The most inner part of the detector is the beam pipe, where the electron and positron bunches collide. The beam pipe is surrounded by the multilayer drift chamber (MDC). The next sub-detector is the time-of-flight system (TOF). Then follows the electromagnetic calorimeter (EMC). A superconducting magnet creates a homogeneous magnetic field with a strength of 1 T inside the beam pipe, the MDC, the TOF and the EMC. Most outside, there is a muon chamber (MUC). All the sub detector systems will be explained in detail in the following.

**Figure 2.2.:** Cross-sectional view of the upper half of the BESIII detector with its components.

### 2.2.1. Interaction Region and Beam Pipe

The electron and positron beams delivered by BEPCII are focused to the interaction point (IP) by six pairs of quadrupole magnets and two beam bending dipoles. The beams collide with a crossing angle of 11 mrad. The interaction region is covered by the 29.6 cm long beam pipe made of a 0.6 mm thick Beryllium tube to shield the vacuum pressure of  $5 \cdot 10^{-10}$  torr at the IP. The central Beryllium part is welded on double wall copper extensions. A cross-sectional view of the beam pipe is shown in Fig. 2.3. Beryllium has a low density and a low atomic number. This minimizes multiple scattering of the particles produced in the  $e^+e^-$  collisions in the beam pipe material. Moreover, Beryllium has good thermal and electric conductivity in order to withstand the heat load and radio frequency radiation from the beam bunches. The beam pipe is actively cooled with mineral oil.

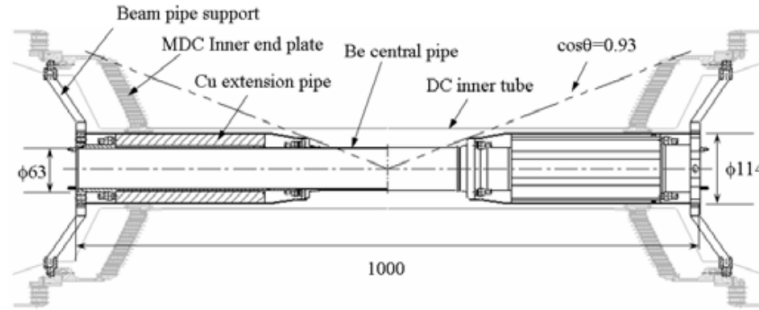
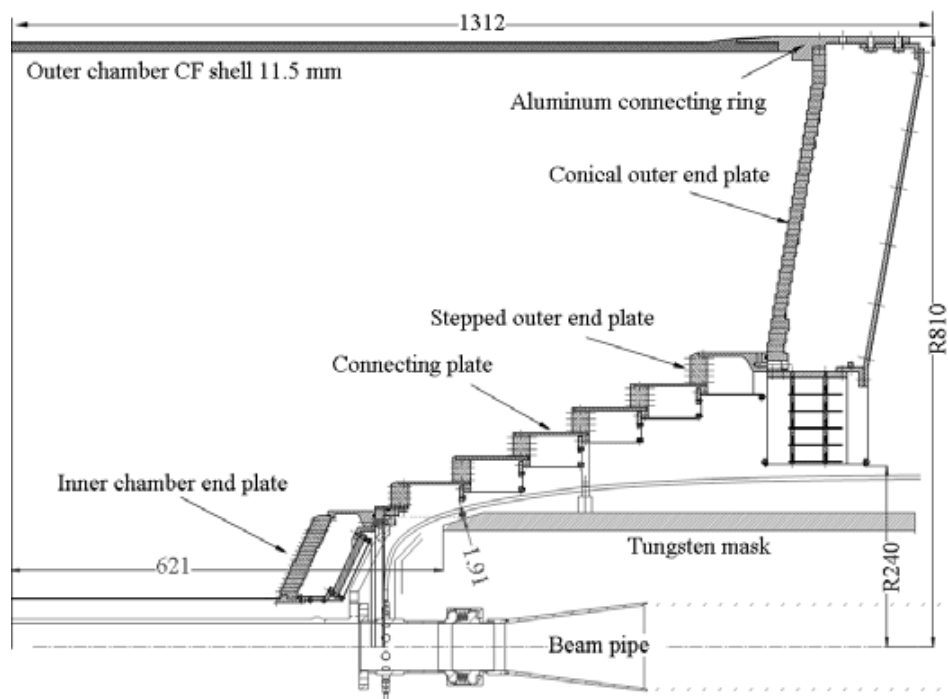


Figure 2.3.: Cross-sectional view of the beam pipe. (Drawing form [72].)

### 2.2.2. Multilayer Drift Chamber

The cylindrical shaped Multilayer Drift Chamber (MDC) is the most important sub-detector system to measure the momentum of charged particles. Moreover, the energy loss per path length  $dE/dx$  of a charged particle can be measured with the MDC, which is needed for particle identification. The MDC consists of an inner and an outer chamber. The inner chamber is installed directly around the beam pipe and is also joined together with the outer chamber. There are 43 layers of  $25 \mu\text{m}$  thick sense wires arranged stepped conically around the beam pipe as depicted in Fig.2.4, making 6796 sense wires in total. The radius of the most inner layer is 59 mm and of the most outer one is 810 mm. In total a polar angle of  $|\cos \theta| < 0.93$  is covered. Each sense wire is surrounded by 8 field wires. Neighboring sense wires share the field wires in between. This unit is called drift cell and its radial position resolution is better than  $130 \mu\text{m}$ . In order to achieve an axial resolution, the layers 1-8 and 21-36 are arranged as small angle stereo layers.



**Figure 2.4.:** Mechanical structure of the MDC. (Drawing from [72].)

These small angle stereo layers are rotated by  $3^\circ - 4^\circ$  against the normal axial arranged layers. This yields an axial position resolution better than 4 mm for the charged tracks. The entire MDC is filled with a mixture of 60% He and 40%  $C_3H_8$  gas at a pressure of 3 mbar above the ambient atmospheric pressure. The mixture reduces the multiple scattering effect of charged particles crossing the MDC, while the  $dE/dx$  resolution remains at the reasonable value of 6%.

The uniform axial magnetic field induced by the superconducting magnet, that surrounds the MDC allows to measure the momentum of charged tracks passing the MDC. The momentum resolution is limited by the position resolution of the single wires and the effect of multiple scattering of the tracks in the gas or the wires of the MDC. For a track with a transversal momentum of 1 GeV/ $c$  the momentum resolution is better than 0.5%. The MDC design parameters are summarized in Table 2.2.

The MDC readout electronics system has to process 6796 sense wires. A block diagram of the readout electronics system is shown in Fig. 2.5. The main components of the readout system are listed below.

- Pre-amplifier
- Charge and Time measurement module (MQT)

**Table 2.2.:** MDC design parameters.

|                                  |  |
|----------------------------------|--|
| radius inner chamber             | 86 mm                                      |
| radius outer chamber             | 810 mm                                     |
| total length                     | 2400 mm                                    |
| angular acceptance inner chamber | $ \cos \theta  < 0.93$                     |
| angular acceptance outer chamber | $ \cos \theta  < 0.83$                     |
| number of layers                 | 43   |
| sense wire                       | gold-plated W, diameter $25 \mu\text{m}$   |
| field wire                       | gold-plated Al, diameter $110 \mu\text{m}$ |
| transverse momentum resolution   | $< 0.5\%$ for 1 GeV tracks at $90^\circ$   |
| dE/dx resolution                 | 6%   |
| single wire resolution           | $< 130 \mu\text{m}$                        |
| position uncertainty             | $< 0.4 \text{ mm}$                         |

- Type I und II fan-out modules (MF-I/II)
- Readout control module (MROC)
- Trigger interface module (MTI)
- PowerPC controller (PPC)

After being amplified by fast trans-impedance preamplifiers, the sense wire signals are sent to the readout crates. Here the signals are split into three branches in order to measure the charge and the timing information and to give input to the L1 trigger, which will be described later on. The digitalization of the timing signal is performed by CERN HPTDC chips [73]. The trigger is provided with the discriminated timing signals. The branch of the incoming wire signal used for charge determination is shaped and integrated by charge amplifiers. The digitalization of this signal type is then performed with analog-to-digital-converter (ADC) chips. The digitalized signals are further processed by FPGA chips for digital integration to obtain the total charge and to send it to the data-acquisition system (DAQ) at the online farm to be stored on hard-disk for further track reconstruction and physics analyses.

### 2.2.3. Time-of-Flight System

The time-of-flight (TOF) sub-detector system consists of a barrel part and two end cap parts. The barrel TOF detector is made of two staggered layers of plastic scintillators with photomultiplier tube (PMT) readouts at both ends of the scintillator plates. The end caps only have a single layer of plastic scintillators, also with

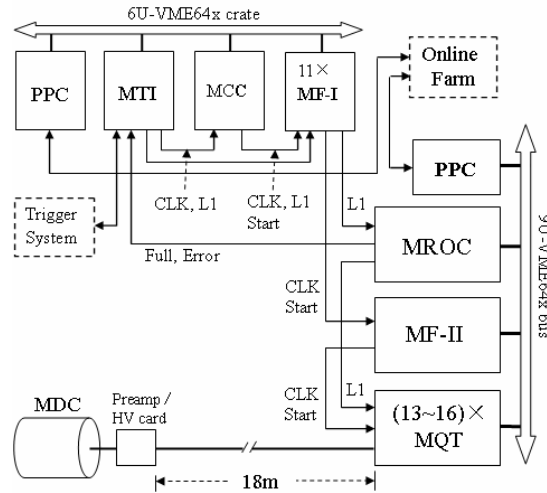


**Figure 2.5.:** Block diagram of the MDC readout electronics. (Drawing from [72].)

PMT readouts. The thickness of each layer is 5 cm. The inner radius of the first layer in the barrel is 0.81 m, which is exactly on top of the MDC outer edges. The scintillator layers of the barrel TOF detector are 2.3 m long. The end cap part of the TOF system is placed behind the end plates of the outer MDC chamber with an inner radius of 1.15 m. The polar angle coverage is  $|\cos\theta| < 0.82$  for the barrel and  $0.85 < |\cos\theta| < 0.95$  for the end caps. A gap exists between the barrel and the end caps containing support structures for the MDC. Each layer in the barrel contains 88 plastic scintillation counters of the type BICRON BC-408. The end caps are made of 48 trapezoidal scintillation counters.

The time resolution of the TOF system is 80 ps for the two layers in the barrel and 110 ps in for the single layer system in the end caps for muons with a momentum of 1 GeV/c. The main contributions to these uncertainties stem from the scintillator counter intrinsic time resolution, the global timing marker (accelerator RF clock), the determination of the interaction vertex of the 15 mm long electron/positron bunches, the uncertainty of the axial position of the hit points including light propagation speed in the scintillator, the time resolution of the readout electronics and the uncertainty of the expected flight time calculated from the momentum measured from the MDC (0.5% momentum resolution). For other particles like kaons, pions and protons, the time resolution is approximately 20% larger. The simulated K/ $\pi$  separation capability of the barrel TOF is shown in Fig. 2.6. The thick solid line represents the time difference between kaons and pions arriving at the inner TOF layer that is necessary to separate kaons and pions with a significance of 3 standard deviations as function of the polar angle. The dashed thick line represents the same if both layers are used. Kaons and pions

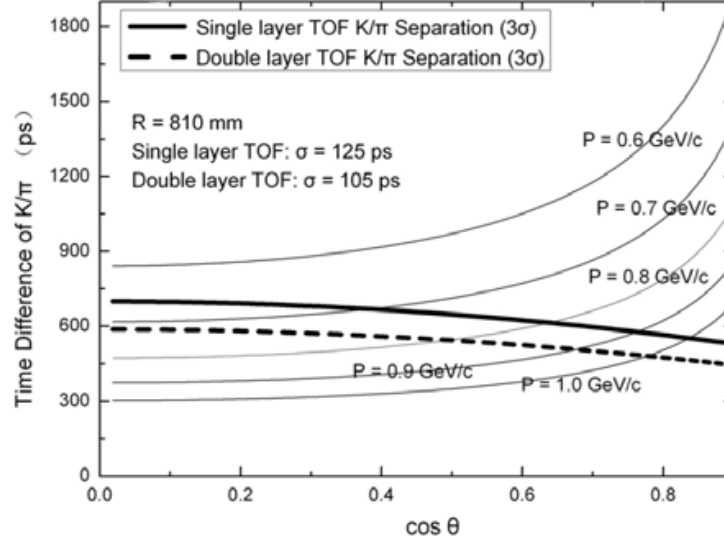


**Figure 2.6.:**  $K/\pi$  separation capability as functions of  $\cos \theta$ . (Drawing form [72].)

can be separated with a  $3\sigma$  significance if their momenta are below  $0.7 \text{ GeV}/c$  at  $\cos \theta = 0$ , which is in the center of the barrel, or  $1 \text{ GeV}/c$  at  $\cos \theta = 0.8$ , which corresponds to the outer border of the barrel at the gap. The  $3\sigma$   $K/\pi$  separation limit of the end cap TOF is between  $0.9 - 1 \text{ GeV}/c$ , since the time resolution is worse than in the barrel. The TOF readout system, shown in Fig. 2.7 consists of preamplifiers, signal time and amplitude measurement circuits, L1 trigger circuits and a laser calibration system. The PMT preamplifiers have 448 channels from all the scintillation counters. Similar to the MDC readout system, time and charge measurement modules are contained in the front end electronics (FEE) on HPTDC and FlashADC chips. Each FEE unit processes signals from 16 preamplifiers. Moreover there are two L1 trigger fast control modules. These modules provide L1 readout control forming the L1 sub-trigger system. All the basic TOF design parameters are summarized in Table 2.3.

**Table 2.3.:** Properties of the TOF system

|                            |   |
|----------------------------|---|
| inner radius barrel        | 810 mm  |
| outer radius barrel        | 870 mm  |
| scintillator dimensions    | $2380 \text{ mm} \times 50 \text{ mm} \times 50 \text{ mm}$ |
| angular acceptance barrel  | $ \cos \theta  < 0.83$                                      |
| angular acceptance endcaps | $0.85 <  \cos \theta  < 0.95$                               |
| total time resolution      | 80 ps (barrel), 110 ps (end caps)                           |

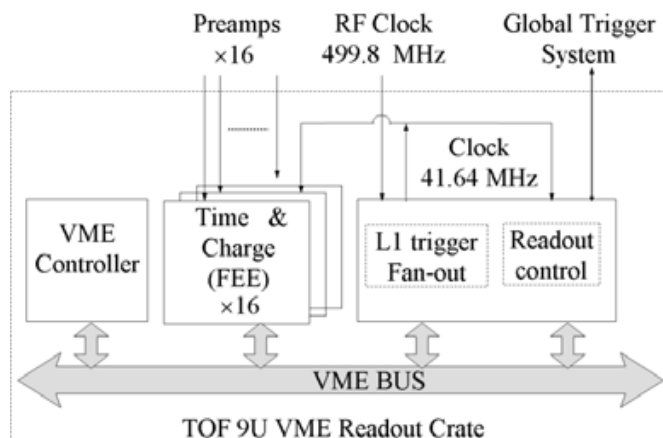


Figure 2.7.: Architecture of the TOF readout electronics crate. (Drawing from [72].)

### 2.2.4. Electromagnetic Calorimeter

The electromagnetic calorimeter (EMC) is a sub-detector system that measures the energy deposition of charged, as well as neutral particles passing its detector material. The energy deposit of charged particles in the EMC gives additional information for the particle identification (PID) system. Electrons and charged pions, for example, interact differently with the EMC detector material. The shapes of the showers that particles produce within the EMC is also used by the PID system to distinguish between different species. Photons, which are invisible to the MDC, can be detected by the EMC, since they usually deposit their entire energy in the crystals. In rare cases photons convert into an  $e^+e^-$  pair within the detector and cannot be reconstructed by the EMC. An electromagnetic calorimeter with a good spatial and energy resolution plays a key role for the spectrum of possible physics applications of a multi purpose detector like BESIII.

Similar to the TOF, the EMC is divided in a barrel part covering  $|\cos\theta| < 0.8$  and two end caps covering  $0.86 < |\cos\theta| < 0.93$ . The EMC consists of 6240 CsI(Tl) crystals arranged in 44 rings in the barrel and  $2 \times 6$  rings in the end caps. As shown in Fig. 2.8, each crystal covers an angle of  $3^\circ$  in polar and azimuthal direction and points towards the IP, in the center of the detector, with a tilt of  $1.5^\circ$  in the azimuthal angle direction and  $3^\circ$  in the direction of the polar angle. This corresponds to an offset of  $\pm 5$  cm from the IP in the axial direction. The small tilt of the crystal orientation prevents photons from flying exactly parallel through the gaps between the crystals, if coming from the IP. The shape of the crystals is a truncated pyramid with a quadratic front face of 5.2 cm and a rear face of 6.4 cm. The crystal length is 28 cm, which corresponds to 15 radiation lengths of the CsI(Tl) material. This provides an energy resolution of  $\leq 2.5\%$  for a 1 GeV

photon. The EMC can measure shower energies between 20 MeV and 2 GeV with a sampling cycle time of 50 ns. The photo diodes reading out the scintillation light

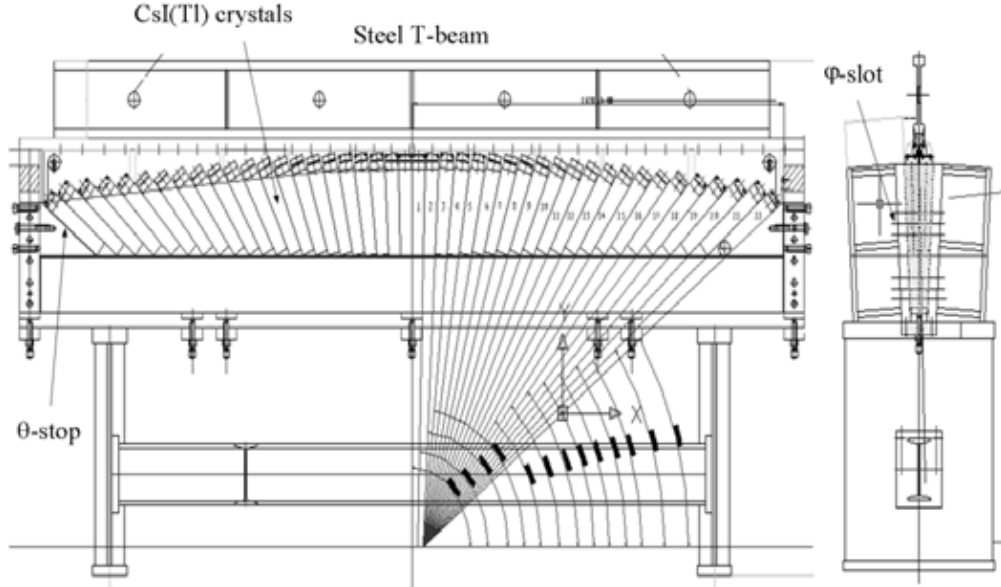


**Figure 2.8.:** Side and cross-sectional views of the barrel super module assembly jig. (Drawing form [72].)

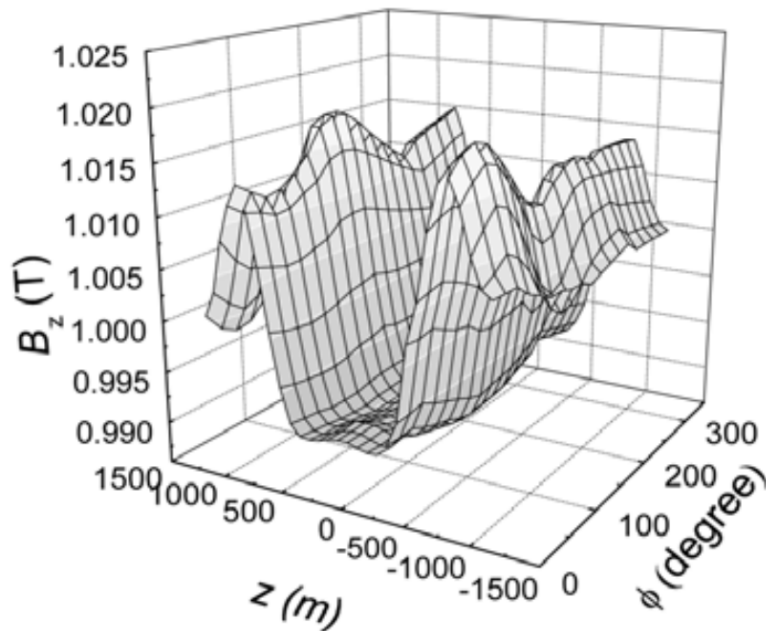
of the crystals, provide a voltage, which is proportional to the energy deposited in the crystal. After preamplification, this signal is digitalized by ADCs. The energy  $E$  can then be calculated by

$$E = \frac{ADC - PED}{e \cdot c}.$$

$ADC$  is the digitalized output voltage (mV), which is measured experimentally by the calorimeter. The pedestal value  $PED$  is the constant background noise rate of the electronics. The electronics gain  $e$  (mV/C) is the conversion constant between the output voltage from the ADC readout electronics and the input charge of the preamplifier. This constant is known from the design of the electronics. It is further calibrated with test pulses to the preamplifier. The energy conversion constant  $c$  (C/MeV) was measured before the final assembly of the EMC for each crystal. Test beams of photons and charged particles, for example electrons with known energy where used for this measurements. The design properties of the EMC are summarized in Table 2.4.

|                                 |   |
|---------------------------------|---|
| inner radius barrel             | 940 mm  |
| barrel length                   | 2750 mm   |
| inner radius endcaps            | 500 mm  |
| Number of CsI(Tl) crystals      | 6240 (5280 in barrel and 960 in endcaps)                        |
| crystal length                  | 280 mm  |
| crystal front and rear sizes    | $5.2 \times 5.2 \text{ cm}^2$ and $6.4 \times 6.4 \text{ cm}^2$ |
| angular acceptance barrel       | $ \cos \theta  < 0.83$  |
| angular acceptance endcaps      | $0.85 <  \cos \theta  < 0.95$                                   |
| total acceptance of $4\pi$      | 93%   |
| energy resolution               | $\frac{2.3\%}{\sqrt{E(\text{GeV})}} \otimes 1\%$                |
| position resolution in xy-plane | $\sigma_{xy} < \frac{6 \text{ mm}}{\sqrt{E(\text{GeV})}}$       |

Table 2.4.: Design properties of the EMC

Figure 2.9.: Distribution of the Magnetic field in the axial direction  $B_z$ . (Drawing form [72].)

### 2.2.5. Superconducting Solenoid Coil

The superconducting solenoid (SC) provides a uniform axial magnetic field of 1 T around the interaction region, the MDC, TOF and EMC sub-detectors. The magnetic field map is shown in Fig 2.9. This magnetic field causes a curvature in the particle trajectories due to the Lorentz force, which is measured by the MDC to determine the momenta of the charged particles. The SC consists of the superconducting solenoid itself and a steel flux return yoke with a weight of about 498 metric tons, which serves as a hadron absorber. The flux return yoke provides structure and support for the inner detector parts and consists of nine layers of steel in the barrel and eight layers in the end caps. This segmented layer structure is instrumented with MUC system described in the next subsection.

### 2.2.6. Muon Chamber

The Muon chamber (MUC) is necessary for an efficient separation between muons and pions. The MDC and TOF systems alone cannot provide a sufficiently efficient identification due to the relatively similar masses of muons and pions. The MUC consists of nine layers of resistive plate counters (RPC) in the barrel region and eight layers in the endcaps. The barrel RPC layers are inserted between the steel plates of the flux return yoke of the SC. The inner radius of the barrel part of the detector is 1.7 m and the outer radius is 2.62 m. The angular resolution of the MUC is modest due to multiple scattering of the muons in the EMC and the steel of the magnet yoke. However, the resolution is sufficient to associate MUC hits with the tracks reconstructed from the MDC and TOF systems, which have a much better resolution. The RPCs are made of phenolic paper laminate.

The RPC single gas gaps are shown in Fig. 2.10, where the phenolic paper laminate is addressed with Bakelite. The electrodes are vapor-coated on the phenolic paper laminate resistive plates with a thickness of 2 mm. A 2 mm gas gap separates the Bakelite plates. The gas is a mixture of Ar/C<sub>2</sub>F<sub>4</sub>H<sub>2</sub>/C<sub>4</sub>H<sub>10</sub> with a mixing ratio of 50:42:8. Spacers of 12 mm diameter each 10 cm serve as support structure to hold and separate the Bakelite plates. Two single RPC modules are stacked together to a double-gap design in the MUC. This improves the muon detection efficiency. The readout strips are placed in between the double-gap. The muon tracking efficiency is about 98%. Important MUC design parameters are summarized in Table 2.5.

### 2.2.7. Trigger System

The BESIII trigger system decides, whether a recorded collision event is written to disc or whether it will be discarded. As shown in Fig. 2.11, the trigger system

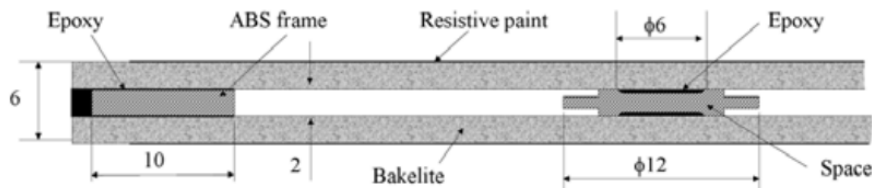


**Figure 2.10.:** Cross-sectional view of the RPC gas gap (left) and the double gap RPC (right). (Drawing form [72].)

**Table 2.5.:** Design properties of the MUC

|                                      |                               |
|--------------------------------------|-------------------------------|
| inner/outer radius barrel            | 1700 mm / 2620 mm             |
| total steel plate thickness barrel   | 56 cm                         |
| inner/outer distance to IP end caps  | 2050 mm / 2800 mm             |
| total steel plate thickness end caps | 43 cm                         |
| number of layers barrel/end caps     | 9/8                           |
| angular acceptance barrel            | $ \cos \theta  < 0.75$        |
| angular acceptance endcaps           | $0.75 <  \cos \theta  < 0.89$ |
| total acceptance of $4\pi$           | 89%                           |
| average efficiency barrel/end caps   | 96% / 95%                     |

consists of a two level based system with a Level-1 (L1) FPGA based hardware trigger and a Level-3 software trigger<sup>1</sup>. Whether an event will be written to disc or not must be decided within a few micro seconds, since the physics event rate is 2 kHz at the maximum instantaneous luminosity of  $10^{33}/\text{cm}^{-2}\text{s}^{-1}$ , which is near the  $J/\psi$ -resonance region. On top of the desired physics events, there are background contributions from cosmic rays, which are estimated to occur with a rate of 1.5 kHz. Beam related background contributions pollute the spectrometer with a rate of  $1.3 \cdot 10^4$  kHz. This kind of background stems from electrons or positrons lost from the focusing in the storage ring due to the high beam currents. The L1 trigger must be capable to suppress the beam-related and cosmic backgrounds to a rate lower than 2 kHz, which is the physics event rate. To meet these time requirements, the maximum L1 trigger rate is 4 kHz. After the collision the trigger decision, which determines if the L1 trigger accepts the signal or not, takes  $6.4 \mu\text{s}$ . Figure 2.11 shows the block diagram of the L1 trigger. The hardware parts close to the detector are the read-out front-end electronics of the four sub-detectors. They provide the input information for the trigger decision. The L1 trigger performs simple track finding from the MDC, TOF hit patterns, isolated cluster energy finding and energy summation in the EMC. The L1 decision latency is dominated

<sup>1</sup>There is no trigger subsystem addressed with Level-2.

by the  $3\ \mu\text{s}$  decay time of the EMC material. The L1 trigger reduces the rate of cosmic-ray backgrounds to a level of 0.2 kHz, whereas the rate of the beam related backgrounds after the L1 trigger is  $\leq 2\ \text{kHz}$ . More detailed information on the trigger can be found in [74, 75].

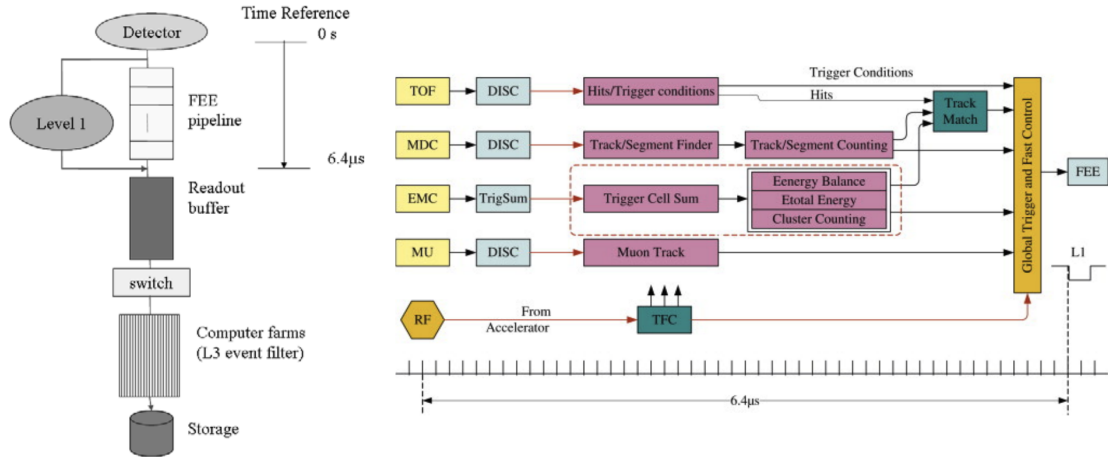


**Figure 2.11.:** Data flow of the trigger (left). Block diagram of the trigger system (right). (Drawings from [72] and [75].)

## 2.3. Software Framework

This section contains descriptions of all software packages that are used to analyze the data taken by the BESIII detector and the Monte Carlo simulations of these data.

### 2.3.1. Geant4

The Geant4 (**Geometry and tracking**) software platform is developed at CERN [76, 77]. Most of the modern particle physics experiments for example BaBar, ATLAS, PANDA, BELLEII and BESIII use Geant4 to simulate the detector responses. It is based on the object oriented C++ programming language. The particles produced in the  $e^+e^-$  collisions change their energy and direction of their momenta due to scattering processes with the detector material and the gases used in the detector. Monte Carlo (MC) methods are instrumented to quantitatively simulate these interactions between the particles and the detected material. The Geant4 software platform provides a precise simulation of the detector response of particles generated by a MC simulation of physical processes. Any geometrical shape of

matter and a large variety of materials can be used in the simulation. Therefore, the Geometry Design Markup Language(GDML) [78] is used to store the geometry information.

### 2.3.2. CERN ROOT

The ROOT software framework is developed at CERN since 1994 [79]. This software provides a large number of C++ classes and libraries for general data analysis. The framework libraries are available for all the most common operating systems like Windows, Linux, Mac OS X and many more. It is the successor of the famous FORTRAN based PAW software framework. ROOT is designed to face the analysis of the extensive amounts of data produced at the LHC experiments. Presently, ROOT also finds more and more scopes of applications for example in data-mining. ROOT can be used as a compiled binary program linked with the necessary ROOT libraries or as an interpreter for command chains or macros.

Root version 5.34 is extensively used to produce all plots and histograms in this work.

### 2.3.3. BESIII Offline Software System

The BESIII offline software system (BOSS), is the software framework that is used to reconstruct, calibrate and analyze the data collected by the detector, as well as to simulate certain physical processes and their interaction with the detector. It consists of more than 100 libraries for the detector sub-systems, their calibration, MC generators, reconstruction algorithms and tools like kinematic fitting, and particle identification. The libraries are written in the C++ programming language and partially based on the GAUDI package [80] of CERN ROOT introduced above and compiled with the CMT framework. BOSS runs on scientific Linux version SLC5 and SLC6. Each library of the BOSS framework has been implemented by the experts of the corresponding detector sub-system. The architecture of the BOSS framework is shown in Fig. 2.12. After generating a physical event in a Monte Carlo Simulation, the BOSS software also simulates the readout electronics, noise, dead channels, and the trigger system using Geant4. These informations mimicking the digital readout of the detector sub-systems is stored in a raw data file, which has the same format as the digital information of the real data taken by the detector electronics. The reconstruction package proceeds real and simulated data from a raw file into a Data-Summary-Tape (DST) file. Within this process a Kalman-filter performs the fitting for the charged track reconstruction. The clustering algorithm transforms calibrated ADC values of each crystals into energies and merges the energy deposits of close by crystals to electromagnetic

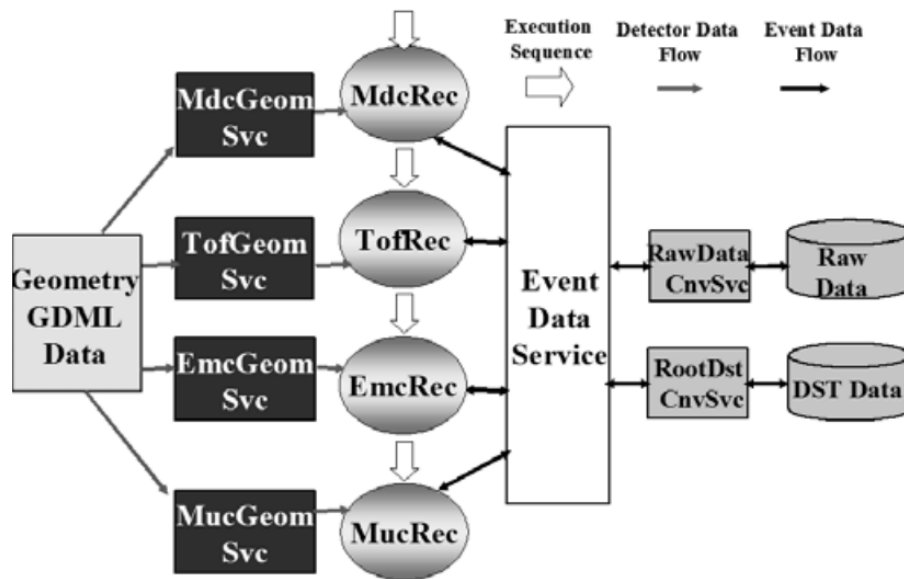


**Figure 2.12.:** The overall BESIII software architecture. Picture taken from [72]

showers in the EMC. Also the time measurements of the TOF system are calculated from the TOF electronics output in this step. At last the hit information of the MUC is transformed into tracks. Last, the reconstruction package merges the informations of the sub-detector systems, if they are found to belong to the same particle. For each physics analysis or efficiency study, the user has to implement his/her own software package to analyse the DST files of data and simulations. The BOSS version used in this work is BOSS6.6.4.p01, since the used data set is reconstructed with this BOSS version.

A good example of a BOSS package is the EventDisplay class. This class allows to display the information of all the sub-detector systems for each event separately. Fig. 2.13 shows the event display of a  $e^+e^- \rightarrow J/\psi\pi^+\pi^-$  event in the plane perpendicular to the beam axis. The  $J/\psi$  immediately decays into a  $\mu^+\mu^-$  pair. That is why four tracks can be seen in the picture. One can nicely see, how the charged tracks leave a curved trace in the MDC and pass through the TOF, EMC and MUC.

## 2.4. BESIII Data Sets

The center-of-mass (c.m.) energy of the BESIII experiment can be adjusted between 2 GeV and 4.6 GeV. This region refers to as the  $\tau$ -charm region, as it

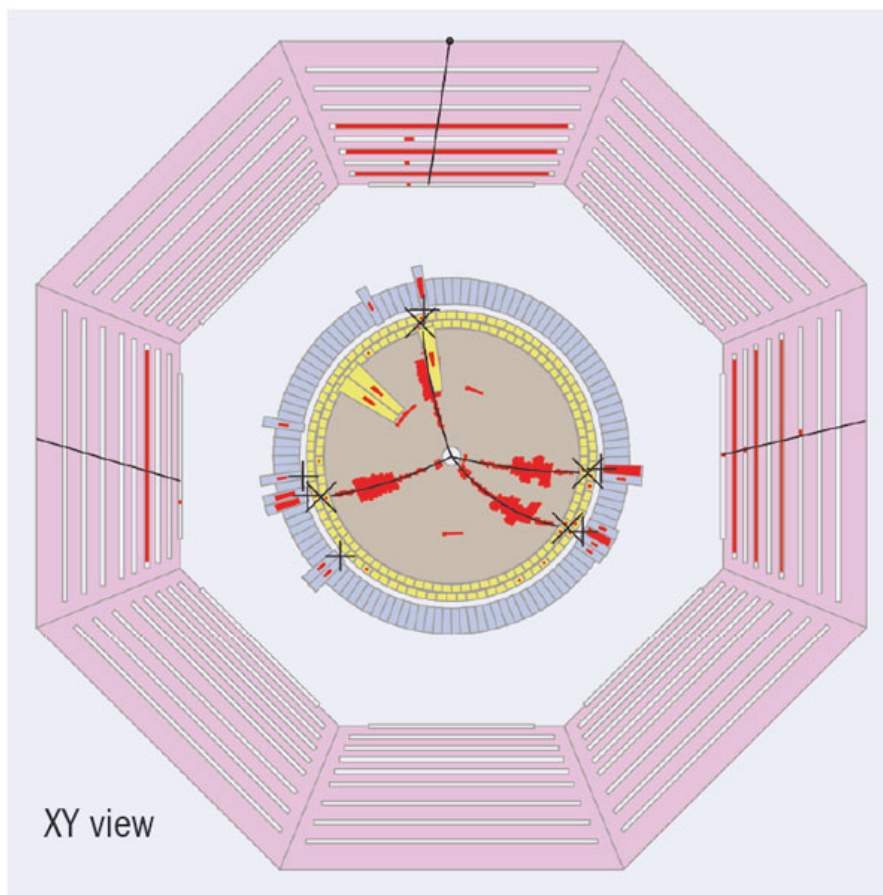


**Figure 2.13.:** Graphical display of an  $e^+e^- \rightarrow J/\psi\pi^+\pi^-$  event. The tracks and the detector are shown in the plane perpendicular to the beam axis.

covers the poles of several charmonium resonances, the threshold of open charm, and the threshold for the pair production of tau-leptons. Thus, the main physics goals of the BESIII collaboration are charmonium spectroscopy, light hadron spectroscopy in charmonium decays, D-meson physics,  $\tau$ -physics, XYZ-physics and search for new physics beyond the Standard Model. The BEPCII accelerator belongs to the accelerators with the worlds highest luminosity at energies in the charmonium range, which is shown in Fig. 2.14. The BESIII detector collected the worlds larges data sets at  $\sqrt{s} = 3.096$  GeV,  $\sqrt{s} = 3.684$  GeV and  $\sqrt{s} = 3.773$  GeV. These data sets allow to study the corresponding charmonium resonances  $J/\psi$ ,  $\psi(3686)$  and  $\psi(3770)$  with high precision. Fig. 2.15 shows the size of these data sets taken by the BESIII detector in comparison to the respective data sizes of previous  $e^+e^-$  collider experiments.

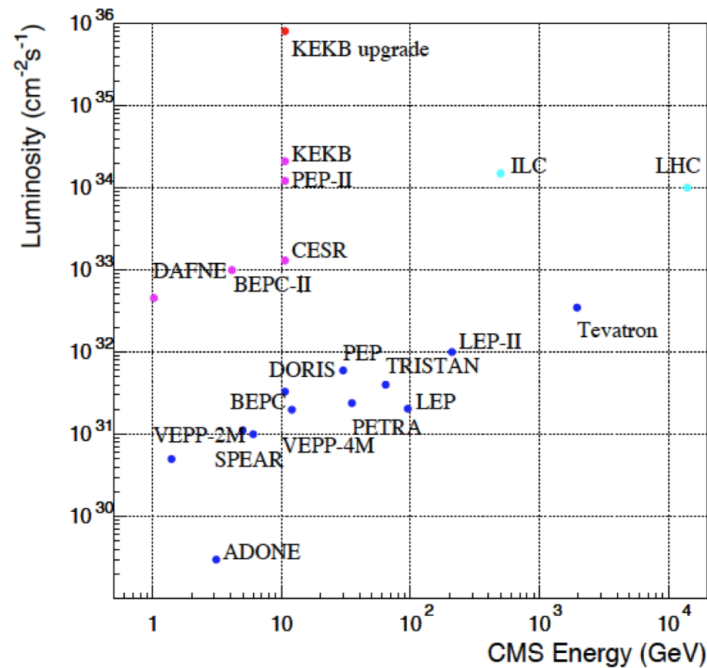


**Figure 2.14.:** Comparison of luminosities versus c.m. energies for several  $e^+e^-$ ,  $p\bar{p}$  and proton-proton Colliders in the world. BEPCII (BESIII, Beijing), DAΦNE (KLOE-II, Frascati), PEP-II (BaBar, Stanford) and KEKB (BELLE, Tsukuba). (Figure from [82].)

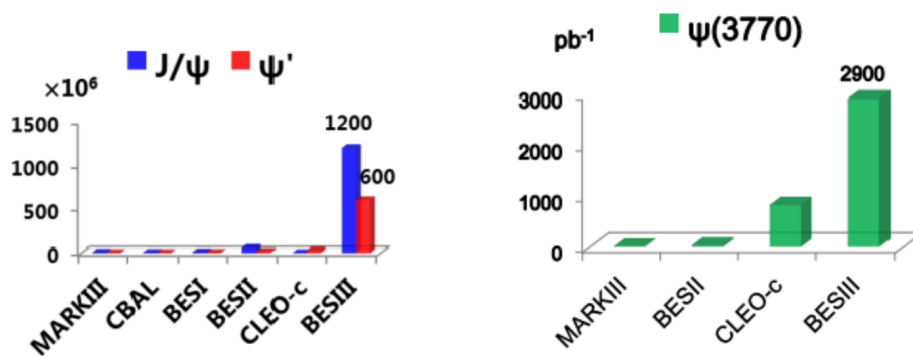


**Figure 2.15.:**  $J/\psi$ ,  $\psi(3686)$  and  $\psi(3770)$  data sets taken by several experiments. In the left histogram the number of events is shown.

The BESIII data sets are about one order of magnitude larger than the data sets, which are taken by the experiments MARKIII, Crystal Ball (CBAL), and CLEO-c. All the BESIII data sets taken in the campaign between 2009 and 2016 are listed in Table 2.6. The data sets with a large integrated luminosity give the opportunity to perform high precision measurements, as for example aimed in the

context of this work. For this thesis, the  $\psi(3770)$  data set taken in 2010 and 2011 is used. It is the largest sample and the c.m. energy is as close as possible to the region most relevant for  $(g - 2)_\mu$ . Detailed information of this data set are given in Table 2.7. Its luminosity has been measured precisely in [84] using Bhabha scattering events.

**Table 2.6.:** List of all BESIII data sets taken until 2016.

| Name                   | Year        | $\sqrt{s}$ [GeV] | $\mathcal{L}$ [ $\text{pb}^{-1}$ ] |
|------------------------|-------------|------------------|------------------------------------|
| R-Scan 1               | 2015        | 2.050-3.080      |                                    |
| $J/\psi$               | 2009        | 3.097            | 106M events                        |
| $\tau$ data            | 2009        | 3.650            | 44                                 |
| $\psi(3686)$           | 2009 + 2012 | 3.686            | 341M events                        |
| $\psi(3770)$ data      | 2010 + 2011 | 3.773            | 2932                               |
| $\psi(3770)$ lineshape | 2010        | 3.643-3.890      | 64                                 |
| R-Scan 2               | 2014        | 3.890-4.220      | 826                                |
| $\psi(4040)$ data      | 2010        | 4009             | 482                                |
| Y(4230) data           | 2012-2013   | 4260             | 1092                               |
| Y(4260) data           | 2012-2013   | 4260             | 826                                |
| Y(4360) data           | 2012-2013   | 4360             | 540                                |
| Y(4420) data           | 2014        | 4420             | 1073                               |
| Y(4600) lineshape      | 2014        | 4.470-4.575      | 268                                |
| Y(4600) data           | 2014        | 4600             | 566                                |

**Table 2.7.:** Detailed information and luminosity [83, 84] about the  $\psi(3770)$  data set, which is used in this thesis. The first error is statistical and the second is the systematic uncertainty. Round 1 was taken in 2010 and round 2 in 2011.

| Round   | Run number                      | Integrated luminosity $\mathcal{L}$ [ $\text{pb}^{-1}$ ] |
|---------|---------------------------------|--|
| Round 1 | 11414 - 13988 and 14395 - 14604 | $927.67 \pm 0.10 \pm 9.2$                                |
| Round 2 | 20448 - 23454                   | $1989.27 \pm 0.15 \pm 19.89$                             |
| Sum     |                                 | $2931.8 \pm 0.18 \pm 29.17$                              |

## 2.5. Monte Carlo Simulations

Monte Carlo (MC) simulations are needed in order to calculate the detection efficiency of a final state, to optimize the event selection criteria and to study background contributions. As mentioned above, the simulation consists of three

steps. In the first step a dedicated MC event generator produces physical processes. In the second step the BOSS framework simulates the response of the detector electronics as if the simulated particles would propagate through all detector sub-systems. In the last step, the track and EMC shower reconstructions are performed. The result is a DST file that looks like real data.

The PHOKHARA 9.1 event generator [85] is used for the simulation of the process  $e^+e^- \rightarrow \pi^+\pi^-2\pi^0\gamma_{ISR}$ , which is the main topic of this work. PHOKHARA 9.1 is a dedicated initial state radiation (ISR) event generator. It simulates ISR events with a precision of 0.5%. The final states  $\mu^+\mu^-$ ,  $\pi^+\pi^-$ ,  $\pi^+\pi^-\pi^0$ ,  $\pi^+\pi^-\eta$ ,  $\pi^+\pi^-\pi^+\pi^-$ ,  $\pi^+\pi^-\pi^0\pi^0$ ,  $K^+K^-$ ,  $K_0\bar{K}_0$ ,  $p\bar{p}$ ,  $n\bar{n}$  and  $\Lambda\bar{\Lambda}$ , are supported up to next-to-leading order (NLO) ISR. Thus, up to two additional ISR photons in the final state are considered. Also final state radiation (FSR) and ISR-FSR interference are supported for the final states  $\mu^+\mu^-$ ,  $\pi^+\pi^-$ ,  $K^+K^-$  and  $p\bar{p}$ . Free parameters in the model of the hadronic currents are fixed by fits to previous experimental results on these channels by BABAR, CMD-2, CLEO-c, KLOE and ALEPH. The generator allows to adjust the parameters specific for certain physics effects and experimental setups, such as the c.m. energy, VP, ISR or fixed c.m. energy mode, maximum and minimum energies of the leading order (LO) and NLO ISR photons, the polar angle range of the particles in the final state, where the range of radiated photons and produced hadrons is adjusted separately. Table 2.8 shows the configuration used for the simulation of the signal process  $e^+e^- \rightarrow \pi^+\pi^-2\pi^0\gamma_{ISR}$ .

**Table 2.8.:** Settings of PHOKHARA 9.1 for the simulation of the signal channel  $e^+e^- \rightarrow \pi^+\pi^-2\pi^0\gamma_{ISR}$ .

| Parameter                                     | Value/Setting       |
|---|---------------------|
| ScanMode                                      | no                  |
| CMS energy                                    | 3.773 GeV           |
| Vacuum polarization                           | yes, by Jegerlehner |
| NLO ISR                                       | yes                 |
| FSR   | no                  |
| FSR NLO                                       | no                  |
| Minimum photon energy (LO)                    | 0.05 GeV            |
| SoftPhotonCutoff (NLO)                        | 0.1 MeV             |
| Minimum photon angle                          | 0.0°                |
| Maximum photon angle                          | 180.0°              |
| Minimum hadrons/muons angle                   | 0.0°                |
| Maximum hadrons/muons angle                   | 180.0°              |
| Narrow Resonances ( $J/\psi$ , $\psi(3686)$ ) | no                  |

The background processes are simulated with the BESEVTGEN [86] event gener-

ator. To simulate the dominating multihadronic background channels, the generator model LUNDAREALAW [87, 88] is used. This model simulates  $e^+e^- \rightarrow q\bar{q} + n\gamma$ ,  $q = u, d, s$  and  $n = 0, 1$ , where the  $q\bar{q}$  pair hadronizes to the multihadronic final states. This MC sample is referred to as Lund- $q\bar{q}$ . The HELPWA generator tool [89] was used to produce a dedicated MC sample for the important background contribution from  $\pi^+\pi^-3\pi^0$ . To simulate a final state, HELPWA uses data input of all kinematic variables of the final state particles to perform a partial wave analysis (PWA) and generate MC samples according to the solution of the PWA. BESEVTGEN is also used to simulate additional background contributions from,  $e^+e^- \rightarrow \gamma_{ISR}J/\psi$ ,  $e^+e^- \rightarrow \gamma_{ISR}\psi(3686)$ ,  $e^+e^- \rightarrow D^+D^-$ ,  $e^+e^- \rightarrow D^0\bar{D}^0$  and non- $D\bar{D}$ . The non- $D\bar{D}$  MC sample contains processes of the type  $e^+e^- \rightarrow \psi(3770)$ , where  $\psi(3770)$  decays to anything except  $D$ -meson pairs, for example  $e^+e^- \rightarrow \psi(3770) \rightarrow \gamma\chi_{c1}$ .

Table 2.9 provides details on the cross sections and event numbers of all MC samples generated and evaluated in the analyses of this work.

**Table 2.9.:** List of all MC samples and their sizes used in the analyses of this work.

| Final state(s)                 | Cross section [pb] | Generator (model)       | Events           |
|--------------------------------|--------------------|-------------------------|------------------|
| $\pi^+\pi^-2\pi^0\gamma_{ISR}$ | 385                | PHOKHARA 9.1            | $10^7$           |
| $\pi^+\pi^-3\pi^0$             | 18                 | BESEVTGEN (HELPWA)      | $2 \cdot 10^6$   |
| $\omega\pi^0\pi^0$             | 80                 | BESEVTGEN (PHSP)        | $2 \cdot 10^6$   |
| $\eta\pi^+\pi^-$               | 41                 | BESEVTGEN (PHSP)        | $2 \cdot 10^6$   |
| Lund- $q\bar{q}$               | 12200              | BESEVTGEN (LUNDAREALAW) | $366 \cdot 10^6$ |
| non- $D\bar{D}$                | 500                | BESEVTGEN (HELAMP)      | $15 \cdot 10^6$  |
| $\gamma_{ISR}J/\psi$           | 1100               | BESEVTGEN (VECTORISR)   | $33 \cdot 10^6$  |
| $\gamma_{ISR}\psi(3686)$       | 3400               | BESEVTGEN (VECTORISR)   | $102 \cdot 10^6$ |
| $D^+D^-$                       | 2880               | BESEVTGEN (VSS)         | $91 \cdot 10^6$  |
| $D^0\bar{D}^0$                 | 3660               | BESEVTGEN (VSS)         | $12 \cdot 10^6$  |



## Chapter 3.

# Physics of Initial State Radiation

---

*For an improved determination of the hadronic vacuum polarization contribution to  $(g - 2)_\mu$  it is necessary to measure the cross section of the hadronic channel  $e^+e^- \rightarrow \pi^+\pi^-2\pi^0$  in the energy range from the kinematic threshold up to a few GeV. However, high precision data for this channel were not available in the desired energy range. This chapter introduces the initial state radiation technique. This technique allows to determine the desired cross section in the relevant energy region from data taken at a collider operating at center of mass energies above the energy range of interest.*

---

### 3.1. Leading Order Initial State Radiation

The center of mass (c.m.) energy of the collision at colliders is fixed. Following the dispersive approach<sup>1</sup> for calculating the hadronic vacuum polarization contribution to  $(g - 2)_\mu$ , referred to as  $a_\mu^{\text{HVP,LO}}$ , it is necessary to determine the energy dependence of the hadronic cross sections. The cross section of the process  $e^+e^- \rightarrow \pi^+\pi^-2\pi^0$  in the energy range below 1.8 GeV is of particular importance for the determination of  $a_\mu^{\text{HVP,LO}}$ .

One possibility to obtain the cross section in the desired energy range is to perform an energy scan. This means to take data at different c.m. energies within the energy range of interest. However, this method suffers from several disadvantages. Firstly, since it is highly time consuming to tune the detector and the accelerator after each change of the c.m. energy, the number of energy points is typically limited. Secondly, the cross section between the accumulated data points remains unknown, so that narrow structures might be lost or underestimated. Lastly, the performance of the accelerator is not constant for different c.m. energies. However, an advantage of the energy scan method is that there are less background contributions.

Therefore it is more efficient to derive the desired cross section for the relevant energy range from a huge data set taken at a higher c.m. energy. Collision data at a higher energy also contain the desired process with an additional photon, which was radiated from the initial state. This process is referred to as Initial State Radiation (ISR). Figure 3.1 illustrates a leading order ISR process. Data from the ISR process  $e^+e^- \rightarrow \pi^+\pi^-2\pi^0\gamma_{\text{ISR}}$  allow to derive the cross section of the channel  $e^+e^- \rightarrow \pi^+\pi^-2\pi^0$  for lower c.m. energies than the one, at which the collision was performed. The analysis described in this thesis is based on the data set collected at a c.m. energy of 3.773 GeV, which corresponds to the largest data set available at BESIII.

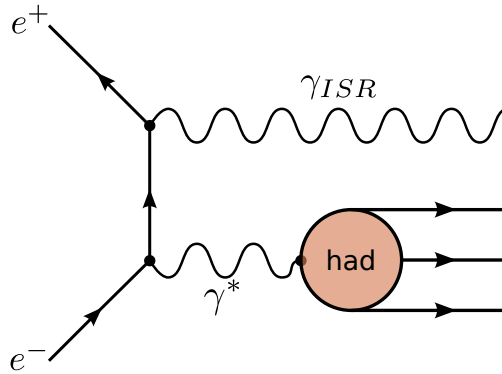


**Figure 3.1.:** Leading order initial state radiation process

<sup>1</sup>Compare section 1.4.2

For the desired accuracy in the ISR analysis, it is important to consider events, in which more than one photon is emitted from the initial state. This results from higher orders in the perturbation expansion of QED. A more detailed description of this issue will follow in section 3.2.

For the leading order process, the effective c.m. energy left for the interaction can be calculated from the energy of the ISR photon. Applying four-momentum conservation gives

$$p_0 = p_{\text{had}} + p_\gamma, \quad (3.1.1)$$

where  $p_0 = (\sqrt{s}, \vec{0})$  denotes the four-momentum of the initial state in the laboratory frame,  $s = E_{\text{CM}}^2$  is the squared c.m. energy,  $p_\gamma = (E_\gamma, \vec{p}_\gamma)$  denotes the four-momentum of the ISR photon and  $p_{\text{had}}$  denotes the sum of the four-momenta of the hadrons in the final state. Squaring both sides of Eq. 3.1.1, using  $p_\gamma^2 = 0$  and considering the Minkowski metric one obtains

$$\begin{aligned} p_0^2 &= (p_{\text{had}} + p_\gamma)^2 = p_{\text{had}}^2 + 2p_{\text{had}}p_\gamma + p_\gamma^2 \\ &= p_{\text{had}}^2 + 2(p_0 - p_\gamma)p_\gamma = p_{\text{had}}^2 + 2p_0p_\gamma \\ &= m_{\text{had}}^2 + 2\sqrt{s}E_\gamma = s \\ \Rightarrow E_\gamma &= \frac{s - m_{\text{had}}^2}{2\sqrt{s}}. \end{aligned} \quad (3.1.2)$$

Moreover, it is considered that  $p_{\text{had}}^2 = m_{\text{had}}^2$ .

The cross section  $\frac{d\sigma_{\text{rad}}}{dm_{\text{had}}}$  of a certain final state with an additional ISR photon, called radiative cross section, can be related to the cross section  $\sigma_{\text{nonrad}}(m_{\text{had}})$  without the ISR photon, which is called non-radiative cross section. This relation is given by [90, 91] and reads

$$\frac{d\sigma_{\text{rad}}}{dm_{\text{had}}} = \frac{d\sigma}{dx} \frac{dx}{dm_{\text{had}}} = \frac{2m_{\text{had}}}{s} W(x, s) \sigma_{\text{nonrad}}(m_{\text{had}}), \quad (3.1.3)$$

where  $x = 1 - \frac{m^2}{s} = \frac{2E_\gamma}{\sqrt{s}}$  and  $W(x, s)$  is the angular integrated radiator function. The leading-order angular dependent radiator function  $H(x, s, \theta)$  is given by

$$H(x, s, \theta) = \frac{\alpha}{\pi x} \left[ \frac{\left(1 - x + \frac{x^2}{2}\right) \sin^2 \theta - \frac{x^2}{2} \sin^4 \theta}{\left(\sin^2 \theta + \frac{4m_e^2}{s} \cos^2 \theta\right)^2} - \frac{4m_e^2 (1 - 2x) \sin^2 \theta - x^2 \cos^4 \theta}{s \left(\sin^2 \theta + \frac{4m_e^2}{s} \cos^2 \theta\right)^2} \right], \quad (3.1.4)$$

in Ref. [90, 91] The function  $H(x, s, \theta)$  describes the amplitude to radiate an initial state photon with energy  $E_\gamma$  under the polar angle  $\theta$ . Eq. 3.1.4 is independent of the photon's azimuthal angle  $\varphi$ . The angular integrated radiator function in leading order is subsequently given by

$$W(x, s) = \int_0^{2\pi} d\varphi \int_0^\pi d\theta \sin(\theta) H(x, s, \theta) = \frac{2\alpha}{\pi x} \left( \ln \frac{s}{m_e^2} - 1 \right) \left( 1 - x + \frac{x^2}{2} \right). \quad (3.1.5)$$

Equation 3.1.5 reveals that the radiator function has a pole at the c.m. energy of the collision. For this reason, it cannot be normalized and therefore not be interpreted as a probability density to radiate a photon. It rather has to be interpreted as an amplitude. Figure 3.2 shows the polar angle dependence of the energy integrated leading order radiator function  $\int_0^1 dx H(x, s, \theta)$ . The ISR photons are dominantly radiated at angles close to zero and 180 degrees, which is along the beam pipe in an experimental setup.

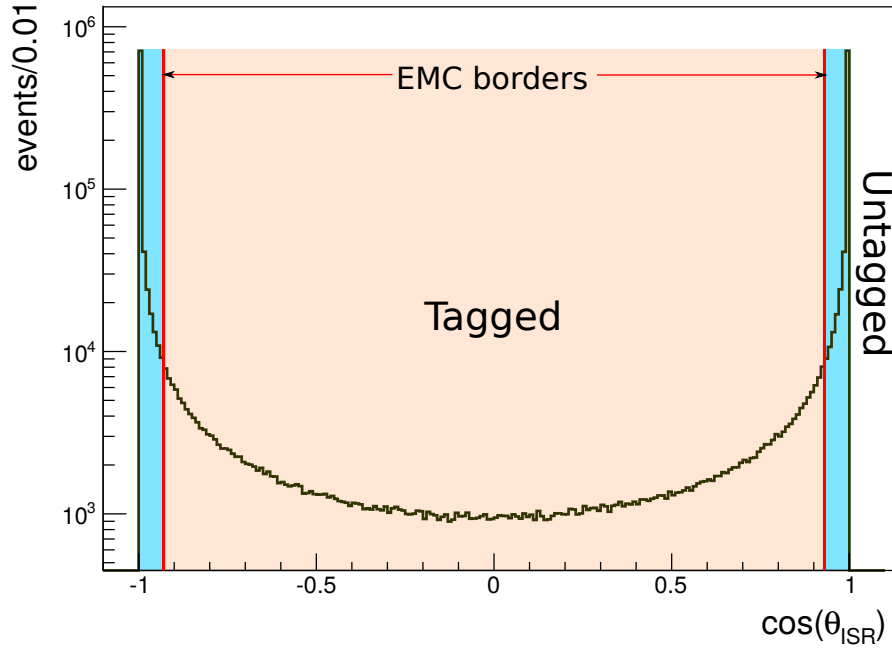


**Figure 3.2.:** Polar angle dependence of the leading order radiator function integrated over photon energy  $\int_0^1 dx H(x, s, \theta)$ . The BESIII detector can detect photons in the orange shaded area, but not in the blue shaded one.

Conventional detector setups at  $e^+e^-$  colliders require a gap in their detector acceptance at small polar angles in order to host the accelerator structures, like beam pipes and focusing magnets. Considering the special shape of the radiator function, ISR events can be reconstructed in two ways, as illustrated in Fig. 3.3. The methods can be characterized as follows:

**ISR Tagged Method** All particles of the final state including the ISR photon are reconstructed in the analysis. A kinematic fit to all particles including the ISR photon can be performed, constraining the total four-momentum to be equal to the c.m. energy of the  $e^+e^-$  collision. Due to the shape of the radiator function this method is statistically limited.

**ISR Untagged Method** The ISR photon is emitted at small polar angles and therefore not reconstructed. All hadrons, however, are fully reconstructed. The four momentum of the missing ISR photon can be predicted by requiring four-momentum conservation. The polar angle of the ISR photon is restricted to angles close to the beam axis, which is outside the acceptance region of the detector. This method provides much higher statistics compared to the tagged mode. Another advantage of this method is the unique signature of the photon polar angle distribution, which can be used to suppress background.

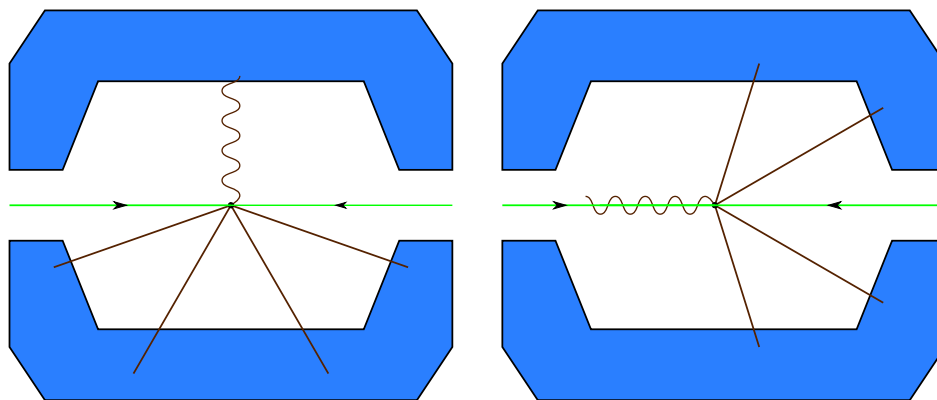


**Figure 3.3.:** Sketch of a tagged ISR event (left) and an untagged ISR event (right). The solid lines represent the final state hadrons and the wiggled line depicts the ISR photon.

Another characteristic signature of an ISR event is that the radiated photon and the total momentum vector of the final state hadrons are back to back. Also, the final state hadrons are boosted in a cone. These kinematic properties are displayed in Fig. 3.4. The opening angle of the cone is small for a high energetic ISR photon.

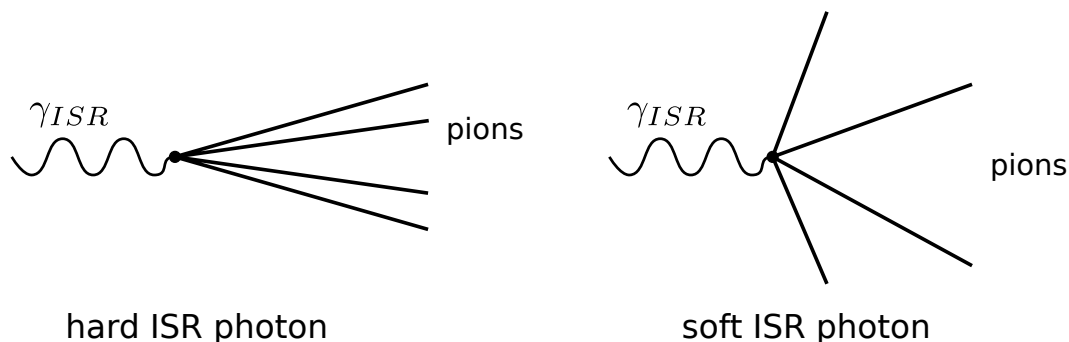


**Figure 3.4.:** Kinematics of an ISR event.

If the ISR photon is lost in the beam pipe, the probability is high to also lose some final state hadrons in the opposite end of the beam pipe. Hence, the efficiency to reconstruct an untagged ISR event with a high energetic ISR photon is reduced. In the BESIII experiment, the efficiency even drops to zero in the untagged mode for invariant masses of the hadrons below about 1 GeV. This corresponds to the kinematic threshold, where the cone radius is always smaller than the beam pipe radius.

## 3.2. Next-to-Leading Order Initial State Radiation

As discussed already above, besides the emission of a single photon from the initial state, it is also possible to emit several photons from the initial state. Figure 3.5 shows two possible Feynman graphs for such next-to-leading order (NLO) ISR processes. For each ISR photon that is emitted from the initial state, the process becomes suppressed by an additional order of the electromagnetic fine structure constant  $\alpha$ . However, in NLO, the radiator function can overcompensate the suppression of the order  $\mathcal{O}(\alpha)$ , if the energy and the polar angle of the second ISR photon are small. Figure 3.6 shows that the NLO effects slightly enhance the

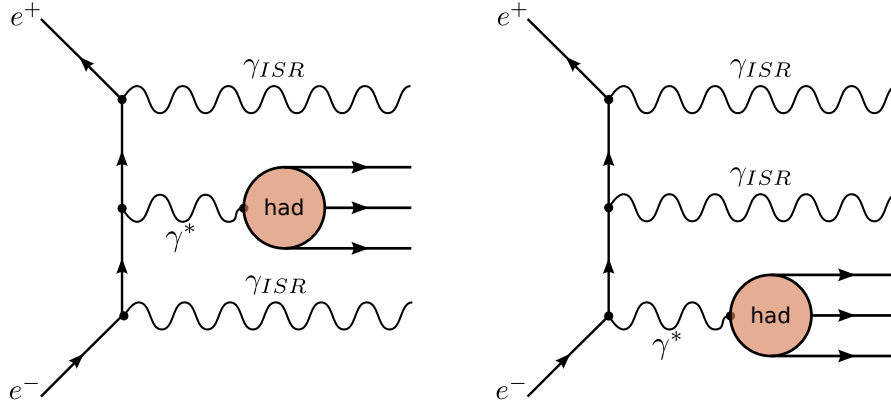


**Figure 3.5.:** Two possible NLO ISR processes.

radiator function for large values of  $x$  compared to the LO case from Eq. 3.1.5. The dependence of the NLO radiator function on the polar angles  $\theta_{\gamma_i}$  and the momentum fractions  $x_{\gamma_i}$  of the two ISR photons  $\gamma_i$ ,  $i = 1, 2$  is shown in Fig. 3.7. The emission of two high energetic ISR photons with large polar angles is negligibly small. However, the radiation of a second low energetic ISR photon with a large polar angle has a non negligible impact on the observed ISR cross sections. Therefore, these effects have to be considered when performing a precise measurement. In fact, the PHOKHARA 9.1 [85] event generator simulates ISR to the NLO precision.

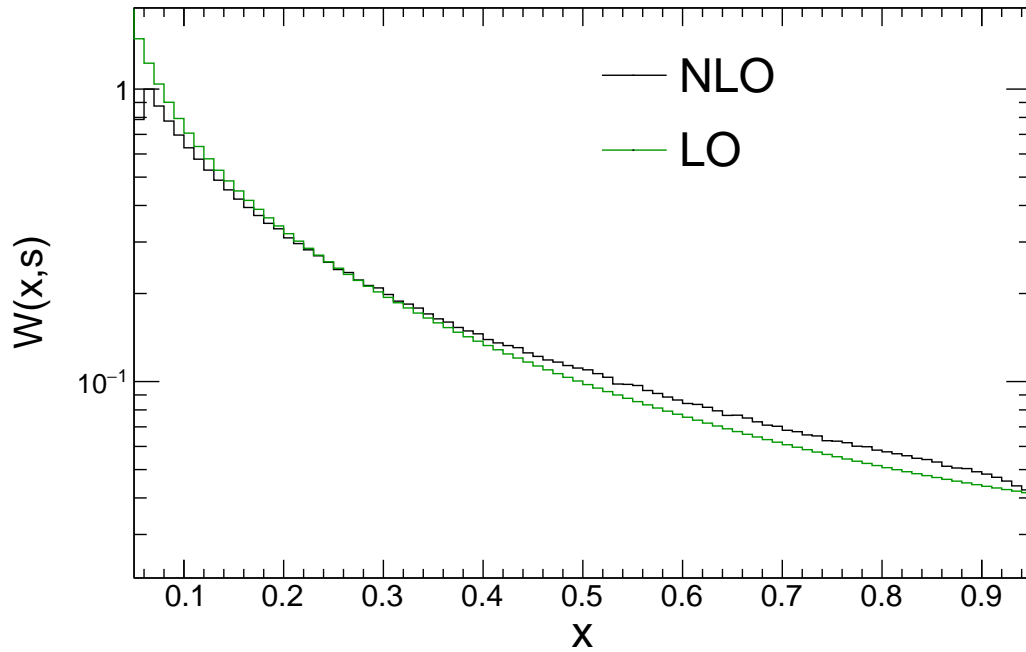


Figure 3.6.:  $x$ -dependence of the LO and NLO radiator functions.

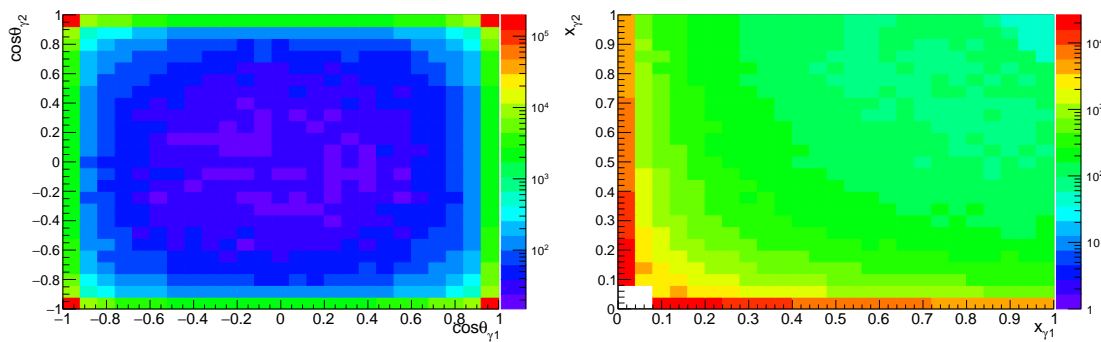


Figure 3.7.: Polar angle  $\theta_{\gamma_i}$  and  $x_{\gamma_i}$  distributions of the NLO radiator function.

### 3.3. Final State Radiation

Also the charged particles in the final state can as well emit photons besides the initial state electrons and positrons. This process is called final state radiation (FSR). Similar to the ISR process, the emission of each photon is suppressed by the radiator function, which contains  $\alpha$  and  $\ln\left(\frac{s}{m^2}\right)$ , where  $m$  is the mass of

the radiating charged particle. This shows that the emission of a FSR photon is less probable for pions than for electrons or positrons. The polar angle and energy dependence of the FSR photons is similar to the ISR photons. Small angles with respect to the mother particle are favored. The leading order (LO) final state radiation process is depicted in the left panel of Fig. 3.8. ISR and FSR events cannot be distinguished kinematically. Hence, the FSR photons produce an irreducible background contribution.

The process of emitting one ISR photon and one FSR photon, as illustrated in the right panel of Fig. 3.8, is referred to as mixed ISR+FSR process. The FSR photons from the ISR+FSR process cause another irreducible background contribution. Moreover, an undetected FSR photon in the final state shifts the invariant mass of the hadronic system towards lower masses. A few percent of the mixed ISR+FSR events will be therefore interpreted as LO FSR events with a reduced invariant mass. The measurement needs to be corrected for this effect in order to achieve the desired precision. The corresponding correction will be explained in more detail in section 7.1.3. The PHOKHARA 9.1 event generator [85] does not contain FSR effects for the process  $e^+e^- \rightarrow \pi^+\pi^-2\pi^0\gamma_{ISR}$ . However, the PHOTOS package [92] is used to consider FSR effects.

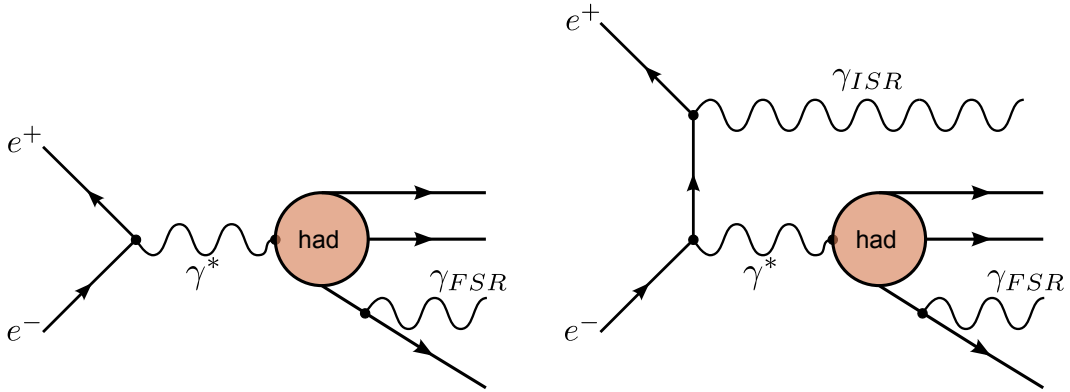


**Figure 3.8.:** LO FSR process (left). NLO FSR process (right).

# Chapter 4.

## Event Selection

---

*This chapter contains the description of how the  $e^+e^- \rightarrow \pi^+\pi^-2\pi^0\gamma_{ISR}$  signal events are selected from data and the Monte Carlo samples. Also the selections of the final states  $\pi^+\pi^-3\pi^0\gamma_{ISR}$  and  $\pi^+\pi^-3\pi^0$  are explained here, which are the most important background contributions to the  $e^+e^- \rightarrow \pi^+\pi^-2\pi^0\gamma_{ISR}$  process. The tagged and untagged ISR modes are applied and considered separately. Exploiting the kinematic and geometrical constraints of the signal processes, criteria are optimized for a high purity, but also a high efficiency of the signal process.*

---

Before starting with the event selection procedure of the signal process  $e^+e^- \rightarrow \pi^+\pi^-2\pi^0\gamma_{ISR}$ , general requirements on good charged tracks, photons and neutral pions are explained in this chapter. The requirements are identical for the events selections of the signal process  $e^+e^- \rightarrow \pi^+\pi^-2\pi^0\gamma_{ISR}$  and also the background processes  $e^+e^- \rightarrow \pi^+\pi^-3\pi^0\gamma_{ISR}$  and  $e^+e^- \rightarrow \pi^+\pi^-3\pi^0$ . In all plots shown in the following, the distributions of the signal Monte Carlo (MC) simulation is always stacked over the distributions of the background contributions. The selection criteria are illustrated with a yellow line. Green lines indicate the variation range for the systematic error studies. The distributions from MC simulations are scaled to the integrated luminosity of the data set in all plots. Plots showing data before the application of a specific requirement have all other selection criteria applied, which will be introduced in the corresponding sections in the following. Only LO ISR events are considered in the event selections.

**Charged Tracks** For the selection of the two charged pions, events with exactly two good charged tracks with net charge zero are required. The radial distance  $r$  of the track helix to the interaction point (IP) is required to be  $r < 1.0$  cm and the axial distance  $z$  must satisfy  $|z| < 10.0$  cm. The polar angle of the tracks must satisfy  $|\cos\theta| < 0.93$ . These conditions have been agreed on inside the BESIII collaboration for the selection of charged tracks and the systematic uncertainties are understood. Additional tracks in the event, that do not pass the vertex selection are ignored.

**EMC showers** Showers in the electromagnetic calorimeter (EMC) are considered to be good photons if they deposit an energy  $E > 25$  MeV in the barrel ( $|\cos\theta| < 0.8$ ) or  $E > 50$  MeV in the end caps ( $0.86 < |\cos\theta| < 0.92$ ). In addition, their timing must hold  $0 \leq \text{TDC} \leq 700$  ns for barrel and the end caps. These are also the BESIII standard requirements on the selection of good photon candidates. Good photon candidates are also required to be separated at least  $20^\circ$  from all charged tracks in the event. The distribution of the angle  $\beta$  between the good photon candidates and the charged pions is shown in Fig. 4.1 for the PHOKHARA 9.1 signal MC.

**Neutral Pions** Only the  $\pi^0 \rightarrow \gamma\gamma$  decay channel, which has a branching fraction of  $(98.823 \pm 0.034)\%$  [31], is reconstructed. For each event a list of all possible pairs of two photons with an invariant mass  $M(\gamma\gamma)$  within  $100 \text{ MeV} \leq M(\gamma\gamma) \leq 160 \text{ MeV}$  is created. From this list another list is built with combinations of two neutral pions, such that no photon is used for both  $\pi^0$ . This list is called double- $\pi^0$ -list. Also a list with respective valid combinations of three neutral pions, called triple- $\pi^0$ -list is built.

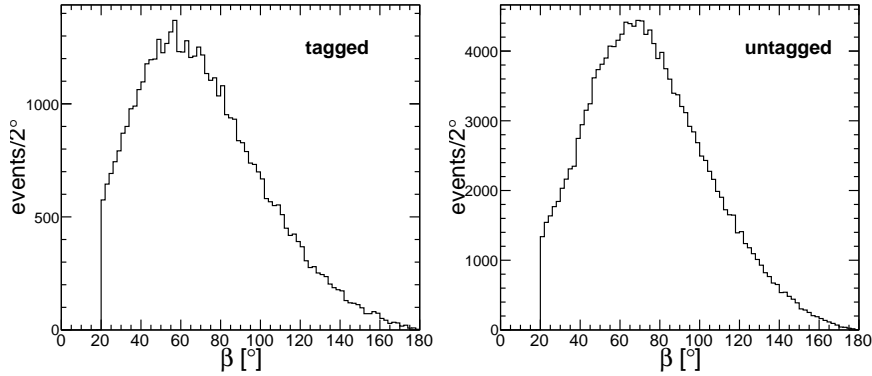


**Figure 4.1.:** Angle  $\beta$  between a charged pion and the closest EMC shower for both tracks in the events of the PHOKHARA 9.1 signal MC simulation.

**ISR Photon** The energy of the ISR photon,  $E_{ISR}$ , is required to be  $E_{ISR} > 360$  MeV. In the untagged modes  $E_{ISR}$  is the missing energy. Assuming LO ISR, this corresponds to  $m_{\text{had}} < 3.4 \text{ GeV}/c^2$  according to Eq.3.1.2 for a c.m. energy of 3.773 GeV. The threshold is applied because of the vast background due to low energetic ISR photons, which cannot be distinguished by a kinematic fit from the photons of the  $\pi^0$  decay. A MC study is performed to check, whether the kinematic fit correctly assigns the EMC shower of the ISR photon candidate to the true ISR photon. Figure 4.2 shows the angle  $\alpha$  between the momentum of the ISR photon at the generator level and the reconstructed shower in the EMC, which is assigned to the ISR photon after the kinematic fit. The angular distribution clearly shows that the angle is well below  $2^\circ$ . Due to the shower size assumed by the clustering algorithm, the minimum angle between different EMC showers is at least  $3^\circ$ , as mentioned in section 2.2. Hence, the fit does identify the ISR photon correctly.

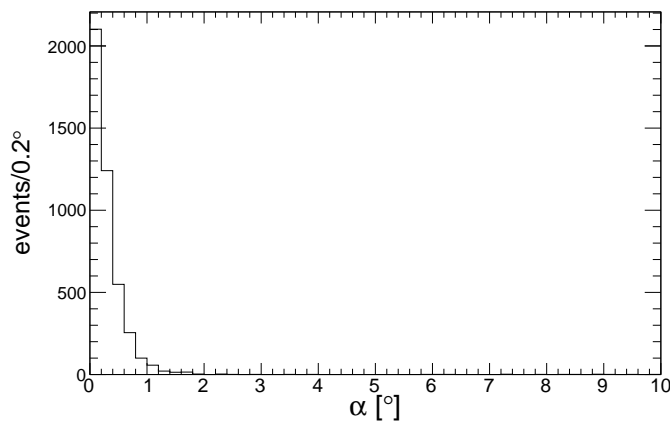


**Figure 4.2.:** Angle  $\alpha$  between the true and the reconstructed ISR photon.

**Kinematic Fit** For each channel a fit for all possible combinations of the two charged tracks, the double- or triple- $\pi^0$ -list and every additional photon as the ISR photon candidate is performed. In the non-ISR analysis of  $e^+e^- \rightarrow \pi^+\pi^-3\pi^0$ , there is no ISR photon candidate. Combinations are excluded, if the ISR photon is also used as decay photon for one of the neutral pions. In MC simulations the correction of the helix parameters according to [93] is applied.

The fits are constrained by the four momentum conservation and the neutral pion mass of the two photon pairs<sup>1</sup>. In case of the untagged ISR mode, a missing track for the ISR photon instead of a real EMC shower is used. From all these fits the one with the least  $\chi_{nC}^2$  is kept. The absolute requirement on the  $\chi^2$  is channel specific.

**$K_s$  Rejection** In the region  $480 < M(\pi^0\pi^0) < 520 \text{ MeV}/c^2$  all the analyses suffer from a small  $K_s$  background contribution originating from the final states  $e^+e^- \rightarrow K_s K \pi(\pi)(\gamma_{ISR})$ . If an event has at least one  $\pi^0\pi^0$  combination with  $480 < M(\pi^0\pi^0) < 520 \text{ MeV}/c^2$ , the PID system, introduced in section 2.2, is used to calculate the  $\pi$  and K probabilities  $P_{\pi/K}$  for both charged tracks. The  $K_s$  contamination is strongly suppressed by rejecting events with  $P_\pi < P_K$  for at least one of the charged tracks.

## 4.1. Event Selection for $e^+e^- \rightarrow \pi^+\pi^-2\pi^0\gamma_{ISR}$

**Vertex Fit (untagged) and IP distance (tagged and untagged)** A vertex fit is performed to find the intersection point of the helices of the two charged pion tracks. A value of  $\chi_{vertex}^2 < 500$  is required for the vertex fit of the two oppositely charged tracks. Figure 4.3 shows the vertex position distribution in the xy-plane for the ISR untagged method. In this method a structure in data around  $r_{vertex} = 3 \text{ cm}$  is observed. Since the position of the structure agrees with the position of the beam pipe, these vertices presumably stems from interactions of the beam with the beam pipe. The IP positions of the data sets taken in 2010 and 2011 are shifted relative to each other by 8 mm, due to calibration of the beam orbit. The beam lost in the beam pipe appears as missing energy, which is misidentified as the untagged ISR photon.

<sup>1</sup>In the following the expression  $\chi_{nC}^2$  denotes the  $\chi^2$  value of the fit, where  $n$  constraints are applied.

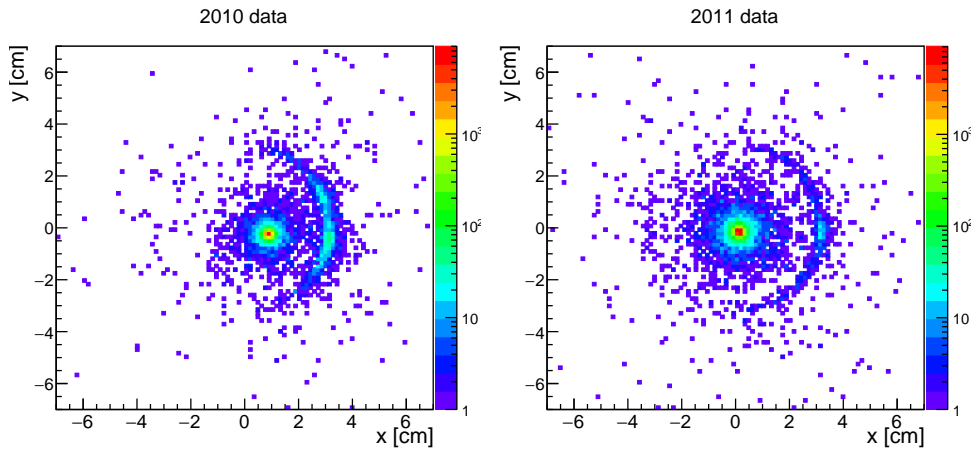


**Figure 4.3.:** Vertex position distribution in the xy-plane of the untagged method.

The beam related background is removed by requiring  $r_{vertex} < 2.0$  cm. Figure 4.4 shows the distributions of the radial and axial distances of the point of closest approach of each individual track (helix) to the IP after the vertex fit requirement.

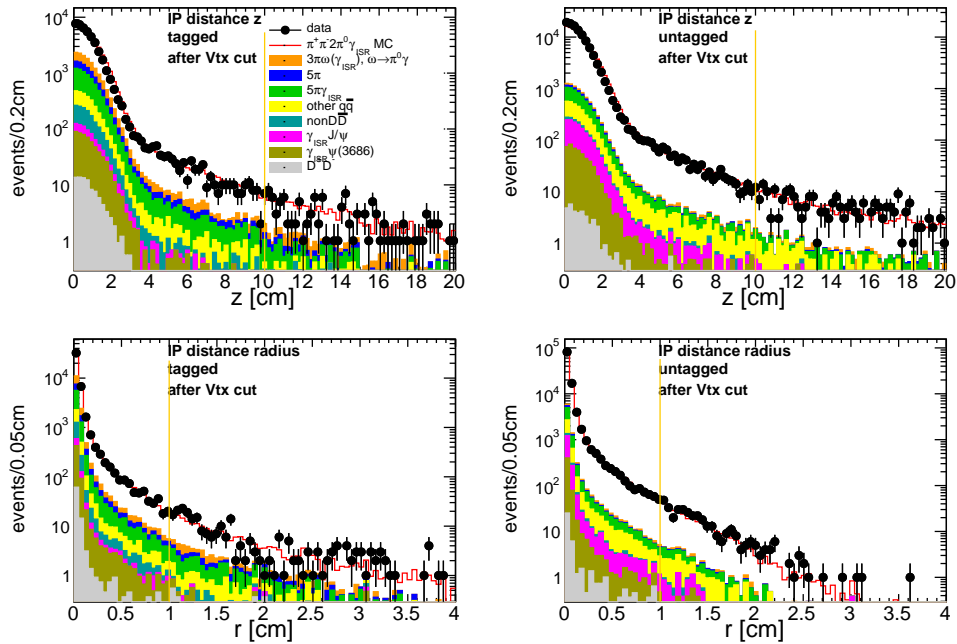


**Figure 4.4.:** Distance from the interaction point of both charged tracks after the vertex fit selection of the process  $e^+e^- \rightarrow \pi^+\pi^-2\pi^0\gamma_{ISR}$ .

**Number of EMC Showers** Figure 4.5 shows the multiplicity distribution of the number of good EMC showers. Required are less than eight good photons for tagged as well as for untagged events.

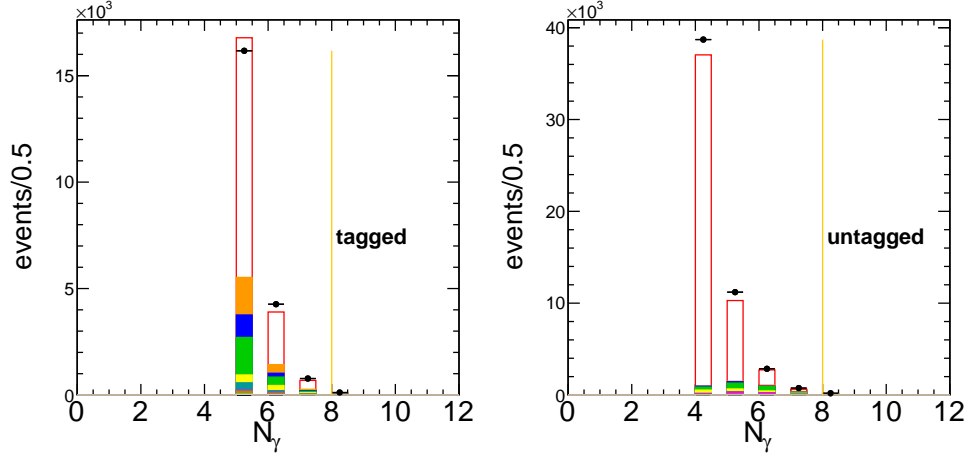


**Figure 4.5.:** Number of good EMC showers of the process  $e^+e^- \rightarrow \pi^+\pi^-2\pi^0\gamma_{ISR}$ .

**Neutral Pions** Fig. 4.6 shows the two photon mass distributions for the  $\pi^0$  reconstruction for the tagged and the untagged method. The left panels show the  $\pi^0$  candidate with the higher momentum and the right panels show the  $\pi^0$  particle with the lower momentum. As expected, the two photon mass distributions show a clear peak around the nominal  $\pi^0$  mass of  $135 \text{ MeV}/c^2$ . Data and MC are in good agreement. This proves the stability of the  $\pi^0$  reconstruction in the event selection procedure.

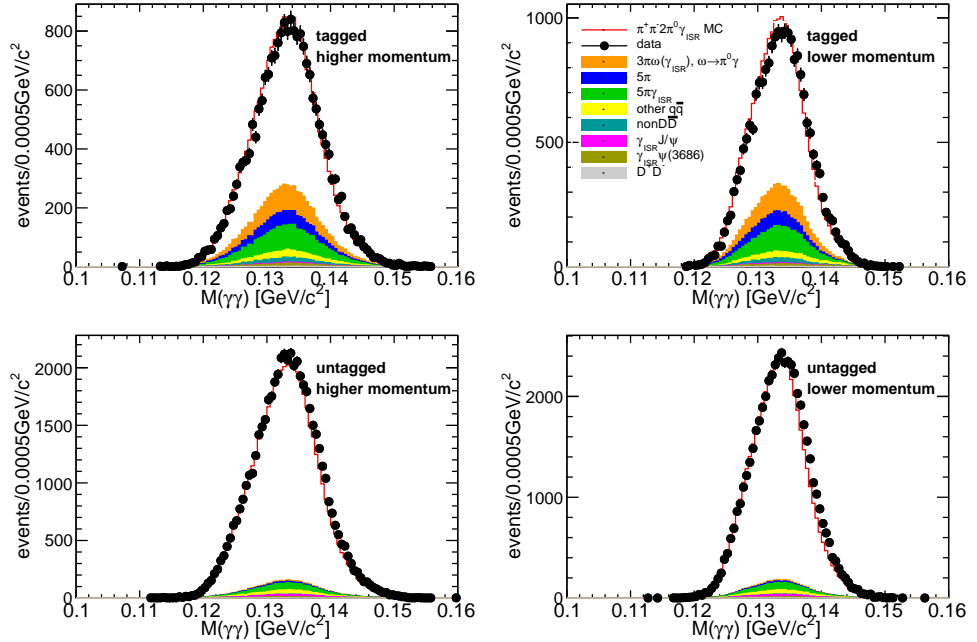


**Figure 4.6.:** Two photon mass distribution for both  $\pi^0$  candidates of the process  $e^+e^- \rightarrow \pi^+\pi^-2\pi^0\gamma_{ISR}$ .

**Kinematic Fit** For the tagged ISR method, the kinematic fit contains the four pions and the ISR photon. In the case of the untagged analysis, the ISR photon is treated as a massless particle with unknown momentum, which is to be determined by the fit. In both methods, the  $\pi^0$  masses are constrained in the fit. In case of the tagged analysis, events with  $\chi_{6C}^2 > 60$  are rejected. In case of the untagged ISR method, the best fit of the event is required to satisfy  $\chi_{3C}^2 < 30$  to accept the event. The  $\chi_{6C}^2/3C$  distributions for both ISR methods are shown in Fig. 4.7.

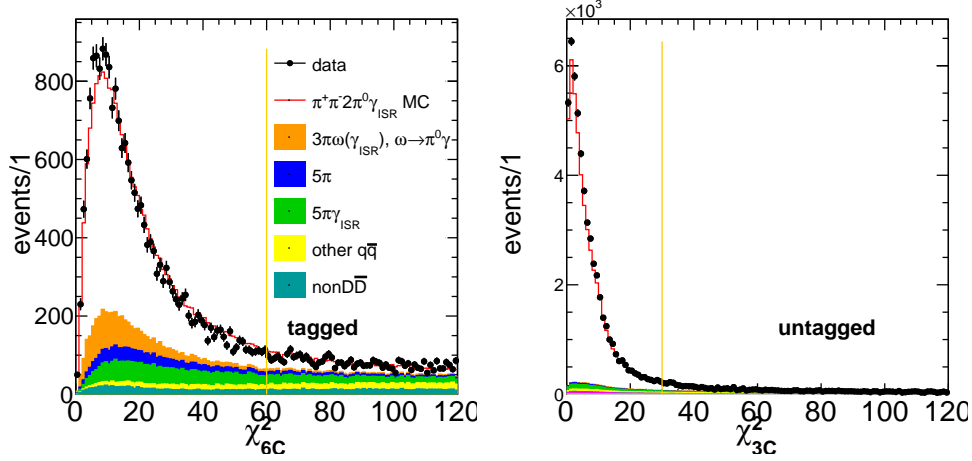


Figure 4.7.:  $\chi^2$  distributions of the kinematic fits of the process  $e^+e^- \rightarrow \pi^+\pi^-2\pi^0\gamma_{ISR}$ .

**Energy of the ISR Photon** Figure 4.8 shows the energy distributions of the ISR photons for the tagged and the untagged method.

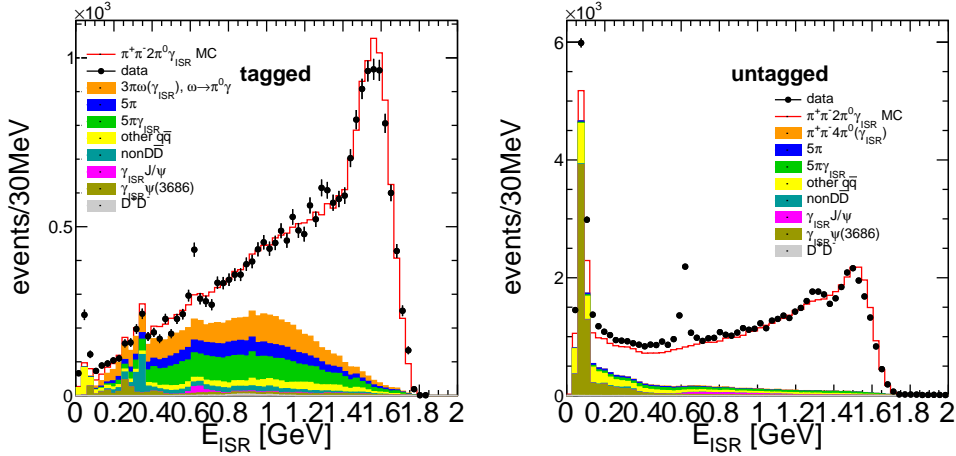


Figure 4.8.: Energy distributions of the ISR photon of the process  $e^+e^- \rightarrow \pi^+\pi^-2\pi^0\gamma_{ISR}$ .

At small energies  $E_{ISR}$  of the ISR photon, the kinematic fit cannot distinguish the ISR photon from  $\pi^0$  decay photons. For energies smaller than

500 MeV, the background level is rising steeply to a signal to background ratio of below 1:4. Therefore, events with  $E_{ISR} < 360$  MeV are rejected for both analysis modes.

**$K_s$  Rejection** As explained before, in the  $2\pi^0$  mass region  $480 < M(\pi^0\pi^0) < 520$  MeV/ $c^2$ , a  $K_s$  veto using the PID system is performed to veto the background contribution  $e^+e^- \rightarrow K_s K \pi(\pi)(\gamma_{ISR})$ . The  $M(\pi^0\pi^0)$  mass distribution is shown in Fig. 4.9. The  $K_s$  peak is obvious in the distributions from data and MC simulations.

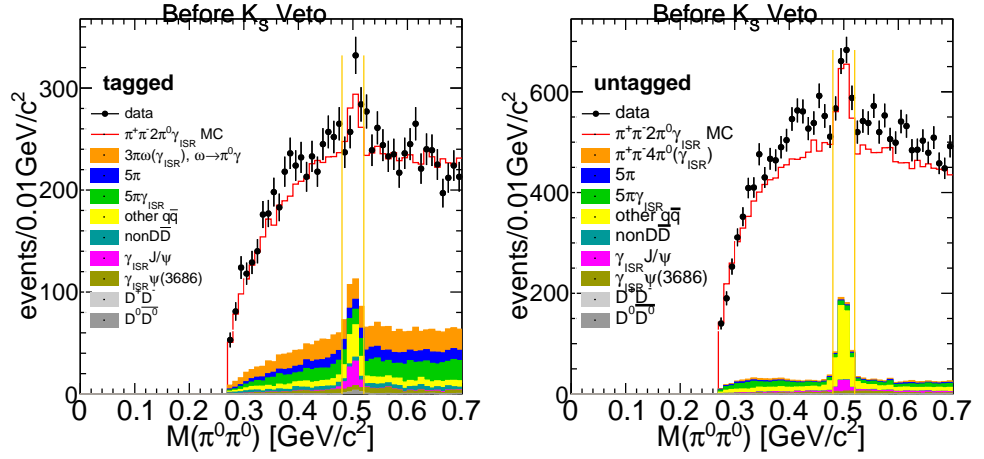


Figure 4.9.:  $M(\pi^0\pi^0)$  distribution before the  $K_s$  veto of the process  $e^+e^- \rightarrow \pi^+\pi^-2\pi^0\gamma_{ISR}$ .

For good pion tracks, the probability calculated by the PID system to be a pion,  $P_\pi$ , should be higher than the probability to be a Kaon,  $P_K$ . Hence, events with  $P_\pi < P_K$  are rejected. The PID distribution for the  $K_s$  rejection is shown in Fig. 4.10.

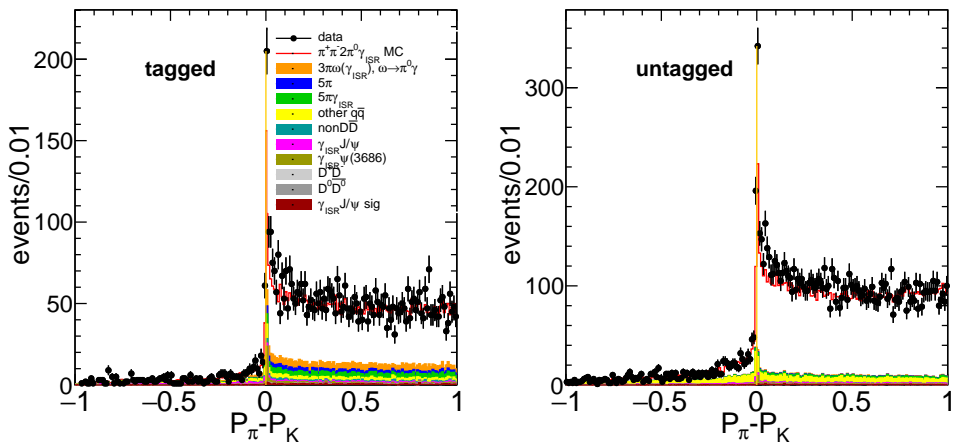
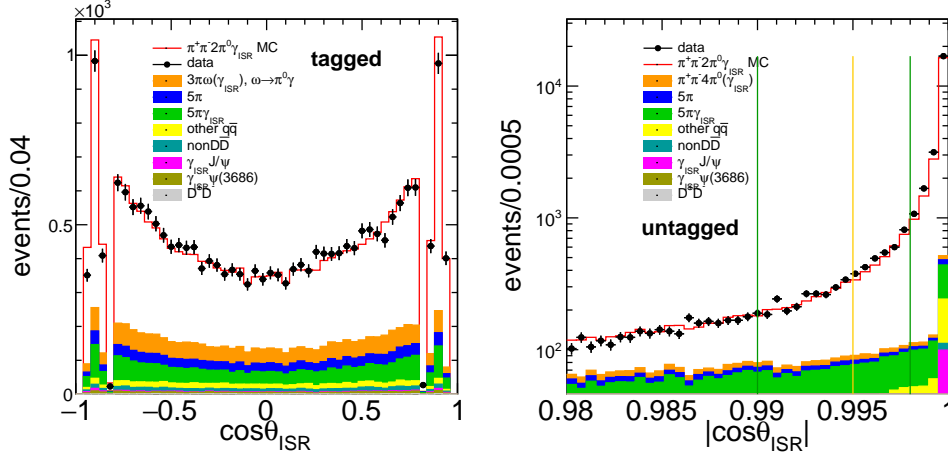


Figure 4.10.: Kaon PID distribution of the process  $e^+e^- \rightarrow \pi^+\pi^-2\pi^0\gamma_{ISR}$ .

**Polar Angle of the ISR Photon (untagged)** In case of the untagged method  $|\cos\theta_{ISR}| > 0.995$  is required for the polar angle of the missing ISR photon. This selection provides a good signal to background ratio, since the region with  $|\cos\theta_{ISR}| \leq 0.995$  is dominated by background. Fig. 4.11 shows the polar angle distribution of the ISR photon for tagged and untagged methods. For both methods, Fig. 4.11 shows good agreement between data and simulation for the distribution of the polar angle of the ISR photon.



**Figure 4.11.:** Polar angle distributions of the ISR photon of the process  $e^+e^- \rightarrow \pi^+\pi^-2\pi^0\gamma_{ISR}$ .

**Misidentified ISR Photons (tagged method only)** For the tagged method a condition on the quantity  $M(\gamma_{ISR}\gamma) = (p_\gamma + p_{ISR})^2$  is applied.  $M(\gamma_{ISR}\gamma)$  is calculated for the combination of each of the up to six EMC showers in the event and the ISR photon. Events are rejected, if  $|M(\gamma_{ISR}\gamma) - m_{\pi^0}^{\text{detector}}| < 40$  MeV, where  $m_{\pi^0}^{\text{detector}} = 134.6 \pm 0.5$  MeV is the neutral pion mass obtained by a fit to data in section 5.3. For the tagged ISR method, the left panel of Fig. 4.12 shows a peak at the  $\pi^0$  mass on top of a broad distribution.

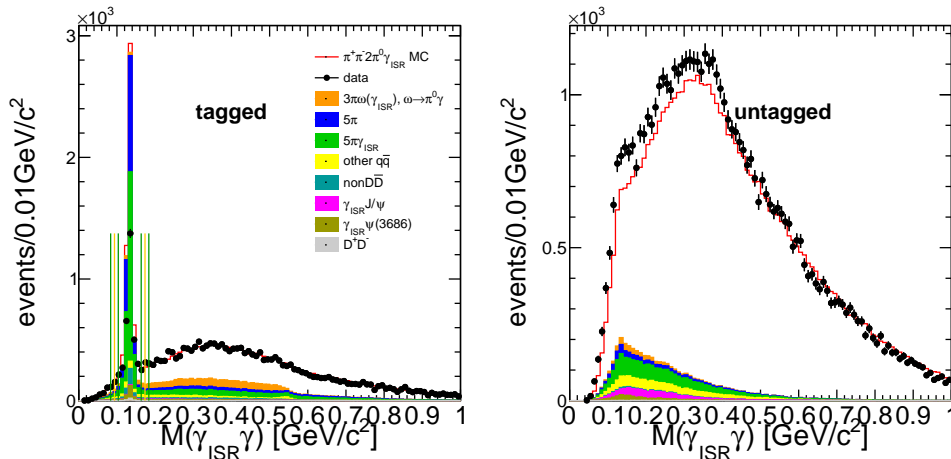


**Figure 4.12.:**  $M(\gamma_{ISR}\gamma)$  distributions of the process  $e^+e^- \rightarrow \pi^+\pi^-2\pi^0\gamma_{ISR}$ .

In the reconstruction of the events contributing to the peak, a photon from a  $\pi^0$  decay has been wrongly assigned as ISR photon. Rejecting these events reduces the background contributions from the reaction  $e^+e^- \rightarrow \pi^+\pi^-3\pi^0$ , where one of the neutral pions cannot be reconstructed completely, but one of its decay photons is misidentified as the ISR photon. In the case of the untagged method, there are slightly more events in data compared to the MC simulations. This is due to the large missing  $J/\psi$  contribution in the PHOKHARA 9.1 event generator. Moreover, for the untagged method, the right panel of Fig. 4.12 does not show a peak at the  $\pi^0$  mass. The reason for the missing  $\pi^0$  peak in the untagged method is that the polar angle range of the ISR photon in the untagged method is limited to  $|\cos\theta_{ISR}| > 0.995$ , whereas the polar angle range of the ISR photons in the tagged method is  $|\cos\theta_{ISR}| < 0.93$ . This means that the polar angle range of the tagged method is almost two orders of magnitude larger than the range of the untagged method. The decay photons of the neutral pions are distributed uniformly. Hence, the probability to misinterpret a photon from a  $\pi^0$  decay as the ISR photon is almost two orders of magnitudes lower in the untagged method compared to the tagged method.

**Angle between ISR Photon and Neutral Pions (tagged)** Let  $\alpha$  denote the minimum angle between the ISR photon and the neutral pions. In data, shown in the upper left panel of Fig. 4.13, two distinct enhancements are observed.

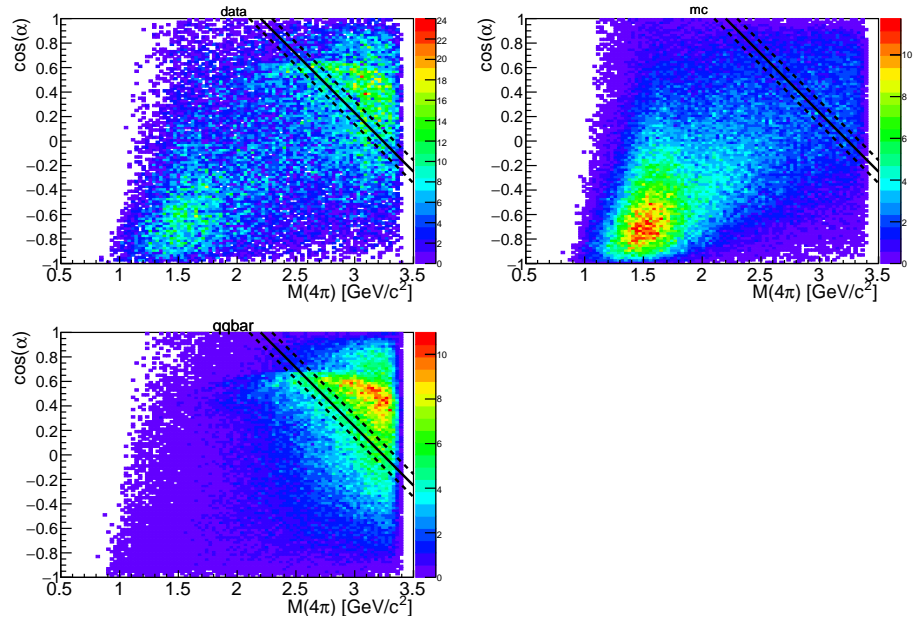


**Figure 4.13.:** Distribution of the minimal angle  $\cos\alpha$  between the ISR photon and the neutral pions. The black line is the cut. The dashed lines are for the systematic error study of  $e^+e^- \rightarrow \pi^+\pi^-2\pi^0\gamma_{ISR}$ .

One at low masses and negative  $\cos \alpha$  and the other at high masses and large  $\cos \alpha$ . The comparison with signal MC in the upper right panel and qqbar MC in the lower left panel reveals that only the enhancement at low masses and negative  $\cos \alpha$  is due to the signal process. In order to reduce the  $e^+e^- \rightarrow \pi^+\pi^-3\pi^0\gamma_{ISR}$  background contribution in the tagged method, events that have  $\cos \alpha > -0.96\text{GeV}^{-1}M(\pi^+\pi^-2\pi^0) + 3.12$  are rejected. This is the upper right area marked with the black line in Fig. 4.13. The condition is not applied in the untagged method.

All criteria used for the event selection of the process  $e^+e^- \rightarrow \pi^+\pi^-2\pi^0\gamma_{ISR}$  are summarized in Table 4.1. Table 4.2 shows the number of events in data, signal MC simulation and background simulations that survive the events selection of the tagged and untagged methods.

**Table 4.1.:** Summary of the event selection criteria of the process  $e^+e^- \rightarrow \pi^+\pi^-2\pi^0\gamma_{ISR}$ .

|   | tagged  | untagged                          |
|---|---|-----------------------------------|
| <b>Vertex Fit</b>   | -   | $r_{vertex} < 2.00$ cm            |
| <b>Charged tracks</b>   | $N_{ch} = 2$ (net charge 0)<br>$r < 1.0$ cm<br>$ z  < 10.0$ cm                                    |                                   |
| <b>Good Photons</b>   | $E > 25$ MeV (barrel)<br>$E > 50$ MeV (end caps)<br>$0 \leq \text{TDC} \leq 14$<br>$N_\gamma < 8$ |                                   |
| <b><math>\pi^0</math> Mass</b>  | $100 < M(\gamma\gamma) < 160$ MeV/ $c^2$  |                                   |
| <b><math>\pi^0</math> Candidates</b>  | $\geq 2$ non overlapping  |                                   |
| <b>Fake ISR</b>   | $ M(\gamma_{ISR}\gamma) - m_{\pi^0}  > 40$ MeV/ $c^2$   | -                                 |
| <b><math>\cos \alpha</math></b>   | $< -0.96\text{GeV}^{-1}M(\pi^+\pi^-2\pi^0) + 3.12$  | -                                 |
| <b>ISR Photon</b><br>$ \cos \theta $  | $E_{ISR} > 360$ MeV<br>$< 0.93$   | $E_{miss} > 360$ MeV<br>$> 0.995$ |
| <b><math>K_s</math> rejection</b><br>$480 < M(\pi^0\pi^0) < 520$ MeV/ $c^2$ | $P_\pi - P_K < 0$   | $P_\pi - P_K < 0$                 |
| <b>Kinematic Fit</b>  | $\chi_{6C}^2 < 60$  | $\chi_{3C}^2 < 30$                |

**Table 4.2.:** Summary of the number of events after the selection of the process  $e^+e^- \rightarrow \pi^+\pi^-2\pi^0\gamma_{ISR}$ .

|   | tagged | untagged |
|---|--------|----------|
| data  | 21320  | 53696    |
| signal MC                                   | 14203  | 46767    |
| $3\pi\omega(\gamma_{ISR})$ MC (tagged only) | 2250   | -        |
| $6\pi(\gamma_{ISR})$ MC (untagged only)     | -      | 314      |
| $5\pi$ MC                                   | 1282   | 305      |
| $5\pi\gamma_{ISR}$ MC                       | 2232   | 1261     |
| other $q\bar{q}$ MC                         | 676    | 948      |
| $nonD\bar{D}$ MC                            | 437    | 94       |
| $J/\psi\gamma_{ISR}$ MC                     | 106    | 555      |
| $\psi(3686)\gamma_{ISR}$ MC                 | 243    | 244      |
| $D^+D^-$ MC                                 | 4      | 6        |

## 4.2. Event Selection for $e^+e^- \rightarrow \omega\pi^0\gamma_{ISR}$

Events stemming from the process  $e^+e^- \rightarrow \omega\pi^0$  are obtained from fits to the  $\omega$  resonance in the  $M(\pi^+\pi^-\pi^0)$  distributions of the selected  $e^+e^- \rightarrow \pi^+\pi^-2\pi^0\gamma_{ISR}$  events. In order to calculate the reconstruction efficiency of  $e^+e^- \rightarrow \omega\pi^0\gamma_{ISR}$ , this kind of events has to be selected in the PHOKHARA 9.1  $e^+e^- \rightarrow \pi^+\pi^-2\pi^0\gamma_{ISR}$  signal MC. All event selection criteria shown in Table. 4.1 are applied. In addition, a mass window of  $720 < M(\pi^+\pi^-\pi^0) < 830 \text{ MeV}/c^2$  in the tagged ISR method and  $720 < M(\pi^+\pi^-\pi^0) < 850 \text{ MeV}/c^2$  in the untagged method is required to select the  $\omega$  resonance. The omega peak is slightly broader in the untagged ISR method. Figure 4.14 shows the  $M(\pi^+\pi^-\pi^0)$  distribution of the PHOKHARA 9.1 simulation. For every event only the mass of the pion combination is shown, which yields the  $M(\pi^+\pi^-\pi^0)$  value closest to the mass of the  $\omega$  resonance. Obviously, a small non-resonant  $\omega$  contribution is still remaining in the signal simulation. This background is removed by a sideband subtraction, since it is sufficiently linear. The sideband regions are defined as  $610 < M(\pi^+\pi^-\pi^0) < 720 \text{ MeV}/c^2$  and  $830 < M(\pi^+\pi^-\pi^0) < 940 \text{ MeV}/c^2$  for the tagged mode. For the untagged mode, the sideband regions are  $590 < M(\pi^+\pi^-\pi^0) < 720 \text{ MeV}/c^2$  and  $850 < M(\pi^+\pi^-\pi^0) < 980 \text{ MeV}/c^2$ . Hence, the sideband rescaling factor is  $\frac{1}{2}$ . Although, the absolute contribution of  $e^+e^- \rightarrow \omega\pi^0\gamma_{ISR}$  is underestimated by the simulation, the efficiency is correct, since the momentum and angular distributions are simulated correctly.

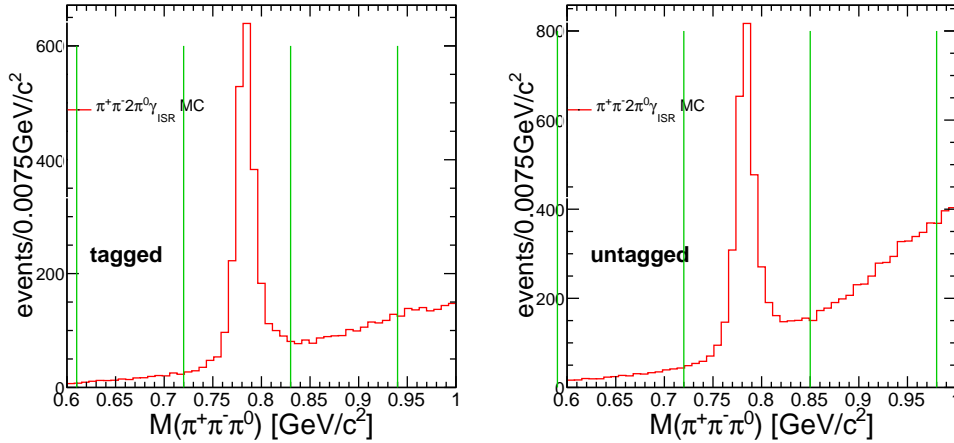


**Figure 4.14.:**  $M(\pi^+\pi^-\pi^0)$  distribution after the  $e^+e^- \rightarrow \pi^+\pi^-2\pi^0\gamma_{ISR}$  event selection. Green lines mark the signal and sideband regions.

### 4.3. Event Selection for the Background

#### 4.3.1. Event Selection for $e^+e^- \rightarrow \pi^+\pi^-3\pi^0\gamma_{ISR}$

The process  $e^+e^- \rightarrow \pi^+\pi^-3\pi^0\gamma_{ISR}$  gives a large background contribution to the process  $e^+e^- \rightarrow \pi^+\pi^-2\pi^0\gamma_{ISR}$ . However, the process  $e^+e^- \rightarrow \pi^+\pi^-3\pi^0\gamma_{ISR}$  is barely known experimentally and the quality of the MC description is unclear. In order to gain a precision of about 10%, which is mandatory for a reliable background subtraction in the  $e^+e^- \rightarrow \pi^+\pi^-2\pi^0\gamma_{ISR}$  analysis, a measurement is performed to validate the quality of the MC description and to correct the MC distributions.

An MC study showed that the signal reconstruction efficiency in the  $e^+e^- \rightarrow \pi^+\pi^-3\pi^0\gamma_{ISR}$  channel is less than one percent in the ISR tagged method and the signal to background ratio is below 1:4. Therefore, in the following, only the  $e^+e^- \rightarrow \pi^+\pi^-3\pi^0\gamma_{ISR}$  ISR untagged method is considered.

**Vertex Fit and IP distance cut** A vertex fit of the two oppositely charged tracks is performed. Events with  $\chi_{vertex}^2 \geq 500$  are rejected. The radial distance of the fitted vertex position to the origin in the center of the beam pipe is shown in Fig. 4.15. The structure in data around  $r_{vertex} = 3$  cm corresponds to the beam related background explained in section 4.1.

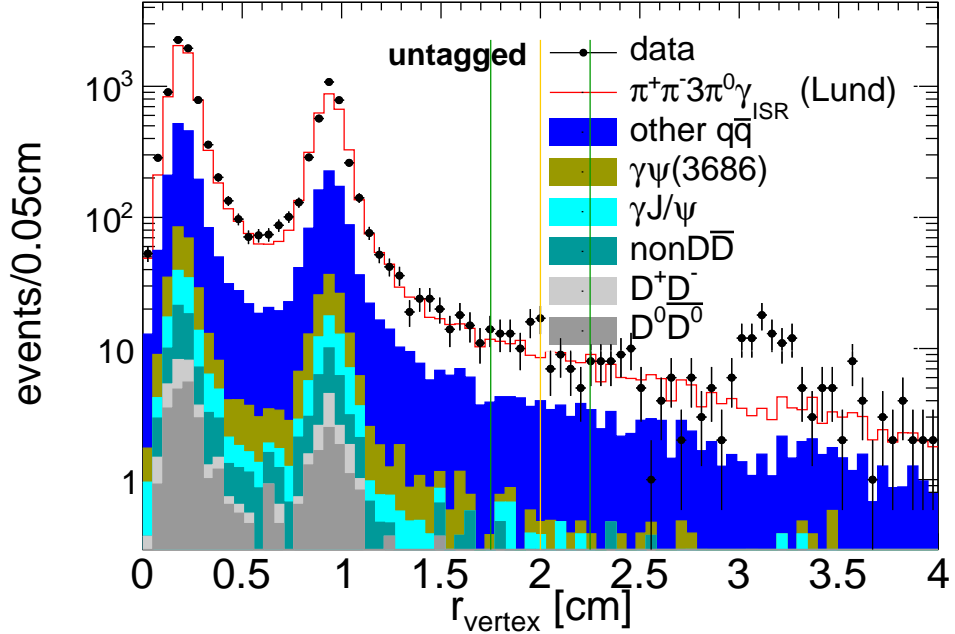


**Figure 4.15.:** Radial distance between the track origin and the interaction vertex of  $e^+e^- \rightarrow \pi^+\pi^-3\pi^0\gamma_{ISR}$ .

The two peaks correspond to the IP positions of the 2010 and 2011 data taking periods as pointed out in section 4.1. The beam related background is removed by requiring  $r_{vertex} < 2$  cm. The distributions of the radial and axial distances of the point of closest approach of the individuals tracks to the IP after the vertex fit condition are shown in Fig. 4.16.

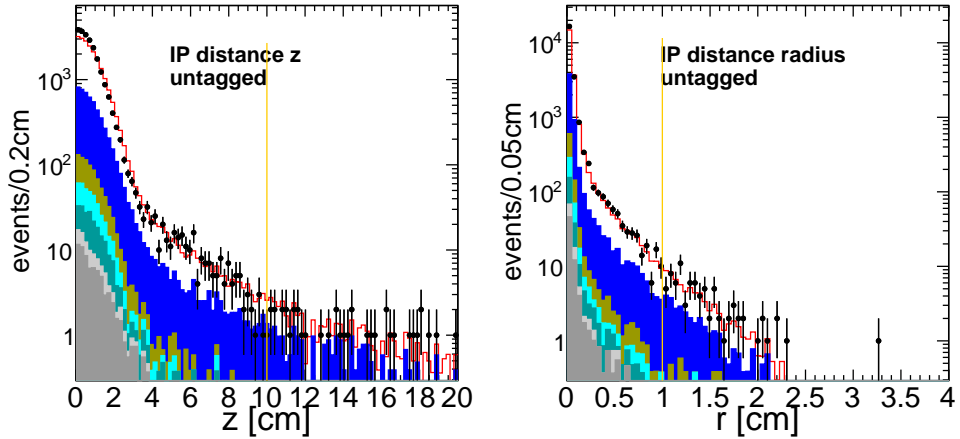


**Figure 4.16.:** Axial (left) and radial (right) distance between the track origin and the interaction vertex after the vertex fit of the process  $e^+e^- \rightarrow \pi^+\pi^-3\pi^0\gamma_{ISR}$ .

**Kinematic Fit** The kinematic fit is performed as explained at the beginning of this chapter, using energy momentum conservation and the masses of the

three neutral pions as constraints, while the untagged ISR photon is treated as massless particle with unknown momenta. The  $\chi_{4C}^2$  distribution is shown in Fig.4.17. Events with  $\chi_{4C}^2 < 30$  are accepted for the untagged method.

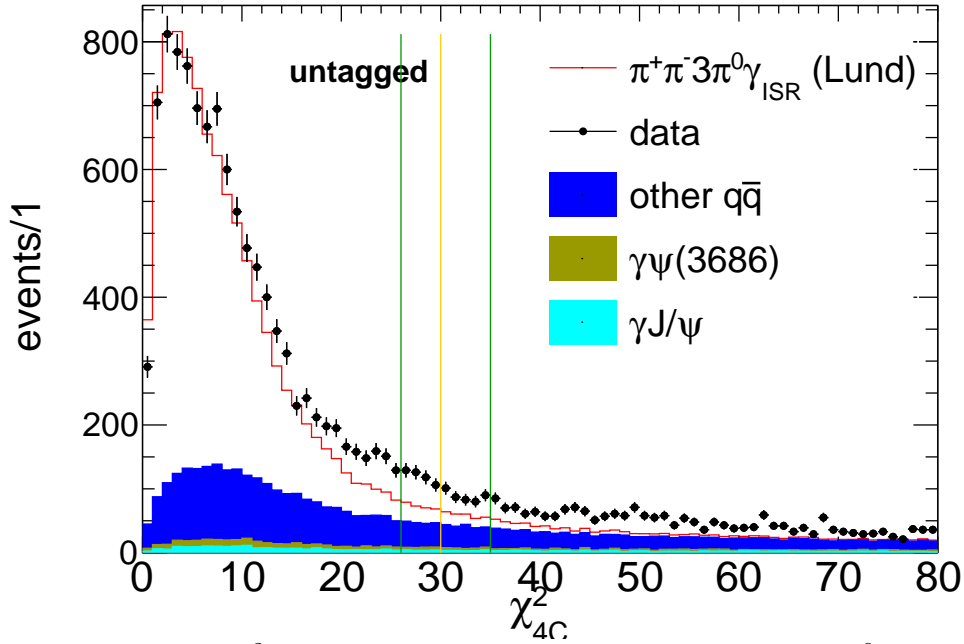
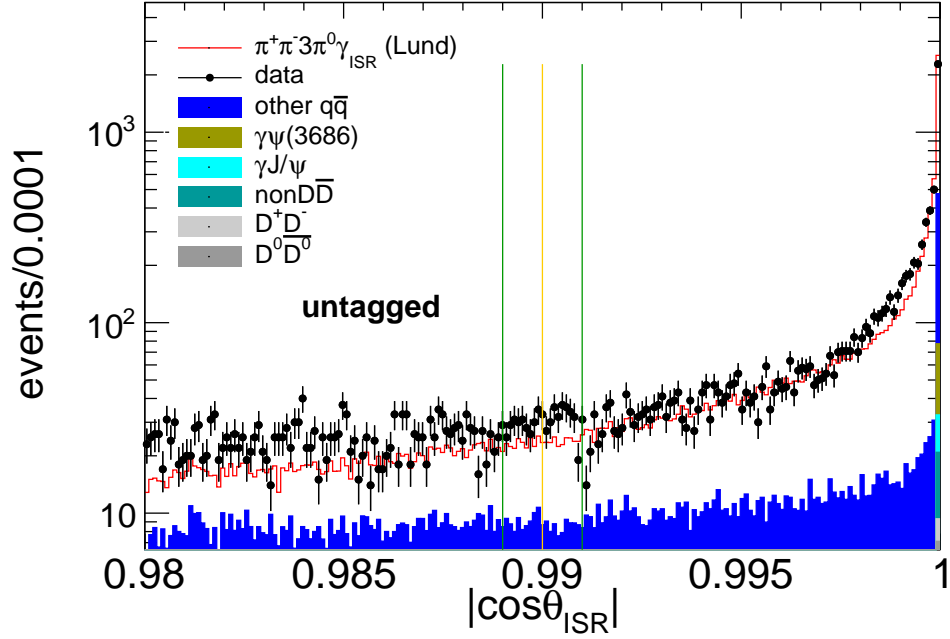


Figure 4.17.:  $\chi_{4C}^2$  distributions of the process  $e^+e^- \rightarrow \pi^+\pi^-3\pi^0\gamma_{ISR}$ .

For a better comparison of the shape between data and the simulations, the scaling of the  $e^+e^- \rightarrow \pi^+\pi^-3\pi^0\gamma_{ISR}$  signal MC simulation is chosen such that the average of the first five bins in data and MC simulation are equal. The corresponding rescaling factor is  $f_{5\pi\gamma_{ISR}} = 0.68$ . This rescaling factor is applied to all plots shown in the  $e^+e^- \rightarrow \pi^+\pi^-3\pi^0\gamma_{ISR}$  event selection section in this section. The uncertainty of the scaling factor is not considered, because it is not used to determine the efficiency nor the cross section.

**ISR polar angle** For the polar angle of the missing ISR photon from the fit,  $|\cos\theta_{ISR}| > 0.990$  is required. This selection provides the optimal signal to background ratio, since the background ratio increases in the region at  $|\cos\theta_{ISR}| \leq 0.990$ . Figure 4.18 shows the polar angle distribution of the untagged ISR photon.



**Figure 4.18.:** Polar angle distribution of the untagged ISR photon of the process  $e^+e^- \rightarrow \pi^+\pi^-3\pi^0\gamma_{ISR}$ .

**$K_s$  Rejection** The rejection of background contributions containing  $K_s$  is performed analogously to the methods described in section 4.1. Here, there are three combinations to calculate  $M(\pi^0\pi^0)$ . The PID distribution for the  $K_s$  rejection is shown in Fig. 4.19. Events with  $P_\pi - P_K < 0$  are rejected.

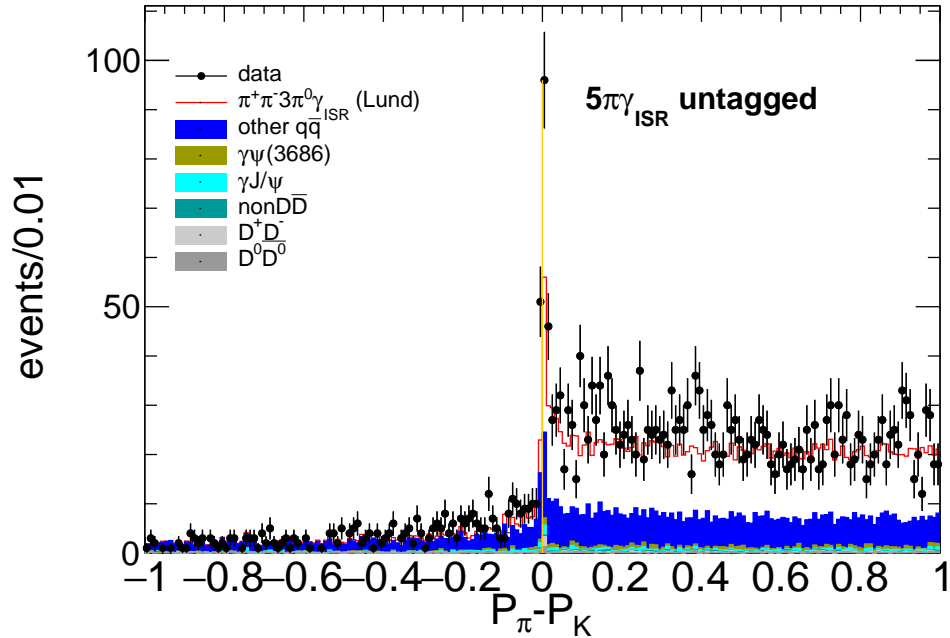


**Figure 4.19.:** Difference of Kaon and Pion identification probabilities for the  $K_s$  rejection in the process  $e^+e^- \rightarrow \pi^+\pi^-3\pi^0\gamma_{ISR}$ .

All criteria used for the event selection of the process  $e^+e^- \rightarrow \pi^+\pi^-3\pi^0\gamma_{ISR}$  are summarized in Tab. 4.3. In total, 10996 events survive the event selection in data, 13646 in the signal simulation and 2637 in the background MC simulations.

**Table 4.3.:** Summary of all event selection criteria for the untagged  $\pi^+\pi^-3\pi^0\gamma_{ISR}$  final state.

|                                      |   |
|--------------------------------------|---|
| <b>Charged tracks</b>                | $N_{ch} = 2$ (net charge 0)<br>$r < 1.0$ cm<br>$ z  < 10.0$ cm<br>$r_{vertex} < 2$ cm             |
| <b>Good Photons</b>                  | $E > 25$ MeV (barrel)<br>$E > 50$ MeV (end caps)<br>$0 \leq \text{TDC} \leq 14$<br>$N_\gamma < 8$ |
| <b><math>\pi^0</math> Masses</b>     | $100 < M(\gamma\gamma) < 160$ MeV/ $c^2$  |
| <b><math>\pi^0</math> Candidates</b> | $\geq 3$ non overlapping  |
| <b>ISR Photon</b>                    | $E_{ISR} > 360$ MeV<br>$ \cos\theta  > 0.990$   |
| <b>Kinematic Fit</b>                 | $\chi_{4C}^2 < 30$  |
| <b><math>K_s</math> rejection</b>    | $P_\pi - P_K < 0$ if $480 < M(\pi^0\pi^0) < 520$ MeV/ $c^2$                                       |

### 4.3.2. Event Selection for $e^+e^- \rightarrow \omega 2\pi^0\gamma_{ISR}$

The process  $e^+e^- \rightarrow \pi^+\pi^-3\pi^0\gamma_{ISR}$  has significant contributions from resonant channels like  $e^+e^- \rightarrow \omega 2\pi^0\gamma_{ISR}$  and  $e^+e^- \rightarrow \eta\pi^+\pi^-\gamma_{ISR}$ . These sub-channels are studied explicitly, as good knowledge of their contributions is vital to the understanding of the full  $e^+e^- \rightarrow \pi^+\pi^-3\pi^0\gamma_{ISR}$  process. This section focuses on the selection of  $e^+e^- \rightarrow \omega 2\pi^0\gamma_{ISR}$ .

All criteria shown in Table. 4.3 of the  $e^+e^- \rightarrow \pi^+\pi^-3\pi^0\gamma_{ISR}$  event selection are applied. In every event the combination of two charged and one neutral pion is selected, which has an invariant mass closest to the omega peak. A mass window of  $720 < M(\pi^+\pi^-\pi^0) < 850$  MeV/ $c^2$  is applied to this invariant mass distribution in order to select good  $e^+e^- \rightarrow \omega 2\pi^0$  candidates. A nonresonant  $\omega$  background contribution is left after subtracting the background contributions from other processes using the MC simulations. It is removed by a sideband subtraction, since the simulations indicate a sufficiently linear nonresonant background contributions. The sideband regions are defined as  $590 < M(\pi^+\pi^-\pi^0) < 720$  MeV/ $c^2$  and  $850 < M(\pi^+\pi^-\pi^0) < 980$  MeV/ $c^2$ . Hence the sideband rescaling factor is  $\frac{1}{2}$ . The right panel of Fig. 4.20 shows the  $M(\pi^+\pi^-\pi^0)$  distribution after background and sideband subtraction. The lower and upper bounds of the sideband regions are

marked with green lines in Fig. 4.20. The signal region is between the two yellow lines.

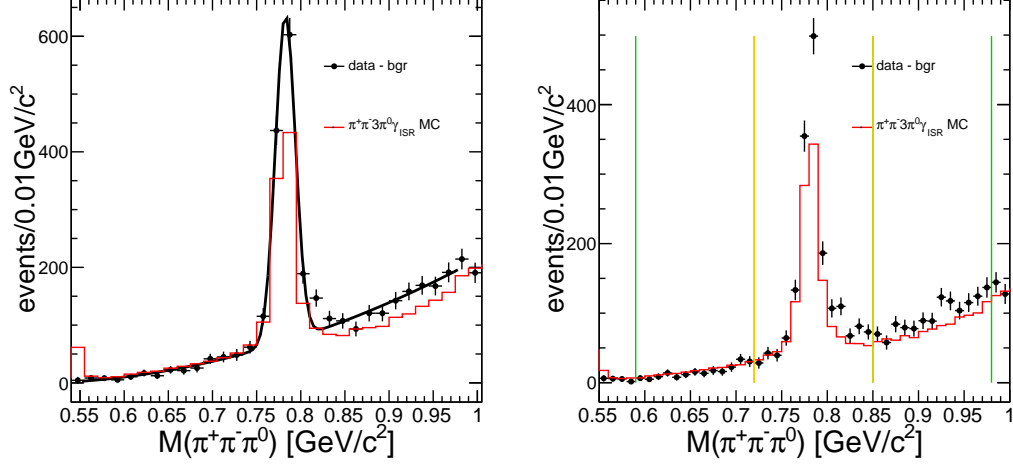


**Figure 4.20.:**  $M(\pi^+\pi^-\pi^0)$  distribution after the  $e^+e^- \rightarrow \pi^+\pi^-3\pi^0\gamma_{ISR}$  selection and background subtraction with a  $\omega$  fit (left) and with marked sideband subtraction (right).

A fit of the  $M(\pi^+\pi^-\pi^0)$  distribution after background subtraction, but before sideband subtraction with a Gaussian plus a polynomial is performed in order to cross check the sideband subtraction method. The fit is shown in the left panel of Fig. 4.20 and yields  $1071 \pm 33$  events in the  $\omega$  peak, where the fit quality is  $\chi^2/\text{ndf} = 1.08$ . Using the sideband subtraction,  $1090 \pm 33$  events are obtained in data, which is in good agreement with the fit result within errors.

### 4.3.3. Event Selection for $e^+e^- \rightarrow 5\pi\gamma_{ISR}$ excluding $\eta$ , and $e^+e^- \rightarrow \eta\pi^+\pi^-\gamma_{ISR}$

In order to select the  $e^+e^- \rightarrow \eta\pi^+\pi^-\gamma_{ISR}$  sub-channel of  $e^+e^- \rightarrow \pi^+\pi^-3\pi^0\gamma_{ISR}$ , all event selection criteria of the  $e^+e^- \rightarrow \pi^+\pi^-3\pi^0\gamma_{ISR}$  event selection are applied. Additionally, a mass window of  $M(\pi^0\pi^0\pi^0) < 600 \text{ MeV}/c^2$  is applied on the invariant mass of the three neutral pions. The right panel of Fig. 4.21 shows the  $M(\pi^0\pi^0\pi^0)$  distribution after subtracting background contributions according to MC distributions. The mass window is indicated by orange lines. After background subtraction using MC distributions, the remaining nonresonant background is negligible. A fit of the  $M(\pi^0\pi^0\pi^0)$  distribution after background subtraction, but before sideband subtraction with a Gaussian plus a polynomial is performed in order to cross check the subtraction method. The fit, shown in the left panel of Fig. 4.21, yields  $196 \pm 14$  events in the  $\eta$  peak, where the fit quality

is  $\chi^2/\text{ndf} = 0.58$ . Using the sideband subtraction method,  $192 \pm 13$  events are obtained in data, which is in agreement with the fit result within errors.

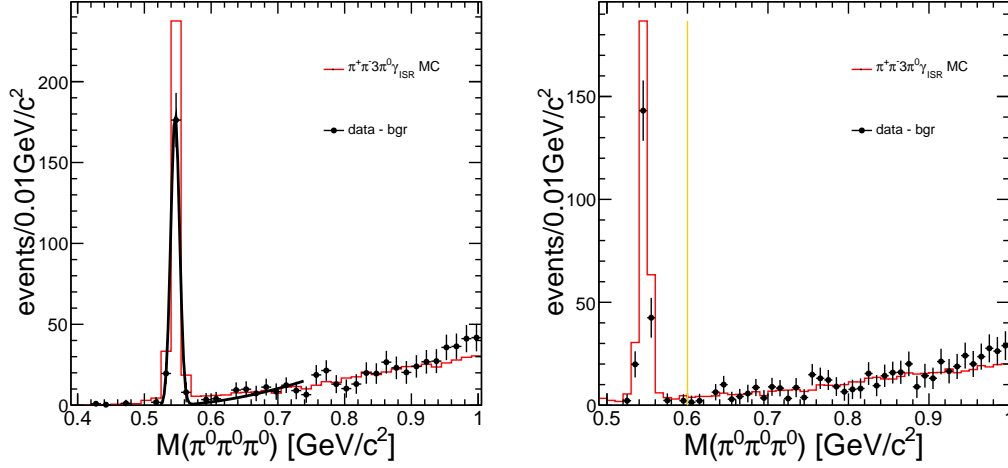


**Figure 4.21.:**  $M(\pi^0\pi^0\pi^0)$  distribution after the  $e^+e^- \rightarrow \pi^+\pi^-3\pi^0\gamma_{ISR}$  selection and background subtraction with a  $\eta$  fit (left) and after additional sideband subtraction (right).

Also the process  $e^+e^- \rightarrow \pi^+\pi^-3\pi^0\gamma_{ISR}$  without a contribution of the  $\eta$  meson in the  $3\pi^0$  subsystem is measured in this thesis. To select events of this type, all event selection criteria of the  $e^+e^- \rightarrow \pi^+\pi^-3\pi^0\gamma_{ISR}$  event selection are applied. Additionally, the selection criteria of the  $\eta$  meson discussed before are inverted to  $M(\pi^0\pi^0\pi^0) > 600 \text{ MeV}/c^2$ , in order to reject all events containing a contribution of the  $\eta$  meson. The loss of nonresonant  $e^+e^- \rightarrow \pi^+\pi^-3\pi^0\gamma_{ISR}$  events under the  $\eta$  resonance peak is negligible, as shown in Fig. 4.21.

#### 4.3.4. Event Selection for $e^+e^- \rightarrow \pi^+\pi^-3\pi^0$

Also the process  $e^+e^- \rightarrow \pi^+\pi^-3\pi^0$  at 3.773 GeV creates a large background contribution to the analysis of the  $e^+e^- \rightarrow \pi^+\pi^-2\pi^0\gamma_{ISR}$  process. The  $e^+e^- \rightarrow \pi^+\pi^-3\pi^0$  process is barely known experimentally and the quality of the MC description is unclear. In order to gain a precision of about 10% in the knowledge of this channel, a measurement is performed to validate the quality of the MC description and to correct the MC distributions. The MC sample, referred to as  $\pi^+\pi^-3\pi^0$  in the following, combines the MC samples of  $e^+e^- \rightarrow \omega 2\pi^0$  and  $e^+e^- \rightarrow \eta\pi^+\pi^-$  with the sample of  $e^+e^- \rightarrow \pi^+\pi^-3\pi^0$  without intermediate contributions of  $\omega$  and  $\eta$  resonances, produced with the HELPWA generator. The data-driven generator model HELPWA simulates events according to a PWA performed on the results of the measurement described below to simulate events accordingly.

**Kinematic Fit** The kinematic fit is performed as explained in the beginning of this chapter. Here the fit has seven constraints. These are the three pion masses plus four constraints from requiring energy-momentum conservation. The  $\chi^2_{7C}$  distribution is shown in Fig.4.22. Events with  $\chi^2_{7C} < 50$  are accepted.

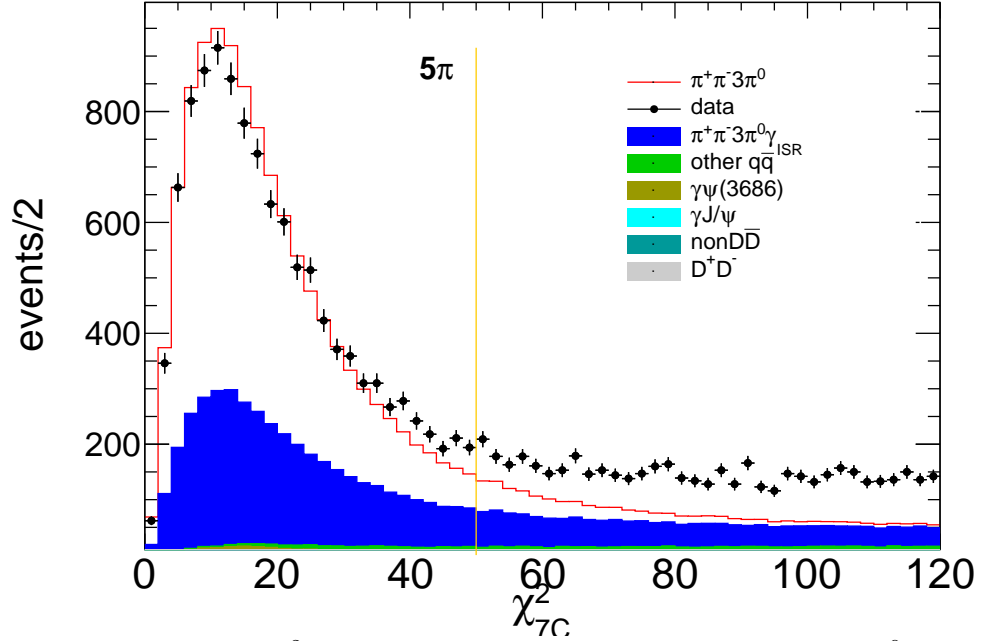


**Figure 4.22.:**  $\chi^2_{7C}$  distribution of the process  $e^+e^- \rightarrow \pi^+\pi^-3\pi^0$ .

**$K_s$  Rejection** The suppression of background contribution from  $K_s$  is performed analogously to section 4.1. The PID distribution for the  $K_s$  rejection is shown in Fig. 4.23. Events with  $P_\pi < P_K$  are rejected.

All the cuts used for the event selection are summarized in Tab. 4.4.

**Table 4.4.:** Summary of the event selection criteria for the  $e^+e^- \rightarrow \pi^+\pi^-3\pi^0$  final state.

|                                      |   |
|--------------------------------------|---|
| <b>Charged tracks</b>                | $N_{ch} = 2$ (net charge 0)<br>$r < 1.0$ cm<br>$ z  < 10.0$ cm                                    |
| <b>Good Photons</b>                  | $E > 25$ MeV (barrel)<br>$E > 50$ MeV (end caps)<br>$0 \leq \text{TDC} \leq 14$<br>$N_\gamma < 8$ |
| <b><math>\pi^0</math> Masses</b>     | $100 < M(\gamma\gamma) < 160$ MeV/ $c^2$  |
| <b><math>\pi^0</math> Candidates</b> | $\geq 3$ non overlapping  |
| <b>Kinematic Fit</b>                 | $\chi^2_{7C} < 50$  |
| <b><math>K_s</math> rejection</b>    | $P_\pi - P_K < 0$ if $480 < M(\pi^0\pi^0) < 520$ MeV/ $c^2$                                       |

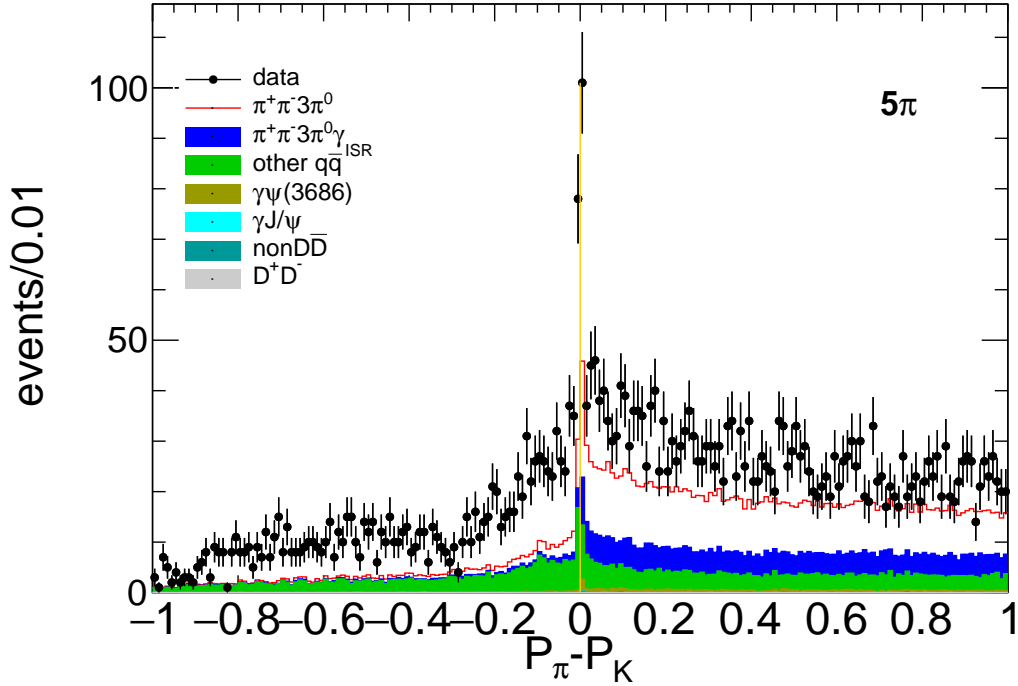


**Figure 4.23.:** Kaon PID distribution for  $K_s$  rejection of the process  $e^+e^- \rightarrow \pi^+\pi^-3\pi^0$ .

11683  $\pm$  108 events survive the event selection in data, 8061  $\pm$  89 in the signal simulation and 4594  $\pm$  67 in the background MC simulations.

#### 4.3.5. Event Selection for $e^+e^- \rightarrow \omega 2\pi^0$

The  $e^+e^- \rightarrow \pi^+\pi^-3\pi^0$  final state has two relatively large sub-channels, which are  $e^+e^- \rightarrow \omega 2\pi^0$  and  $e^+e^- \rightarrow \eta\pi^+\pi^-$ . These sub-channels are also selected explicitly. This is important for the understanding of the  $e^+e^- \rightarrow \pi^+\pi^-3\pi^0$  process. This section contains the selection for the  $e^+e^- \rightarrow \omega 2\pi^0$  sub-channel.

All event selection criteria of the  $e^+e^- \rightarrow \pi^+\pi^-3\pi^0$  event selection are applied. Additionally, There is only one entry per event, stemming from the  $\pi^0$  candidate whose the  $M(\pi^+\pi^-\pi^0)$  value is closest to the mass of the  $\omega$  resonance.  $720 < M(\pi^+\pi^-\pi^0) < 850 \text{ MeV}/c^2$  is required.

A nonresonant background below the  $\omega$  signal peak is left after subtracting the background contributions from other processes using MC simulations. This background is removed by a sideband subtraction, since the simulations indicate that it is sufficiently linear. The sideband regions are defined as  $590 < M(\pi^+\pi^-\pi^0) < 720 \text{ MeV}/c^2$  and  $850 < M(\pi^+\pi^-\pi^0) < 980 \text{ MeV}/c^2$ . Hence, the sideband rescaling factor is  $\frac{1}{2}$ . The right panel of Fig. 4.24 shows the  $M(\pi^+\pi^-\pi^0)$  distribution after background and sideband subtraction. A fit of the  $M(\pi^+\pi^-\pi^0)$  distribution after background subtraction, but before sideband subtraction with a double-Gaussian plus a polynomial is performed in order to cross check the sideband subtraction

method. The fit, shown in the left panel of Fig. 4.24, yields  $884 \pm 117$  events in the  $\omega$  resonance peak, whereas the fit quality is  $\chi^2/\text{ndf} = 1.06$ . Using the sideband subtraction,  $858 \pm 29$  events are obtained in data, which is in agreement with the fit result within errors.

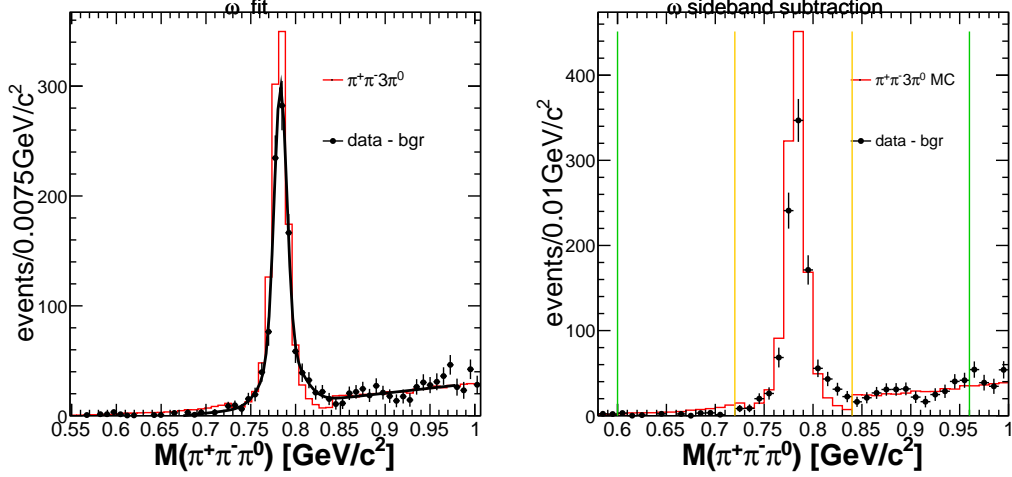


**Figure 4.24.:**  $M(\pi^+\pi^-\pi^0)$  distribution after the  $e^+e^- \rightarrow \pi^+\pi^-3\pi^0$  selection and background subtraction with a  $\omega$  fit (left) and with sideband subtraction (right).

#### 4.3.6. Event Selection for $e^+e^- \rightarrow \eta\pi^+\pi^-$

The  $e^+e^- \rightarrow \eta\pi^+\pi^-$  sub-channel of  $e^+e^- \rightarrow \pi^+\pi^-3\pi^0$  is selected as well. All criteria of the  $e^+e^- \rightarrow \pi^+\pi^-3\pi^0$  event selection are applied. Additionally,  $M(\pi^0\pi^0\pi^0) < 600 \text{ MeV}/c^2$  is required for the invariant mass of the three neutral pions. The right panel of Fig. 4.25 shows the  $M(\pi^0\pi^0\pi^0)$  distribution after background subtraction. A nonresonant  $\eta$  background is remaining after the background subtraction of the other background contributions from MC simulation. This background is removed by a sideband subtraction. The sideband regions are chosen as  $400 < M(\pi^+\pi^-\pi^0) < 500 \text{ MeV}/c^2$  and  $600 < M(\pi^+\pi^-\pi^0) < 700 \text{ MeV}/c^2$ . Hence, the sideband rescaling factor is  $\frac{1}{2}$ . The lower sideband region does not contain any events. A fit of the  $M(\pi^0\pi^0\pi^0)$  distribution after background subtraction, but before sideband subtraction with a Gaussian plus a polynomial is performed in order to cross check the sideband subtraction. The fit, shown in the left panel of Fig. 4.25, yields  $558 \pm 39$  events in the  $\eta$  peak, whereas the fit quality is  $\chi^2/\text{ndf} = 1.41$ . Using the sideband subtraction mode,  $572 \pm 24$  events are obtained in data, which is in agreement with the fit result within errors.

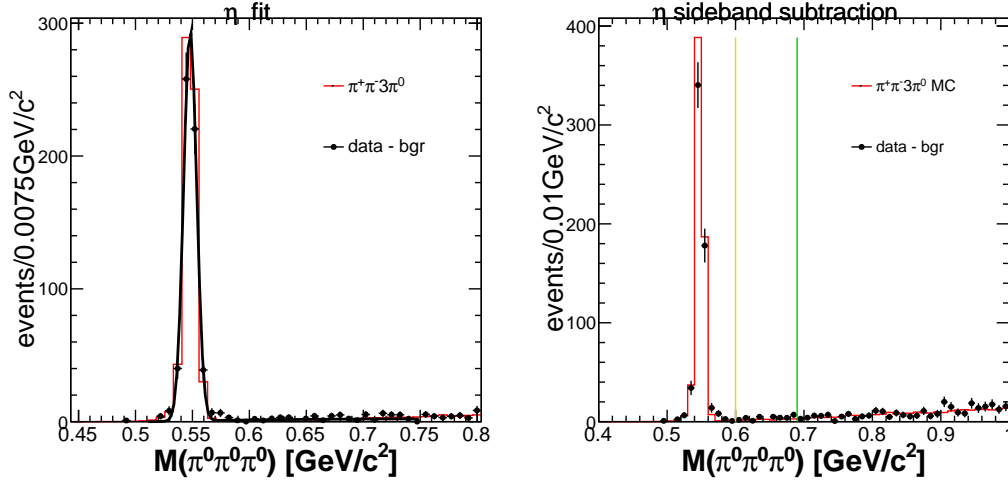


**Figure 4.25.:**  $M(\pi^0\pi^0\pi^0)$  distribution after the  $e^+e^- \rightarrow \pi^+\pi^-3\pi^0$  selection and background subtraction with a  $\eta$  fit (left) and with sideband subtraction (right).

#### 4.4. Mass Resolution of the $\pi^+\pi^-2\pi^0$ Mass Spectrum

The resolution of  $M(\pi^+\pi^-2\pi^0)$  is important in order to choose a reasonable interval width of the  $M(\pi^+\pi^-2\pi^0)$  distribution, from which the cross section will be calculated. The resolution achieved in the detection and event reconstruction described in section 4.1 is investigated based on signal MC simulations. To this end, the quantity  $M(\pi^+\pi^-2\pi^0)^{fit} - M(\pi^+\pi^-2\pi^0)^{true}$  is plotted. Here,  $M(\pi^+\pi^-2\pi^0)^{fit}$  is calculated from the four momenta of the four pions obtained from the kinematic fit and  $M(\pi^+\pi^-2\pi^0)^{true}$  is calculated from the four momenta at the event generator level. The resulting distribution is fitted with a double Gaussian. The  $M(\pi^+\pi^-2\pi^0)^{fit} - M(\pi^+\pi^-2\pi^0)^{true}$  distributions and their fits for the tagged and untagged ISR modes are shown in Fig. 4.26. The fit yields a resolution of  $(15.24 \pm 0.25)$  MeV for the tagged ISR method and  $(15.47 \pm 0.05)$  MeV for the untagged method. These values are taken from the widths of the broader Gaussian in the fit function. The mass shifts, defined as the average mean value of the two Gaussians, are  $(0.64 \pm 0.52)$  MeV and  $(-1.13 \pm 0.06)$  MeV for the tagged and the untagged method, respectively. Even though the mass shift of the untagged method is significant, it is still negligible compared to the width of the distribution. The results prove that the reconstruction and fitting procedures work correctly and give reasonable results. Furthermore, the result suggests to choose a  $M(\pi^+\pi^-2\pi^0)$  intervals with a width of 30 MeV. An unfolding of the  $M(\pi^+\pi^-2\pi^0)$  is not necessary, since the chosen interval width is narrow enough to resolve any structures,

except the  $J/\psi$  resonance, which is not located in the region relevant for  $(g-2)_\mu$ .

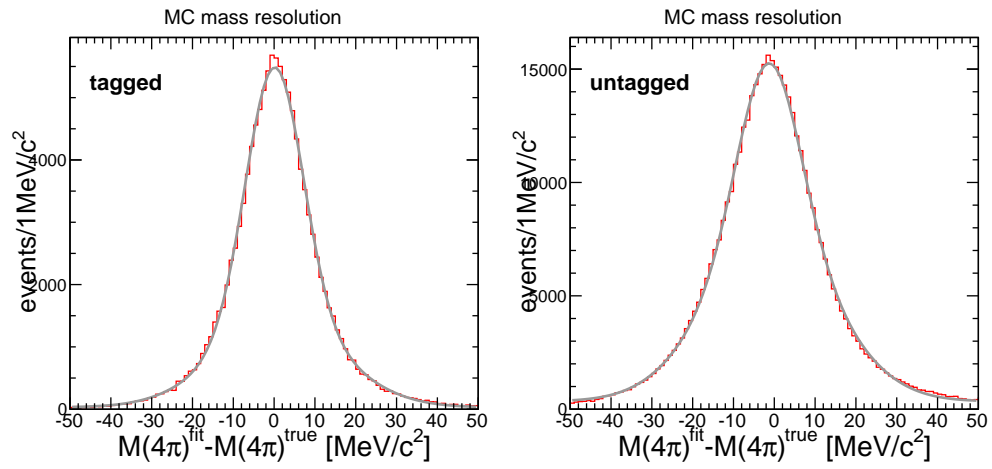


**Figure 4.26.:** Mass resolution of  $M(\pi^+\pi^-\pi^0)$  mass spectrum in signal simulation.

## Chapter 5.

### Background of

$$e^+e^- \rightarrow \pi^+\pi^-2\pi^0\gamma_{ISR}$$

---

*After the event selection of the process  $e^+e^- \rightarrow \pi^+\pi^-2\pi^0\gamma_{ISR}$  there are remaining background contributions, mainly from  $e^+e^- \rightarrow \pi^+\pi^-3\pi^0$  and  $e^+e^- \rightarrow \pi^+\pi^-3\pi^0\gamma_{ISR}$ . These background channels need to be simulated in MC and subtracted from data. In order to achieve a high precision measurement of the signal process  $e^+e^- \rightarrow \pi^+\pi^-2\pi^0\gamma_{ISR}$ , all background contributions have to be understood to a high accuracy to achieve a small systematic uncertainty associated to the background subtraction. However, the processes  $e^+e^- \rightarrow \pi^+\pi^-3\pi^0\gamma_{ISR}$  and  $e^+e^- \rightarrow \pi^+\pi^-3\pi^0$  at a c.m. energy of 3.773 GeV and below are essentially unknown experimentally. Therefore, these processes are also measured in this thesis with a precision on the 10% level. With this measurement the MC simulations can be adjusted accordingly. The ISR mass spectrum of the process  $e^+e^- \rightarrow \pi^+\pi^-2\pi^0\gamma_{ISR}$  is also presented in this chapter before and after correcting the background contributions.*

---

Applying the event selection for the process  $e^+e^- \rightarrow \pi^+\pi^-2\pi^0\gamma_{ISR}$ , explained in chapter 4, the four pion mass spectrum is obtained, which is defined as  $M^2(4\pi) = (p_{\pi^+} + p_{\pi^-} + p_{\pi^0,1} + p_{\pi^0,2})^2$ , where  $p_{\pi^{\pm,0}}$  denote the the four-momenta of the four pions in the final state. The event yields in dependence of  $M(\pi^+\pi^-2\pi^0)$  for the tagged and untagged methods are shown in Fig. 5.1. The  $J/\psi$  resonance is not contained in the PHOKHARA 9.1 signal simulation. The sum of the signal MC simulation and background MC simulations overestimates data in the region  $M(\pi^+\pi^-2\pi^0) > 2 \text{ GeV}/c^2$ . The composition of the background contributions and their fraction in data are shown in Fig. 5.2.

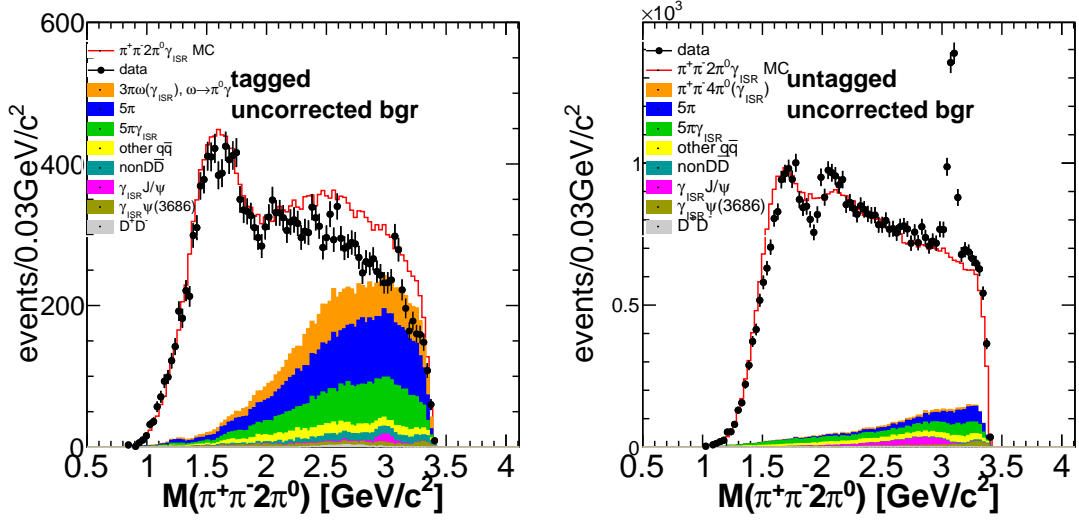


**Figure 5.1.:** Mass spectrum of the  $e^+e^- \rightarrow \pi^+\pi^-2\pi^0\gamma_{ISR}$  events the before the correction of the background contributions and before efficiency corrections.

It is known that the signal is contaminated by background contributions from the  $\pi^+\pi^-3\pi^0$  and  $\pi^+\pi^-3\pi^0\gamma_{ISR}$  final states, which get large above  $M(\pi^+\pi^-2\pi^0) \gtrsim 2 \text{ GeV}$ . This background contribution stems from  $e^+e^- \rightarrow \pi^+\pi^-3\pi^0(\gamma_{ISR})$  events, where at least one photon was too low energetic to be accepted or were emitted at polar angles, which are outside the acceptance region of the detector. As a consequence, the rest of the final state is misidentified as the  $e^+e^- \rightarrow \pi^+\pi^-2\pi^0\gamma_{ISR}$  signal. Those  $e^+e^- \rightarrow \pi^+\pi^-3\pi^0(\gamma_{ISR})$  events can not be distinguished kinematically from the real  $e^+e^- \rightarrow \pi^+\pi^-2\pi^0\gamma_{ISR}$  signal events. However, the background channels are poorly known experimentally and theoretically. Hence, the precision of their prediction in the MC simulations is unknown and presumably bad. This makes them the most probable reason for the discrepancy observed between data and the simulations in the tagged mode.

Another large background contribution from  $e^+e^- \rightarrow \pi^+\pi^-\pi^0\omega\gamma_{ISR}$ , with  $\omega \rightarrow \pi^0\gamma$  exists in the tagged mode. This contribution has been measured by BaBar [94]

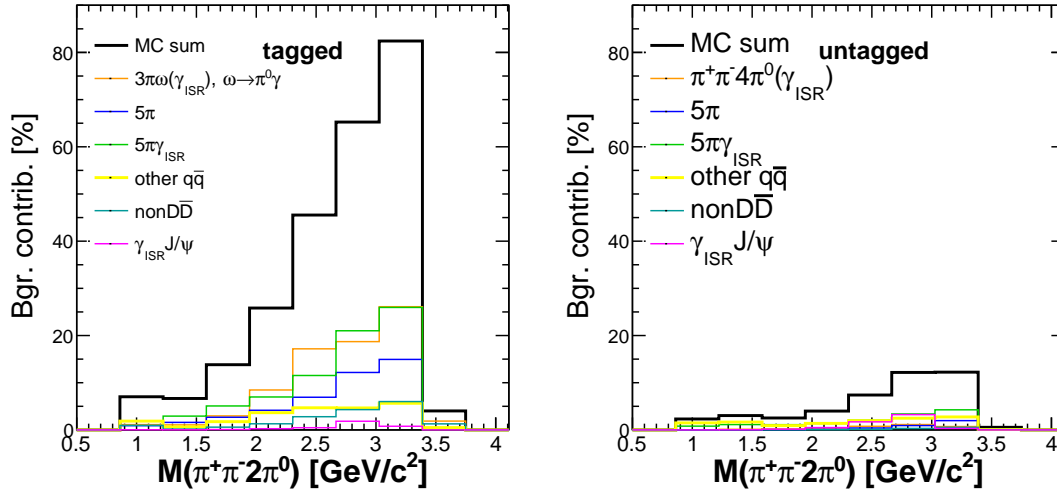


**Figure 5.2.:** Relative amount of the background contributions of the  $e^+e^- \rightarrow \pi^+\pi^-2\pi^0\gamma_{ISR}$  signal channel and their fractions in data.

and found to be sufficiently precise in the Lund- $q\bar{q}$  MC sample. Other important background contributions for both ISR modes are contained in the Lund- $q\bar{q}$  MC sample. These background channels are  $e^+e^- \rightarrow \pi^+\pi^-4\pi^0(\gamma_{ISR})$ ,  $e^+e^- \rightarrow \pi^+\pi^-\pi^0\eta(\gamma_{ISR})$  and  $e^+e^- \rightarrow K_s K\pi(\gamma_{ISR})$ , where the kaon is misidentified as a pion and with a subsequent decay  $K_s \rightarrow 2\pi^0$ . Background contributions from  $e^+e^- \rightarrow D^+D^-$  and  $e^+e^- \rightarrow D^0\bar{D}^0$  are found to be negligible.

In the following, the analyses of the  $e^+e^- \rightarrow \pi^+\pi^-3\pi^0(\gamma_{ISR})$  channels, which have been presented in chapter 4, will be used to improve the precision of the corresponding background simulations. The correction procedures of these background contributions are explained in the following sections 5.1 and 5.2. After applying these corrections, the systematic uncertainty of subtracting the  $e^+e^- \rightarrow \pi^+\pi^-3\pi^0$  and  $e^+e^- \rightarrow \pi^+\pi^-3\pi^0\gamma_{ISR}$  background contributions from the  $M(\pi^+\pi^-2\pi^0)$  spectrum is equal to the total uncertainties of the measurements of  $e^+e^- \rightarrow \pi^+\pi^-3\pi^0$  and  $e^+e^- \rightarrow \pi^+\pi^-3\pi^0\gamma_{ISR}$ . Additional systematic uncertainties due to intermediate structures in the  $\pi^+\pi^-3\pi^0$  and  $\pi^+\pi^-3\pi^0\gamma_{ISR}$  final states are also taken into account, but discussed later in chapter 11. The distributions of the intermediate structures in  $e^+e^- \rightarrow \pi^+\pi^-3\pi^0$  and  $e^+e^- \rightarrow \pi^+\pi^-3\pi^0\gamma_{ISR}$  are presented in sections 8.2 and 8.3. Kinematic variables like momenta and polar angle distributions of the pions are shown in Fig. A.1 as well as Fig. A.2 in appendix A. All these distributions indicate that the intermediate structures and the kinematic variables are described well by the MC simulations. This gives a good confidence that the efficiencies obtained from the simulations are correct and yield reasonable uncertainties. The uncertainties will be discussed in detail in chapter 11.

As shown in Fig. 5.2, the  $q\bar{q}$  background contribution gives large contributions in the region of  $M(\pi^+\pi^-2\pi^0) \lesssim 1.5$  GeV. The absolute validation of this contribution is investigated in section 5.3.

## 5.1. Correction of the $e^+e^- \rightarrow \pi^+\pi^-3\pi^0$ Background

For each event that is selected as  $e^+e^- \rightarrow \pi^+\pi^-3\pi^0$  in data and in the simulation, the whole  $e^+e^- \rightarrow \pi^+\pi^-2\pi^0\gamma_{ISR}$  event selection procedure of the tagged and untagged methods is applied as well. This is needed to find out in which mass range the  $e^+e^- \rightarrow \pi^+\pi^-3\pi^0$  events contribute to the background in the  $M(\pi^+\pi^-2\pi^0)$  spectrum by being misidentified as  $e^+e^- \rightarrow \pi^+\pi^-2\pi^0\gamma_{ISR}$  events. The  $M(\pi^+\pi^-2\pi^0)$  mass spectrum arising from misidentified  $e^+e^- \rightarrow \pi^+\pi^-3\pi^0$  events is shown in Fig. 5.3 for the tagged and untagged ISR modes.

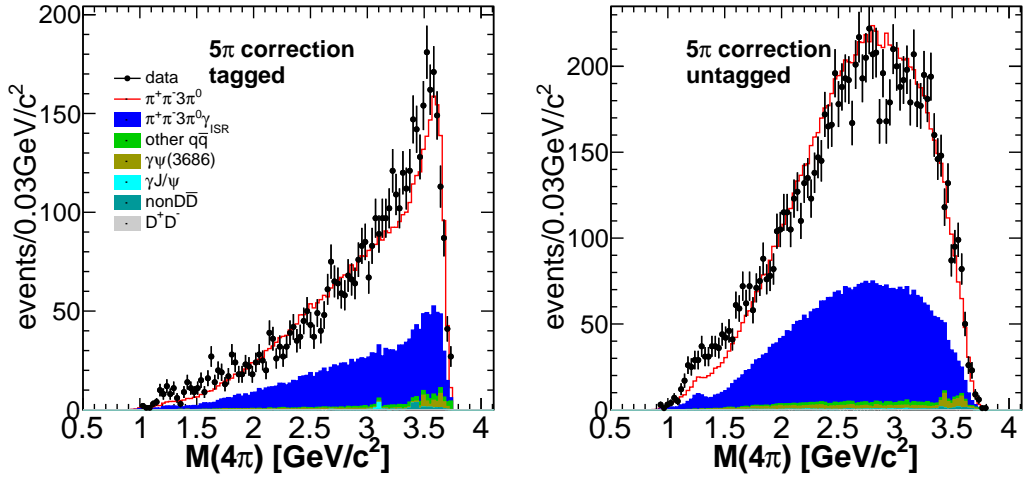


**Figure 5.3.:** Correction of the  $e^+e^- \rightarrow \pi^+\pi^-3\pi^0$  background in the  $e^+e^- \rightarrow \pi^+\pi^-2\pi^0\gamma_{ISR}$  analysis.

For these events, which have successfully passed the  $e^+e^- \rightarrow \pi^+\pi^-3\pi^0$  as well as the  $e^+e^- \rightarrow \pi^+\pi^-2\pi^0\gamma_{ISR}$  event selection, the background stemming from  $e^+e^- \rightarrow \pi^+\pi^-3\pi^0$  is subtracted both from data and from the full MC cocktail. The remaining event yield is divided by the  $e^+e^- \rightarrow \pi^+\pi^-3\pi^0$  simulation. This ratio represents the correction to be applied to the  $e^+e^- \rightarrow \pi^+\pi^-3\pi^0$  simulation. The correction obtained is shown in Fig. 5.4 for the tagged and the untagged ISR methods, respectively. A comparison of the shape of the  $e^+e^- \rightarrow \pi^+\pi^-3\pi^0$  background MC before and after applying the correction is shown in Fig. 5.5.

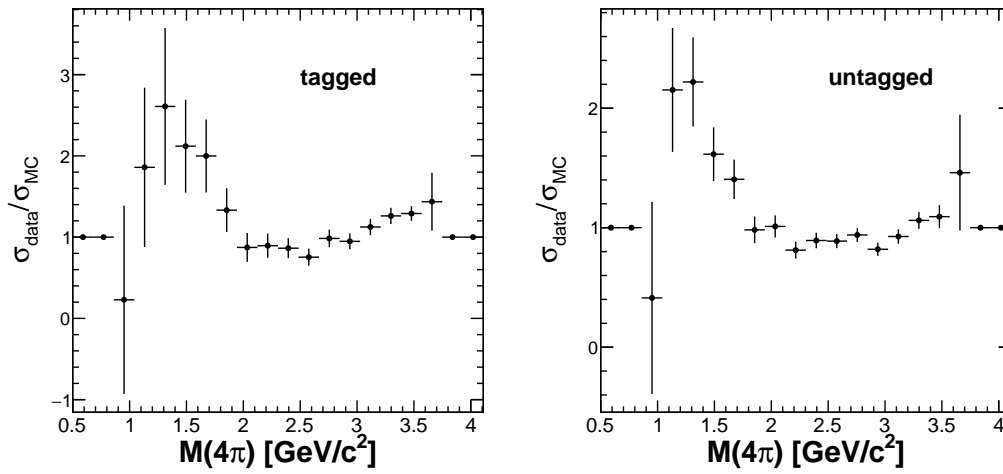


Figure 5.4.: Correction of the  $e^+e^- \rightarrow \pi^+\pi^-3\pi^0$  background in the  $e^+e^- \rightarrow \pi^+\pi^-2\pi^0\gamma_{ISR}$  analysis.

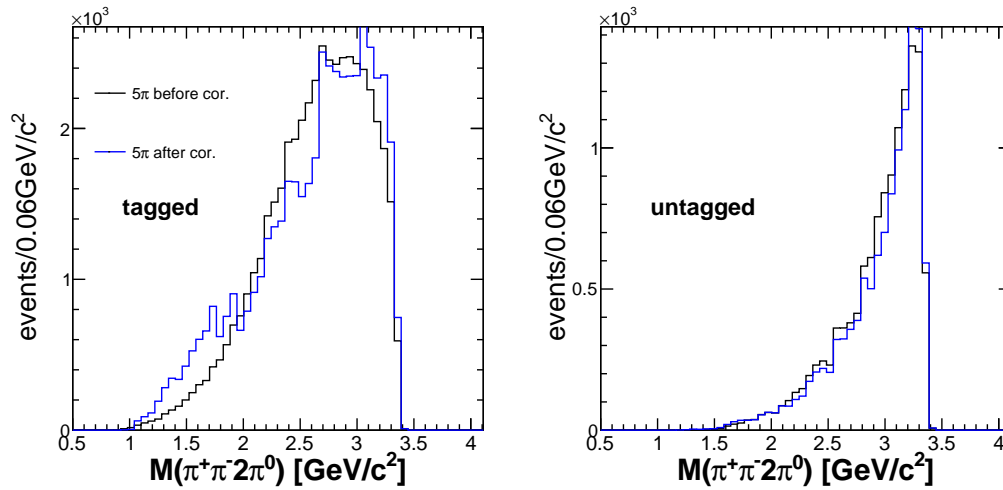
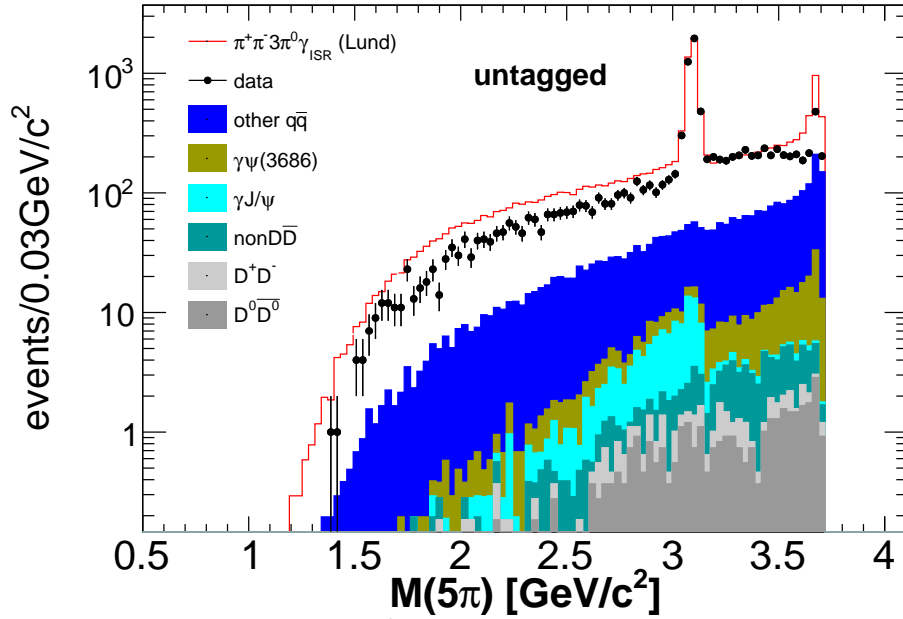


Figure 5.5.: Comparison of the  $e^+e^- \rightarrow \pi^+\pi^-3\pi^0$  background to the  $e^+e^- \rightarrow \pi^+\pi^-2\pi^0\gamma_{ISR}$  final state before and after applying the  $\pi^+\pi^-3\pi^0$  correction.

## 5.2. Correction of the $e^+e^- \rightarrow \pi^+\pi^-3\pi^0\gamma_{ISR}$ Background

The  $M(\pi^+\pi^-3\pi^0)$  mass spectrum obtained after the  $e^+e^- \rightarrow \pi^+\pi^-3\pi^0\gamma_{ISR}$  event selection is shown in Fig. 5.6. Up to a rescaling factor of about two, data is qualitatively in relative good agreement with the shape of the Lund- $q\bar{q}$  MC simulation in the mass region  $M(\pi^+\pi^-3\pi^0) < 3.1 \text{ GeV}/c^2$ , which is below the  $J/\psi$  peak. In the inclusive  $\gamma_{ISR}J/\psi$  MC sample, the decay  $J/\psi \rightarrow \pi^+\pi^-3\pi^0$  is identified on the MC generation level and moved to the red  $\pi^+\pi^-3\pi^0\gamma_{ISR}$  MC histogram. In the mass region above the  $J/\psi$  peak up to  $3.5 \text{ GeV}/c^2$  MC obviously underestimates data. Above  $M(\pi^+\pi^-3\pi^0) \gtrsim 3.5 \text{ GeV}/c^2$  the MC overestimates again data. Although, the simulation does not describe data perfectly in the absolute scale, the kinematic variables shown in Fig. A.4 of appendix A and the intermediate resonances shown in Fig. 8.7 in section 8.3 prove that the Lund- $q\bar{q}$  MC simulation can be used to obtain a reliable signal reconstruction efficiency.



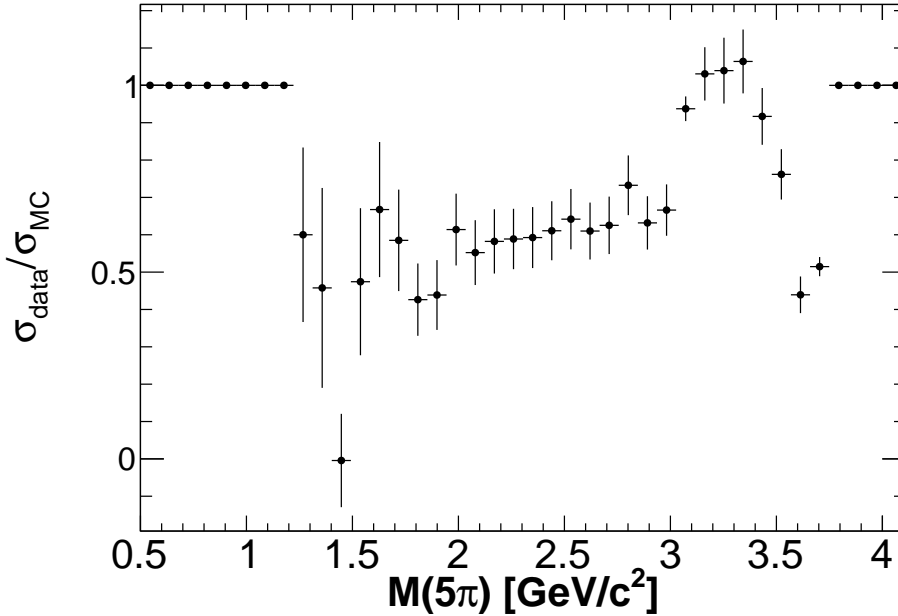
**Figure 5.6.:**  $e^+e^- \rightarrow \pi^+\pi^-3\pi^0$  mass spectrum without efficiency correction

Table 5.1 shows the composition of the background contributions for the  $e^+e^- \rightarrow \pi^+\pi^-3\pi^0\gamma_{ISR}$  channel. These are contained in the Lund- $q\bar{q}$  MC sample. The other background contributions are small. From the  $M(\pi^+\pi^-3\pi^0)$  mass spectrum in Fig. 5.6, the correction histogram can be obtained by dividing data after background subtraction by the reconstructed  $e^+e^- \rightarrow \pi^+\pi^-3\pi^0\gamma_{ISR}$  MC distribution. This correction is shown in Fig 5.7. In the region below the  $J/\psi$  resonance, the correction is around 0.5. For each  $e^+e^- \rightarrow \pi^+\pi^-3\pi^0\gamma_{ISR}$  event in the MC simulations that was successfully selected as an  $e^+e^- \rightarrow \pi^+\pi^-2\pi^0\gamma_{ISR}$  event, the true

five pion mass,  $M(\pi^+\pi^-3\pi^0)^{true}$ , is stored. These values of  $M(\pi^+\pi^-3\pi^0)^{true}$  stem from the MC generator, before taking into account detector resolution effects.

**Table 5.1.:** Background composition of the  $\pi^+\pi^-3\pi^0\gamma_{ISR}$  final state.

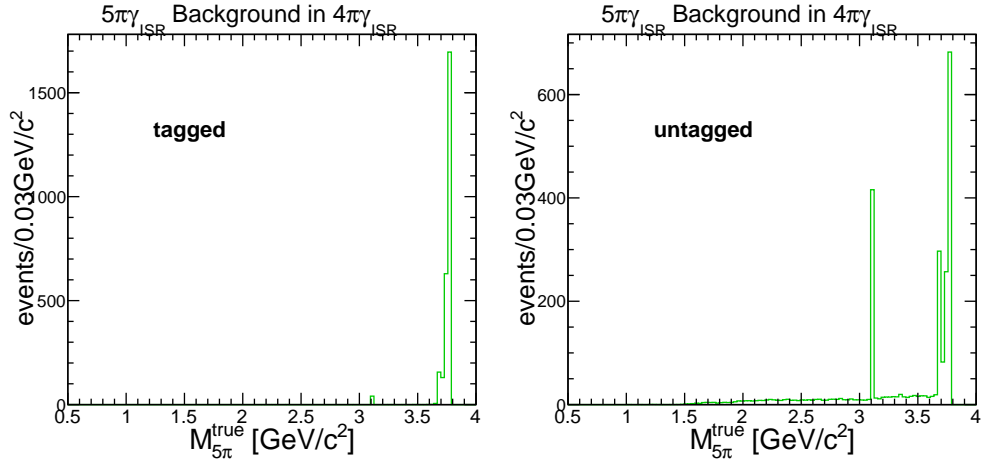
| final state  | fraction in all background [%] | fraction in signal [%] |
|--|--------------------------------|------------------------|
| $\pi^+\pi^-4\pi^0$   | 38                             | 10                     |
| $\pi^+\pi^-4\pi^0\gamma_{ISR}$                                       | 23                             | 6                      |
| $\pi^+\pi^-5\pi^0$   | 5                              | 1.3                    |
| $\pi^+\pi^-5\pi^0\gamma_{ISR}$                                       | 4                              | 1                      |
| $\pi^+\pi^-2\pi^0\omega\gamma_{ISR}, \omega \rightarrow \pi^0\gamma$ | 3                              | 1                      |
| $2\pi^+2\pi^-4\pi^0$   | 3                              | 1                      |
| $2\pi^+2\pi^-4\pi^0\gamma_{ISR}$                                     | 3                              | 1                      |
| $\pi^+\pi^-2\pi^0\omega, \omega \rightarrow \pi^0\gamma$             | 2                              | 0.5                    |
| 186 other  | each < 2                       | each < 0.5             |



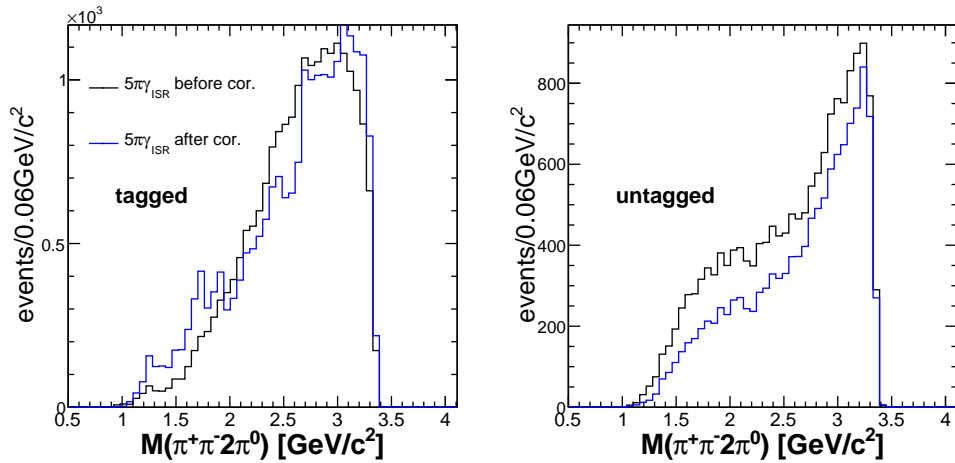
**Figure 5.7.:** Correction of the  $e^+e^- \rightarrow \pi^+\pi^-3\pi^0\gamma_{ISR}$  background to  $e^+e^- \rightarrow \pi^+\pi^-2\pi^0\gamma_{ISR}$ .

Figure 5.8 shows the  $M(\pi^+\pi^-3\pi^0)^{true}$  distribution for  $e^+e^- \rightarrow \pi^+\pi^-3\pi^0\gamma_{ISR}$  background events. In the tagged mode for  $e^+e^- \rightarrow \pi^+\pi^-2\pi^0\gamma_{ISR}$ , most of the  $e^+e^- \rightarrow \pi^+\pi^-3\pi^0\gamma_{ISR}$  background has values of  $M(\pi^+\pi^-3\pi^0)^{true}$  above  $3.7 \text{ GeV}/c^2$ . A few events are found with  $M(\pi^+\pi^-3\pi^0)^{true} < 3.7 \text{ GeV}/c^2$  in the untagged mode. This mass region is not covered in the  $e^+e^- \rightarrow \pi^+\pi^-3\pi^0\gamma_{ISR}$  measurement and the correction can not be applied for these events. However, these events have an ISR photon energy of  $E_{ISR} < 72 \text{ MeV}$  and they can be hardly distinguished kinematically from the non-ISR channel  $e^+e^- \rightarrow \pi^+\pi^-3\pi^0$ . Also their internal

resonance structure as well as the pion momenta and polar angle distributions are sufficiently similar to the ones of the non-ISR process  $e^+e^- \rightarrow \pi^+\pi^-3\pi^0$ . For this reason, the  $e^+e^- \rightarrow \pi^+\pi^-3\pi^0$  correction can be safely applied for these events, which is discussed in the previous section. The  $e^+e^- \rightarrow \pi^+\pi^-3\pi^0\gamma_{ISR}$  background events with  $M(\pi^+\pi^-3\pi^0)^{true} < 3.7 \text{ GeV}/c^2$  in the  $e^+e^- \rightarrow \pi^+\pi^-2\pi^0\gamma_{ISR}$  analysis are then weighted by the correction factor obtained in Fig 5.7 according to their true  $M(\pi^+\pi^-3\pi^0)^{true}$  value. Events with  $M(\pi^+\pi^-3\pi^0)^{true} > 3.7 \text{ GeV}/c^2$  are scaled according to Fig. 5.4. The difference between  $M(\pi^+\pi^-3\pi^0)^{true}$  values in the MC simulation and the fitted  $M(\pi^+\pi^-3\pi^0)$  values from data or MC is less than half the width of the  $M(\pi^+\pi^-3\pi^0)$  intervals and hence negligibly small. A comparison of the shape of the  $e^+e^- \rightarrow \pi^+\pi^-3\pi^0\gamma_{ISR}$  background MC before and after applying the correction is shown in Fig. 5.9.



**Figure 5.8.:** Correction of the  $e^+e^- \rightarrow \pi^+\pi^-3\pi^0\gamma_{ISR}$  background channel to  $e^+e^- \rightarrow \pi^+\pi^-2\pi^0\gamma_{ISR}$  events.



**Figure 5.9.:** Comparison of the  $e^+e^- \rightarrow \pi^+\pi^-3\pi^0\gamma_{ISR}$  background contribution to the  $e^+e^- \rightarrow \pi^+\pi^-2\pi^0\gamma_{ISR}$  final state before and after the correction.

### 5.3. Normalization of the Remaining $q\bar{q}$ Contribution

The inclusive Lund- $q\bar{q}$  MC sample which is based on the LUNDAREALAW generator model [87, 88], simulates a large number of hadronic final states excluding the  $J/\psi$  resonance but including ISR. The shape of the background contribution to  $e^+e^- \rightarrow \pi^+\pi^-2\pi^0\gamma_{ISR}$  events, which is obtained by this Lund- $q\bar{q}$  simulation is reliable up to a total scaling factor. This is due to the models used in the MC generator. Therefore, the scaling of this MC sample needs to be checked. The luminosity of the generated Lund- $q\bar{q}$  MC sample corresponds to  $\mathcal{L}_{q\bar{q}} = 30 \text{ fb}^{-1}$ . Hence, this MC sample can be rescaled to the luminosity of data with a scaling factor of  $s = \frac{\mathcal{L}_{data}}{\mathcal{L}_{q\bar{q}}} = 0.098$ . This scaling factor is applied to the MC sample before calculating the renormalization factors in this section. Hence, the Lund- $q\bar{q}$  MC describes data perfectly, if a renormalization factor of one would be obtained. The validation of the Lund- $q\bar{q}$  scaling factor can be performed by a data MC comparison of the number of  $\pi^0$  candidates as the dominant background from the Lund- $q\bar{q}$  sample stems from these events, in which a decay photon from a  $\pi^0$  particle is misidentified as an ISR photon. For this purpose, the invariant mass of the ISR photon and any other photon recorded in the event,  $M(\gamma_{ISR}\gamma)$ , is calculated. This quantity is given by

$$M(\gamma_{ISR}\gamma)^2 = (p_{ISR}^\mu + p_{\gamma,i}^\mu)^2, \quad i = 1 \dots 6.$$

The quantity  $M(\gamma_{ISR}\gamma)$  is expected to be equal in data and the Lund- $q\bar{q}$  MC sample after correcting the  $e^+e^- \rightarrow \pi^+\pi^-3\pi^0\gamma_{ISR}$  contribution within the Lund- $q\bar{q}$  MC according to section 5.2 and subtracting the background contributions of other MC samples from data. The  $e^+e^- \rightarrow \pi^+\pi^-3\pi^0$  background contributions are added to the Lund- $q\bar{q}$  MC histogram, instead of subtracting them from data. Their scaling factor is already adjusted to data by the  $e^+e^- \rightarrow \pi^+\pi^-3\pi^0$  measurement that was put into the HELPWA MC generator. Up to 6 combinations of  $M(\gamma_{ISR}\gamma)$  have to be calculated per event. To obtain the  $M(\gamma_{ISR}\gamma)$  distribution, all the  $e^+e^- \rightarrow \pi^+\pi^-2\pi^0\gamma_{ISR}$  signal event selection criteria explained before in section 4 are applied, except the selection on  $M(\gamma_{ISR}\gamma)$  itself and the  $\cos\alpha$  requirement. It was found that the potential Lund- $q\bar{q}$  background is suppressed by the  $\cos\alpha$  requirement quite effectively. In order to obtain sufficient statistics for the calibration procedure described here, the  $\cos\alpha$  requirement is hence not applied here. The distribution of  $M(\gamma_{ISR}\gamma)$  is shown in Fig. 5.10. Background contributions from the non-DD MC sample,  $e^+e^- \rightarrow \gamma_{ISR}J/\psi$ ,  $e^+e^- \rightarrow \gamma_{ISR}\psi(3686)$  and  $e^+e^- \rightarrow D\bar{D}$  are subtracted from data. Hence, only Lund- $q\bar{q}$  events plus  $e^+e^- \rightarrow \pi^+\pi^-3\pi^0$  events are compared between data and MC. As expected, a peak at the neutral pion mass in data and in the Lund- $q\bar{q}$  MC sample can be seen in Fig. 5.10. The

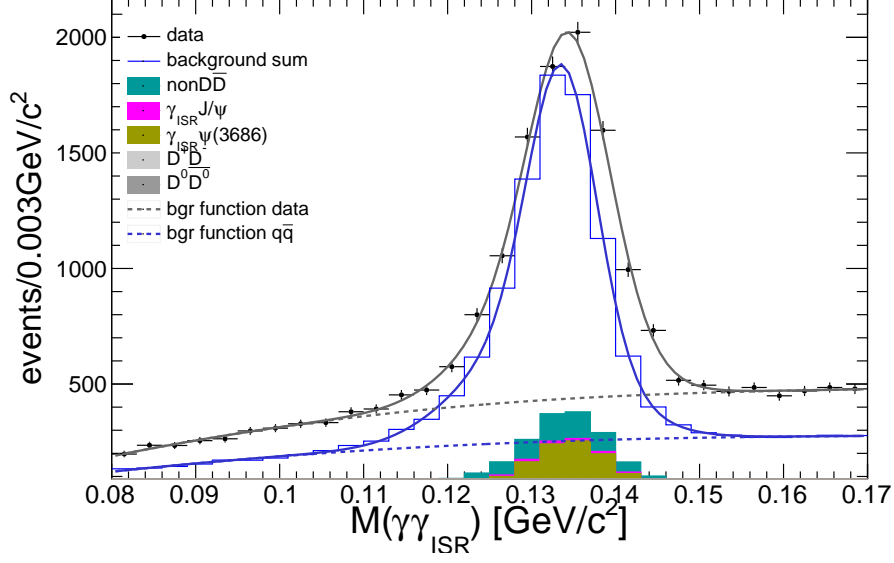


**Figure 5.10.:**  $M(\gamma_{ISR}\gamma)$  spectrum. Data and the simulations show a peak at the  $\pi^0$  mass.

$e^+e^- \rightarrow \pi^+\pi^-3\pi^0\gamma_{ISR}$  contribution within Lund- $q\bar{q}$  is adjusted according to the correction obtained in section 5.2, as mentioned before. In fact the peaks do not have equal height. This means that the Lund- $q\bar{q}$  sample has to be rescaled with a rescaling factor  $f$ . This additional scaling factor  $f$  is obtained by taking the ratio of the number of events in the  $\pi^0$  mass peaks in data and in the Lund- $q\bar{q}$  MC sample

$$f = \frac{N_{\gamma_{ISR}\gamma}^{data}}{N_{\gamma_{ISR}\gamma}^{q\bar{q}}}, \quad (5.3.1)$$

where  $N_{\gamma_{ISR}\gamma}$  denotes the number of events in the  $\pi^0$  peak of the  $M(\gamma_{ISR}\gamma)$  spectrum in data or Lund- $q\bar{q}$  MC, respectively. The resulting scaling factor  $s_{tot}$ , which will be applied on the Lund- $q\bar{q}$  MC sample is then given by  $s_{tot} = f \frac{\mathcal{L}_{data}}{\mathcal{L}_{q\bar{q}}}$ .

The number of  $\pi^0$  candidates in the peaks are determined with two different fit methods for the entire  $M(\pi^+\pi^-2\pi^0)$  spectrum and also in bins of the invariant mass  $M(\pi^+\pi^-2\pi^0)$ . In the first method the  $M(\gamma_{ISR}\gamma)$  distribution in Fig. 5.10 is fitted with a double Gaussian for the  $\pi^0$  peak plus a fourth order polynomial for the tail

$$f(x) = \frac{N_1}{\sqrt{2\pi}\sigma_1} e^{-\left(\frac{x-\mu_1}{2\sigma_1}\right)^2} + \frac{N_2}{\sqrt{2\pi}\sigma_2} e^{-\left(\frac{x-\mu_2}{2\sigma_2}\right)^2} + \sum_{i=0}^4 a_i x^i.$$

Applying the fitted parameters according to  $N_{\gamma_{ISR}\gamma} = N_1 + N_2$  to Eq.5.3.1 for data

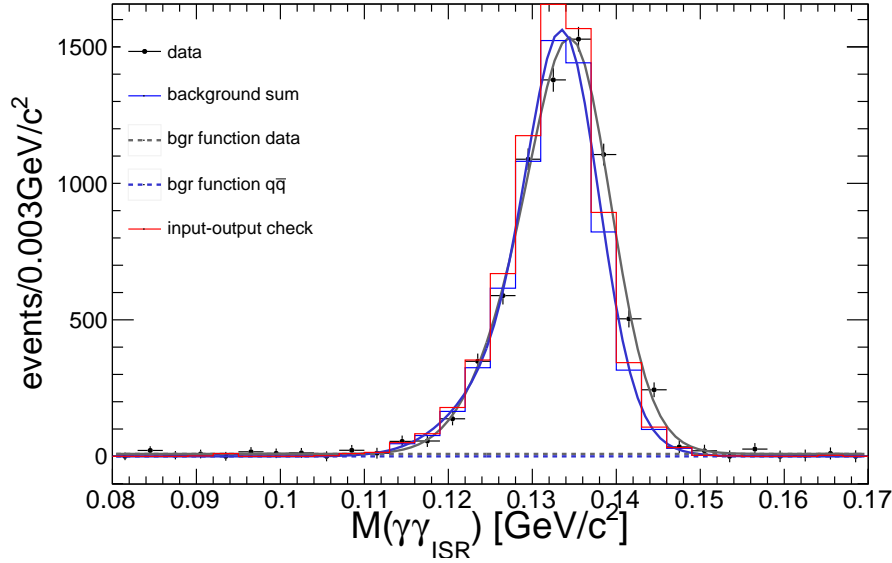


**Figure 5.11.:**  $M(\gamma_{ISR}\gamma)$  distribution after background subtraction.

and MC, the rescaling factor of method „1 global“ is obtained. Its value is shown in Table 5.2.

In the second method, the *ShowBackground* function of the Cern-ROOT framework is used to subtract the tail in the  $M(\gamma_{ISR}\gamma)$  distribution. This function determines the shape of the background automatically and gives a histogram as output, that describes the background shape. Such a background histogram is subtracted from data and the  $q\bar{q}$  histograms shown before. Afterwards, the remaining peak is fitted with a double Gaussian plus a first order polynomial for potentially remaining backgrounds. The result is shown in Fig. 5.11. All the event selection criteria were applied to obtain the  $M(\gamma_{ISR}\gamma)$  distribution except the  $M(\gamma_{ISR}\gamma)$  selection itself. Also here, the scaling factor is obtained by using the integrated event number in the Gaussians with Eq. 5.3.1. The result, addressed with „2 global“, is shown in Table 5.2.

In the next step the scaling factor will be calculated for nine bins of  $M(\pi^+\pi^-2\pi^0)$ . The  $M(\gamma_{ISR}\gamma)$  spectrum is fitted according to the second method again with a double Gaussian in order to describe the peak plus a first order polynomial for the background. Fig. 5.12 shows the nine  $M(\gamma_{ISR}\gamma)$  distributions for different regions of  $M(\pi^+\pi^-2\pi^0)$  and the respective fits. Again the scaling factor is determined using Eq.5.3.1 for each bin by dividing the peak heights of data by the ones of the Lund- $q\bar{q}$  MC. A constant behavior of the scaling factor in dependence of  $M(\pi^+\pi^-2\pi^0)$  is identified. Thus a constant function is fitted to the 9 points. The

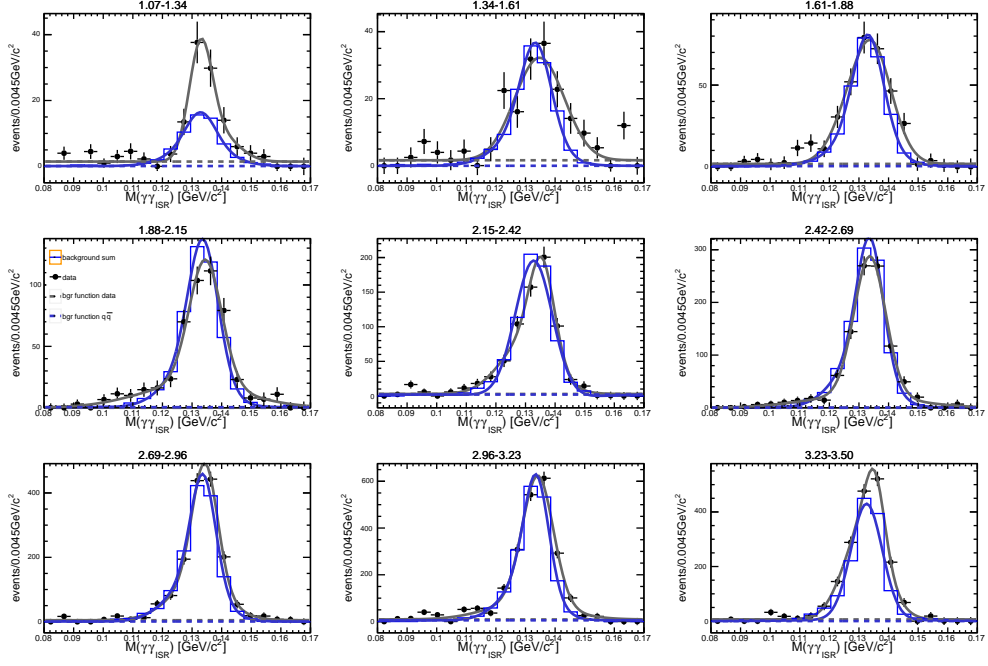


Figure 5.12.:  $M(\gamma_{ISR}\gamma)$  split into 9 intervals of  $M(\pi^+\pi^-2\pi^0)$ .

fit result, which is addressed by „2 local“ is shown in Table 5.2. Fig. 5.13 shows that the scaling factor is sufficiently flat as a function of  $M(\pi^+\pi^-2\pi^0)$  if also the systematic error is considered.

This cross check shows the consistency of this procedure, since all the numbers of Table 5.2 agree with each other within uncertainties.

Table 5.2.: Rescaling factors for the Lund- $q\bar{q}$  MC sample

| Method   | rescaling factor         |
|----------|--------------------------|
| 1 global | $1.058 \pm 0.038_{stat}$ |
| 2 global | $1.061 \pm 0.081_{stat}$ |
| 2 local  | $1.109 \pm 0.031_{stat}$ |

The largest difference between all the numbers presented in Table 5.2 is used as systematic uncertainty. One obtains:

$$\Delta f_{sys} = f_{max} - f_{min} = 0.051.$$

Finally, the results of all the three methods are combined. Fig.5.13 shows all the three methods and the fit to the  $M(\pi^+\pi^-2\pi^0)$  dependent method. The final result for the scaling factor is taken as the average of the three values in Table 5.2. The final value is:

$$f = 1.087 \pm 0.056_{sys+stat}. \quad (5.3.2)$$

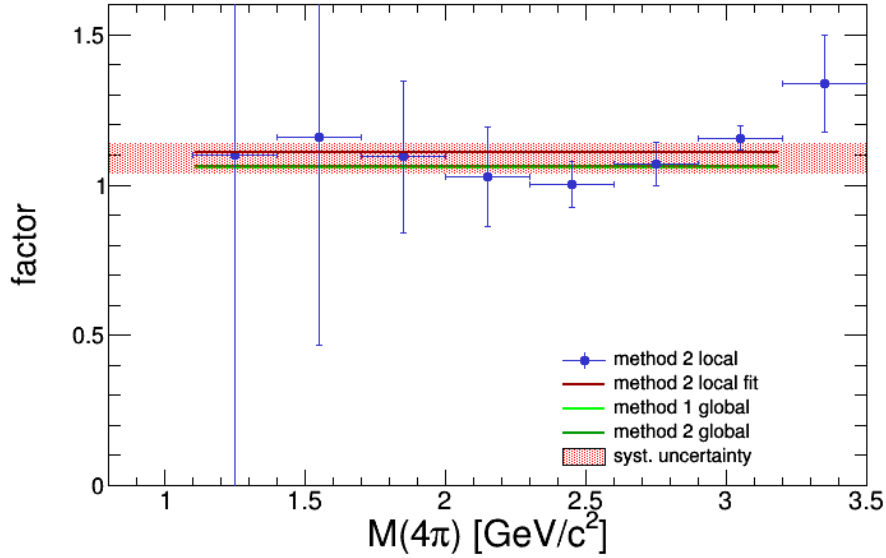


**Figure 5.13.:** Summary of all methods: Rescaling factor in bins of  $M(\pi^+\pi^-2\pi^0)$  (blue dots), fit to the blue dots with a constant (red line), first global method (light green line) and second global method (dark green line).

This factor will be multiplied to the given luminosity of the Lund- $q\bar{q}$  simulation sample. The scaling factor after this correction is  $s = f \frac{\mathcal{L}_{data}}{\mathcal{L}_{q\bar{q}}} = 0.106$ . This additional scaling is only used for the tagged mode, not for the untagged mode, since Fig. 4.12 of chapter 4 shows that the  $M(\gamma_{ISR}\gamma)$  peak and the corresponding discrepancy between data and MC do not appear in the untagged ISR method.

Last, an input-output check is performed. Therefore, the scaling factor is applied to the  $q\bar{q}$  curve in Fig. 5.10 and the background subtraction of the second method is applied. The result, shown as a red histogram in Fig. 5.11, reproduces the expected shape. Hence, the input-output check proves the procedure to be valid. A small shift of the  $\pi^0$  mass between data and MC can still be observed, as before the rescaling, but this effect is negligible and is not supposed to be corrected by this the rescaling procedure.

## 5.4. Background Subtraction Crosscheck with the Sideband Subtraction

In the previous section the  $q\bar{q}$  rescaling factor was determined for the tagged mode. This method cannot be applied to the untagged mode, as the ISR photon is not detected in the corresponding selection. Therefore, a sideband subtraction of the

background is performed to estimate the accuracy of the nominal scaling of the background MC samples.

The sideband subtraction is performed in the  $\chi_{6C/3C}^2$  distribution for different bins of  $M(\pi^+\pi^-2\pi^0)$ . The  $\chi_{6C/3C}^2$  distribution of Fig. 4.7 reveals that the background is sufficiently flat in the untagged mode but peaks at small  $\chi_{6C/3C}^2$  in the tagged mode. Hence, this method is only reliable for the untagged mode. For the tagged mode it can only serve as cross check, but can not be used to give a good estimation of the background MC rescaling factor. The signal region is defined as the region  $0 < \chi^2 < 60$ , whereas the region  $60 < \chi^2 < 120$  defines the sideband. Moreover, the following definitions are used:

- $D_1$  the number of data events in the signal region,
- $D_2$  the number of data events in the sideband region,
- $N_{s1}$  the number of signal events in the signal region,
- $N_{s2}$  the number of signal events in the sideband region,
- $N_{b1}$  the number of background events in the signal region,
- $N_{b2}$  the number of background events in the sideband region,
- $a = N_{s1}/N_{s2}$ ,
- $b = N_{b1}/N_{b2}$ .

The parameters  $a$  and  $b$  have to be determined in bins of  $M(\pi^+\pi^-2\pi^0)$  from the MC samples for signal and background, respectively. From the definitions mentioned above it follows:

$$\begin{aligned} D_1 &= N_{s1} + N_{b1}, \\ D_2 &= N_{s2} + N_{b2}. \end{aligned}$$

After some algebra one finds for the number of background events in the signal region  $N_{b1}$ :

$$N_{b1} = \frac{b}{a-b} (D_2 - aD_1) \quad (5.4.1)$$

which only depends on the number of data events and on ratios  $D_1, D_2$  of MC event numbers  $a, b$ . The absolute scale of the MC sample cancels out. Fig. 5.14 shows the  $N_{b1}$  distribution in bins of the hadronic mass  $M(\pi^+\pi^-2\pi^0)$ , where as Fig. 5.15 shows the ratio between the number of background events determined

by the sideband method and the number given by the background MC samples. The additional  $q\bar{q}$  rescaling factor is applied in the tagged case. Hence, the ratio is expected to be close to one, if the rescaling is vital. Fig. 5.15 shows that this is indeed the case within the given statistical uncertainties, but only up to 2 GeV in the tagged mode.

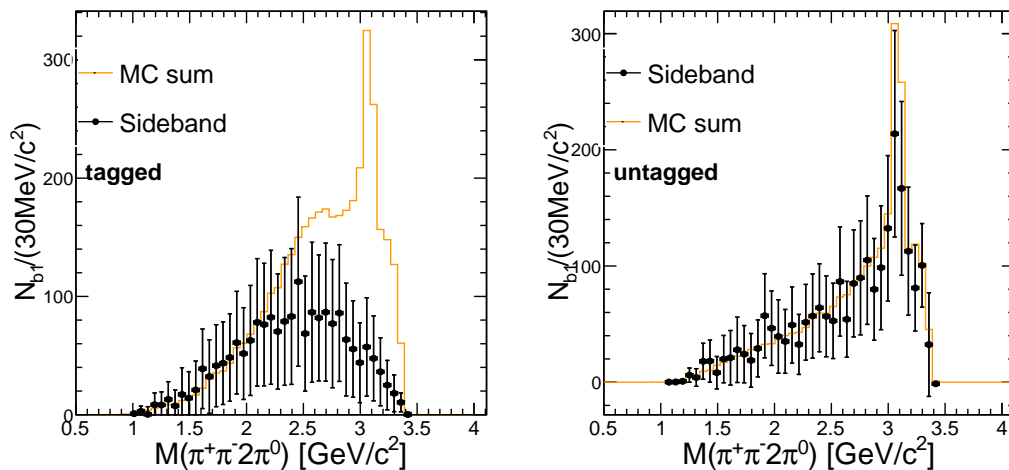


**Figure 5.14.:** Comparison of the number of background events between the sideband subtraction method and the MC simulation

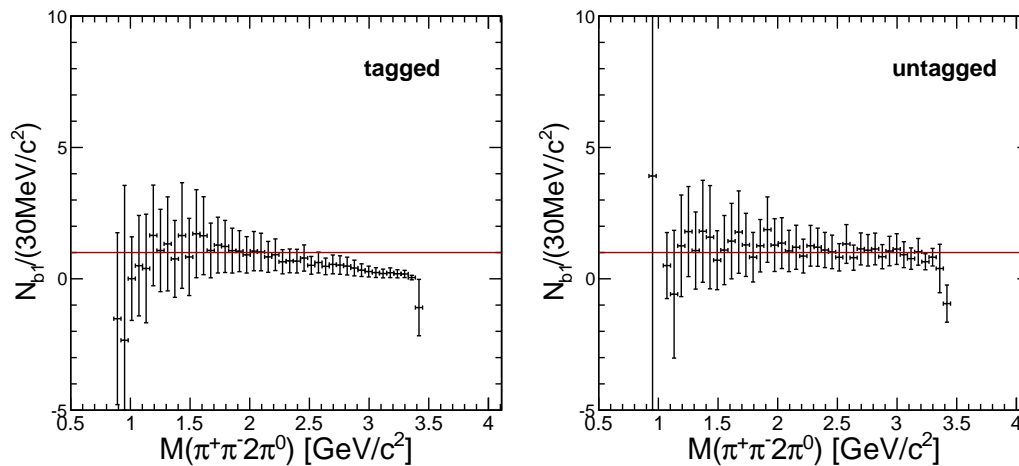


**Figure 5.15.:** Difference of the number of background events between the sideband subtraction method and the MC simulation

The sideband to MC ratio integrated over the whole  $M(\pi^+\pi^-2\pi^0)$  range is  $1.022 \pm 0.122$  for the untagged mode. For the tagged mode  $1.062 \pm 0.244$  is obtained in the region below 2 GeV. This proves that the background is well described by the

MC samples for the untagged mode and also for the tagged mode after rescaling. This method suggests an error of 12.2% for the background subtraction in untagged mode. To be conservative, a 20% uncertainty is assumed for the subtraction of background contributions described with the Lund- $q\bar{q}$  sample.

## 5.5. Mass Spectrum of $\pi^+\pi^-2\pi^0$ after Background Corrections

Applying the corrections of the  $e^+e^- \rightarrow \pi^+\pi^-3\pi^0$  and  $e^+e^- \rightarrow \pi^+\pi^-3\pi^0\gamma_{ISR}$  background contributions as well as the rescaling of the Lund- $q\bar{q}$  MC described in section 5.3, the mass distribution obtained from data can again be compared to the corrected MC sum of signal and background. This is shown in Fig. 5.16 for the tagged and untagged ISR methods, respectively. A significantly improved data-MC agreement is observed with respect to the situation before the correction, shown in Fig. 5.1.

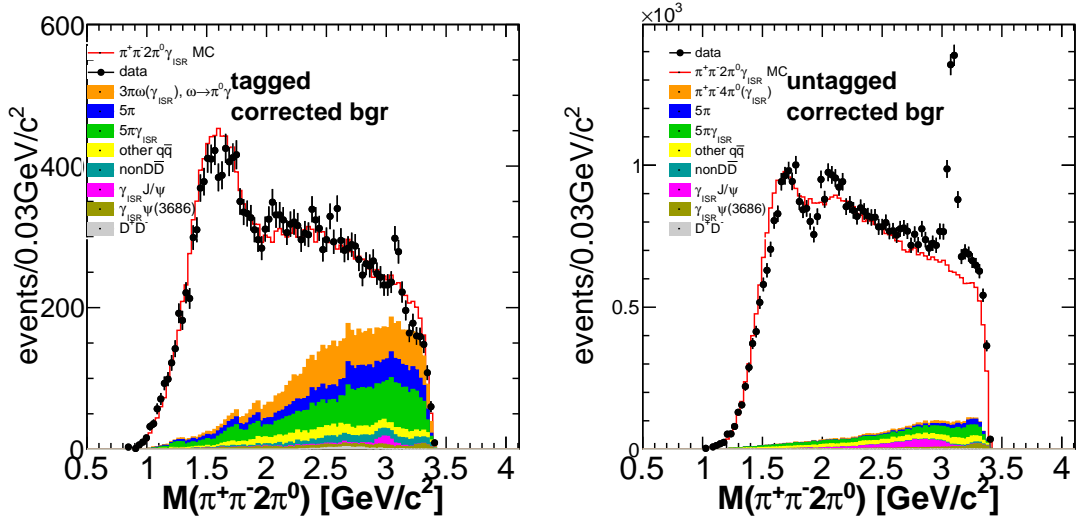


**Figure 5.16.:**  $\pi^+\pi^-2\pi^0$  mass spectrum after correction of all background contributions, before efficiency correction.

## Chapter 6.

# $\pi^0$ Reconstruction Efficiency

---

*One of the most important source of systematic uncertainty is the  $\pi^0$  efficiency. In particular, the difference of the efficiency between data and MC in reconstructing a  $\pi^0$ . In this chapter two control channels,  $\psi(3686) \rightarrow J/\psi\pi^0\pi^0$  and  $e^+e^- \rightarrow \omega\pi^0$  are used to investigate the differences of the  $\pi^0$  reconstruction efficiency between data and MC simulation. The control channels contain two  $\pi^0$  in their final states to account for any possible effects of mis-combined photons. A  $\pi^0$  efficiency correction is obtained to improve the precision of the  $e^+e^- \rightarrow \pi^+\pi^-2\pi^0\gamma_{ISR}$  measurement. The remaining uncertainty on the  $\pi^0$  reconstruction is the uncertainty of this  $\pi^0$  efficiency study, which is much smaller than the initial data-MC difference of the  $\pi^0$  reconstruction efficiency.*

---

One of the major sources of systematic uncertainty is the difference between data and simulation in the reconstruction efficiency of the  $\pi^0$  particles in the final state. Since the final states investigated in the context of this thesis contain two or three neutral pions and an ISR photon, a dedicated study is performed. Potential sources of the uncertainty stem from taking wrong combinations of photons or from misidentified photon candidates used to form a  $\pi^0$  candidate. Hence, it is important to study the  $\pi^0$  reconstruction efficiency in a channel containing at least two neutral pions, similarly to the topology of the signal channels. The basic idea of the efficiency study performed here is to choose a clean and well known final state and reconstruct all particles except one of the two  $\pi^0$ . Imposing four momentum conservation of all final state particles, the missing  $\pi^0$  four-momentum can be predicted. This is realized by performing a two constraint kinematic fit, where one of the  $\pi^0$  is treated as a missing particle, called  $\pi_{miss}^0$ . The two constraints are the  $\pi^0$  masses. The second „tagged“  $\pi^0$ , which needs to be reconstructed in the detector, will be referred to as  $\pi_{tag}^0$ . This set of events containing a predicted  $\pi^0$  is called test sample. Let  $N_{tot}$  be the number of events in the test sample. The fit result of the four momentum of  $\pi_{miss}^0$  can be considered as a prediction of the measured four-momentum of a particle, which must have been reconstructed in an efficient event. If matching  $\pi^0$  candidates cannot be found, the event is regarded as inefficient. If at least one matching  $\pi^0$  candidate is found, a 6C kinematic fit is performed testing each potential  $\pi^0$  candidate. The candidate that yields the least  $\chi_{6C}^2$  value is kept. If the best candidate yields  $\chi_{6C}^2 < 60$ , which is the same requirements as used in the untagged ISR analysis, the event is regarded as efficient, otherwise it is considered as inefficient. Let  $N_{eff}$  be the number of all efficient events.

In order to study the efficiency of neutral pions with momenta below 0.45 GeV data taken at the  $\psi(3686)$  peak are used to study the process  $e^+e^- \rightarrow \psi(3686) \rightarrow J/\psi\pi^0\pi^0$ . This channel has huge statistics and background contributions are negligibly small. For the efficiency of pions with momenta above 0.45 GeV the process  $e^+e^- \rightarrow \omega\pi_{tag}^0$  with  $\omega \rightarrow \pi^+\pi^-\pi_{miss}^0$  from the  $\psi(3770)$  data set is analyzed. The narrow  $\omega$  resonance provides an unambiguous signature, which is exploited to reject background contributions. It needs to be shown that the  $\pi^0$  efficiencies obtained from different final states give sufficiently similar results and can be combined.

## 6.1. $\pi^0$ Efficiency in the $J/\psi\pi^0\pi^0$ Channel

For the low momentum  $\pi^0$  reconstruction efficiency study, The 106M  $\psi(2S)$  events taken in 2009 are investigated. The analysis is performed with the BOSS version 6.6.4.p01, which is the same version used for the main analysis. The inclusive MC sample containing  $e^+e^- \rightarrow \psi(3686)$  events, generated with BESEVTGEN is

used. The sample is separated into the signal process  $e^+e^- \rightarrow J/\psi\pi^0\pi^0$  and the remaining background events. The  $J/\psi$  is reconstructed only from its decay into lepton pairs. The  $\pi^0$  is reconstructed from its decay to photon pairs.

### 6.1.1. Event Selection

Events with exactly two charged tracks with opposite charges are selected. The BESIII standard cuts  $r < 1$  cm and  $|z| < 10$  cm for the fiducial volume of the points of closest approach of the charged tracks to the interaction point are applied. Since the  $J/\psi$  decays into leptons with high momenta, the charged tracks must have momenta above 1 GeV. The BESIII standard requirements for the selection of good photons are applied as explained in chapter 4. For the particle identification (PID) the energy deposit  $E$  in the EMC and the momentum  $p$  of the track from the MDC is calculated. An individual charged track is identified as a muon, if  $0 < E/p < 0.4$ . Charged tracks with  $0.8 < E/p < 1.2$  are identified as electrons. Events are accepted, if both charged tracks are either muons or electrons. Figure 6.1 shows the scatter plot of  $E/p$  for both leptons. For the reconstruction of  $J/\psi$  from lepton pairs, the invariant mass  $M(\ell^+\ell^-)$  is required to be within the mass window  $3.04 < M(\ell^+\ell^-) < 3.14$  GeV. The lepton mass distribution is shown in Fig. 6.2. Furthermore, at least one  $\pi^0$  candidate is required to form the  $\pi_{tag}^0$ . The  $\pi_{tag}^0$  cannot be chosen by the least  $\chi^2$  of a kinematic fit, since this would bias the resolution of the tagged neutral pion. For the  $\pi^0$  reconstruction, the same criteria as described in chapter 4 are applied.

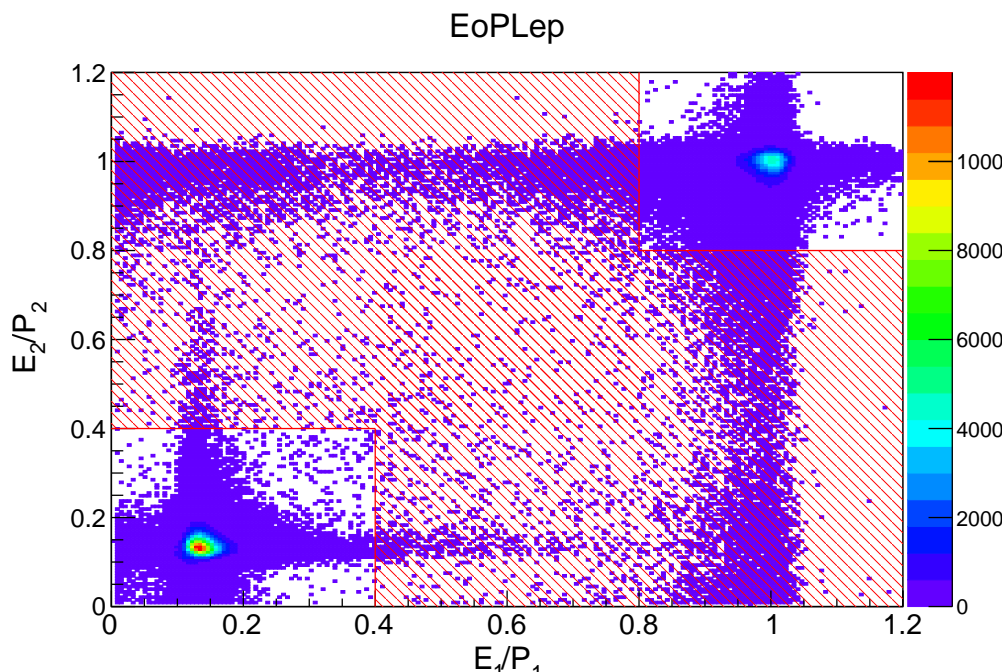
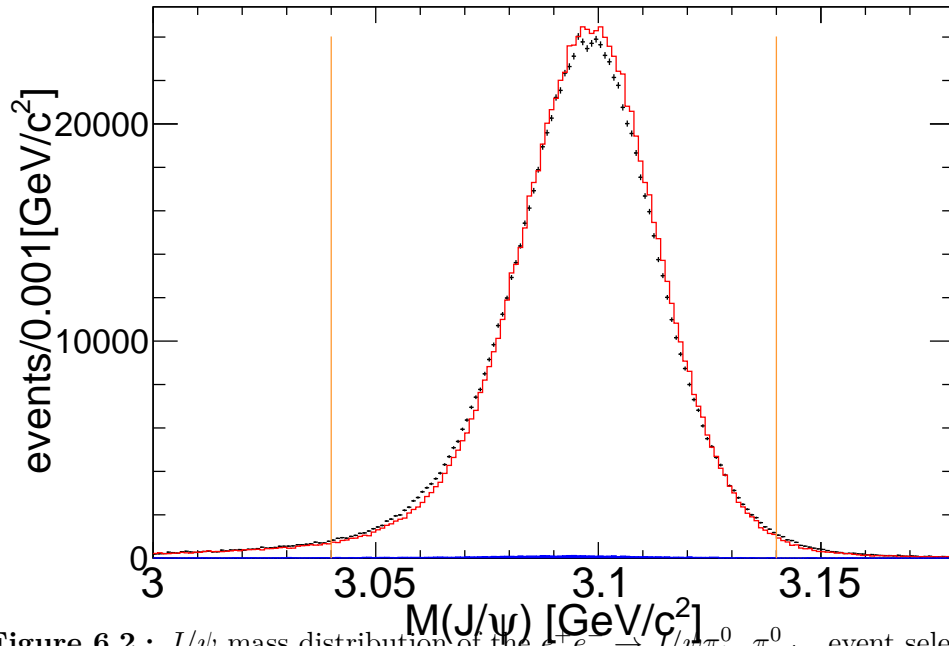
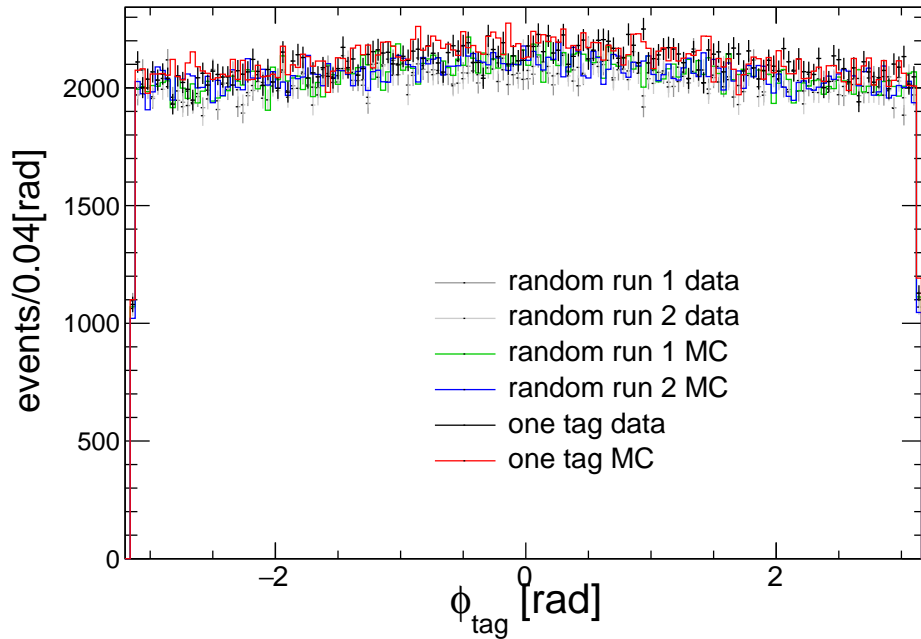


Figure 6.1.: Lepton PID for the  $J/\psi$  reconstruction in the process  $e^+e^- \rightarrow J/\psi\pi^0\pi^0$ .



**Figure 6.2.:**  $J/\psi$  mass distribution of the  $e^+e^- \rightarrow J/\psi\pi_{tag}^0\pi_{miss}^0$  event selection.

For events with more than one  $\pi_{tag}^0$  candidate, it is chosen randomly among all available  $\pi^0$  candidates. The analysis is performed twice with different random seeds in order to estimate the systematic uncertainty of this method. Figure 6.3 shows the azimuthal angle distributions obtained with different random seeds.



**Figure 6.3.:** Azimuthal angle distribution of  $\pi_{tag}^0$ .

As expected, the azimuthal angle distributions are flat. The two analyses with different seeds are similar, but do not coincide exactly. For the final result, the

two methods are combined together by using their average. A 2C kinematic fit of the final state  $J/\psi\pi_{tag}^0\pi_{miss}^0$  is performed with both  $\pi^0$  masses constrained. The momentum  $p_{\pi_{miss}^0}$  of  $\pi_{miss}^0$  is predicted by the fit by closing the kinematic relations  $p_{\pi_{miss}^0} = p_0 - p_{\pi_{tag}^0} - p_{J/\psi}$ , where  $p_0$  is the initial boost vector of the collision. Events with  $\chi_{2C}^2 > 15$  are rejected. Fig. 6.4 shows the  $\chi_{2C}^2$  distribution. The agreement between data and simulation is very good and the background contributions are negligible. Table 6.1 summarizes all the event selection criteria.

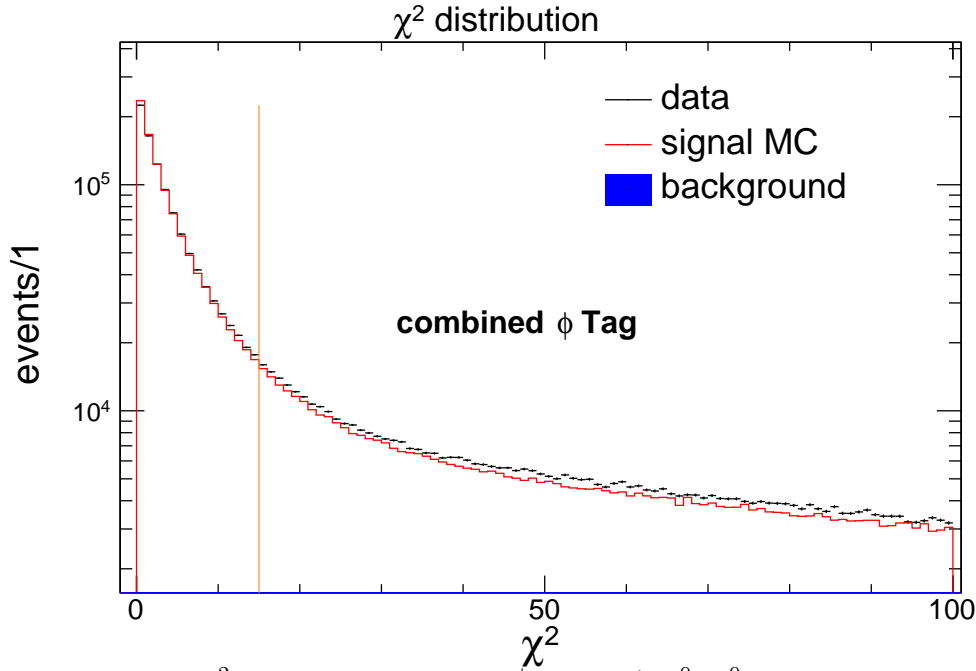


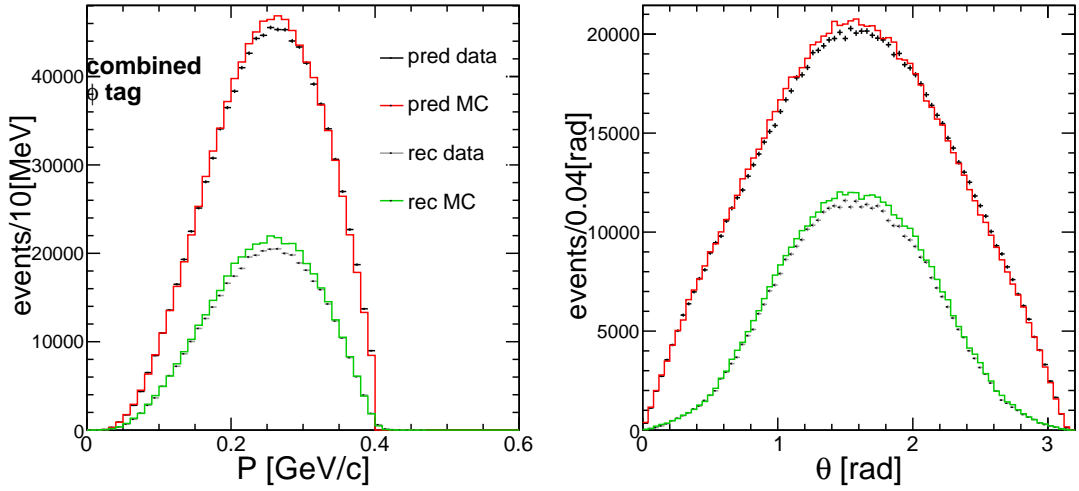
Figure 6.4.:  $\chi_{2C}^2$  distribution of the  $e^+e^- \rightarrow J/\psi\pi_{tag}^0\pi_{miss}^0$  event selection.

Table 6.1.: Summary of event selection criteria for  $J/\psi\pi_{tag}^0\pi_{miss}^0$  events.

|                                       |   |
|---------------------------------------|---|
| <b>Charged tracks</b>                 |   |
| #                                     | 2 (net charge 0)                              |
| R                                     | 1.0 cm  |
| z                                     | 10.0 cm                                       |
| <b>Good Photons</b>                   |   |
| $E$ (barrel)                          | > 25 MeV                                      |
| $E$ (end caps)                        | > 50 MeV                                      |
| TDC                                   | < 700 ns                                      |
| angle to closest charged track        | > 20°   |
| #                                     | < 8   |
| <b><math>\pi^0</math> Window</b>      | $100 < M(\gamma\gamma) < 160 \text{ MeV}/c^2$ |
| <b><math>\pi^0</math> Candidates</b>  | $\leq 5$ non overlapping                      |
| <b><math>2\pi^0</math> Candidates</b> | $\leq 2$ non overlapping                      |
| <b><math>J/\psi</math> Window</b>     | $3.04 < M(\ell\ell) < 3.14 \text{ GeV}/c^2$   |
| <b>Kinematic Fit</b>                  | $\chi_{2C}^2 \leq 15$                         |

### 6.1.2. Determination of the Efficiency

For all the events in the  $e^+e^- \rightarrow J/\psi\pi_{rec}^0\pi_{tag}^0$  test sample a  $\pi^0$  candidate denoted by  $\pi_{rec}^0$  is searched for in the detector, which matches to the predicted candidate  $\pi_{miss}^0$ . As pointed out in the beginning of chapter 6, the criteria for an event in the test sample to be efficient is the 6C kinematic fit of  $\ell^+\ell^-\pi_{rec}^0\pi_{tag}^0$ , where the two  $\pi^0$  masses and the four momentum conservation are constrained. Every combination is rejected for which the fit yields  $\chi_{6C}^2 > 60$ . Figure 6.5 shows the momentum and polar angle distributions of the predicted and the reconstructed neutral pions for data and MC.



**Figure 6.5.:** Momentum and polar angle distributions of the missing and the reconstructed  $\pi^0$  in data and MC.

By definition, there is at least one efficient  $\pi^0$  in each event, which is the  $\pi_{tag}^0$ . Considering in addition that the two  $\pi^0$  in the final state  $J/\psi\pi^0\pi^0$  cannot be distinguished, the efficiency  $\varepsilon$  to reconstruct a single  $\pi^0$  cannot be calculated conventionally as  $\varepsilon = N_{eff}/(N_{eff} + N_{ineff})$ . The equation describes the efficiency to reconstruct the whole  $J/\psi\pi^0\pi^0$  event. Which is different from the desired single  $\pi^0$  reconstruction efficiency in the presence of a second  $\pi^0$ . The proper way to calculate the reconstruction efficiency of a single  $\pi^0$  in dependence of its momentum  $p$  is given by:

$$\varepsilon(p) = \frac{N_{good}(p)}{N_{all}(p)} = \frac{N_{eff}(p) + N_{tag}(p)}{N_{eff}(p) + N_{tag}(p) + N_{ineff}(p)}, \quad (6.1.1)$$

with  $N_{all}(p) = N_{eff}(p) + N_{tag}(p) + N_{ineff}(p)$  and  $N_{good}(p) = N_{eff}(p) + N_{tag}(p)$ , where  $N_{tag}$  is the number of reconstructed  $\pi_{tag}^0$ ,  $N_{eff}$  is the number of efficiently reconstructed predicted  $\pi_{miss}^0$  and  $N_{ineff}$  is the number of inefficient events, where a

$\pi_{rec}^0$  candidate could not be found for the  $\pi_{miss}^0$  according to the criterion described above. Eq. 6.1.1 treats every  $\pi_{tag}^0$  as an efficiently reconstructed  $\pi^0$ . Hence, it gives the correct efficiency to reconstruct a single  $\pi^0$ . By definition, the number of  $e^+e^- \rightarrow J/\psi\pi^0\pi^0$  events, where both  $\pi^0$  were lost do not belong to the test sample. Other  $\pi^0$  reconstruction efficiency studies [95, 96] have demonstrated that the data-MC difference of the single  $\pi^0$  reconstruction efficiency is as small as a few percent. Hence, the data-MC difference of events, where both  $\pi^0$  are lost is negligible. Eq. 6.1.1 implies a lower bound of the efficiency of 50%, in the case where none of the  $\pi_{miss}^0$  could be reconstructed. This is not a problem, since the interesting quantity will be the relative difference between data and MC  $\varepsilon_{data}/\varepsilon_{MC} - 1$ , which will no longer suffer from this problem. The left panel of Fig. 6.6 shows the final  $\pi^0$  reconstruction efficiency for data and the signal simulation in dependence of the  $\pi^0$  momentum.

The relative efficiency difference between data and MC is defined as

$$\Delta\varepsilon_{\pi^0} = \varepsilon_{data}/\varepsilon_{MC} - 1,$$

where  $\varepsilon_{data}$  and  $\varepsilon_{MC}$  are calculated according to Eq. 6.1.1. This quantity can be used in the main analyses of  $e^+e^- \rightarrow \pi^+\pi^-2\pi^0\gamma_{ISR}$  and  $e^+e^- \rightarrow \pi^+\pi^-3\pi^0(\gamma_{ISR})$  as a multiplicative correction to the event reconstruction efficiency obtained from signal MC.

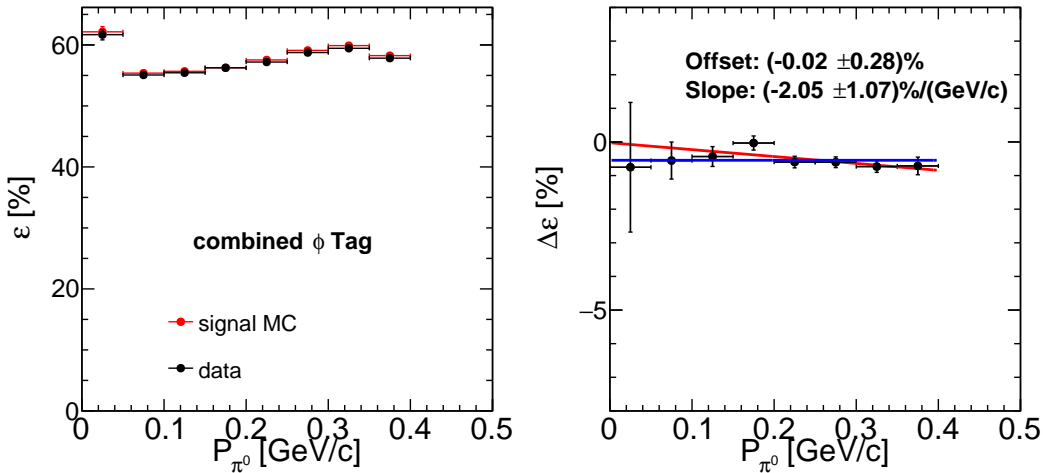


**Figure 6.6.:**  $\pi^0$  reconstruction efficiency in dependence of the pion momentum (left) and the relative difference between data and MC (right). The blue line is a constant fit and the red line is a linear fit.

The  $\Delta\varepsilon_{\pi^0}$  distribution in dependence of the momentum is shown in the right panel of Fig. 6.6 and the corresponding numbers are also listed in Table 6.2. The efficiency and the relative difference in different intervals of the polar angle are

shown in Fig. 6.7 and found to be sufficiently flat. Hence, the  $\pi^0$  efficiency correction is approximately independent of the polar angle of the neutral pions.

**Table 6.2.:**  $\pi^0$  efficiency in dependence of the  $\pi^0$  momentum in the  $J/\psi\pi^0\pi^0$  channel, where  $N_{all}(p) = N_{eff}(p) + N_{tag}(p) + N_{ineff}(p)$  and  $N_{good}(p) = N_{eff}(p) + N_{tag}(p)$ .

| $P_{\pi^0} [GeV/c]$ | <b>data</b>        |                    |                   |
|---------------------|--------------------|--------------------|-------------------|
|                     | $N_{all}(p)$       | $N_{good}(p)$      | $\varepsilon[\%]$ |
| 0.00 – 0.05         | $3296 \pm 58$      | $2033 \pm 46$      | $61.7 \pm 0.9$    |
| 0.05 – 0.10         | $52945 \pm 231$    | $29158 \pm 172$    | $55.1 \pm 0.2$    |
| 0.10 – 0.15         | $184770 \pm 433$   | $102429 \pm 323$   | $55.4 \pm 0.1$    |
| 0.15 – 0.20         | $351378 \pm 596$   | $197637 \pm 448$   | $56.2 \pm 0.1$    |
| 0.20 – 0.25         | $490993 \pm 703$   | $280839 \pm 532$   | $57.2 \pm 0.1$    |
| 0.25 – 0.30         | $539122 \pm 737$   | $316738 \pm 564$   | $58.8 \pm 0.1$    |
| 0.30 – 0.35         | $446378 \pm 671$   | $265376 \pm 517$   | $59.5 \pm 0.1$    |
| 0.35 – 0.40         | $212964 \pm 466$   | $123162 \pm 353$   | $57.8 \pm 0.1$    |
| Total               | $2281846 \pm 1518$ | $1317372 \pm 0.00$ | $57.73 \pm 0.03$  |
| $P_{\pi^0} [GeV/c]$ | <b>MC</b>          |                    |                   |
|                     | $N_{all}(p)$       | $N_{good}(p)$      | $\varepsilon[\%]$ |
| 0.00 – 0.05         | $3305 \pm 57$      | $2054 \pm 45$      | $62.1 \pm 0.8$    |
| 0.05 – 0.10         | $53759 \pm 232$    | $29771 \pm 173$    | $55.4 \pm 0.2$    |
| 0.10 – 0.15         | $183664 \pm 429$   | $102259 \pm 320$   | $55.7 \pm 0.1$    |
| 0.15 – 0.20         | $356951 \pm 597$   | $200836 \pm 448$   | $56.3 \pm 0.1$    |
| 0.20 – 0.25         | $507947 \pm 713$   | $292284 \pm 541$   | $57.5 \pm 0.1$    |
| 0.25 – 0.30         | $556069 \pm 746$   | $328680 \pm 573$   | $59.1 \pm 0.1$    |
| 0.30 – 0.35         | $452353 \pm 673$   | $270912 \pm 520$   | $59.9 \pm 0.1$    |
| 0.35 – 0.40         | $207990 \pm 456$   | $121149 \pm 348$   | $58.2 \pm 0.1$    |
| Total               | $2322038 \pm 1524$ | $1347945 \pm 0.00$ | $58.05 \pm 0.03$  |

In order to give a momentum dependent efficiency correction, the momentum distribution of the relative efficiency difference  $\Delta\varepsilon_{\pi^0}$  is fitted with a first order polynomial. The obtained fit parameters are

$$\begin{aligned} \Delta\varepsilon_{\pi^0}(p) &= a \cdot p + b, \text{ with} \\ a &= (-2.05 \pm 1.07) \cdot \text{GeV}^{-1}\%, \\ b &= (-0.02 \pm 0.28)\% \text{ and} \\ \chi^2/\text{ndf} &= 0.70. \end{aligned}$$

The fit quality of the blue constant fit in Fig. 6.6 is  $\chi^2/\text{ndf} = 1.13$ . Hence the constant hypothesis is rejected. The negative sign of the result above at  $\pi^0$  momenta below 0.15 GeV/c indicates that the MC overestimates the  $\pi^0$  reconstruction

efficiency of data. The result is in agreement with the previous  $\pi^0$  efficiency measurement [95] that has been performed in the same final state, but with BOSS version 6.5.5. The result of this measurement was conservatively estimated to be 3% for the entire momentum range.

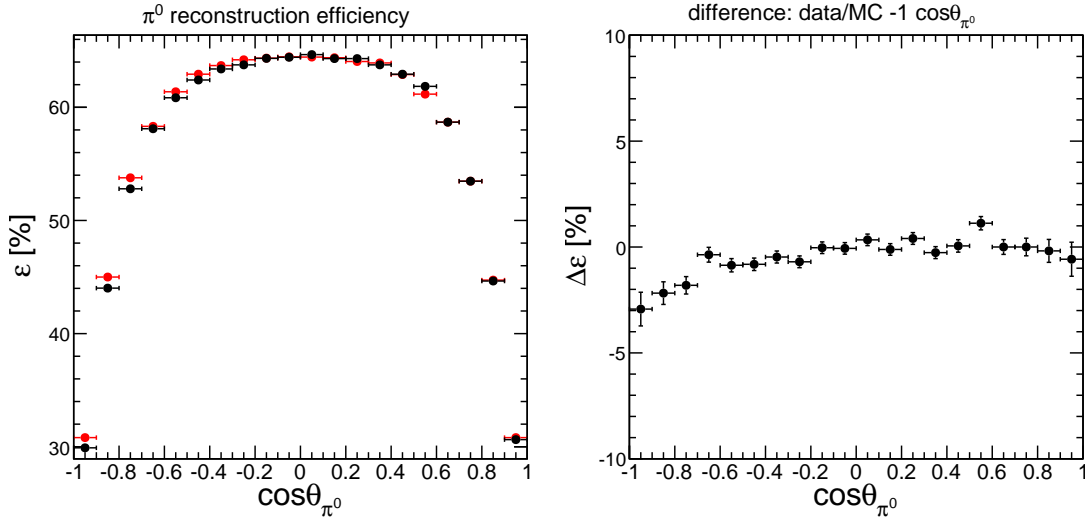


**Figure 6.7.:**  $\pi^0$  reconstruction efficiency in dependence of the pion polar angle (left) and the relative difference between data and MC (right).

As additional cross check, the  $\pi^0$  reconstruction efficiency is studied as a two dimensional function of the predicted and the tagged  $\pi^0$  momenta. In this case the efficiency is defined as

$$\varepsilon_{\pi^0}(p_{miss}, p_{tag}) = \frac{N_{eff}(p_{miss}, p_{tag})}{N_{eff}(p_{miss}, p_{tag}) + N_{ineff}(p_{miss}, p_{tag})}.$$

The two dimensional distributions of the efficiency in data and MC are shown in Fig. 6.8. Background contributions from MC are subtracted from data. The efficiency distributions show a strong correlation between the momenta of the tagged and the predicted  $\pi^0$ . This is because of the limited phase space available for the two  $\pi^0$  in the  $\psi(3686) \rightarrow J/\psi\pi^0\pi^0$  process. Moreover, the plots show that a  $\pi^0$  efficiency correction cannot be performed as a function of both  $\pi^0$ , since the efficiency distribution does not cover the entire two-dimensional momentum space. In addition, the relative difference between data and MC of the efficiency as a function of both  $\pi^0$  momenta is flat in the region with sufficient statistics. This proves the stability of the efficiency calculated according to Eq. 6.1.1

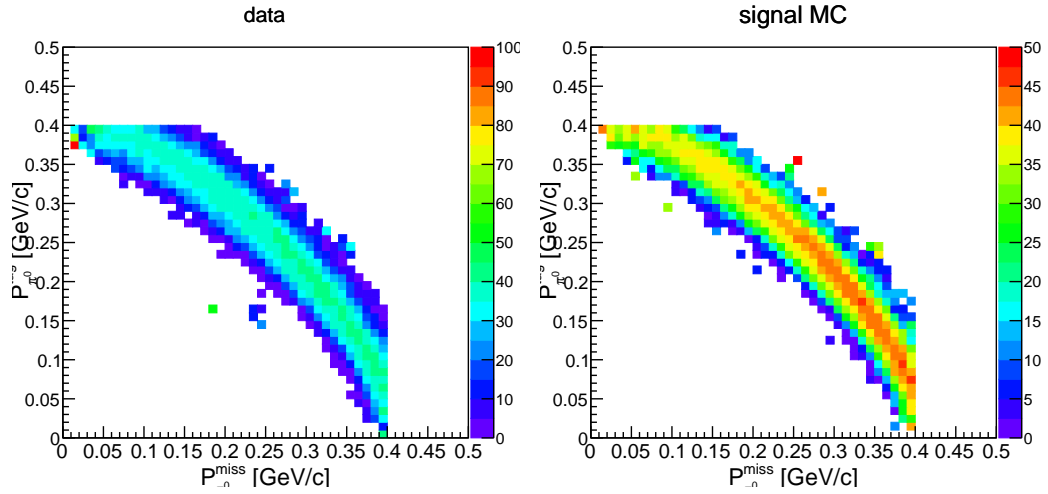


**Figure 6.8.:**  $\pi^0$  reconstruction efficiency as a function of both  $\pi^0$  momenta in the  $e^+e^- \rightarrow J/\psi\pi^0\pi^0$  channel.

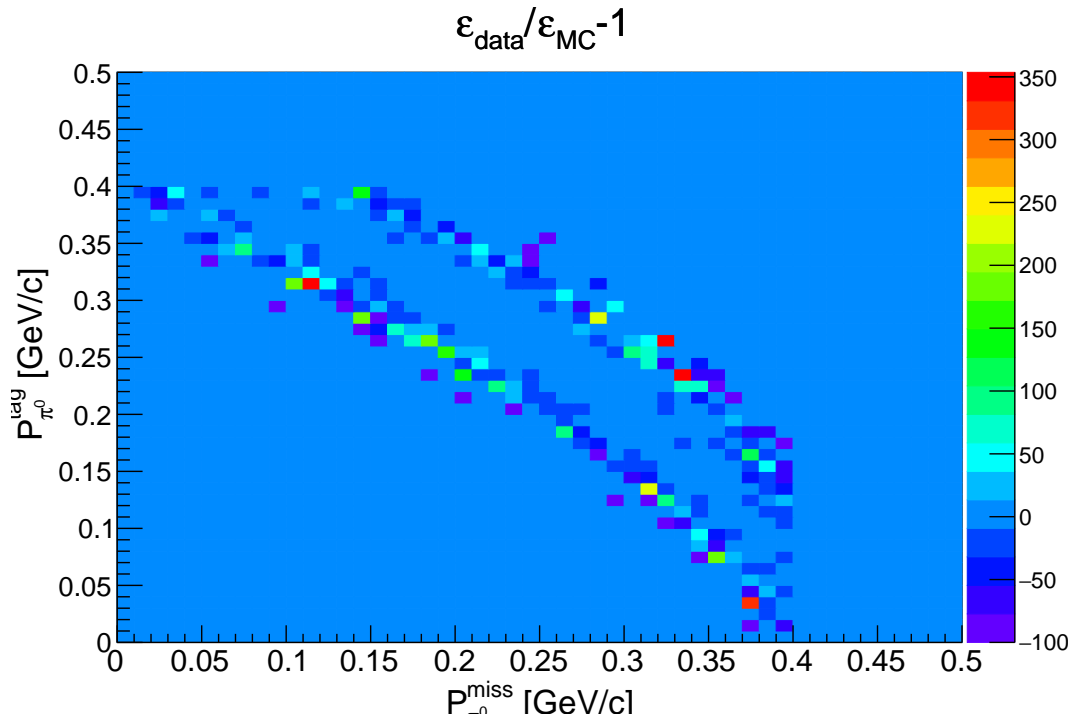


**Figure 6.9.:** Relative difference between data and MC of the  $\pi^0$  efficiency as a function of both  $\pi^0$  momenta in the  $e^+e^- \rightarrow J/\psi\pi^0\pi^0$  channel.

### 6.1.3. Systematic Uncertainty

The systematic uncertainties from the luminosity, tracking and the position of the interaction point cancel out in the ratio of the efficiencies.

First, the systematic uncertainty coming from the event selection of the test sample is estimated. The selection criteria are varied in an appropriate range and the  $\pi^0$  efficiency correction factor  $\Delta\varepsilon_{\pi^0}$  is determined with the varied selection. The largest deviation from the result of  $\Delta\varepsilon_{\pi^0}$  obtained with the default selection criteria is taken as systematic uncertainty. The applied variations and the determined uncertainties are listed in Table 6.3. Moreover, the difference between the two analyses with different initial random seeds is taken as a systematic uncertainty, which is 0.43%. In order to estimate the uncertainty of the  $\chi_{6C}^2$  requirement, which is used to decide if a reconstructed  $\pi^0$  candidate is efficient, the  $\chi_{6C}^2$  selection is changed by  $\pm 10$ . In addition, the so-called cone method is used to decide if a reconstructed  $\pi^0$  candidate is efficient instead of the  $\chi_{6C}^2$  requirement. In this method a reconstructed  $\pi^0$  candidate is efficient, if the angle  $\alpha$  between the predicted and the reconstructed  $\pi^0$  candidates fulfills  $1 - \cos \alpha < 0.03$  and their relative energy difference is less than 40%. The resulting uncertainty is listed in Table 6.3.

Table 6.3 shows all contributions to the systematic uncertainties. Since they can be assumed to be uncorrelated, their quadratic sum is 0.68%.

**Table 6.3.:** Systematic uncertainties for  $\pi^0$  efficiency study in  $J/\psi\pi_{tag}^0\pi_{miss}^0$ .

| Source                       | Variation Range   | Error [%] |
|------------------------------|---|-----------|
| Selection $\chi_{2C}^2$ cut  | $11 < \chi_{2C}^2 < 19$                                       | 0.15      |
| Efficiency $\chi_{6C}^2$ cut | $20 < \chi_{6C}^2 < 40$                                       | 0.23      |
| Cone + $\Delta E$ Method     | -   | 0.43      |
| $J/\psi$ window              | $3.02 < M_{low}^{cut} < 3.06$<br>$3.12 < M_{up}^{cut} < 3.16$ | 0.04      |
| Bgr. Subrt.                  | $\pm 10\%$ Bgr.   | 0.06      |
| Tag Mode                     | -   | 0.43      |
| Bining                       | 5 MeV $\rightarrow$ 10 MeV                                    | 0.05      |
| Fit range                    | border -5 MeV   | 0.07      |
| Total                        | -   | 0.68      |

## 6.2. $\pi^0$ Efficiency in the $\omega\pi^0$ Channel

Neutral pions with momenta above 450 MeV cannot be accessed in the  $\psi(2S) \rightarrow J/\psi\pi^0\pi^0$  process. For these  $\pi^0$  with higher momenta, the process  $e^+e^- \rightarrow \omega\pi_{tag}^0$  with  $\omega \rightarrow \pi^+\pi^-\pi_{miss}^0$  is investigated at a c.m. energy of 3.773 GeV. In order to

benefit from the narrow  $\omega$  width, the predicted neutral pion  $\pi_{miss}^0$  is chosen to be the one coming from the  $\omega$  decay. In this way, background contributions can be reduced. The momenta of the  $\omega$  resonance and the  $\pi_{tag}^0$  are fixed to 1.80 GeV up to resolution effects, since  $e^+e^- \rightarrow \omega\pi^0$  is a two body process. The upper bound of the momentum of the  $\pi_{miss}^0$  is also 1.80 GeV, which only occurs in the very rare case, when the two charged pions from the decay of the  $\omega$  resonance have zero momentum. This implies that the two  $\pi^0$  in the final state can be distinguished by their momenta. Therefore, the  $\pi_{tag}^0$  candidate can be chosen by the best  $\chi^2$  of a kinematic fit without introducing a resolution bias, if there is more than one possible candidate. Moreover, due to the momentum separation of the two neutral pions, the calculation of the single  $\pi^0$  reconstruction efficiency according to Eq. 6.1.1 simplifies to

$$\varepsilon(p) = \frac{N_{eff}(p)}{N_{eff}(p) + N_{ineff}(p)}. \quad (6.2.1)$$

This is because  $N_{tag}(p < 1.75 \text{ GeV})$  is zero in the momentum range of the predicted neutral pion, as explained above. The Momentum distributions of the predicted and the tagged neutral pions are shown later in Fig. 6.16, which clearly shows the momentum separation. In this analysis, the Lund- $q\bar{q}$  MC sample is used for the signal simulation, since the form factor models used in the scan mode of the PHOKHARA 9.1 generator are not optimized in the c.m. energy region of  $\psi(3770)$ . The signal simulation is split into three parts, which are: (1) pure  $e^+e^- \rightarrow \omega\pi_{tag}^0$  events, (2)  $e^+e^- \rightarrow \pi^+\pi^-2\pi^0$  continuum events without an  $\omega$  resonance and (3)  $e^+e^- \rightarrow \pi^+\pi^-2\pi^0\gamma_{ISR}$  events with and without an  $\omega$  resonance. These three contributions are kinematically identical. In data they cannot be distinguished by the event selection explained in the following.

### 6.2.1. Event Selection

Events with exactly two charged tracks with opposite charge and at least one  $\pi^0$  candidate are selected. The BESIII standard cuts  $r < 1 \text{ cm}$  and  $|z| < 10 \text{ cm}$  for the fiducial volume of points of closest approach of the charged tracks to the interaction point are applied. Moreover,  $E_{EMC}/p_{MDC} < 0.8$  is required for both charged pion candidates in order to reject electrons. If the  $E_{EMC}/p_{MDC}$  cannot be determined, the pion candidates are kept. Figure 6.10 shows the  $E_{EMC}/p_{MDC}$  distributions for positively and negatively charged pions separately.

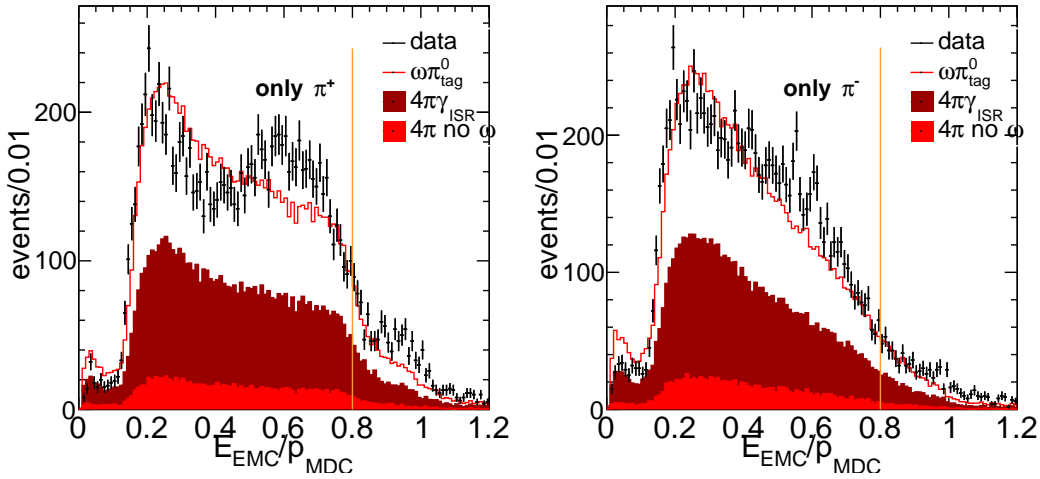


**Figure 6.10.:** Energy deposit in the EMC over the track momentum separated by the charge of the pions of the  $e^+e^- \rightarrow \omega\pi^0$  final state.

There is a background contamination of events with  $E_{EMC}/p_{MDC} > 0.8$  in particular for the  $\pi^+$ . These events presumably come from radiative Bhabha scattering. Moreover, in the case of  $\pi^+$ , the MC simulations cannot describe data well in the region  $0.2 < E_{EMC}/p_{MDC} < 0.7$ . Figure 6.11 shows the  $E_{EMC}/p_{MDC}$  plotted versus the momenta of the charged pions.

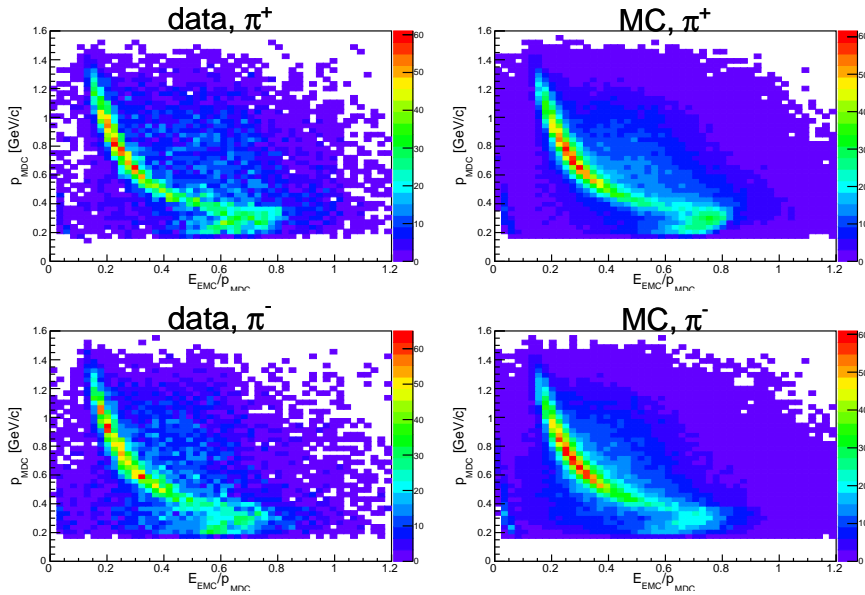


**Figure 6.11.:**  $E_{EMC}/p_{MDC}$  versus the momenta separated by the charge of the pions for for the  $e^+e^- \rightarrow \omega\pi^0$  final state.

The two dimensional distribution shows the same structures in data compared to MC. An additional structure in data, which would suggest a further background contribution, cannot be observed. However, the accumulation of low momentum events begins at  $E_{EMC}/p_{MDC} \approx 0.5$  in data, but starts at  $E_{EMC}/p_{MDC} \approx 0.7$

in MC. Hadronic showers are not described completely in the simulations. The integrated number of events in data and MC below  $E_{EMC}/p_{MDC} = 0.8$  are  $N_{data} = 24276 \pm 156$  and  $N_{MC} = 23144 \pm 152$ , which is in reasonable agreement. It can be assumed that other reactions do not contribute significantly.

The BESIII standard requirements for the selection of good photons, as explained in chapter 4, are applied. Furthermore, at least one  $\pi^0$  candidate is required to form the  $\pi_{tag}^0$ . For the  $\pi^0$  reconstruction, the same criteria as in the main analysis of  $e^+e^- \rightarrow \pi^+\pi^-2\pi^0\gamma_{ISR}$  is applied, which is the mass window  $100 \text{ MeV} < M(\gamma\gamma) < 160 \text{ MeV}$ . A two constraint kinematic fit of the  $\pi^+\pi^-\pi_{miss}^0\pi_{tag}^0$  final state is performed for all available  $\pi_{tag}^0$  candidates. The momentum of  $\pi_{miss}^0$  is predicted by the fit by imposing four-momentum conservation. The constraints are the two  $\pi^0$  masses. The  $\omega$  width is large compared to the detector resolution to be constrained in the kinematic fit. In case of multiple  $\pi_{tag}^0$  candidates, the one which yields the smallest  $\chi_{2C}^2$  is kept. Events with  $\chi_{2C}^2 < 15$  and  $680 < M(\pi^+\pi^-\pi_{miss}^0) < 860 \text{ MeV}/c^2$  are accepted. The  $\chi_{2C}^2$  and the  $\omega$  mass distributions are shown in Fig. 6.12. All selection criteria, except the ones shown in the plots are applied.

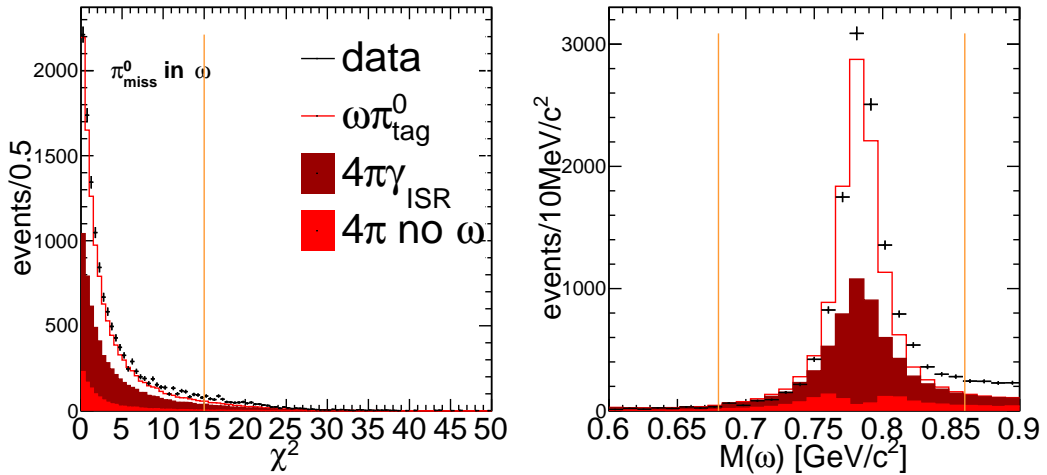


**Figure 6.12.:** Event selection of the  $\omega\pi^0$  final state for the  $\pi^0$  reconstruction efficiency.

The wrong combination of three pions  $\pi^+\pi^-\pi_{tag}^0$ , shown in Fig. 6.13, always results in invariant masses well above the  $\omega$  mass, as expected from the two body kinematics. A misidentification of the  $\pi^0$  is ruled out. However, an excess of events is observed in data above  $M(\pi^+\pi^-\pi_{tag}^0) > 3.45 \text{ GeV}/c^2$  that cannot be described by the Lund- $q\bar{q}$  MC simulation. These events appear as  $e^+e^- \rightarrow \pi^+\pi^-2\pi^0$  signal events in the PHOKHARA 9.1 simulation. However, the PHOKHARA 9.1 generator underestimates this contribution significantly, which becomes evident when comparing the corresponding contributions in the spectra of the left and right panels in Fig. 6.13. The difference can be attributed to the inadequately

optimized form factors in PHOKHARA 9.1, as mentioned above. Events with  $M(\pi^+\pi^-\pi_{tag}^0) > 3.45 \text{ GeV}/c^2$  are removed from the selection in order to avoid this region to spoil the data-MC comparison. These events correspond to  $\pi_{miss}^0$  with momenta below 200 MeV. The reconstruction efficiency of these low momentum  $\pi^0$  is already known from the  $e^+e^- \rightarrow \psi(3686) \rightarrow J/\psi\pi^0\pi^0$  study with sufficiently high precision. All the event selection criteria are summarized in Table 6.4.

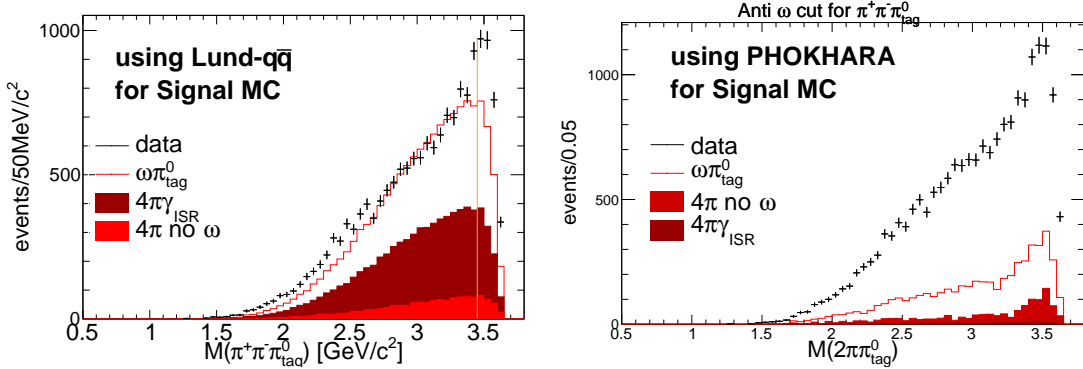


Figure 6.13.: Comparison of the  $M(\pi^+\pi^-\pi_{tag}^0)$  mass distribution between PHOKHARA 9.1 and Lund- $q\bar{q}$ .

Table 6.4.: Summary of event selection criteria for  $\omega\pi_{tag}^0$  events.

|   |   |
|---|---|
| <b>Charged tracks</b>                         |   |
| #   | $\geq 2$ (net charge 0)                           |
| $R$   | 1.0 cm  |
| $z$   | 10.0 cm   |
| $E/p$   | $< 0.8$   |
| <b>Good Photons</b>                           |   |
| $E$   | $> 25 \text{ MeV}$ (barrel)                       |
|   | $> 50 \text{ MeV}$ (end caps)                     |
| TDC   | $< 700 \text{ ns}$                                |
| angle to closest charged track                | $> 20^\circ$                                      |
| #   | $< 8$   |
| <b><math>\pi^0</math> Window</b>              | $100 < M(\gamma\gamma) < 160 \text{ MeV}/c^2$     |
| <b><math>\pi^0</math> Candidates</b>          | $\leq 5$ non overlapping                          |
| <b><math>2\pi^0</math> Candidates</b>         | $\leq 2$ non overlapping                          |
| <b><math>\omega</math> Window</b>             | $680 < M(\omega) < 860 \text{ MeV}/c^2$           |
| <b><math>\pi^+\pi^-\pi_{tag}^0</math> cut</b> | $M(\pi^+\pi^-\pi_{tag}^0) < 3.45 \text{ GeV}/c^2$ |
| <b>Kinematic Fit</b>                          | $\chi_{2C}^2 \leq 15$                             |

### 6.2.2. Determination of the Efficiency

The event selection plots reveal that the simulation of the  $\omega\pi^0$  final state is not perfect and there are differences between data and MC remaining. However, these differences do not have any impact on the relative data-MC difference, if the cross section shape in MC does not reproduce data correctly. However, the angular distributions of the pions must be described well in MC to keep the statement above valid. Therefore, the Dalitz plot of the  $\omega$  resonance must be simulated correctly. Figure 6.14 shows the Dalitz plot for the  $\omega$  resonance in data and MC.

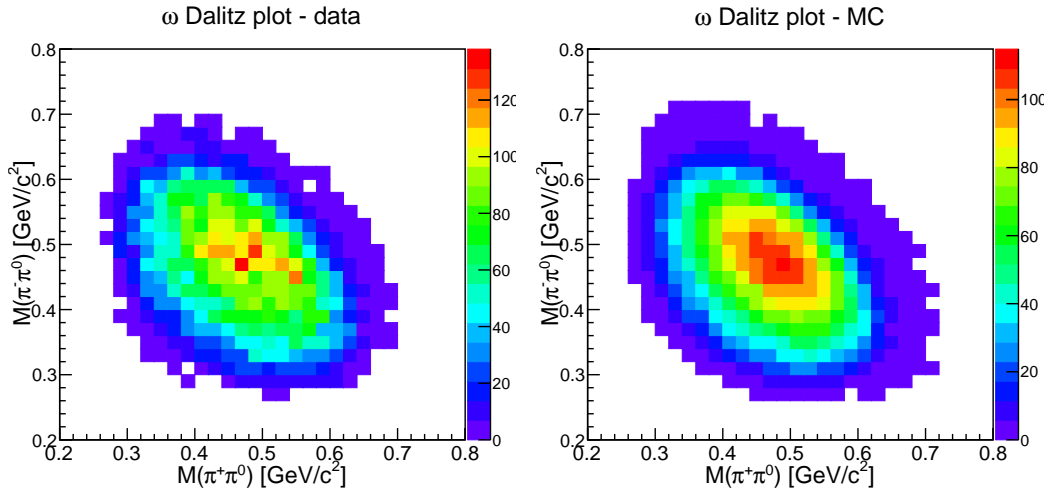


Figure 6.14.:  $\omega$ -Dalitz plot

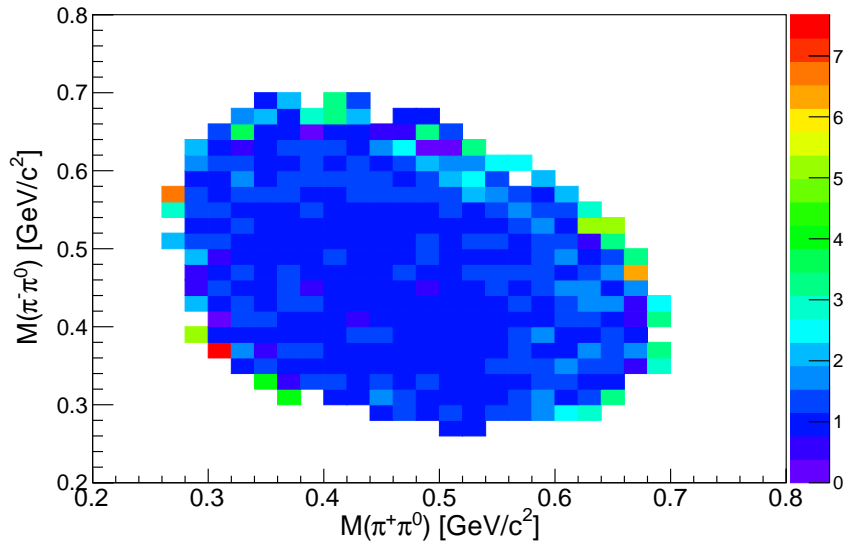
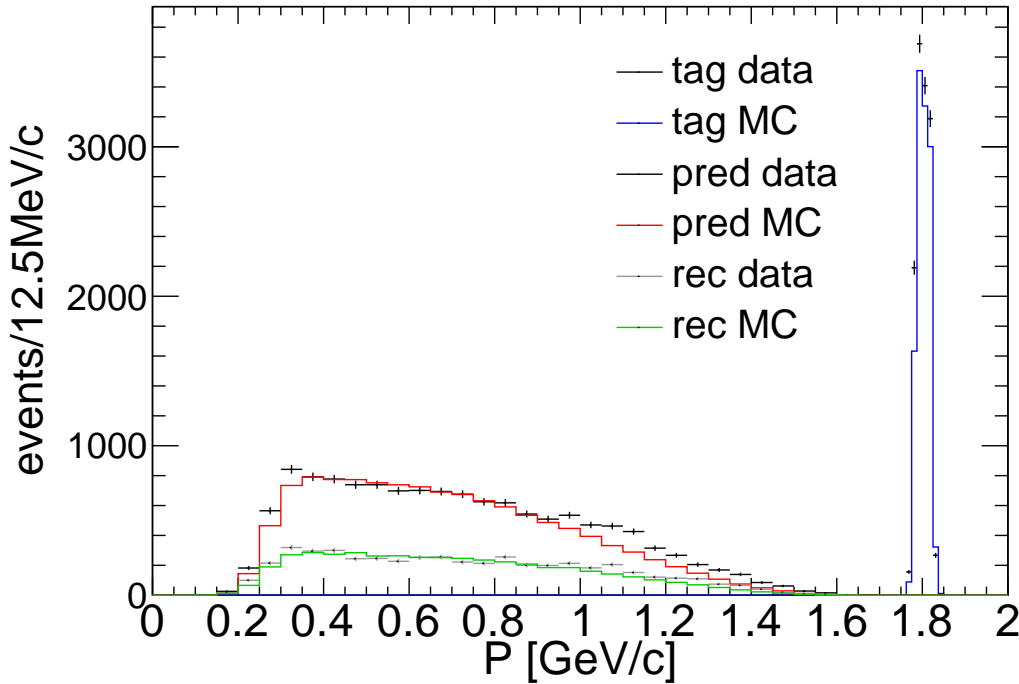


Figure 6.15.: Ratio between data and MC of the  $\omega$ -Dalitz plot.

The Dalitz plot volume is not uniformly populated, which would correspond to a pure phase-space simulation of the decay of the  $\omega$  resonance. The two dimensional

shapes agree well between data and MC. The ratio between data and MC of the Dalitz plot is shown in Fig. 6.15. The ratio is constant, except border effects, where statistics is low. Hence, the Dalitz decay of the  $\omega$  is described correctly in the Lund- $q\bar{q}$  MC, which implies that the angular distributions of the pions are simulated correctly.

For all the events in this test sample, a  $\pi^0$  candidate denoted by  $\pi_{rec}^0$  is searched for in the detector that matches to the missing one  $\pi_{miss}^0$ . As pointed out above the criteria for an event in the test sample to be efficient is the 6C kinematic fit of  $\pi^+\pi^-\pi_{rec}^0\pi_{tag}^0$ , where the two  $\pi^0$  masses and the four momentum conservation are constrained. The  $\pi^0$  candidate is accepted if the fit yields  $\chi_{6C}^2 < 60$ . Fig. 6.16 shows the momentum distributions of the tagged, the missing and the reconstructed neutral pions for data and MC. The highest momenta of the  $\pi_{miss}^0$  is about 1.5 GeV, while the momenta of  $\pi_{tag}^0$  are approximately 1.8 GeV. Hence, the predicted and the tagged  $\pi^0$  are well separated.



**Figure 6.16.:** Momentum distributions of all  $\pi^0$  in data and MC.

The yields of the total and the efficient  $e^+e^- \rightarrow \omega\pi_{tag}^0$  events are obtained in the  $\omega$ -mass distribution  $M(\omega)$ . These are given in 200 MeV intervals of the momentum  $P_{miss}$  of the predicted neutral pion in the range  $0.2 < P_{miss} < 1.6$  GeV. A double Gaussian for the  $\omega$  resonance peak plus a first order polynomial for the background is fitted to data and MC. The fits for the total number of events are shown in Fig. 6.17, and Fig. 6.18 shows the fits for efficient events only. The yields  $N_{tot}(p)$  and  $N_{eff}(P_{miss})$  are obtained from the integrals of the respective double Gaussians

after the fit.

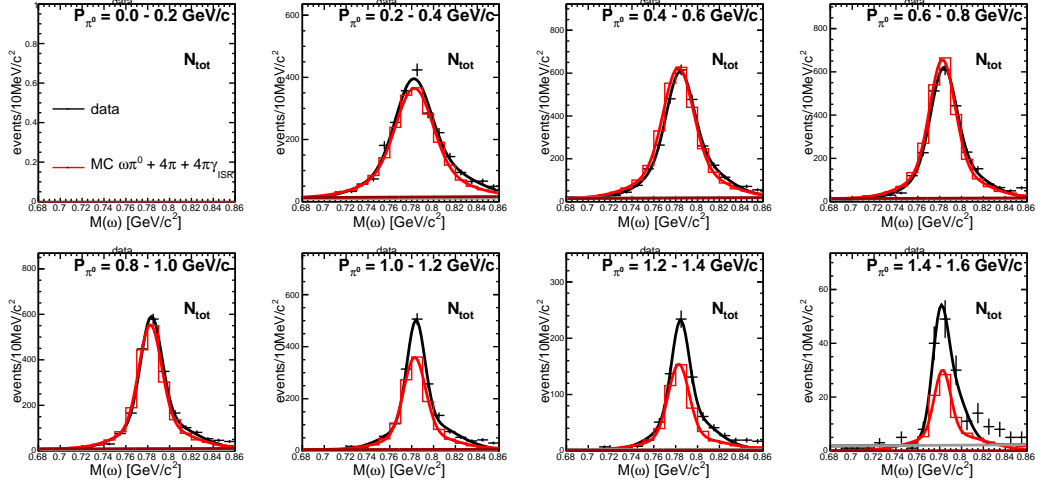


**Figure 6.17.:**  $\omega$  mass distribution fits of efficient plus inefficient  $e^+e^- \rightarrow \omega\pi_{tag}^0$  events in data and signal MC for different momenta of the  $\pi_{miss}^0$ .

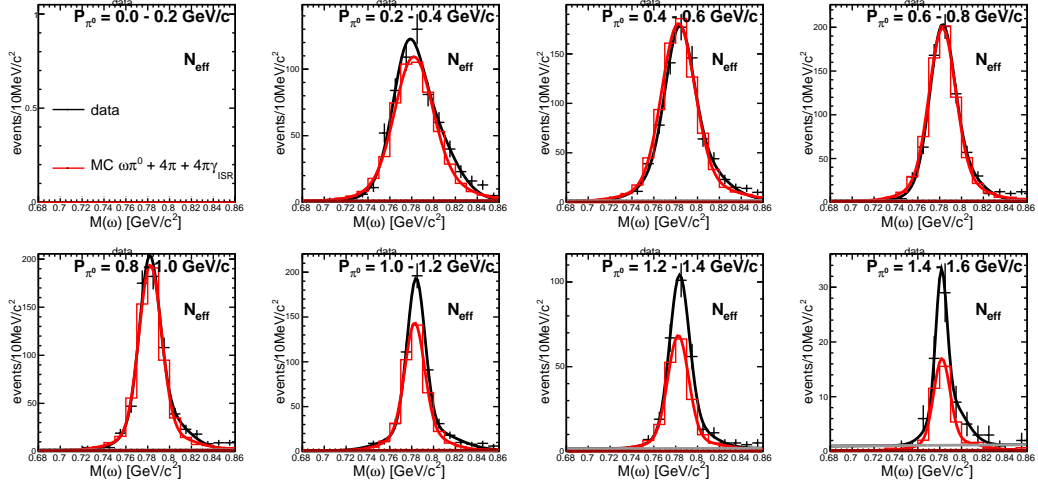


**Figure 6.18.:**  $\omega$  mass distribution fits of only efficient  $e^+e^- \rightarrow \omega\pi_{tag}^0$  events in data and signal MC for different momenta of the  $\pi_{miss}^0$ .

The efficiency for data and MC is calculated according to Eq. 6.2.1, using  $N_{tot}(p) = N_{eff}(p) + N_{ineff}(p)$ . The efficiencies obtained from the fits to data and to the MC sum are listed in Table 6.5 and are also shown in the left plot of Fig. 6.19. As explained above, the summed MC sample contains the three final states  $\omega\pi_0$ ,  $\pi^+\pi^-2\pi^0$  without  $\omega$  and  $\pi^+\pi^-2\pi^0\gamma_{ISR}$  (with and without  $\omega$ ). The left panel of Fig. 6.19 also shows that the shapes of the efficiencies of the three MC contributions are similar to each other. The efficiency of the  $e^+e^- \rightarrow \pi^+\pi^-2\pi^0\gamma_{ISR}$  contribution is smaller because the additional ISR photon distorts the assumed two body kinematics. As expected, the average efficiency in MC matches very well

to the one of data. Therefore, the three MC contributions can be compared safely to data to obtain the  $\pi^0$  reconstruction efficiency.

**Table 6.5.:** Fit results of the fit to the  $\omega$  mass peaks in various momentum ranges of the  $\pi_{miss}^0$  for the  $\pi^0$  efficiency study in  $\omega\pi_{tag}^0$ .

| $P_{\pi^0}[GeV/c]$ | <b>data</b>     |               |                   |
|--------------------|-----------------|---------------|-------------------|
|                    | $N_{tot}$       | $N_{eff}$     | $\varepsilon[\%]$ |
| 0.2 – 0.4          | $2177 \pm 49$   | $603 \pm 25$  | $27.7 \pm 1.0$    |
| 0.4 – 0.6          | $2601 \pm 54$   | $735 \pm 28$  | $28.3 \pm 0.9$    |
| 0.6 – 0.8          | $2431 \pm 51$   | $677 \pm 27$  | $27.8 \pm 0.9$    |
| 0.8 – 1.0          | $2084 \pm 47$   | $604 \pm 25$  | $29.0 \pm 1.0$    |
| 1.0 – 1.2          | $1599 \pm 40$   | $519 \pm 23$  | $32.5 \pm 1.2$    |
| 1.2 – 1.4          | $710 \pm 27$    | $268 \pm 17$  | $37.8 \pm 1.9$    |
| 1.4 – 1.6          | $134 \pm 13$    | $62 \pm 9$    | $46.5 \pm 4.9$    |
| Total              | $11737 \pm 108$ | $3468 \pm 59$ | $29.5 \pm 0.4$    |
| $P_{\pi^0}[GeV/c]$ | <b>MC</b>       |               |                   |
|                    | $N_{tot}$       | $N_{eff}$     | $\varepsilon[\%]$ |
| 0.2 – 0.4          | $1869 \pm 14$   | $530 \pm 7$   | $28.4 \pm 0.3$    |
| 0.4 – 0.6          | $2745 \pm 17$   | $785 \pm 9$   | $28.6 \pm 0.3$    |
| 0.6 – 0.8          | $2436 \pm 16$   | $691 \pm 8$   | $28.4 \pm 0.3$    |
| 0.8 – 1.0          | $1885 \pm 14$   | $581 \pm 8$   | $30.8 \pm 0.3$    |
| 1.0 – 1.2          | $1157 \pm 11$   | $387 \pm 6$   | $33.4 \pm 0.4$    |
| 1.2 – 1.4          | $500 \pm 7$     | $199 \pm 4$   | $39.8 \pm 0.7$    |
| 1.4 – 1.6          | $91 \pm 3$      | $38 \pm 2$    | $41.8 \pm 1.6$    |
| Total              | $10682 \pm 32$  | $3212 \pm 18$ | $30.1 \pm 0.4$    |

The right plot of Fig. 6.19 shows the relative efficiency difference between data and MC  $\Delta\varepsilon_{\pi^0} = \varepsilon_{data}/\varepsilon_{MC} - 1$  (black dots). Also the result of the  $e^+e^- \rightarrow J/\psi\pi^0\pi^0$  study (blue dots) and its fit (dashed blue line) is shown for comparison. The extrapolation of the  $e^+e^- \rightarrow J/\psi\pi^0\pi^0$  fit function agrees well with the result from  $e^+e^- \rightarrow \omega\pi^0$ . Considering the errors, Fig. 6.20 shows, that the polar angle distribution of the  $\pi_{miss}^0$  is sufficiently flat. Hence the  $\pi^0$  reconstruction efficiency correction is independent from the polar angle.

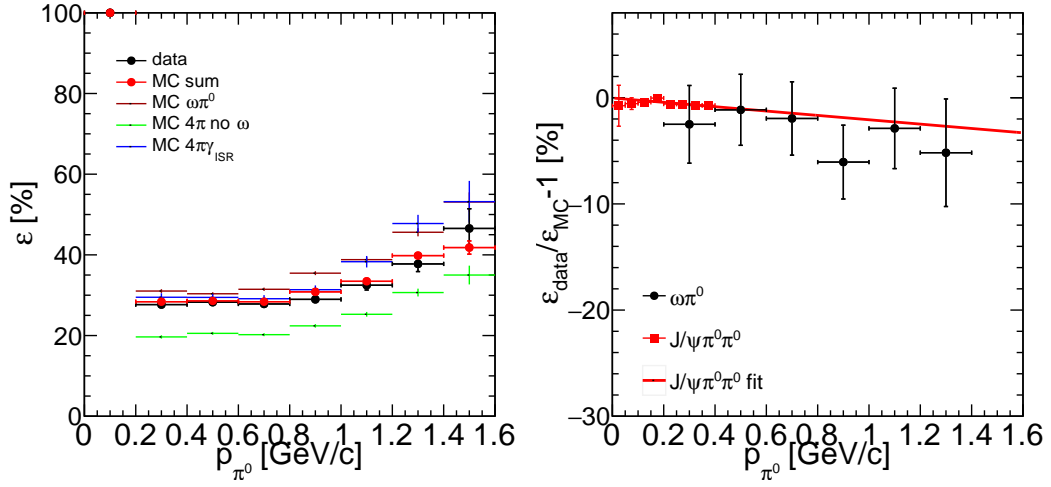


**Figure 6.19.:**  $\pi^0$  reconstruction efficiency and its relative difference between data and MC in the  $\omega\pi_{tag}^0$  final state.

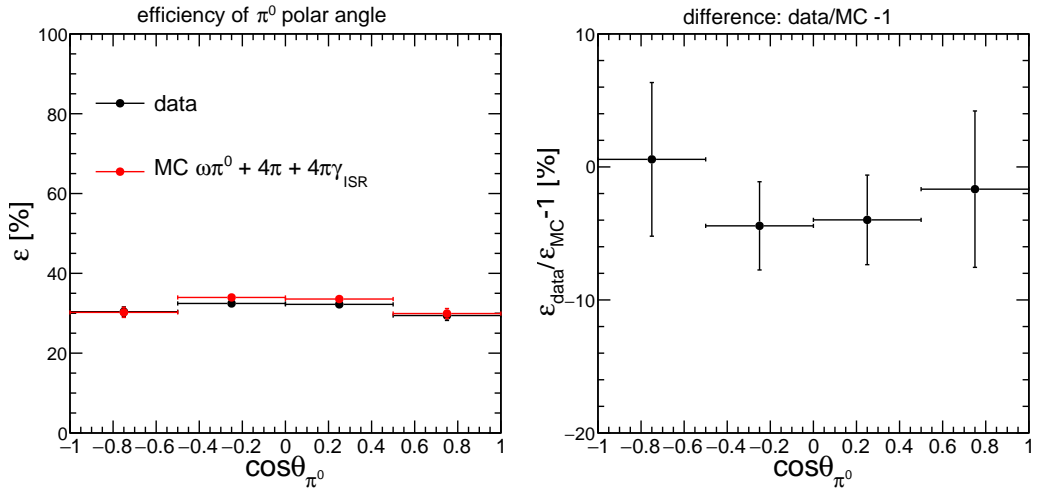


**Figure 6.20.:**  $\pi^0$  efficiency in intervals of the  $\pi_{miss}^0$  polar angle.

### 6.2.3. Systematic Uncertainty

The systematic uncertainties from the luminosity, tracking and the position of the interaction point cancel out in the ratio of the efficiencies.

First, the systematic uncertainty coming from the event selection of the test sample is estimated. Here, the selection criteria are varied in an appropriate range and determine the  $\pi^0$  efficiency correction factor  $\Delta\epsilon_{\pi^0}$ . The largest deviation from the result of  $\Delta\epsilon_{\pi^0}$  obtained with the default selection criteria is taken as systematic uncertainty from the considered selection criteria. The applied variations and

the determined uncertainties are listed in Table 6.6. In addition, the systematic uncertainties coming from the binning of the fitted histograms, the background shape and the relative scaling of the three MC contributions are considered. The corresponding uncertainties are also shown in Table 6.6.

**Table 6.6.:** Systematic uncertainties for  $\pi^0$  efficiency study in  $\omega\pi_{tag}^0$ .

| Source                         | Variation Range            | Error [%] |
|--------------------------------|----------------------------|-----------|
| Selection $\chi_{2C}^2$ cut    | $11 < \chi_{2C}^2 < 19$    | 0.61      |
| Efficiency $\chi_{6C}^2$ cut   | $20 < \chi_{6C}^2 < 40$    | 0.64      |
| Anti- $\omega$ cut             | $3420 < M^{cut} < 3495$    | 0.20      |
| Fit binning                    | 10 MeV $\rightarrow$ 8 MeV | 0.02      |
| Fit shape                      | 2.order poly.              | 0.03      |
| relative scale<br>of MC contr. | $\pm 10\%$ rescaling       | 0.52      |
| Total                          | -                          | 1.05      |

Since all the systematics can be assumed to be uncorrelated, the total systematic uncertainty is taken as the quadratic sum which is 1.05%.

## 6.3. Combined $\pi^0$ Efficiency

### 6.3.1. Cross Checks and Combination Study

Cross checks are performed in order to judge, whether or not the results from the two channels can be combined.

#### Overlap Region

The relative difference between the two methods is compared for MC and data,  $\varepsilon(MC1)/\varepsilon(MC2) - 1$  and  $\varepsilon(data1)/\varepsilon(data2) - 1$ , where  $\varepsilon(MC1)$ ,  $\varepsilon(data1)$  denote the efficiencies in MC and data for the  $e^+e^- \rightarrow \omega\pi^0$  channel and  $\varepsilon(MC2)$ ,  $\varepsilon(data2)$  describe the corresponding for the  $e^+e^- \rightarrow J/\psi\pi^0\pi^0$  channel. The comparison can only be performed in the overlap region  $200 \text{ MeV} < p_{\pi^0} < 400 \text{ MeV}$ . The  $e^+e^- \rightarrow \omega\pi^0$  channel provides only one interval in the overlap region. Taking the mean of the intervals in that region for the  $e^+e^- \rightarrow J/\psi\pi^0\pi^0$  channel,

$$\begin{aligned}\varepsilon(MC1)/\varepsilon(MC2) - 1 &= (-38.0 \pm 1.2) \% , \\ \varepsilon(data1)/\varepsilon(data2) - 1 &= (-39.0 \pm 3.6) \%\end{aligned}$$

is obtained. Their difference of 1.0% is covered within the statistic and systematic uncertainties in that region. The relative difference between data and MC of the  $\pi^0$

reconstruction efficiency is found to be in good agreement for the  $e^+e^- \rightarrow J/\psi\pi^0\pi^0$  and the  $e^+e^- \rightarrow \omega\pi^0$  method in the overlap region.

### Comparison of the $\pi^0$ Photon Polar Angle Distributions

The results of the relative efficiency differences can be combined safely, if the shape of the photon polar angle distributions are sufficiently similar. These distributions are shown in Fig. 6.21 and Fig. 6.22 for the  $e^+e^- \rightarrow J/\psi\pi^0\pi^0$  or the  $e^+e^- \rightarrow \omega\pi^0$  methods, respectively. A sufficient agreement between the methods is observed, such that they can be combined safely.

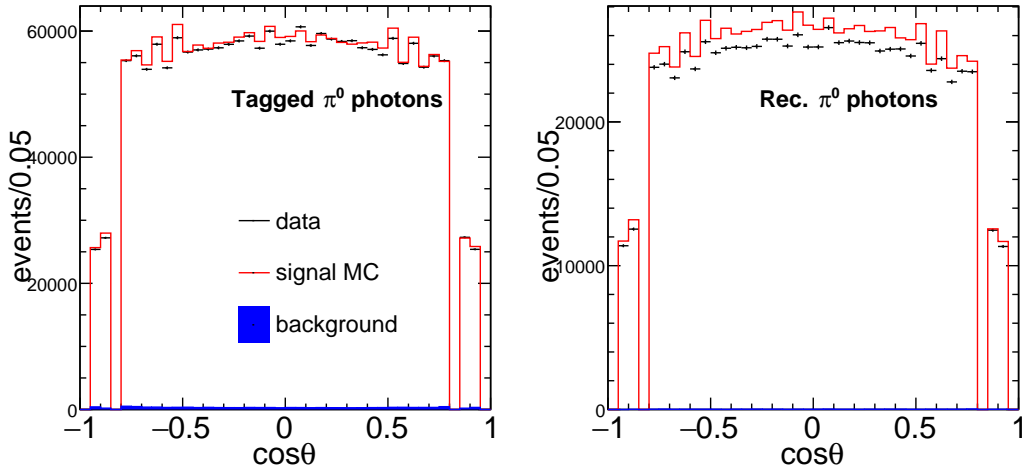


**Figure 6.21.:** Photon polar angle distributions of the tagged and the reconstructed  $\pi^0$  for the  $e^+e^- \rightarrow J/\psi\pi^0\pi^0$  method.

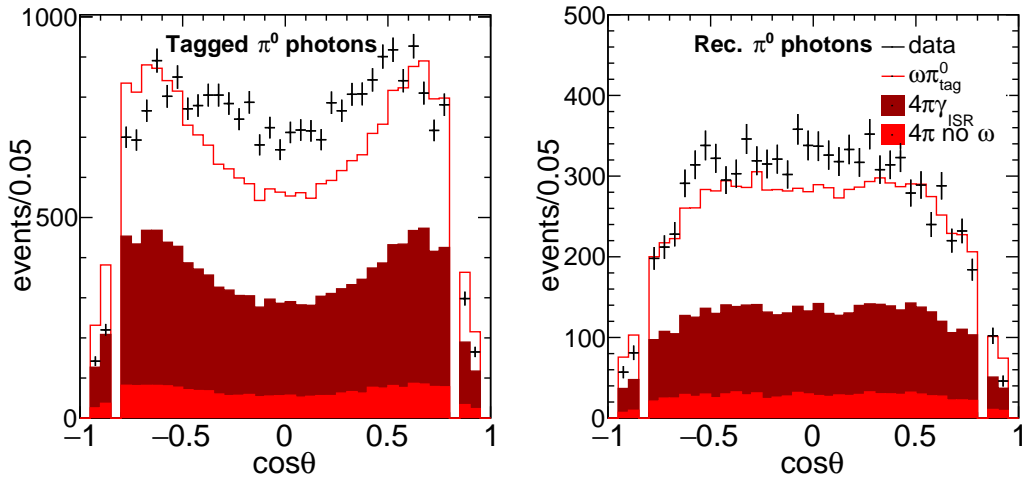


**Figure 6.22.:** Photon polar angle distributions of the tagged and the reconstructed  $\pi^0$  for the  $e^+e^- \rightarrow \omega\pi^0$  method.

The shoulder at  $|\cos\theta| \lesssim 0.8$  in the distribution of the reconstructed photons

is due to the requirement on  $M(\pi^+\pi^-\pi_{tag}^0)$ . The shape of the photon polar angle distribution of the reconstructed  $\pi^0$  in the  $e^+e^- \rightarrow \omega\pi^0$  method matches with all photon polar angle distributions of the  $e^+e^- \rightarrow J/\psi\pi^0\pi^0$  method. In addition, the  $\pi^0$  reconstruction efficiencies of both methods as a function of the polar angle, shown in Fig. 6.7 and Fig. 6.20, are flat within the errors. The findings further support that the results of the two channels can be safely combined.

### Effects of Intermediate Structures

The effects on the efficiency of different masses and quantum numbers of intermediate resonances denoted with  $X$  are tested in this section. For this test, MC simulations of the process  $e^+e^- \rightarrow X\pi^0\pi^0$  are performed. Four different cases of masses and quantum numbers of the intermediate resonance  $X$  are considered, as shown in Table 6.7.

**Table 6.7.:** Choices for different configurations of the intermediate resonance.

| Mode        | Mass [GeV]   | $J^{PC}$ |
|-------------|--------------|----------|
| 1 (default) | $M_{J/\psi}$ | $1^{--}$ |
| 1           | 1            | $1^{--}$ |
| 2           | 2            | $1^{--}$ |
| 3           | $M_{J/\psi}$ | $1^{+-}$ |

The efficiency is determined for the four configurations in the Dalitz plots of the resonance  $X$  and the two  $\pi^0$  as shown in Fig. 6.23.  $M(X\pi^0)$  is shown on the x-axis and  $M(\pi_{tag}^0\pi_{pred}^0)$  on the y-axis. The efficiency is calculated according to Eq. 6.1.1. hence, there are both, tagged and predicted  $\pi^0$  used to calculate  $M(J/\psi\pi^0)$  on the x-axis. The four Dalitz plots only differ in their phase space volume according to the mass of  $X$ . The efficiencies obtained with different masses and quantum numbers of the resonance are divided by the default efficiency of  $J/\psi\pi^0\pi^0$ . The resulting scatter plots are shown in Fig. 6.24. Except border effects, these plots show that the efficiency ratios are flat. Moreover, the total efficiencies for the four cases of the intermediate resonance  $X$  are calculated. The values for the total efficiencies obtained by integrating over the Dalitz plots are shown in Table 6.8. The different sizes of the phase-spaces are taken into account by dividing the total efficiencies by the size of the respective phase-space. The total efficiencies obtained for the four different cases of the intermediate resonance  $X$  agree well with each other within the errors. Fig. 6.24 and Table 6.8 prove, that the dependence of the efficiency on the mass of the resonance  $X$  is negligible. Therefore, the two methods can be combined safely.

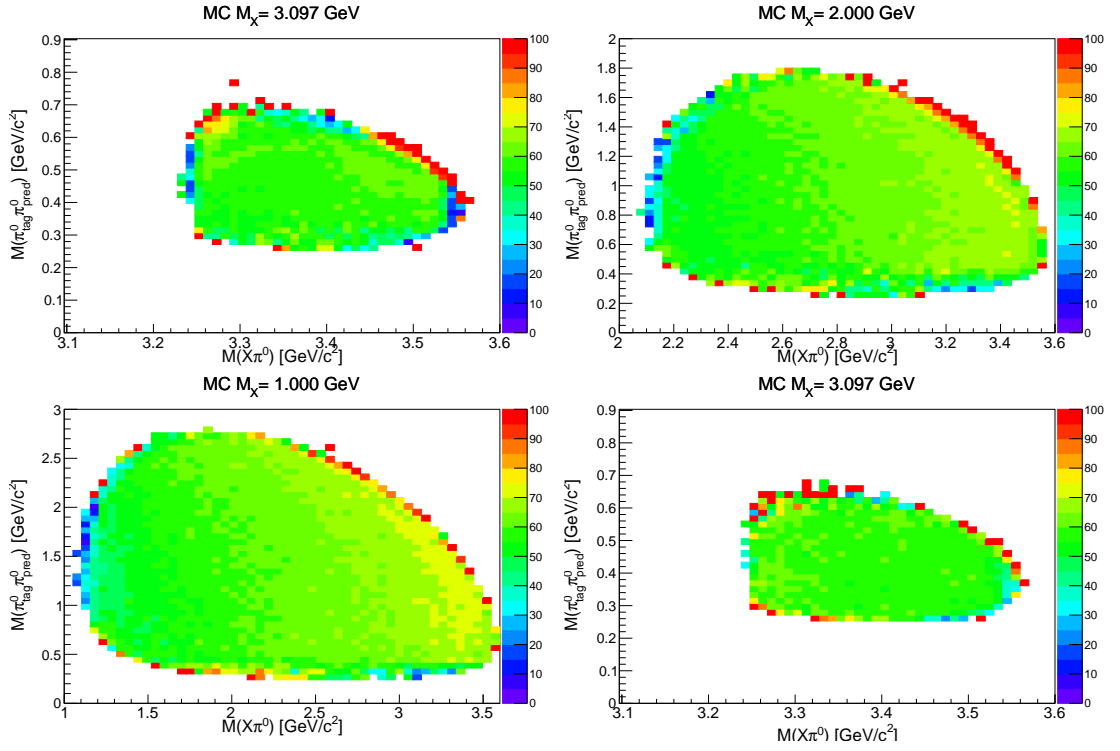


**Figure 6.23.:** Efficiency in the Dalitz plot of MC. The bottom right panel shows  $J^{PC} = 1^{+-}$ , all other are  $J^{PC} = 1^{--}$ .

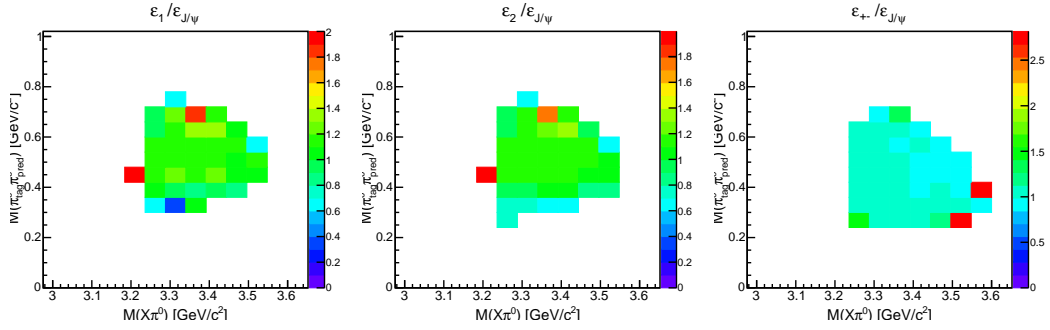


**Figure 6.24.:** Efficiencies of the modified MC divided by the standard MC.

**Table 6.8.:** Total efficiencies in MC for different configurations of the intermediate resonance in the final state.

| Mode                                   | $\varepsilon_{total} [\%]$ |
|--|----------------------------|
| default ( $J/\psi$ )                   | $60.2 \pm 0.52$            |
| $M_X = 1 \text{ GeV}, J^{PC} = 1^{--}$ | $60.6 \pm 0.51$            |
| $M_X = 2 \text{ GeV}, J^{PC} = 1^{--}$ | $60.6 \pm 0.51$            |
| $M_X = 3 \text{ GeV}, J^{PC} = 1^{+-}$ | $61.1 \pm 0.53$            |

### 6.3.2. Combining the Results and Combined Fit

In order to give a single result for the entire momentum region, the results of the  $\pi^0$  reconstruction efficiency of the two methods  $e^+e^- \rightarrow \psi(3686) \rightarrow J/\psi\pi^0\pi^0$  and  $e^+e^- \rightarrow \omega\pi^0$  are combined. In the overlap region, the error weighted mean of both methods is calculated. The combined result is shown in Fig. 6.25. For the final result, a fit with a linear function is performed to the combined relative difference between data and MC of the  $\pi^0$  reconstruction efficiency  $\Delta\varepsilon_{\pi^0}(p)$ . The fit yields

$$\Delta\varepsilon_{\pi^0}(p) = a \cdot p + b, \quad (6.3.1)$$

$$a = (-2.41 \pm 0.87) \cdot \text{GeV}^{-1}\%, \quad (6.3.1)$$

$$b = (0.06 \pm 0.24)\%, \quad (6.3.2)$$

$$w = 0.94, \quad (6.3.3)$$

$$\chi^2/\text{ndf} = 0.50,$$

where  $w$  is the correlation coefficient of the parameters  $a$  and  $b$  obtained by the fit. The small value of the  $\chi^2/\text{ndf}$  indicates that the errors are overestimated. Hence, the statistical error of the  $\pi^0$  reconstruction efficiency is conservative.

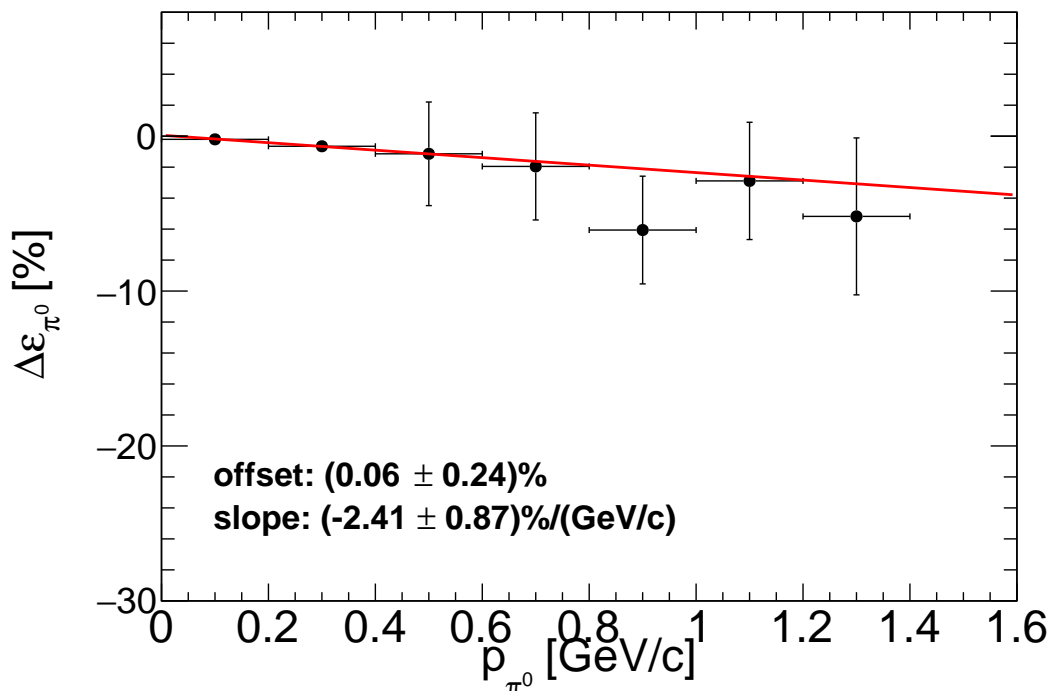


**Figure 6.25.:** Combined relative difference between data and MC of the  $\pi^0$  reconstruction efficiency.

The relative difference between data and MC is described by the function

$$\begin{aligned}\Delta\varepsilon_{\pi^0}(p) &= \frac{\varepsilon_{data}}{\varepsilon_{MC}} - 1 \\ &= (0.06 - 2.41 \text{ GeV}^{-1} c \cdot p) \%, \end{aligned} \tag{6.3.4}$$

where  $\varepsilon_{MC}$  and  $\varepsilon_{data}$  are the absolute  $\pi^0$  reconstruction efficiencies as defined above for simulation and data, respectively. The negative sign indicates that the MC simulations overestimate the  $\pi^0$  reconstruction efficiency with respect to data.

## Chapter 7.

# Determination of the Cross Sections

---

*The respective event yields in the invariant mass spectra of the pion systems of the processes  $e^+e^- \rightarrow \pi^+\pi^-2\pi^0\gamma_{ISR}$  and  $e^+e^- \rightarrow \pi^+\pi^-3\pi^0\gamma_{ISR}$  are used to determine the cross section of  $e^+e^- \rightarrow \pi^+\pi^-2\pi^0$  and its sub-process  $e^+e^- \rightarrow \omega\pi^0$ . Moreover, the cross sections of  $e^+e^- \rightarrow \pi^+\pi^-3\pi^0$  and its sub-processes  $e^+e^- \rightarrow \pi^+\pi^-3\pi^0$  excluding the  $\eta$  resonance,  $e^+e^- \rightarrow \eta\pi^+\pi^-$  and  $e^+e^- \rightarrow \omega2\pi^0$  are calculated. Differential cross sections are determined from the background subtracted invariant mass spectra, correcting for efficiencies as well as vacuum polarization and final state radiation effects. In case of the final states  $\pi^+\pi^-2\pi^0\gamma_{ISR}$  and  $\omega\pi^0\gamma_{ISR}$ , the cross section is determined for the tagged and untagged ISR methods separately. The error weighted mean of the two methods is calculated for each  $M(\pi^+\pi^-2\pi^0)$  interval in the next step as the final result of these cross sections. In addition, the results are discussed and compared with previous experimental measurements of the corresponding cross sections.*

---

## 7.1. Determination of the $e^+e^- \rightarrow \pi^+\pi^-2\pi^0$ Cross Section

The non-radiative cross section of  $e^+e^- \rightarrow \pi^+\pi^-2\pi^0$  is calculated from the selected  $e^+e^- \rightarrow \pi^+\pi^-2\pi^0\gamma_{ISR}$  events after subtracting the background contributions evaluated in chapter 5 and presented with their corrected MC distributions in Fig. 5.16. The background subtracted invariant mass spectra are presented in Fig. 7.1. In

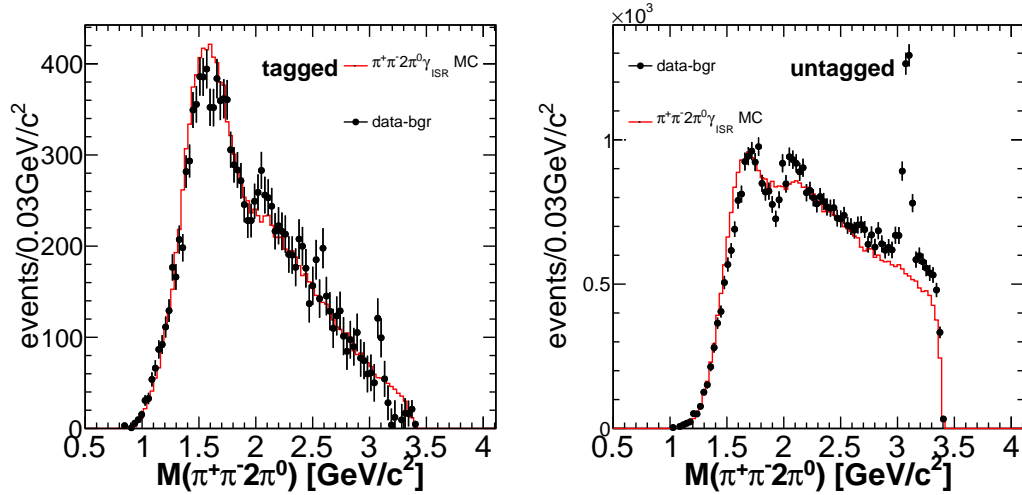


**Figure 7.1.:**  $\pi^+\pi^-2\pi^0$  mass spectrum after subtraction of all corrected background contributions but before efficiency correction.

order to obtain the final  $e^+e^- \rightarrow \pi^+\pi^-2\pi^0\gamma_{ISR}$  cross section from the spectra of Fig. 5.16, several corrections need to be considered and calculated. These are introduced in the following sections.

### 7.1.1. Reconstruction Efficiency of $e^+e^- \rightarrow \pi^+\pi^-2\pi^0\gamma_{ISR}$

The the  $M(\pi^+\pi^-2\pi^0)$  dependent reconstruction efficiency  $\varepsilon(M(\pi^+\pi^-2\pi^0))$  is extracted from MC simulations. It is defined as

$$\varepsilon(M(\pi^+\pi^-2\pi^0)) = \frac{N_{rec}(M(\pi^+\pi^-2\pi^0))}{N_{gen}(M(\pi^+\pi^-2\pi^0))}. \quad (7.1.1)$$

Here,  $N_{gen}(M(\pi^+\pi^-2\pi^0))$  is the number of generated events as a function of  $M(\pi^+\pi^-2\pi^0)$ ,  $N_{rec}(M(\pi^+\pi^-2\pi^0))$  is the respective number of events after the full event selection described in chapter 4. The event generator PHOKHARA 9.1 [85] is used to produce the signal MC simulations. Figure 7.2 reveals a strong dependence of the reconstruction efficiency on  $M(\pi^+\pi^-2\pi^0)$  due to detector acceptance,

kinematics of the four pion channel, and the event selection. Starting from values in the order of a few permille at and close to threshold, the reconstruction efficiency rises to its maximum values at masses between 2.5 GeV and 3 GeV, before it drops again towards the highest achievable  $M(\pi^+\pi^-2\pi^0)$ . This is due to energy resolution effects from the requirement on the minimum energy of the ISR photon. In the tagged mode, the additional selection criterion on the minimum angle  $\cos\alpha$  between the ISR photon and the neutral pions causes a further, significant reduction of the reconstruction efficiency above  $M(\pi^+\pi^-2\pi^0) > 2.6$  GeV.

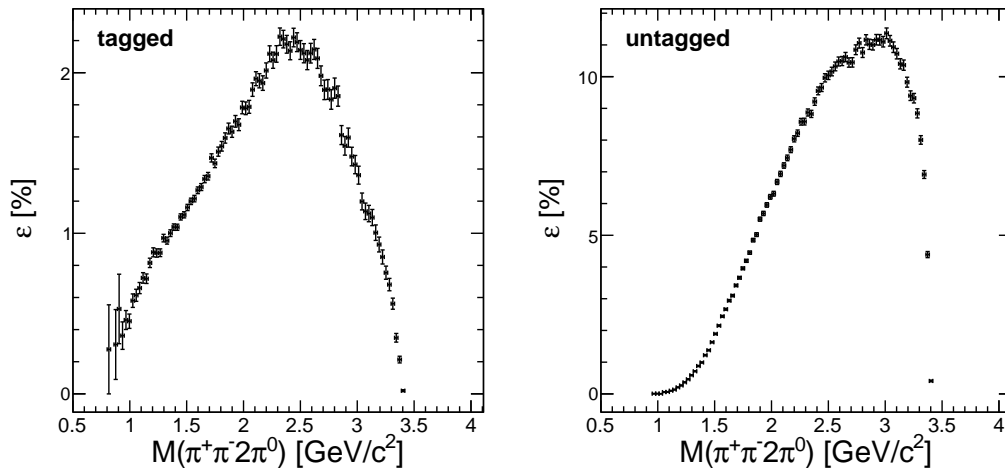


**Figure 7.2.:** Signal reconstruction efficiency of the  $\pi^+\pi^-\pi^0\pi^0\gamma_{ISR}$  final state.

The shape of the reconstruction efficiency can be explained with the special kinematic properties of the ISR events. As explained in section 3.1, the pions in the final state are emitted in a cone, which is oriented back-to-back with the ISR photon. The opening angle of the cone is small, if the boost of the final state system is large. This is the case if the ISR photon energy is high. Events with a high energetic ISR photon have a small  $M(\pi^+\pi^-2\pi^0)$  due to the relation  $E_{ISR} = \frac{E_{CM}^2 - M(\pi^+\pi^-2\pi^0)^2}{2E_{CM}}$ . This special kinematic is depicted in Fig. 7.3, which was shown before as Fig. 3.4. Because of extensive use in this section, it is repeated for the convenience of the reader. In the untagged ISR method, the ISR photon is lost in the beam pipe. The final state pions are boosted in a cone, which is directed in the opposite hemisphere of the detector. If the mass of the pion system  $M(\pi^+\pi^-2\pi^0)$  is small, then the cone is small and the probability to lose a pion in the beam pipe in the opposite direction to the ISR photon becomes large. For large masses of the  $M(\pi^+\pi^-2\pi^0)$  system, the energy of the ISR photon is small and the four pions span a large cone. Thus, the probability to lose at least one of the four pions in the beam pipe in the opposite direction to the ISR photon is much smaller compared to the case of a high energetic ISR photon. Consequently,

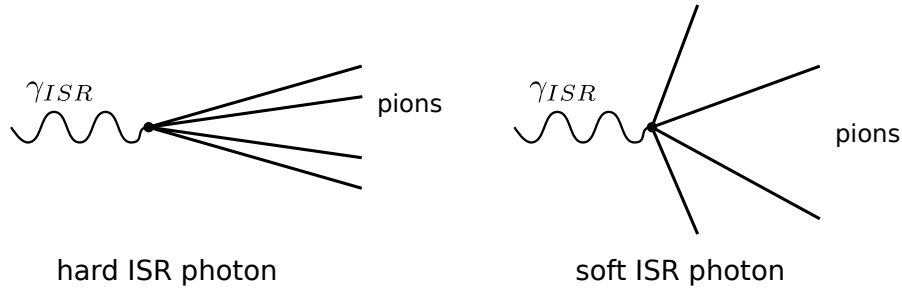


**Figure 7.3.:** Kinematic of ISR events with soft and hard ISR photons.

a high reconstruction efficiency is expected for large values  $M(\pi^+\pi^-2\pi^0)$  and the efficiency shows a fast drop towards smaller values of  $M(4\pi)$ . The described behavior can be observed in the left panel in Fig. 7.2. Additionally, the efficiency decreases at the upper border at  $M(\pi^+\pi^-2\pi^0) \gtrsim 3.2 \text{ GeV}$ .

In the tagged analysis, the low  $M(\pi^+\pi^-2\pi^0)$  events hit the barrel in a small cone. A large reconstruction efficiency is expected. However, it is smaller than for high  $M(\pi^+\pi^-2\pi^0)$ , because the decay of the neutral pions compensates for the focusing effect of the small cone. The opening angles of the photons from the decay of low momentum  $\pi^0$  are rather large, even close to the back-to-back configuration they have in the rest frame of the neutral pion. Thus, these photons escape the narrow cone given by the boost of the ISR photon. Unlike the photons from the decay of high momentum pions, which, in the laboratory frame, are boosted into a narrow cone around the direction of the  $\pi^0$  momentum, the photons from the decay of low momenta pions have a higher probability to escape detection in the beam pipe or the gap between barrel and endcap. However, this effect does not compensate for the focusing effect completely, thus, the efficiency of low  $M(\pi^+\pi^-2\pi^0)$  events is larger and drops slower compared to the untagged mode.

### 7.1.2. Efficiency Correction for $\pi^0$ Reconstruction

Differences between data and simulations were found in reconstruction efficiencies of neutral pions, in chapter 6. In order to correct for these differences, each reconstructed event in the simulation is weighted by a factor  $w_2$  depending on the momenta of the two neutral pions  $P_{\pi_{1,2}^0}$  according to

$$w_2(P_{\pi_1^0}, P_{\pi_2^0}) = \left(1 + \Delta\varepsilon_{\pi^0}(P_{\pi_1^0})\right) \left(1 + \Delta\varepsilon_{\pi^0}(P_{\pi_2^0})\right), \quad (7.1.2)$$

where  $\Delta\varepsilon_{\pi^0}$  is the relative difference between data and MC of the  $\pi^0$  reconstruction efficiency from Eq. 6.3.4. Weighting the events in the simulation can be interpreted as a multiplicative correction to the signal reconstruction efficiency of the process

$e^+e^- \rightarrow \pi^+\pi^-2\pi^0\gamma_{ISR}$  defined in Eq. 7.1.1. Hence, the corrected efficiency reads

$$\varepsilon(m)_{\text{cor}} = \varepsilon(m)w_2(P_{\pi_1^0}, P_{\pi_2^0}) = \frac{N_{\text{rec}}(m)}{N_{\text{gen}}(m)}w_2(P_{\pi_1^0}, P_{\pi_2^0}), \quad (7.1.3)$$

with  $m \equiv M(\pi^+\pi^-2\pi^0)$ . Figure 7.4 shows the  $e^+e^- \rightarrow \pi^+\pi^-2\pi^0\gamma_{ISR}$  signal reconstruction efficiency  $\varepsilon$  with and without the  $\pi^0$  efficiency correction. A significant difference is found especially for masses between 2 GeV and 3.2 GeV, demonstrating the importance of the applied corrections for the correctness of the cross section measurement.

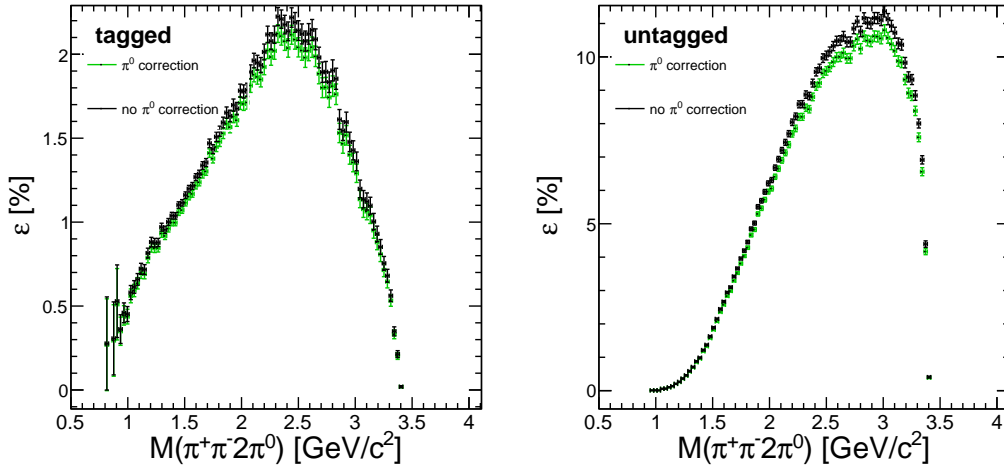


**Figure 7.4.:** Comparison between the  $\pi^0$  efficiency corrected and the uncorrected  $M(\pi^+\pi^-2\pi^0)$  mass spectrum.

### 7.1.3. Final State Radiation Correction

Similar to initial state leptons also the final state particles can radiate photons. The process is referred to as Final State Radiation (FSR). Due to their vanishing electric charge, the neutral pions cannot emit a photon in leading order. However, due to the charge of their constituent quarks, the radiation of an even number of photons is allowed. The emission of two FSR photons is highly suppressed  $\mathcal{O}(\alpha_{QED}^2)$  compared to the emission of a single FSR photon  $\mathcal{O}(\alpha_{QED})$ . Hence, FSR from the neutral pions is negligible and FSR is only considered from the two charged pions. The leading-order (LO) FSR processes  $e^+e^- \rightarrow \pi^+\pi^-2\pi^0\gamma_{FSR}$  and  $e^+e^- \rightarrow \pi^+\pi^-3\pi^0\gamma_{FSR}$  are negligible, since the corresponding production cross sections are small at the c.m. energy of 3.773 GeV. However, the cross sections of the mixed ISR+FSR process  $e^+e^- \rightarrow \pi^+\pi^-2\pi^0\gamma_{ISR}\gamma_{FSR}$ , depicted in Fig. 7.5, is in the order of a few percent compared to the pure ISR signal process  $e^+e^- \rightarrow \pi^+\pi^-2\pi^0\gamma_{ISR}$ .

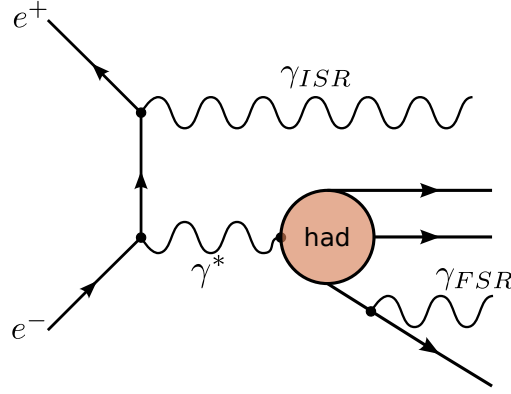


**Figure 7.5.:** Simultaneous ISR+FSR process.

The FSR photons are not considered in the event reconstruction procedure, since they cannot be distinguished from ISR photons. The cross section of the process  $e^+e^- \rightarrow \pi^+\pi^-2\pi^0$  at a c.m. energy of 3.773 GeV is well below 0.1 nb. Events of the type  $e^+e^- \rightarrow \pi^+\pi^-2\pi^0\gamma_{FSR}$  is further suppressed by an additional factor of  $\alpha_{QED}$ . Hence, the LO FSR process, where the FSR photon is misidentified as an ISR photon is negligible. The invariant mass of the final state pions appears lower, if an FSR photon was emitted in addition to the ISR photon. Hence, the ISR+FSR effect causes a shift in the mass spectra towards lower values of  $M(\pi^+\pi^-2\pi^0)$ . The mass spectra, Fig. 7.1 have to be corrected for this shift. To this end, two MC simulations of the signal process are generated, on the one hand including ISR+FSR effects, on the other hand including only next-to-leading order ISR, so two ISR photons. The correction is determined from the ratio of cross sections of these simulations via

$$\delta_{\text{ISR+FSR}} = \frac{\sigma(\text{ISR+FSR})}{\sigma(\text{NLO ISR})}. \quad (7.1.4)$$

The relevant cross sections are determined from MC simulations performed with the PHOKHARA 9.1 [85] event generator. FSR is not implemented for the three and four pion final states in PHOKHARA 9.1. Therefore, the FSR has to be simulated with the PHOTOS [92] package. Interference effects between ISR and FSR photons are neglected. The ISR+FSR correction factor  $\delta_{\text{ISR+FSR}}$  depends on  $M(\pi^+\pi^-2\pi^0)$  and is shown in Fig. 7.6.

After applying the  $\delta_{\text{ISR+FSR}}$  correcting, FSR effects are removed from the cross section. However, for the calculation of  $a_\mu$ , the „bare“ cross section with LO FSR effects  $\sigma(\text{hadrons}(\gamma_{FSR}))$  is needed. Therefore, the FSR effects have to be reintroduced to the „Born“ cross section using the relation introduced in Ref. [97]

$$\frac{\sigma(\text{hadrons}(\gamma_{FSR}))}{\sigma(\text{hadrons})} = 1 + \eta(s) \frac{\alpha}{\pi} = \delta_{FSR}, \quad (7.1.5)$$

where  $\eta(s)$  is the theoretical Schwinger FSR correction factor. The correction as a function of the invariant mass of the pion system is shown in Fig. 7.7, which

describes the FSR correction for a non-radiative processes using scalar QED.

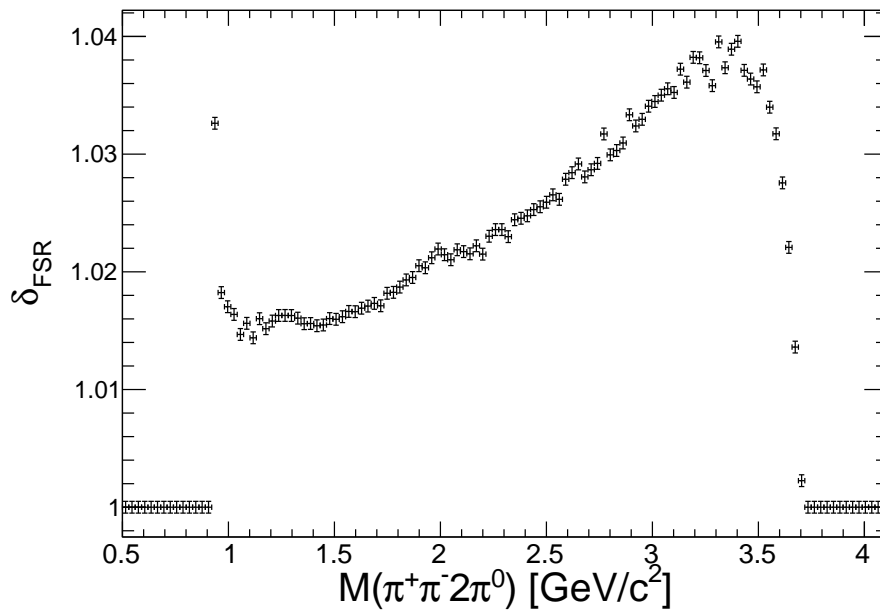


Figure 7.6.: FSR correction for the  $\pi^+\pi^-2\pi^0\gamma_{ISR}$  channel.

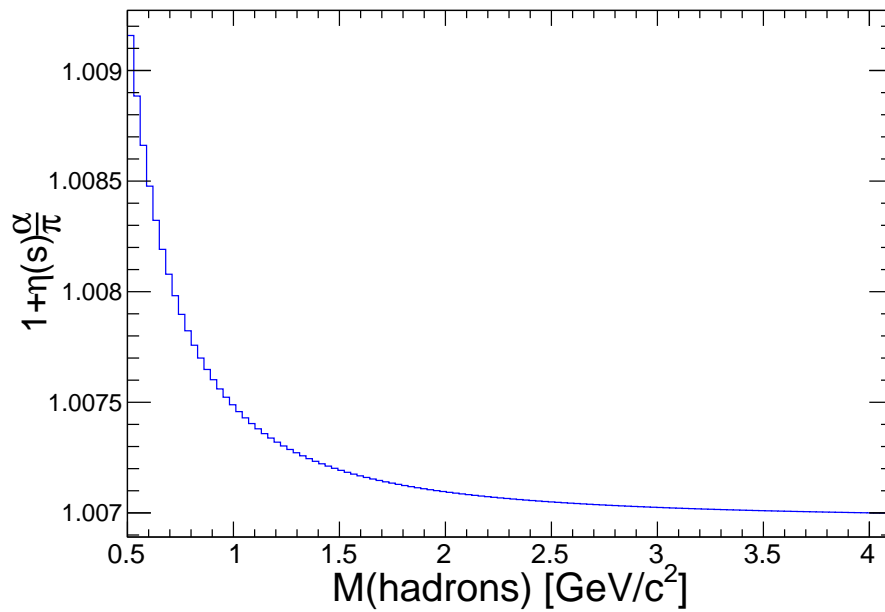


Figure 7.7.: Schwinger FSR correction function  $\eta(s)$

#### 7.1.4. Vacuum Polarization Correction

The measured four pion mass spectrum  $M(\pi^+\pi^-2\pi^0)$  in data includes vacuum polarization (VP) effects. The extracted cross section is, thus, referred to as *dressed*

cross section  $\sigma^{dressed}$ . For the calculation of the anomalous magnetic moment of the muon  $a_\mu$  the *bare* cross section  $\sigma^{bare}$ , which is the Born cross section with FSR corrections of Eq.7.1.5 applied is needed. Therefore the measured Born cross section  $\sigma^{Born}$  has to be adjusted considering the running of the finestructure constant. The bare and the dressed cross sections are connected via the relation

$$\sigma^{Born} \delta_{FSR} = \sigma^{bare} = \sigma^{dressed} \left( \frac{\alpha(0)}{\alpha(s)} \right)^2 = \frac{\sigma^{dressed}}{\delta_{VP}}, \quad (7.1.6)$$

where  $\alpha(0) = 1/137$  is the fine structure constant and

$$\alpha(s) = \frac{\alpha(0)}{1 - \Delta\alpha_{lep}(s) - \Delta\alpha_{had}(s)}$$

is the running fine structure constant. The parameters  $\Delta\alpha_{lep}(s)$  are taken from Ref. [99]. Figure 7.8 shows the inverse VP correction factor  $1/\delta_{VP}$ . Narrow resonances with quantum numbers  $J^{PC} = 1^{--}$ , such as  $\omega(782)$ ,  $\phi(1020)$ ,  $J/\psi$  have a large impact in the energy range relevant for this measurement. The VP correction does not depend on the specific final state to be corrected, but only on the c.m. energy, which, in case of this measurement, corresponds to the invariant mass of the hadronic system.

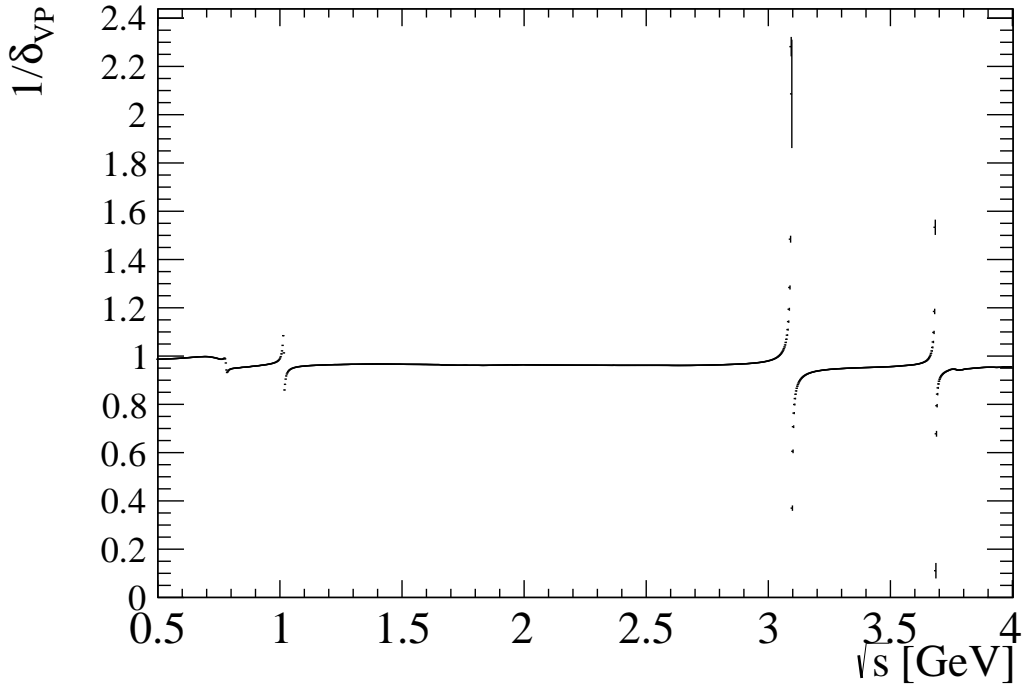


Figure 7.8.: Vacuum polarization correction according to Ref. [99].

### 7.1.5. Calculation of the ISR Cross Section

The relation between a radiative cross section  $\frac{d\sigma}{dm}$  and the corresponding non-radiative Born cross section  $\sigma(m)$  is given by [90, 91]

$$\frac{d\sigma}{dm} = \frac{1}{\epsilon_{\text{cor}}(m)\mathcal{L}\delta_{VP}\delta_{\text{ISR+FSR}}}\frac{dN}{dm} = \frac{2m}{s}W(s,x)\sigma^{\text{Born}}(m), \quad (7.1.7)$$

where  $\mathcal{L}$  is the luminosity of the data set,  $s$  is the c.m. energy,  $m$  is the invariant mass of the hadronic system,  $\epsilon_{\text{cor}}(m)$  is the corrected event reconstruction efficiency shown in Fig. 7.4,  $W(s,x)$  is the radiator function,  $\delta_{VP}$  is the VP correction discussed in section 7.1.4,  $\delta_{\text{ISR+FSR}}$  is the ISR+FSR correction introduced in section 7.1.3 and  $x = 1 - \frac{m^2}{s} = E_{\text{ISR}}/E_{\text{beam}}$ , where  $E_{\text{beam}}$  is the beam energy and  $E_{\text{ISR}}$  is the energy of the ISR photon. Hence, the non-radiative cross section is given by

$$\sigma^{\text{Born}}(m) = \frac{1}{\frac{2m}{s}W(s,x)\epsilon(m)\mathcal{L}\delta_{VP}\delta_{\text{ISR+FSR}}}\frac{dN}{dm}. \quad (7.1.8)$$

The quantity  $\frac{dN}{dm}$  is the background subtracted event yield as a function of invariant mass of the hadronic system. The radiator function  $W(s,x)$  has been discussed in sections 3.1 and 3.2. Figure 7.9 shows the LO and next-to-leading order (NLO) radiator functions, which is extracted from the PHOKHARA 9.1 event generator.

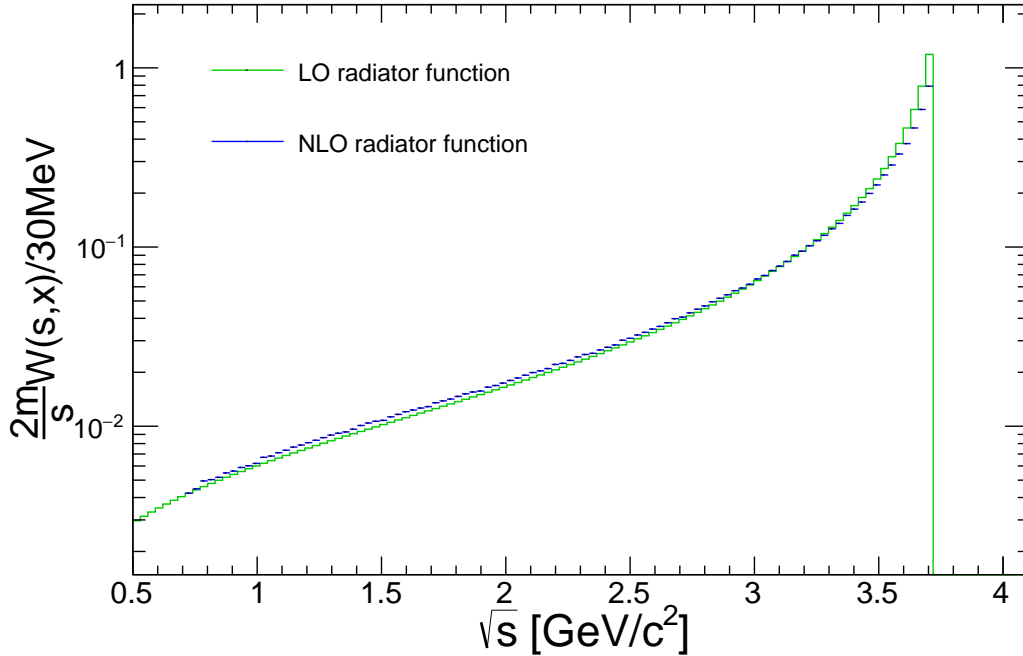


Figure 7.9.: LO and NLO radiator functions from the PHOKHARA 9.1 generator.

Here, the NLO radiator function is applied. The LO radiator function corresponding to Eq. 3.1.5 is shown as a cross check and to see the difference between LO and NLO.

This analysis is based on the data taken on the  $\psi(3770)$  resonance in the years 2010 and 2011, which has an integrated luminosity of  $\mathcal{L} = 2931.8 \text{ pb}^{-1}$  [83, 84].

### 7.1.6. Cross Section of $e^+e^- \rightarrow \pi^+\pi^-2\pi^0$

According to Eq. 7.1.8, the four pion cross section  $\sigma(\pi^+\pi^-2\pi^0)$  is calculated depending on the c.m. energy from the ISR mass spectrum shown in Fig. 7.1. The FSR and VP corrections are applied according to Fig. 7.6 and Fig. 7.8, respectively.

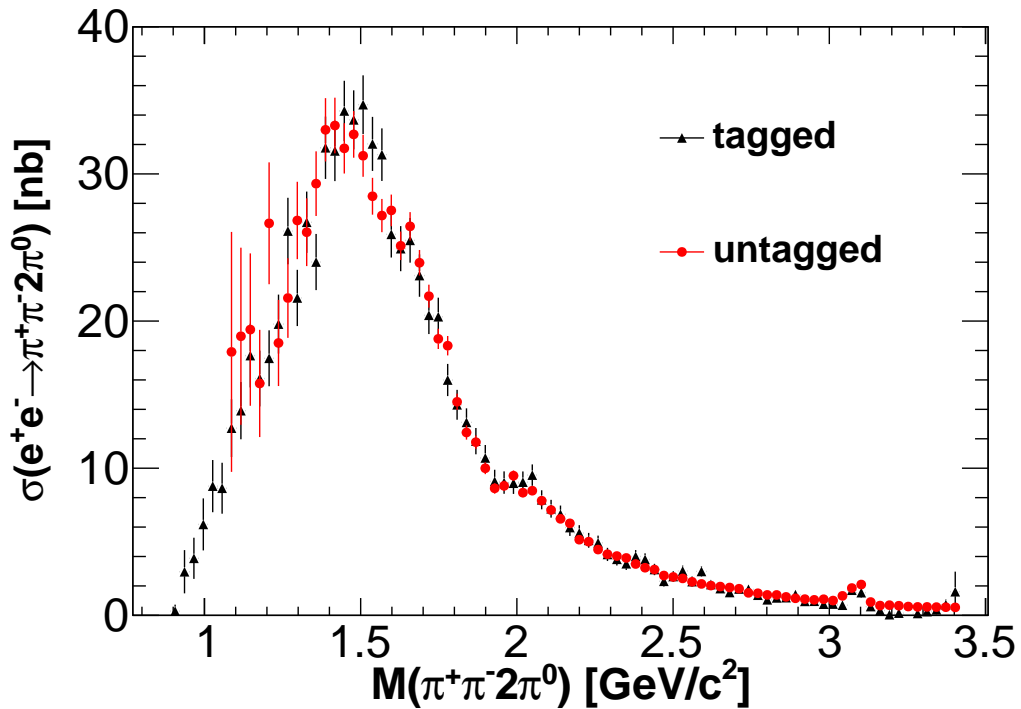


**Figure 7.10.:** Cross section of  $e^+e^- \rightarrow \pi^+\pi^-2\pi^0$  obtained with the tagged and untagged ISR methods. Error bars show statistical errors only. The spectrum is not unfolded, so narrow structures appear smeared with the detector resolution.

The  $e^+e^- \rightarrow \pi^+\pi^-2\pi^0\gamma_{ISR}$  signal reconstruction efficiency, shown in Fig. 7.4 is applied. Figure 7.10 shows the cross sections obtained with the tagged and untagged ISR methods separately. Both resulting cross sections agree well with each other within uncertainties. The untagged method has low statistics at small  $M(\pi^+\pi^-2\pi^0)$ , but large statistics at high masses. The error bars contain statistical errors only. At small  $M(\pi^+\pi^-2\pi^0)$  the tagged method has higher statistics than the untagged one. In contrary, the untagged method is statistically superior to the

tagged one at high  $M(\pi^+\pi^-2\pi^0)$ . Hence, the two methods are complementary in terms of statistics.

For the final result, the error weighted mean of the tagged and untagged methods is calculated. The combined cross section is shown in Fig. 7.11. Error bars show statistical and systematic errors, which are determined in chapter 11. The values of the combined cross section together with its statistical and systematic uncertainties are also listed in Table B.1 of appendix B. The cross section values are not unfolded for detector resolution. Narrow structures, like the  $J/\psi$ , appear smeared with the mass resolution of the detector, not with their natural line width. The mass resolution has been determined in section 4.4 and the width of the  $M(\pi^+\pi^-2\pi^0)$  intervals have been chosen accordingly larger. Except for the  $J/\psi$  resonance, all structures are sufficiently broad to consider the smearing effects negligible. Figure 7.11 shows good agreement within uncertainties between this measurement and previous measurements of the  $e^+e^- \rightarrow \pi^+\pi^-2\pi^0$  cross section [61, 62, 63, 64, 65, 66, 67, 68, 69, 70]. There is a hint at a structure around 2 GeV in data, which does not exist in the PHOKHARA 9.1 signal MC. This structure is also observed by the BaBar measurement [70].

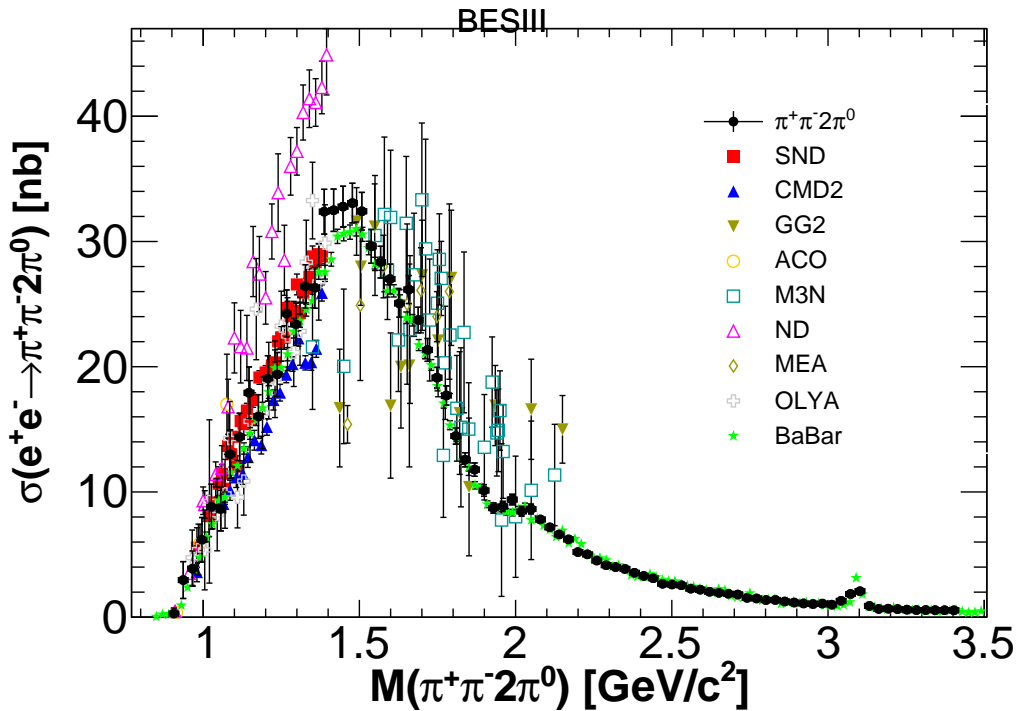


**Figure 7.11.:** Cross section calculated from the error weighted mean of the tagged and untagged modes. Error bars include systematic errors. The spectrum is not unfolded, so narrow structures appear smeared with the detector resolution.

## 7.2. Determination of the $e^+e^- \rightarrow \omega\pi^0$ Cross Section

### 7.2.1. Mass Spectrum of $e^+e^- \rightarrow \omega\pi^0$

In order to obtain the  $e^+e^- \rightarrow \omega\pi^0$  event yield in different intervals of  $M(\omega\pi^0)$ , fits of the  $M(\pi^+\pi^-\pi^0)$  distributions are performed. The  $M(\pi^+\pi^-\pi^0)$  distributions are split into 60 equidistant intervals of  $M(\omega\pi^0)$ . The width of each  $M(\omega\pi^0)$  region is 60 MeV. The fit function consists of a double Gaussian to describe the peak of the  $\omega$ -resonance peak plus a third order polynomial to account for the background contributions. The fits are performed in the region  $710 < M(\pi^+\pi^-\pi^0) < 860$  GeV/ $c^2$ . These fits are shown in Fig. 7.12 and Fig. 7.13 for the tagged and untagged ISR methods, respectively. Empty  $M(\omega\pi^0)$  intervals are not shown. The number of

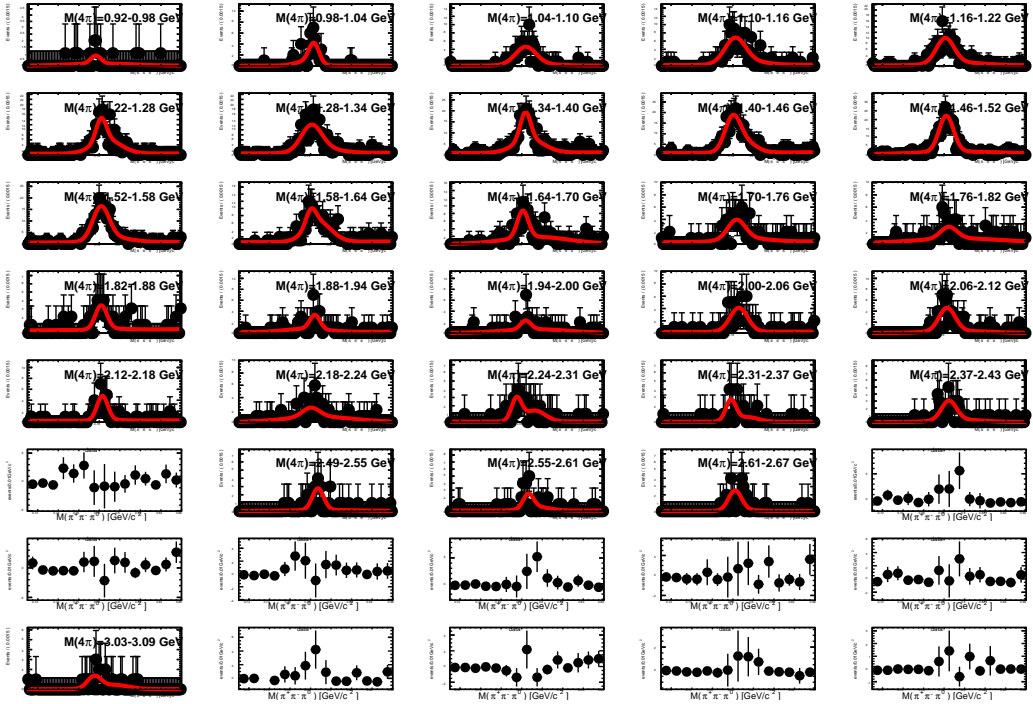


**Figure 7.12.:** Fit of the  $\omega$ -resonance in the  $M(\pi^+\pi^-\pi^0)$  mass spectrum of the  $e^+e^- \rightarrow \pi^+\pi^-2\pi^0\gamma_{ISR}$  tagged ISR method.

the of  $e^+e^- \rightarrow \omega\pi^0$  events per  $M(\omega\pi^0)$  mass interval is obtained by integrating the double Gaussians taken from the fit result in the entire fit region. Resulting event yields for the tagged and untagged ISR methods are shown in Fig. 7.14.

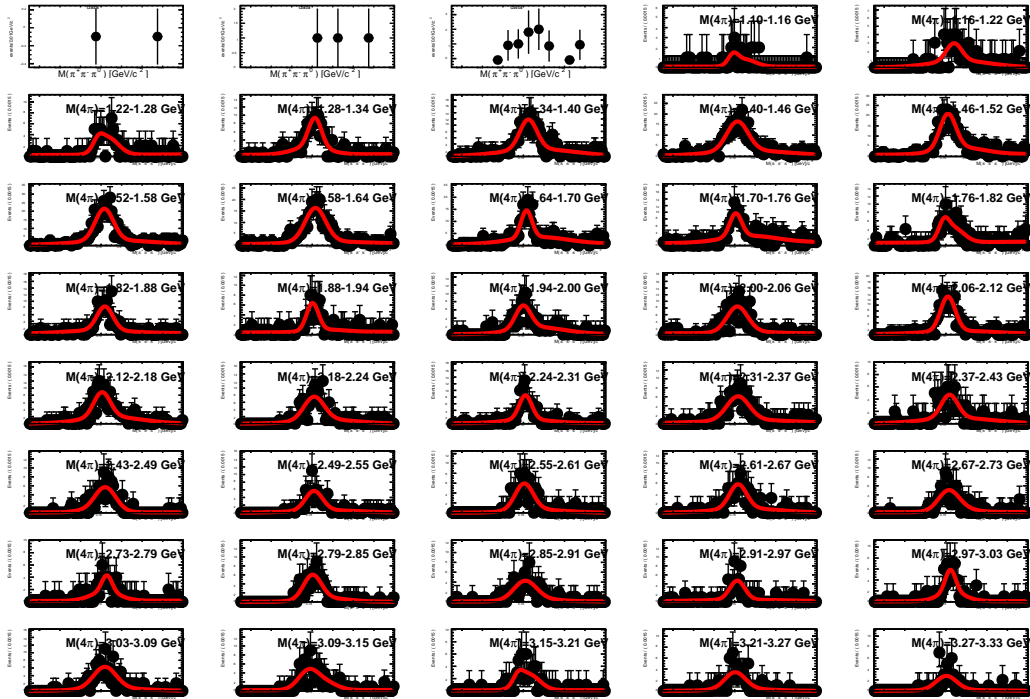


Figure 7.13.: Fit of the  $\omega$ -resonance in the  $M(\pi^+\pi^-\pi^0)$  mass spectrum of the  $e^+e^- \rightarrow \pi^+\pi^-\pi^0\gamma_{ISR}$  untagged ISR method.

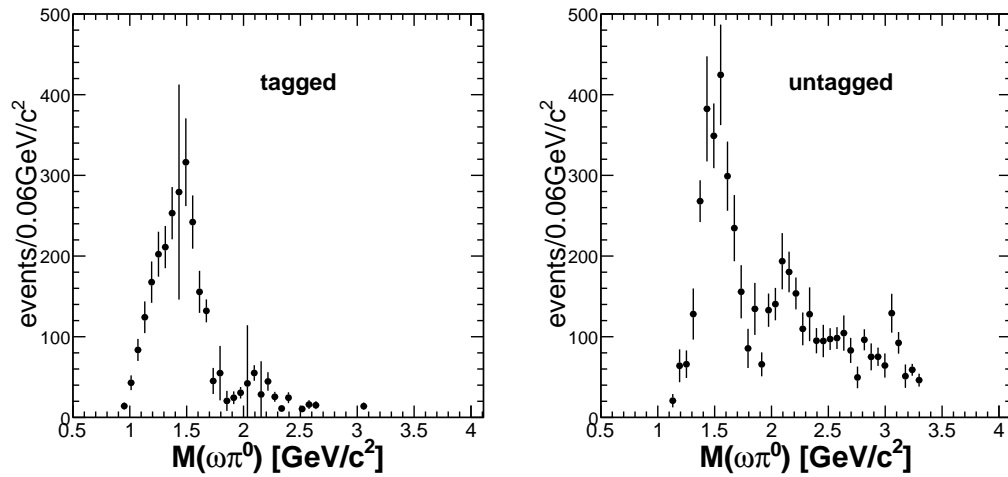


Figure 7.14.:  $e^+e^- \rightarrow \omega\pi^0\gamma_{ISR}$  mass spectrum obtained from the fits to the  $M(\pi^+\pi^-\pi^0)$  distributions before efficiency correction.

### 7.2.2. Cross Section of $e^+e^- \rightarrow \omega\pi^0$

Applying Eq. 7.1.8, the  $e^+e^- \rightarrow \omega\pi^0$  cross section is determined separately for the tagged and untagged mass spectra in Fig. 7.14. The resulting cross sections are shown in Fig. 7.15. The error weighted mean of the tagged and untagged ISR methods is shown in Fig. 7.16 together with previous measurements of this cross section [62, 63, 68, 100, 101, 102, 70].

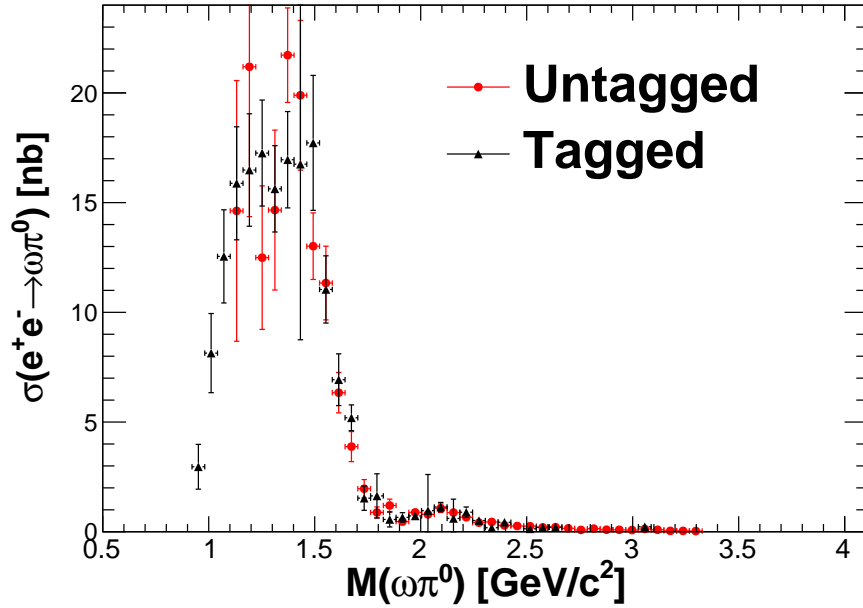


Figure 7.15.: Cross section of  $e^+e^- \rightarrow \omega\pi^0$ .

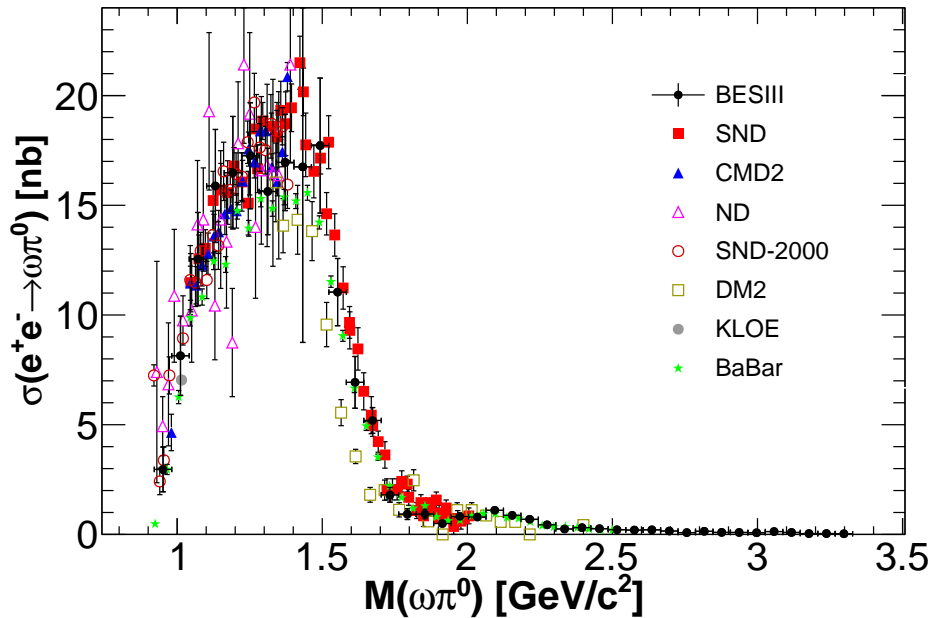


Figure 7.16.: Combined cross section of  $e^+e^- \rightarrow \omega\pi^0$ .

The cross section values of the combined result are listed in Table B.2 of appendix B. The result obtained in this thesis and the previous measurements agree well within uncertainties. There is a hint at a structure around 2 GeV in data, confirmed by the BaBar measurement [70], as also observed in the full  $e^+e^- \rightarrow \pi^+\pi^-2\pi^0$  cross section.

### 7.3. Determination of the $e^+e^- \rightarrow \pi^+\pi^-3\pi^0$ Cross Section via ISR

The mass spectrum of the full  $e^+e^- \rightarrow \pi^+\pi^-3\pi^0\gamma_{ISR}$  process has been shown before in Fig. 5.6 of section 5.2. In this section special attention is paid to the sub-processes  $e^+e^- \rightarrow \omega 2\pi^0\gamma_{ISR}$  and  $e^+e^- \rightarrow \eta\pi^+\pi^-\gamma_{ISR}$ .

#### 7.3.1. Mass Spectra of $e^+e^- \rightarrow \omega 2\pi^0\gamma_{ISR}$ and $e^+e^- \rightarrow \eta\pi^+\pi^-\gamma_{ISR}$

The event selection of the the important sub-processes  $e^+e^- \rightarrow \omega 2\pi^0\gamma_{ISR}$  and  $e^+e^- \rightarrow \eta\pi^+\pi^-\gamma_{ISR}$  of  $e^+e^- \rightarrow \pi^+\pi^-3\pi^0\gamma_{ISR}$  have been described in section 4.3.2 and 4.3.3. Their invariant mass spectra are shown in Fig. 7.17. In order to account for background contributions to the  $e^+e^- \rightarrow \omega 2\pi^0\gamma_{ISR}$  signal, the sideband of the  $\omega$  resonance in the  $M(\pi^+\pi^-\pi^0)$  distribution is subtracted from the mass spectrum. In the  $e^+e^- \rightarrow \eta\pi^+\pi^-\gamma_{ISR}$  spectrum, the nonresonant background contribution is negligible. Similar to the full  $e^+e^- \rightarrow \pi^+\pi^-3\pi^0\gamma_{ISR}$  spectrum, both processes show good agreement between simulation and experiment in the mass region  $M(\pi^+\pi^-3\pi^0) < 3.1 \text{ GeV}/c^2$ . The agreement becomes worse above the  $J/\psi$  resonance region at  $M(\pi^+\pi^-3\pi^0) > 3.1 \text{ GeV}/c^2$ .

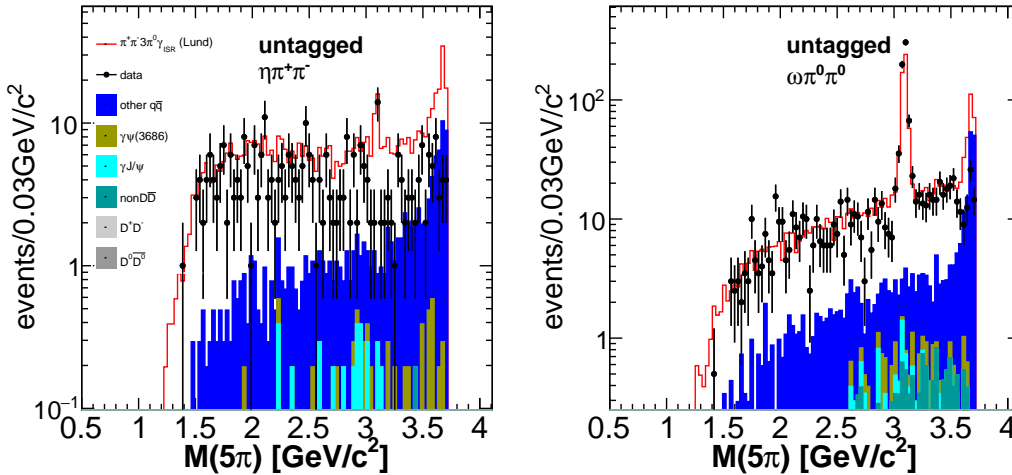


Figure 7.17.: Mass spectra of  $M(\omega 2\pi^0)$  (sideband subtracted) and  $M(\eta\pi^+\pi^-)$ .

### 7.3.2. Reconstruction Efficiency of $e^+e^- \rightarrow \pi^+\pi^-3\pi^0\gamma_{ISR}$

With the MC simulation of the  $M(\pi^+\pi^-3\pi^0)$  mass spectrum, shown in Fig. 5.6, the  $e^+e^- \rightarrow \pi^+\pi^-3\pi^0\gamma_{ISR}$  reconstruction efficiency  $\varepsilon_{rec}$  can be determined. It is defined as  $\varepsilon_{rec}(M(\pi^+\pi^-3\pi^0)) = \frac{N_{rec}(M(\pi^+\pi^-3\pi^0))}{N_{gen}(M(\pi^+\pi^-3\pi^0))} w_3(P_{\pi_1^0}, P_{\pi_2^0}, P_{\pi_3^0})$ , where  $N_{gen}(M(\pi^+\pi^-3\pi^0))$  is the number of generated events as a function of  $M(\pi^+\pi^-3\pi^0)$ ,  $N_{rec}(M(\pi^+\pi^-3\pi^0))$  is the number of events after the event selection and  $w_3(P_{\pi_1^0}, P_{\pi_2^0}, P_{\pi_3^0})$ , contains the  $\pi^0$  efficiency correction. As the  $e^+e^- \rightarrow \pi^+\pi^-3\pi^0\gamma_{ISR}$  reconstruction efficiency depends on three momenta  $P_{\pi_{1,2,3}^0}$  of  $\pi^0$  particles, the weight function  $w_3$  is defined as

$$w_3(P_{\pi_1^0}, P_{\pi_2^0}, P_{\pi_3^0}) = \left(1 + \Delta\varepsilon_{\pi^0}(P_{\pi_1^0})\right) \left(1 + \Delta\varepsilon_{\pi^0}(P_{\pi_2^0})\right) \left(1 + \Delta\varepsilon_{\pi^0}(P_{\pi_3^0})\right). \quad (7.3.1)$$

The reconstruction efficiency is obtained from the Lund- $q\bar{q}$  MC simulation. The distribution of the true  $M(\pi^+\pi^-3\pi^0)$  mass spectrum produced by the MC generator is shown in Fig. 7.18. The peaks of the  $\phi$  and the  $J/\psi$  resonances are artifacts, which have to be attributed to incorrect settings of the generator. The branching fraction for the decay of the  $\phi$  resonance to the  $\pi^+\pi^-3\pi^0$  final state is  $\mathcal{B}(\phi \rightarrow \pi^+\pi^-3\pi^0) \approx \mathcal{O}(10^{-6})$ , consequently, its contribution should be negligibly small. By construction the  $J/\psi$  is not supposed to be included in the Lund- $q\bar{q}$  MC simulation, but in the dedicated  $e^+e^- \rightarrow \gamma_{ISR}J/\psi$  MC sample. However, the number of reconstructed  $e^+e^- \rightarrow \pi^+\pi^-3\pi^0\gamma_{ISR}$  events is zero in the mass region below  $\approx 1.2 \text{ GeV}/c^2$ . Consequently, the appearance of the  $\phi$  resonance in the MC sample does not affect the final result. The  $J/\psi$  events from the Lund- $q\bar{q}$  MC are excluded from the simulation by rejecting the events on the generator level which have an invariant mass of  $|M_{J/\psi} - M(5\pi)_{true}| < 100 \text{ keV}/c^2$ . The excluded region is instead extrapolated from the average of right and left.

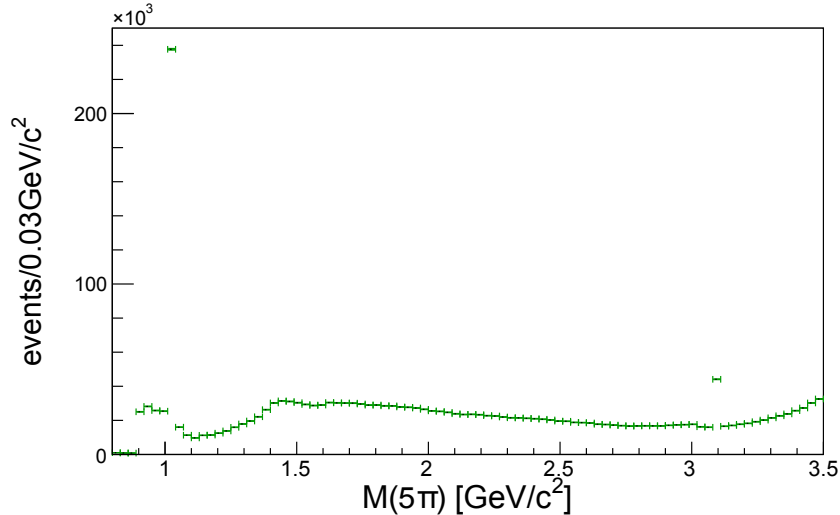
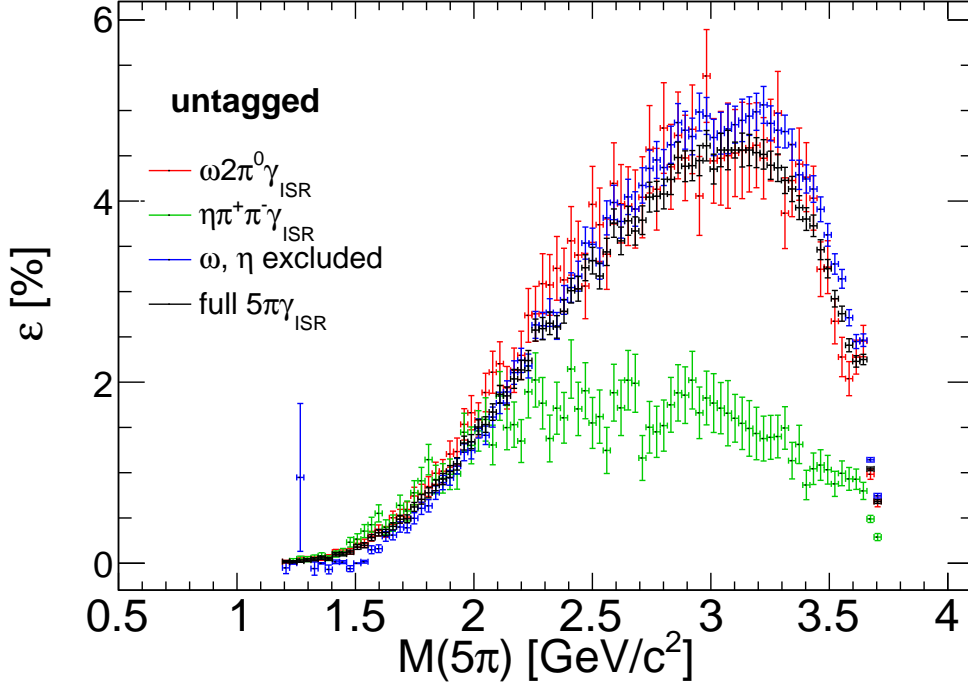


Figure 7.18.: MC true distribution of the  $\pi^+\pi^-3\pi^0$  mass spectrum.

Fig. 7.19 shows the final  $e^+e^- \rightarrow \pi^+\pi^-3\pi^0\gamma_{ISR}$  reconstruction efficiency including the  $J/\psi$  correction and the  $\pi^0$  efficiency correction.



**Figure 7.19.:** Reconstruction efficiencies of the processes  $e^+e^- \rightarrow \pi^+\pi^-3\pi^0\gamma_{ISR}$ ,  $e^+e^- \rightarrow \pi^+\pi^-3\pi^0\gamma_{ISR}$  excluding the  $\eta$  resonance,  $e^+e^- \rightarrow \eta\pi^+\pi^-\gamma_{ISR}$  and  $e^+e^- \rightarrow \omega2\pi^0\gamma_{ISR}$ .

The curves of the reconstruction efficiencies  $e^+e^- \rightarrow \pi^+\pi^-3\pi^0\gamma_{ISR}$  and  $e^+e^- \rightarrow \pi^+\pi^-2\pi^0\gamma_{ISR}$  show a similar shape. The reconstruction efficiencies of the  $e^+e^- \rightarrow \omega2\pi^0\gamma_{ISR}$  and  $e^+e^- \rightarrow \eta\pi^+\pi^-\gamma_{ISR}$  are also shown in Fig. 7.19. The event selection procedures described in section 4.3.2 and 4.3.3 have been applied to the Lund- $q\bar{q}$  MC simulation to obtain these efficiencies.

### 7.3.3. Cross Section of $e^+e^- \rightarrow \pi^+\pi^-3\pi^0$ and Sub-Processes via ISR

According to Eq. 7.1.8, the cross section of the process  $e^+e^- \rightarrow \pi^+\pi^-3\pi^0$  is calculated depending on the c.m. energy. Additionally, the cross sections for the sub-process  $e^+e^- \rightarrow \pi^+\pi^-3\pi^0$  excluding the  $\eta$  resonance,  $e^+e^- \rightarrow \eta\pi^+\pi^-$  and  $e^+e^- \rightarrow \omega2\pi^0$  are calculated.

To derive the FSR corrections required in Eq. 7.1.8 the same procedure is applied, which has been used for the four pion final state in Eq. 7.1.4, based on the Lund- $q\bar{q}$  MC. The FSR correction is shown in Fig. 7.20. The same correction is used for the sub-processes, since the shape of the curves are sufficiently similar.

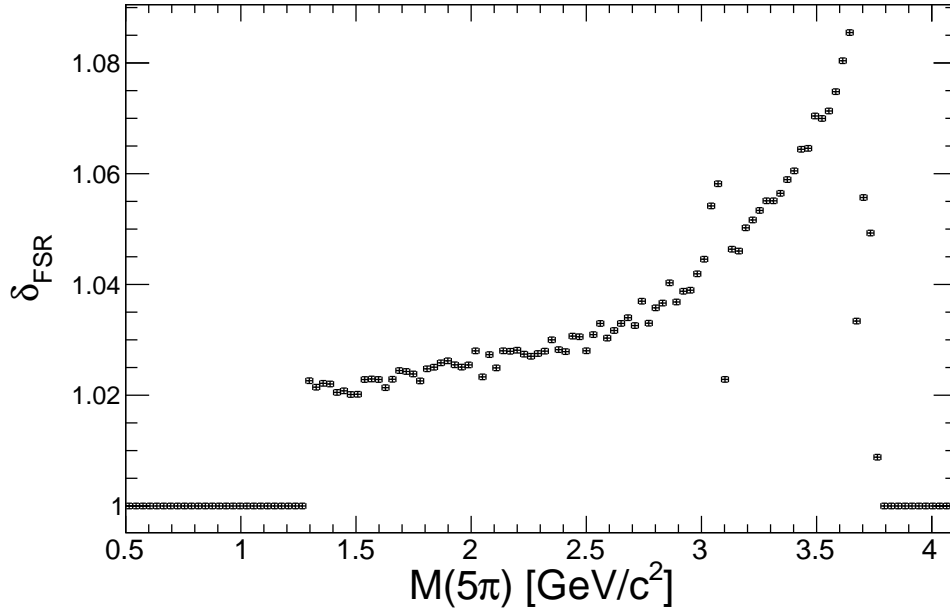


Figure 7.20.: FSR correction for the  $e^+e^- \rightarrow \pi^+\pi^-3\pi^0\gamma_{\text{ISR}}$  processes.

As pointed out in section 7.1.4, the correction for VP effects only depends on the c.m. energy. Thus, the corrections according to Eq. 7.1.6 are applied here. The result for the cross sections are shown in Fig. 7.21.

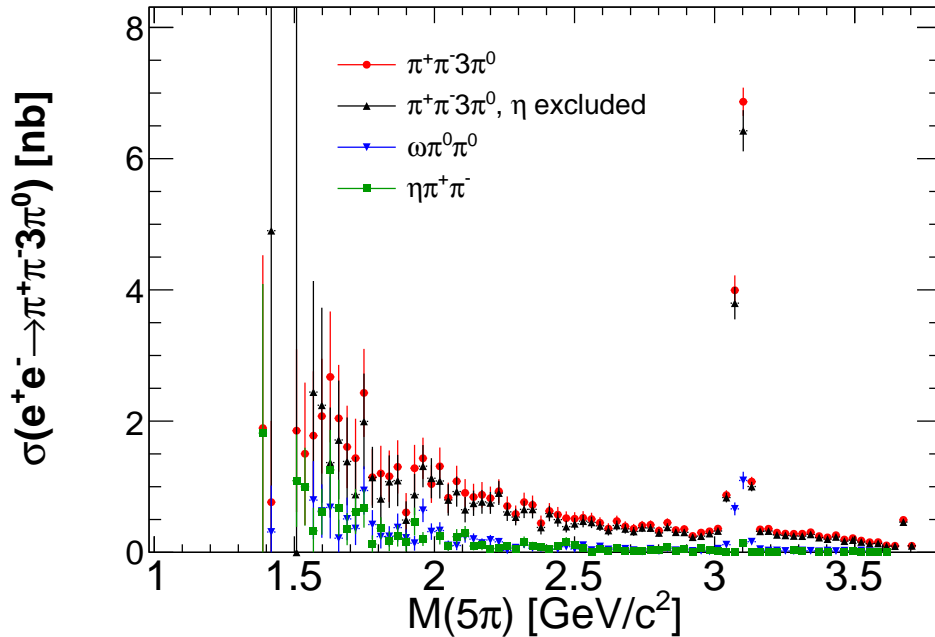


Figure 7.21.: Cross section of  $e^+e^- \rightarrow \pi^+\pi^-3\pi^0$ . The spectrum is not unfolded, so narrow structures appear smeared with the detector resolution. The values of the  $e^+e^- \rightarrow \pi^+\pi^-3\pi^0$  cross section, together with its statistical

and systematic uncertainties are also listed in Table B.3 of appendix B. The cross section values are not unfolded. Narrow structures, like the  $J/\psi$  resonance appear smeared with the detector resolution, not with their natural line width. However, the width of the  $M(\pi^+\pi^-3\pi^0)$  intervals has been chose according to the mass resolution, which has been determined in section 4.4. Hence, the smearing effect is negligible outside the  $J/\psi$  mass region in the  $M(\pi^+\pi^-3\pi^0)$  spectrum, since all other structures are sufficiently broad. No previous result with reasonable uncertainty is available to compare to.

## 7.4. Determination of the $e^+e^- \rightarrow \pi^+\pi^-3\pi^0$ Cross Section without ISR

### 7.4.1. Reconstruction Efficiency of $e^+e^- \rightarrow \pi^+\pi^-3\pi^0$

The reconstruction efficiency of the non-ISR process  $e^+e^- \rightarrow \pi^+\pi^-3\pi^0$  at the c.m. energy of 3.773 GeV is defined as  $\varepsilon_{rec}^{5\pi} = \frac{N_{rec}^{5\pi}}{N_{gen}^{5\pi}} w_3(P_{\pi_1^0}, P_{\pi_2^0}, P_{\pi_3^0})$ .  $w_3(P_{\pi_1^0}, P_{\pi_2^0}, P_{\pi_3^0})$  is the weighting function from Eq. 7.3.1 to account for the data-MC differences of the  $\pi^0$  reconstruction efficiency. The number  $N_{gen}^{5\pi}$  is obtained from the  $e^+e^- \rightarrow \pi^+\pi^-3\pi^0$  MC cocktail via the MC true information from the MC generator. The quantity  $N_{rec}^{5\pi}$  denotes the number of reconstructed events in the signal simulation. The MC cocktail contains the  $e^+e^- \rightarrow \pi^+\pi^-3\pi^0$  contribution simulated with HELPWA [89] as well as phase space simulations of the  $e^+e^- \rightarrow \omega 2\pi^0$  and  $e^+e^- \rightarrow \eta\pi^+\pi^-$  contributions. The HELPWA simulation yields a cross section of 17.97 pb of the  $e^+e^- \rightarrow \pi^+\pi^-3\pi^0$  process excluding  $e^+e^- \rightarrow \omega 2\pi^0$  and  $e^+e^- \rightarrow \eta\pi^+\pi^-$ . The relative contributions of the  $e^+e^- \rightarrow \omega 2\pi^0$  and  $e^+e^- \rightarrow \eta\pi^+\pi^-$  MC contributions to the  $e^+e^- \rightarrow \pi^+\pi^-3\pi^0$  MC cocktail are tuned to match the  $\omega$  or  $\eta$  resonance peaks of the  $e^+e^- \rightarrow \pi^+\pi^-3\pi^0$  final state in data. Their relative contributions are found to be 13.6% for  $e^+e^- \rightarrow \omega 2\pi^0$  and 23.5% for  $e^+e^- \rightarrow \eta\pi^+\pi^-$ , respectively. Finally, an efficiency value of  $\varepsilon_{rec}^{5\pi} = 8.6\%$  is obtained for the full  $e^+e^- \rightarrow \pi^+\pi^-3\pi^0$  process. The efficiencies of the sub-processes are 12.5% for  $e^+e^- \rightarrow \omega 2\pi^0$  or 8.8% for  $e^+e^- \rightarrow \eta\pi^+\pi^-$ , respectively.

### 7.4.2. Cross Section of $e^+e^- \rightarrow \pi^+\pi^-3\pi^0$ at $\sqrt{s} = 3.773$ GeV

The cross section of the processes  $e^+e^- \rightarrow \pi^+\pi^-3\pi^0$  at the c.m. energy of 3.773 GeV without an ISR photon is given by

$$\sigma_{\text{obs}} = \frac{N_{\text{data}} - N_{\text{bgr}}}{\mathcal{L} \varepsilon_{\text{rec}}}, \quad (7.4.1)$$

where  $\mathcal{L}$  is the luminosity of the data set,  $\varepsilon_{rec}$  is the event reconstruction efficiency,  $N_{data}$  is the event yield in data and  $N_{bgr}$  is the number of background events. The signal and background yields  $N_{data}$  and  $N_{bgr}$  are determined from the  $e^+e^- \rightarrow \pi^+\pi^-3\pi^0$  event selection, in data and background MC simulations, respectively. The event selection procedure is described in section 4.3.4. Events of the type  $e^+e^- \rightarrow \pi^+\pi^-3\pi^0\gamma_{ISR}$  can contaminate the event selection, if the energy of the ISR photon is below  $\lesssim 100$  MeV. The ISR events are treated as background contributions in the simulations and are subtracted from data, instead of using an ISR correction factor  $\delta_{ISR}$  to correct for this effect. Since the  $e^+e^- \rightarrow \pi^+\pi^-3\pi^0\gamma_{ISR}$  process is tuned to data according to Fig. 5.7, its simulation is precise enough to subtract this background contribution. The event numbers  $N_{data}$  and  $N_{bgr}$  found after applying the  $e^+e^- \rightarrow \pi^+\pi^-3\pi^0$  event selection to data and MC are shown in Table 7.1. The luminosity of the data set is  $\mathcal{L}_{data} = 2931.8 \text{ pb}^{-1}$  and the efficiency is calculated in the previous section. Applying Eq. 7.4.1, a cross section value of  $\sigma(e^+e^- \rightarrow \pi^+\pi^-3\pi^0)(\sqrt{s} = 3.773 \text{ GeV}) = (28.7 \pm 0.5_{\text{stat}} \pm 2.0_{\text{sys}}) \text{ pb}$  is found. The systematic uncertainties are discussed later in section 11.2.2. The cross sections of the sub-channels  $e^+e^- \rightarrow \omega 2\pi^0$  and  $e^+e^- \rightarrow \eta\pi^+\pi^-$  are calculated analogously. Their efficiencies are determined in the previous section. The branching fractions  $\mathcal{B}(\omega \rightarrow \pi^+\pi^-\pi^0) = (89.2 \pm 0.7) \%$  and  $\mathcal{B}(\eta \rightarrow 3\pi^0) = (32.68 \pm 0.23) \%$  from [31] are used to calculate the total cross sections of the sub-channels. The results are  $\sigma(e^+e^- \rightarrow \omega 2\pi^0)(3.773 \text{ GeV}) = (2.6 \pm 0.1_{\text{stat}} \pm 0.2_{\text{sys}}) \text{ pb}$  and  $\sigma(e^+e^- \rightarrow \eta\pi^+\pi^-)(3.773 \text{ GeV}) = (6.8 \pm 0.3_{\text{stat}} \pm 0.5_{\text{sys}}) \text{ pb}$ , as shown in Table 7.1. The total contributions of  $e^+e^- \rightarrow \omega 2\pi^0\gamma_{ISR}$  and  $e^+e^- \rightarrow \eta\pi^+\pi^-\gamma_{ISR}$  in data are  $(19.6 \pm 0.49) \%$  and  $(2.9 \pm 0.18) \%$ , respectively.

**Table 7.1.:** Numbers for the  $e^+e^- \rightarrow \pi^+\pi^-3\pi^0$  cross section at 3.773 GeV.

| quantity                               | final state                                       |  |  |
|--|---|--|--|
|  | $\pi^+\pi^-3\pi^0$                                | $\omega\pi^0\pi^0$                               | $\eta\pi^+\pi^-$                                 |
| $N_{data}$                             | $11683 \pm 108$                                   | $1042 \pm 32$                                    | $587 \pm 24$                                     |
| $N_{bgr}$                              | $4594 \pm 67$                                     | $184 \pm 32$                                     | $16 \pm 4$                                       |
| $\varepsilon_{rec}^{5\pi}$             | $8.6\%$   | $12.5\%$   | $8.8\%$  |
| $\sigma(e^+e^- \rightarrow f)$<br>[pb] | $28.7 \pm 0.5_{\text{stat}} \pm 2.0_{\text{sys}}$ | $2.6 \pm 0.1_{\text{stat}} \pm 0.2_{\text{sys}}$ | $6.8 \pm 0.3_{\text{stat}} \pm 0.5_{\text{sys}}$ |

# Chapter 8.

## Intermediate Resonances

---

*The processes  $e^+e^- \rightarrow \pi^+\pi^-2\pi^0$  and  $e^+e^- \rightarrow \pi^+\pi^-3\pi^0$  contain a rich spectrum of intermediate structures, some of which are narrow, like the  $\omega$ ,  $\eta$  and  $f_0(980)$  resonances. Many others, such as the  $\rho$ ,  $\sigma$ , and  $a_1(1270)$  resonances are broad. The contribution of these intermediate states are investigated in this chapter. It is of particular interest, whether or whether not intermediate structures are described correctly by the simulations used to determine the detection efficiencies. A good agreement between data and the simulations is needed to obtain a valid and precise result of the cross section measurements.*

---

## 8.1. Intermediate Resonances in

$$e^+e^- \rightarrow \pi^+\pi^-2\pi^0\gamma_{ISR}$$

Besides the mass spectrum of the hadronic final state of the  $e^+e^- \rightarrow \pi^+\pi^-2\pi^0\gamma_{ISR}$  process, also the mass spectra of the intermediate systems  $M(\pi^+\pi^-)$ ,  $M(\pi^0\pi^0)$ ,  $M(\pi^\pm\pi^0)$ ,  $M(\pi^+\pi^-\pi^0)$ ,  $M(\pi^\pm\pi^0\pi^0)$ , and  $M(\pi^0\gamma_{ISR})$  are investigated. These distributions are shown in five regions of  $M(\pi^+\pi^-2\pi^0)$  as indicated in Fig. 8.1-Fig. 8.5. For each of these intermediate mass spectra the differential non-radiative cross sections  $d\sigma/dM$  are calculated from the measurement by subtracting the background, correct for the detector efficiency and dividing out the radiator function. Along with the data points, the distributions extracted from the PHOKHARA 9.1 event generator are shown as solid, red curves. The  $f_0$  contribution in Fig. 8.1 is underestimated in the  $M(\pi^+\pi^-2\pi^0)$  regions between  $1.4\text{ GeV}/c^2$  and  $2.3\text{ GeV}/c^2$ . Above  $1.8\text{ GeV}/c^2$  the  $f_2(1270)$  signal strength is overestimated by the simulation. The  $\rho(770)$  and  $\omega(782)$  resonances are obvious in the  $M(\pi^+\pi^-)$ ,  $M(\pi^\pm\pi^0)$ , and  $M(\pi^+\pi^-\pi^0)$  distributions shown in Fig. 8.2, Fig. 8.3, and Fig. 8.4, respectively. The PHOKHARA 9.1 simulation is in good agreement with data in the  $M(\pi^+\pi^-)$  distributions shown in Fig. 8.2. Figure 8.3 shows that the  $M(\pi^\pm\pi^0)$  distributions are described perfectly by the PHOKHARA 9.1 event generator. In the  $M(\pi^+\pi^-\pi^0)$  distributions, as shown in Fig. 8.4, the  $\omega$  resonance contribution is underestimated. The overall data-MC agreement becomes worse in the region  $M(\pi^+\pi^-2\pi^0) > 2.3\text{ GeV}/c^2$ .

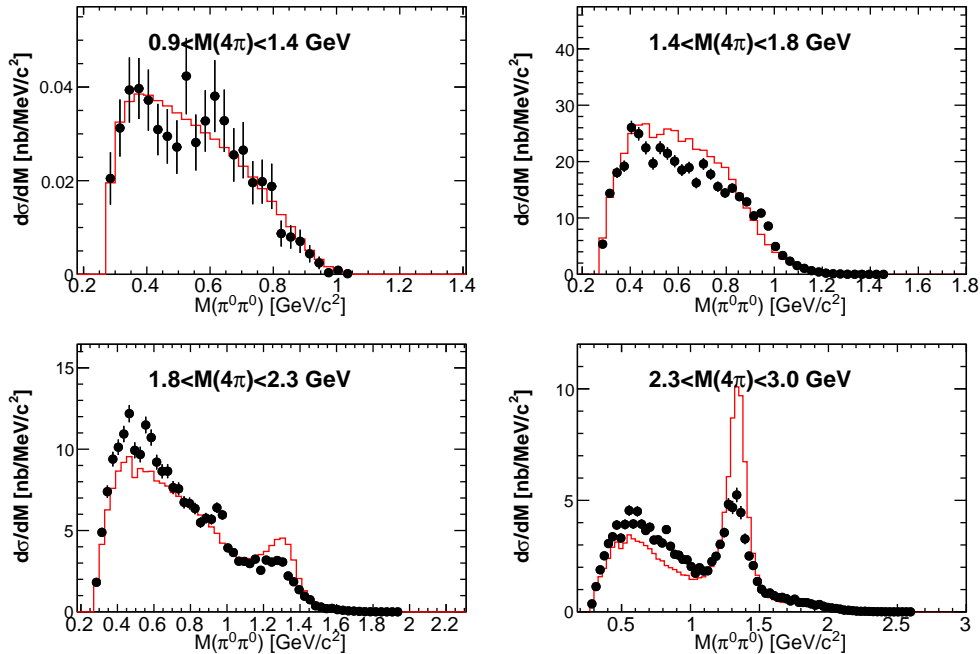
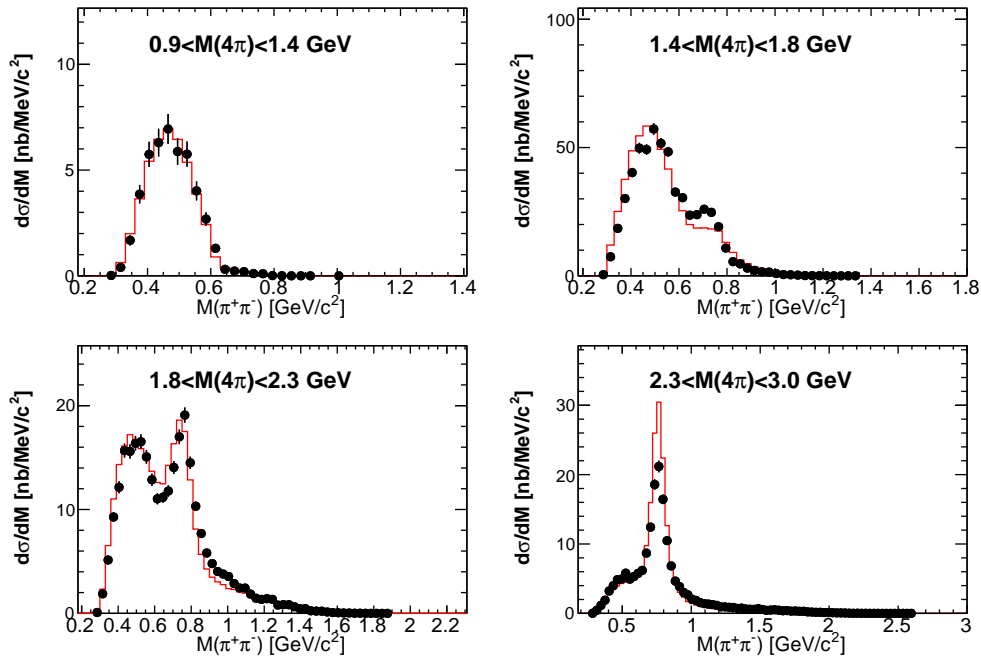
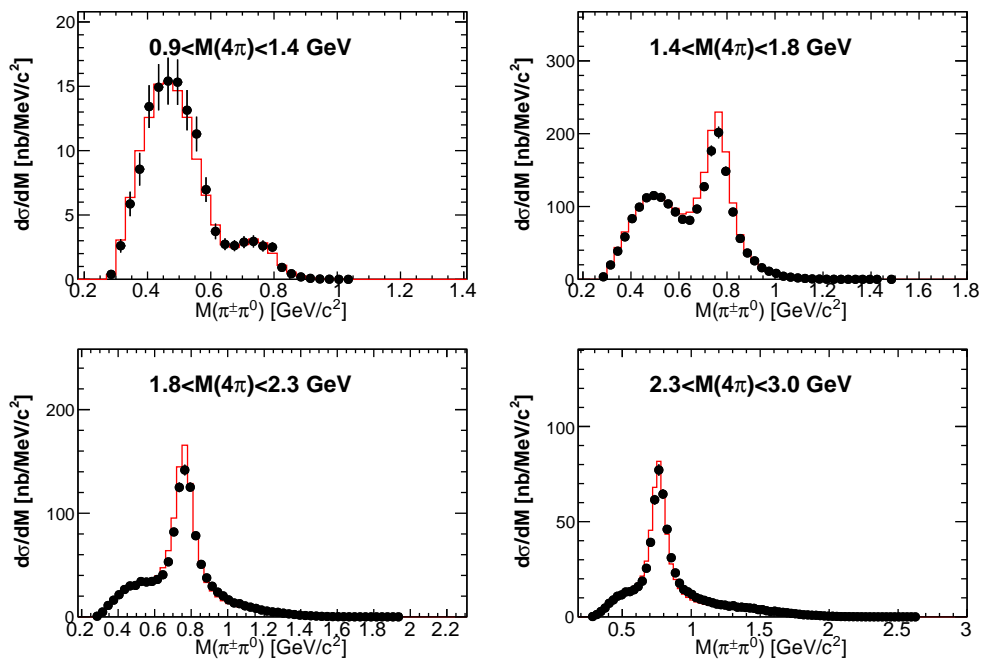
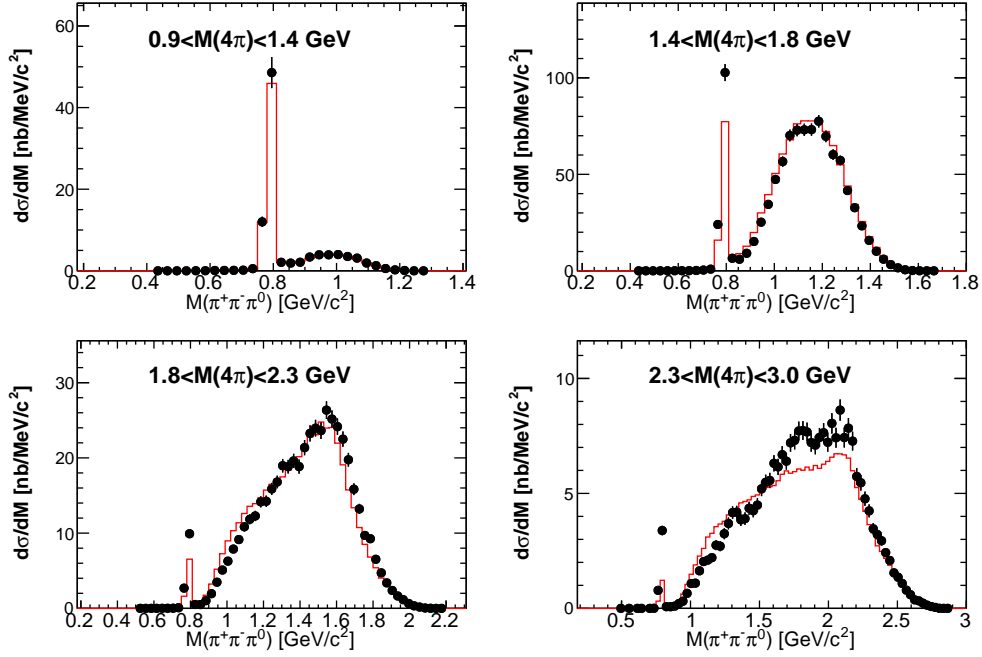
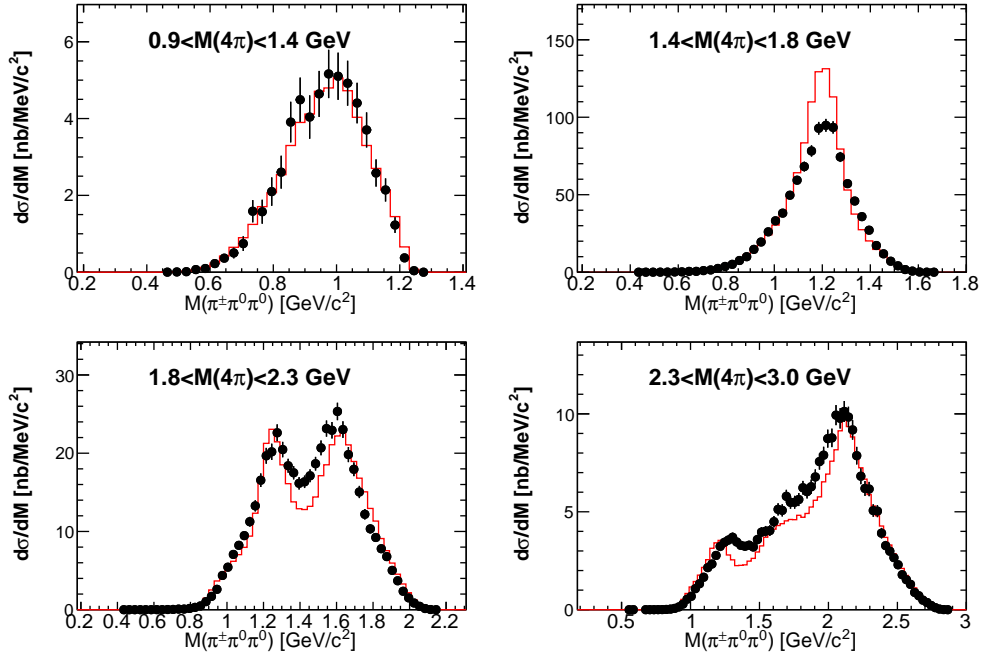


Figure 8.1.:  $\pi^0\pi^0$  intermediate structures.

Figure 8.2.:  $\pi^+\pi^-$  intermediate structures.Figure 8.3.:  $\pi^\pm\pi^0$  intermediate structures.

Figure 8.4.:  $\pi^+\pi^-\pi^0$  intermediate structures.Figure 8.5.:  $\pi^\pm\pi^0\pi^0$  intermediate structures.

There is a reasonable agreement between experiment and the simulation of the shapes of the  $M(\pi^\pm\pi^0\pi^0)$  distributions, shown in Fig. 8.5. The information presented in this section can be used to improve the performance of the  $e^+e^- \rightarrow \pi^+\pi^-\pi^0$  channel of future event generators.

## 8.2. Intermediate Resonances in $e^+e^- \rightarrow \pi^+\pi^-3\pi^0$

The mass spectra of different subsystems of the final state in  $e^+e^- \rightarrow \pi^+\pi^-3\pi^0$  are investigated in order to identify and study intermediate states. The respective distributions before efficiency correction are shown in Fig. 8.6. The MC histograms are stacked. The  $\rho$ ,  $\omega$ ,  $\eta$  and  $J/\psi$  resonance peaks are clearly visible in the distributions, which show good agreement between data and the simulations. The good quality of the simulation provides a reliable reconstruction efficiency for the calculation of the cross section.

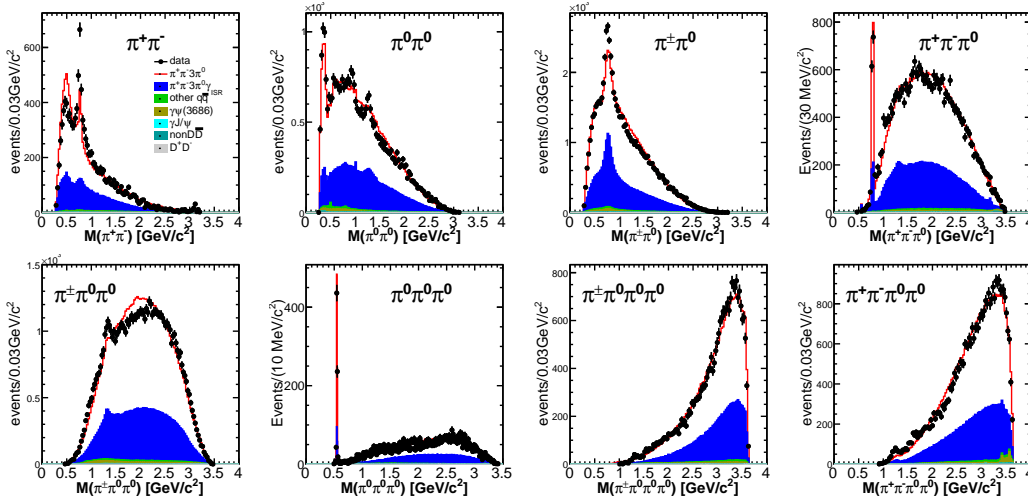


Figure 8.6.: Intermediate structures of the process  $e^+e^- \rightarrow \pi^+\pi^-3\pi^0$ .

## 8.3. Intermediate Resonances in

$$e^+e^- \rightarrow \pi^+\pi^-3\pi^0\gamma_{ISR}$$

The mass spectra of different subsystems of the final state in  $e^+e^- \rightarrow \pi^+\pi^-3\pi^0\gamma_{ISR}$  are investigated in order to identify and study intermediate states. The respective distributions before efficiency correction are shown in Fig. 8.7. The MC histograms are stacked. If required by combinatorics, more than one entry per event is displayed. These distributions show good agreement between data and the Lund- $q\bar{q}$  MC simulation. The resonances  $\rho$ ,  $\omega$ ,  $\eta$  and  $J/\psi$  are obviously visible in the distributions. The good quality of the simulation provides a reliable reconstruction efficiency for the calculation of the cross section.

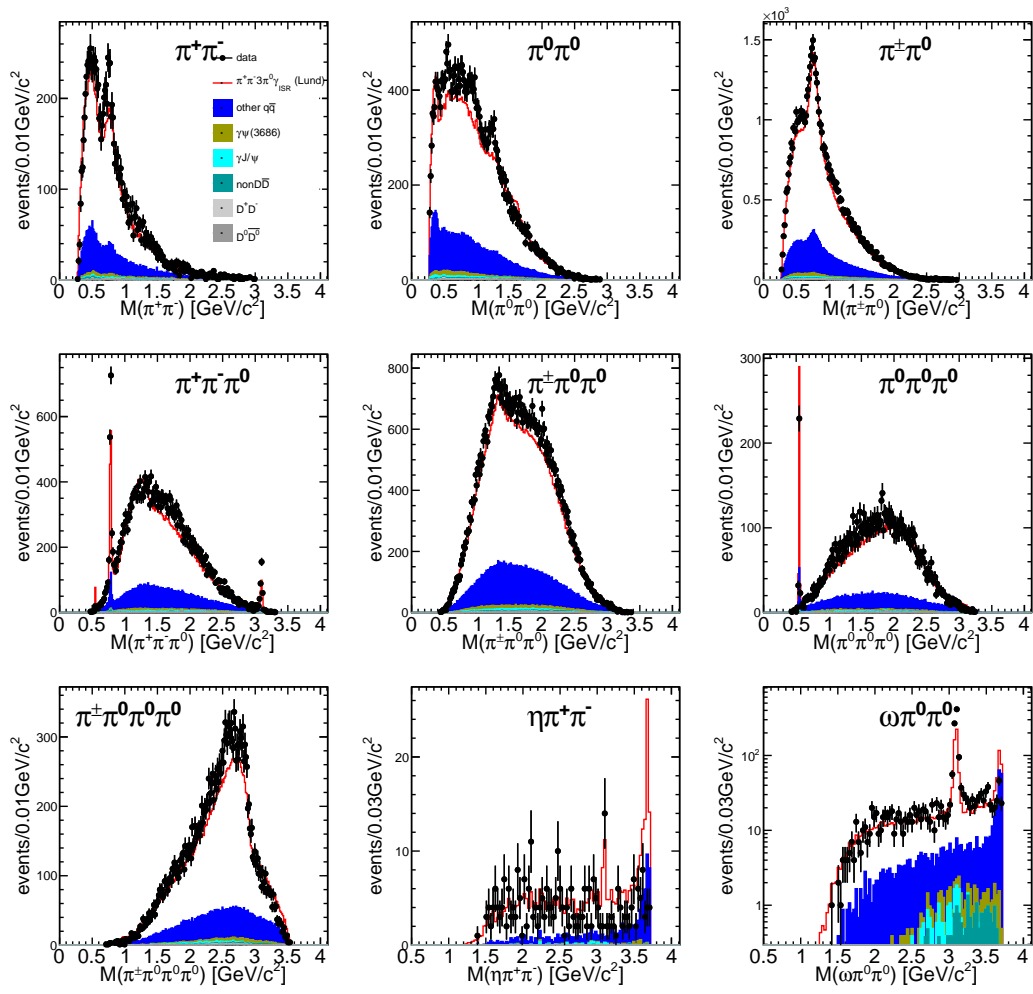


Figure 8.7.: Intermediate structures of the process  $e^+e^- \rightarrow \pi^+\pi^-3\pi^0\gamma_{ISR}$ .

# Chapter 9.

## Contribution to $a_\mu$

---

*This chapter contains the calculation of the contributions of the  $e^+e^- \rightarrow \pi^+\pi^-2\pi^0$  and  $e^+e^- \rightarrow \pi^+\pi^-3\pi^0$  cross section measurements obtained within this thesis to the HVP contribution to the anomalous magnetic moment of the muon,  $a_\mu^{\pi^+\pi^-2\pi^0,LO}$ , and,  $a_\mu^{\pi^+\pi^-3\pi^0,LO}$ . For comparison,  $a_\mu^{\pi^+\pi^-2\pi^0,LO}$  is determined separately for the tagged and untagged ISR methods as well as for their error weighted mean. The final result is compared to calculations of  $a_\mu^{\pi^+\pi^-2\pi^0,LO}$  based on the measurement of the BaBar collaboration. In case of the  $e^+e^- \rightarrow \pi^+\pi^-3\pi^0$  process, also the contributions to  $a_\mu$  of the sub-processes  $e^+e^- \rightarrow \pi^+\pi^-3\pi^0$  excluding the  $\eta$  resonance and  $e^+e^- \rightarrow \eta\pi^+\pi^-$  are computed.*

---

The dispersion integral introduced in Eq. 1.4.5 in section 1.4.2 can be defined for a certain final state  $f = \pi^+\pi^-2\pi^0, \pi^+\pi^-3\pi^0$  as

$$a_\mu^{\text{f,LO}} = \frac{1}{4\pi^3} \int_0^{(1.8\text{ GeV})^2} ds K(s) \sigma_f^{\text{bare}}(s). \quad (9.0.1)$$

In Eq. 9.0.1 the *bare* cross section  $\sigma^{\text{bare}}$  is needed as pointed out in Ref. [104]. However, the cross section measured in this work is the Born cross section as defined in Eq. 7.1.8 of section 7.1.5. The cross section  $\sigma_{\pi^+\pi^-2\pi^0}^{\text{bare}}(s)$  reads as  $\sigma_{\pi^+\pi^-2\pi^0}^{\text{bare}}(s) = \sigma_{\pi^+\pi^-2\pi^0}^{\text{Born}} \delta_{FSR}$ , where  $\delta_{FSR}$  is the theoretical Schwinger correction of Eq. 7.1.5, to reintroduce FSR effects.

The cross sections measured in this thesis are evaluated in the dispersion integral only for c.m. energies from 920 MeV up to 1.8 GeV. Perturbative QCD and R-scan results are used to determine the value of  $a_\mu^{\text{f,LO}}$  for higher c.m. energies. This was pointed out in section 1.5.

The integral requires the cross sections as a function of  $s$ , not of  $M(\pi^+\pi^-2\pi^0) = \sqrt{s}$  as given in Fig.7.11. Therefore, the cross section and all involved corrections are recalculated to match this requirement. The corresponding plots are presented in the following subsections.

A correlation of 100% is assumed between the intervals in the cross section histograms and the systematic uncertainties of  $a_\mu^{\text{f,LO}}$ . Hence, the systematic uncertainties are not calculated using the Gaussian error propagation, but as the linear sum of the errors from all individual  $M(\pi^+\pi^-2\pi^0)$  or  $M(\pi^+\pi^-3\pi^0)$  intervals.

## 9.1. Contribution of $e^+e^- \rightarrow \pi^+\pi^-2\pi^0$ to $a_\mu$

Figure 9.1 shows the fully corrected „bare“ cross section of  $e^+e^- \rightarrow \pi^+\pi^-2\pi^0$  in intervals of the squared c.m. energy  $s$ , as required for the calculation of  $a_\mu^{\pi^+\pi^-2\pi^0,\text{LO}}$ . The yellow dashed line marks the upper integration border at  $s = (1.8\text{ GeV})^2$  to calculate  $a_\mu^{\pi^+\pi^-2\pi^0,\text{LO}}$ . However, this measurement starts only from c.m. energies of 920 MeV. The threshold of the  $e^+e^- \rightarrow \pi^+\pi^-2\pi^0$  cross section is below that. Since the Kernel function in the integral enhances the contribution at lower masses, a non-negligible contribution to  $a_\mu^{\pi^+\pi^-2\pi^0,\text{LO}}$  could be missing in this calculation. Extrapolating from the first valid bin in Fig. 9.1, the differential cross section of  $e^+e^- \rightarrow \pi^+\pi^-2\pi^0$  is estimated to be smaller than 1 nb/120 MeV in the interval from 800 MeV to 920 MeV. Consequently, the cross section below 800 MeV is estimated to be negligibly small. The contribution to  $a_\mu^{\pi^+\pi^-2\pi^0,\text{LO}}$  of the omitted part of the differential cross section is evaluated as  $a_\mu^{\pi^+\pi^-2\pi^0,\text{LO}} \lesssim 0.08 \cdot 10^{-10}$ , which corresponds to an additional uncertainty of 0.43%. It is added in quadrature to the systematic uncertainty of the cross section measurement.

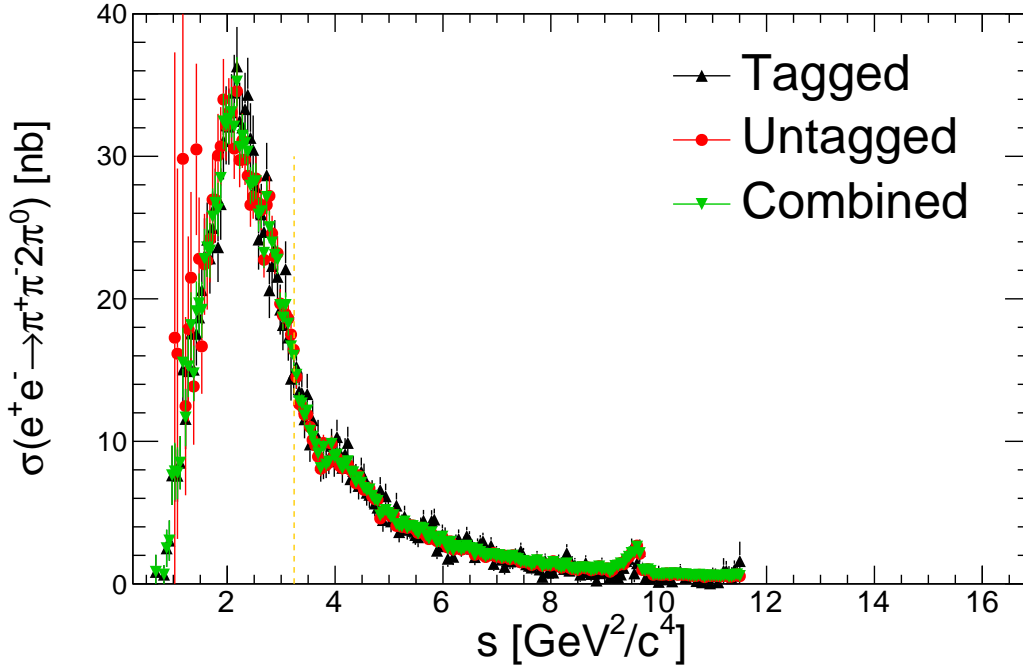


**Figure 9.1.:** Bare cross section of  $e^+e^- \rightarrow \pi^+\pi^-2\pi^0$  in intervals of  $s$ . The FSR correction is included.

Table 9.1 summarizes the resulting values of  $a_\mu^{\pi^+\pi^-2\pi^0, \text{LO}}$  from the tagged and untagged analyses, as well as the combined results. Each result is presented with statistical and systematic uncertainties. The value from the recent BABAR measurement is given for comparison. Within the uncertainties the result agrees with the BaBar result [70] and improves the precision of  $a_\mu^{\pi^+\pi^-2\pi^0, \text{LO}}$ . The combined result of this thesis is closer to the result of the tagged method even though, the statistical uncertainty of the cross section is generally smaller for the untagged method. The reason for this is found in the behavior of the Kernel function in the integral, which favors regions of low c.m. energies. Especially, in the region of  $s < 2 \text{ GeV}^2$ , the smaller statistic uncertainty of the tagged method dominates the error weighted mean of the combined result.

**Table 9.1.:** Results for  $a_\mu^{\pi^+\pi^-2\pi^0, \text{LO}}$ , the first error is of statistical nature, the second one is the systematic uncertainty.

|            | $a_\mu^{\pi^+\pi^-2\pi^0, \text{LO}} / 10^{-10}$ |
|------------|--|
| tagged     | $18.59 \pm 0.32 \pm 0.57$                        |
| untagged   | $19.36 \pm 0.97 \pm 0.57$                        |
| combined   | $18.63 \pm 0.27 \pm 0.57$                        |
| BaBar [70] | $17.9 \pm 0.1 \pm 0.6$                           |

## 9.2. Contribution of $e^+e^- \rightarrow \pi^+\pi^-3\pi^0$ to $a_\mu$

The fully corrected „bare“ cross sections of the three processes  $e^+e^- \rightarrow \pi^+\pi^-3\pi^0$ ,  $e^+e^- \rightarrow \pi^+\pi^-3\pi^0$  excluding the  $\eta$  resonance and  $e^+e^- \rightarrow \eta\pi^+\pi^-$  are shown in Fig. 9.2 in intervals of the squared c.m. energy  $s$ . These „bare“ cross sections are obtained analogously to the corresponding cross sections shown in Fig. 7.21. The Schwinger FSR and VP corrections are applied according to Eq. 7.1.5 and Eq. 7.1.6, respectively.

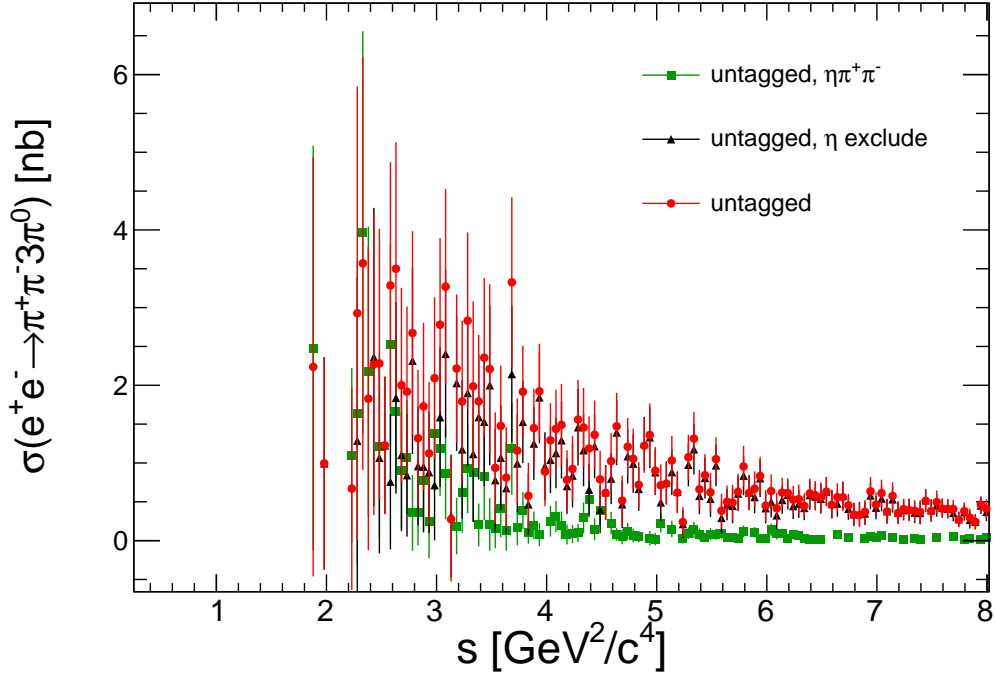


**Figure 9.2.:**  $\pi^+\pi^-3\pi^0$  bare cross section in bins of  $s$ ; VP and FSR corrections are included.

The contribution of the  $\pi^+\pi^-3\pi^0$  final state, calculated using Eq. 9.0.1, is shown in Table 9.2. The contributions from  $e^+e^- \rightarrow \eta\pi^+\pi^-$  and of  $e^+e^- \rightarrow \pi^+\pi^-3\pi^0$  excluding the  $\eta$  resonance are calculated in addition, in order to compare them to the theoretical predictions given in Ref. [42]. The branching fraction  $\mathcal{B}(\eta \rightarrow 3\pi^0) = (32.68 \pm 0.23)\%$  is used in the calculation of  $a_\mu^{\eta\pi^+\pi^-,LO}$ .

**Table 9.2.:** Results for  $a_\mu^{\pi^+\pi^-3\pi^0,LO}$ .

| Mode  | This Work   | Theoretical Estimations [42]                        |
|---|---|---|
| $a_\mu^{\pi^+\pi^-3\pi^0,LO}$                 | $0.65 \pm 0.11_{\text{stat}} \pm 0.09_{\text{sys}}$ | $0.74 \pm 0.07_{\text{stat}} \pm 0.09_{\text{sys}}$ |
| $a_\mu^{\pi^+\pi^-3\pi^0,\text{no } \eta,LO}$ | $0.32 \pm 0.07_{\text{stat}} \pm 0.04_{\text{sys}}$ | $0.36 \pm 0.02_{\text{stat}} \pm 0.03_{\text{sys}}$ |
| $a_\mu^{\eta\pi^+\pi^-,LO}$                   | $1.08 \pm 0.26_{\text{stat}} \pm 0.15_{\text{sys}}$ | $1.15 \pm 0.06_{\text{stat}} \pm 0.08_{\text{sys}}$ |

These contributions to  $a_\mu^{VP,LO}$  have never been measured directly before. The

theoretical estimation of these contributions are partially based on isospin relations between the processes  $e^+e^- \rightarrow \pi^+\pi^-3\pi^0$  and  $e^+e^- \rightarrow \pi^+\pi^-\pi^+\pi^-\pi^0$ . The results of the BESIII measurement presented here are in agreement with the theoretical estimations within uncertainties. The contribution of the process  $e^+e^- \rightarrow \pi^+\pi^-3\pi^0$  and its sub-processes to  $a_\mu^{VP,LO}$  is determined experimentally for the first time in this thesis. Several channels needed in the dispersion approach for  $a_\mu^{VP,LO}$  have not been measured, but their contributions have been estimated using isospin relations. For this reason, this measurement provides important information about the validity of the isospin assumptions in the theoretical prediction of  $a_\mu^{VP,LO}$ , even though the  $a_\mu^{\pi^+\pi^-3\pi^0,LO}$  contribution is smaller than the one of  $a_\mu^{\pi^+\pi^-2\pi^0,LO}$ .



# Chapter 10.

## Branching Fractions

---

*The branching fractions of the resonances  $J/\psi$  and  $\psi(3686)$  to the final states  $\pi^+\pi^-2\pi^0$ ,  $\pi^+\pi^-3\pi^0$  and their sub-channels can be calculated from the cross section measurements. The result serves as a cross check to the analysis.*

---

## 10.1. Calculation of the Branching Fractions

The analyses of the processes  $e^+e^- \rightarrow \pi^+\pi^-2\pi^0\gamma_{ISR}$  and  $e^+e^- \rightarrow \pi^+\pi^-3\pi^0\gamma_{ISR}$  also cover the radiative return to the narrow resonances  $J/\psi$  and  $\psi(3686)$ . Thus, their branching fractions to the corresponding final states, including intermediate resonances can be studied. Here, special attention is paid to the branching fractions  $J/\psi \rightarrow \pi^+\pi^-2\pi^0$ ,  $J/\psi \rightarrow \omega\pi^0$ ,  $J/\psi \rightarrow \pi^+\pi^-3\pi^0$ ,  $J/\psi \rightarrow \omega\pi^0\pi^0$  and  $\psi(3686) \rightarrow \pi^+\pi^-3\pi^0$ . The decay modes  $\psi(3686) \rightarrow \omega\pi^0\pi^0$  and  $\psi(3686) \rightarrow \eta\pi^+\pi^-$  are not considered, because the MC simulations are not reliable for these sub-channels in the mass region above  $M(\pi^+\pi^-3\pi^0) > 3.5 \text{ GeV}/c^2$ . This is indicated by the bad agreement between data and the simulations in the region  $M(\pi^+\pi^-3\pi^0) > 3.5 \text{ GeV}/c^2$  in the mass spectra shown in Fig. 7.17.

In order to obtain the branching fractions  $\mathcal{B}(R \rightarrow f)$  a Gaussian distribution for the resonance peak and a third order polynomial for the non-resonant background is fitted to the cross section spectra shown in Fig. 7.10, Fig. 7.21 and Fig. 10.1, respectively. These spectra are not unfolded and the apparent resonance widths are dominated by the detector resolution. However, the integral of the fitted Gaussians are equal to the integral from zero to infinity of the Breit-Wigner curve of the resonances

$$\sigma_{R \rightarrow f}^{\text{int}} = \int dm \sigma(m^2)_{R \rightarrow f} = \mathcal{B}(R \rightarrow f) \frac{6\pi^2 \Gamma_{ee}^R}{M_R^2} C \quad (10.1.1)$$

where  $\sigma(m^2)_{R \rightarrow f} = \frac{12\pi\Gamma_R\Gamma_{ee}^R\mathcal{B}(R \rightarrow f)}{(M_R^2 - m^2)^2 + M_R^2\Gamma_R^2}$  is the Breit-Wigner line shape,

$R = J/\psi$ ,  $\psi(3686)$  denotes the resonances,  $f = \pi^+\pi^-2\pi^0$ ,  $\omega\pi^0$ ,  $\pi^+\pi^-3\pi^0$ ,  $\omega\pi^0\pi^0$  denotes the considered final states,  $\sigma_{R \rightarrow f}^{\text{int}}$  is the integrated cross section from the fit result,  $\Gamma_{ee}^R$  is the electronic width of the resonance [31],  $M_R^2$  is the mass of the resonance [31] and  $C = (\hbar c)^2 = 389100 (\text{GeV})^2 \text{ nb}$  is a conversion constant. The right hand side of Eq. 10.1.1 is the result of the integral of the Breit-Wigner function. Solving this for the branching fraction gives

$$\mathcal{B}(R \rightarrow f) = \frac{\sigma_{R \rightarrow f}^{\text{int}} M_R^2}{6\pi^2 \Gamma_{ee}^R C}. \quad (10.1.2)$$

For the final states  $\omega\pi^0$  and  $\omega2\pi^0$  the branching fraction  $\mathcal{B}(\omega \rightarrow \pi^+\pi^-\pi^0) = (89.2 \pm 0.7) \%$  [31] has to be included in the denominator of Eq. 10.1.2 and  $\mathcal{B}(\eta \rightarrow 3\pi^0) = (32.68 \pm 0.23) \%$  for the final state  $\eta\pi^+\pi^-$ .

The fits performed for the  $e^+e^- \rightarrow \pi^+\pi^-2\pi^0\gamma_{ISR}$  channel and its  $\omega\pi^0\gamma_{ISR}$  sub-process are shown in Fig. 10.1. Figure 10.2 shows the fits of the  $e^+e^- \rightarrow \pi^+\pi^-3\pi^0\gamma_{ISR}$  process and its sub-channels.

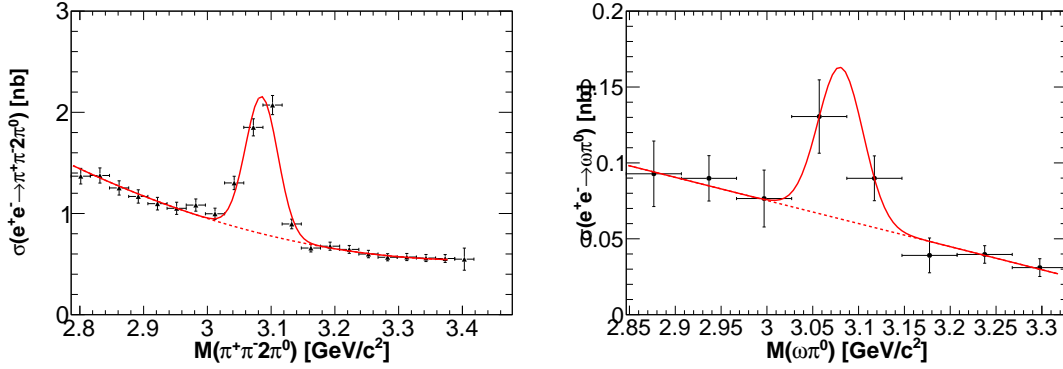


**Figure 10.1.:** Fits to the cross sections of  $e^+e^- \rightarrow \pi^+\pi^-2\pi^0$  and  $e^+e^- \rightarrow \omega\pi^0$  in the  $J/\psi$  region obtained with the untagged ISR analysis.

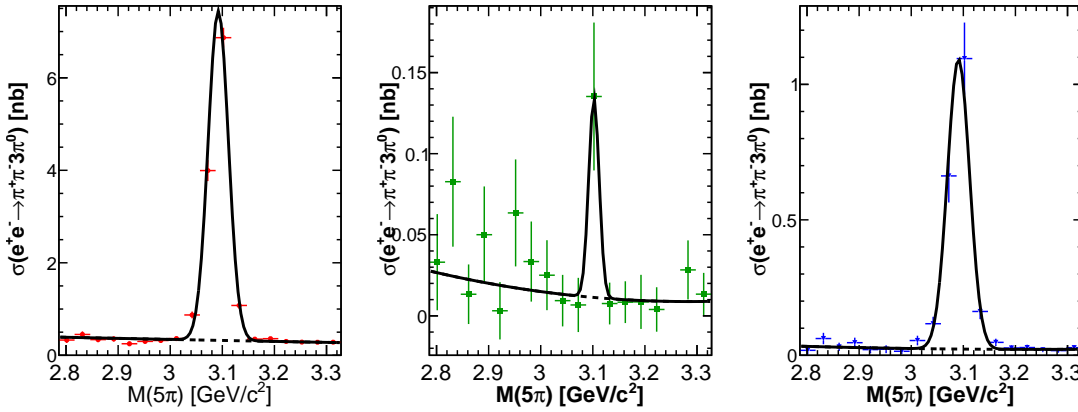


**Figure 10.2.:** Fits to the cross sections of  $e^+e^- \rightarrow \pi^+\pi^-3\pi^0$  and its sub-channels in the  $J/\psi$  region.

The results for the integrated cross sections from the fits, their  $\chi^2/ndf$ , and the results for the branching fractions are listed in Table 10.1.

**Table 10.1.:** Results for the branching fractions of  $J/\psi \rightarrow \pi^+\pi^-2\pi^0$ ,  $\pi^+\pi^-3\pi^0$ ,  $\omega\pi^0\pi^0$  and  $\eta\pi^+\pi^-$ . The last column shows the comparison to previous results listed in the PDG [31]

| final state        | $\chi^2/ndf$ | $\sigma_{R \rightarrow f}^{\text{int}} [\text{nb GeV}]$ | $\mathcal{B}(J/\psi \rightarrow f)/10^{-3}$         | PDG /10 <sup>-3</sup> |
|--------------------|--------------|---|---|-----------------------|
| $\pi^+\pi^-2\pi^0$ | 1.14         | $0.086 \pm 0.006$                                       | $6.46 \pm 0.43_{\text{stat}} \pm 0.27_{\text{sys}}$ | -                     |
| $\omega\pi^0$      | 0.27         | $0.007 \pm 0.002$                                       | $0.52 \pm 0.12_{\text{stat}} \pm 0.03_{\text{sys}}$ | $0.45 \pm 0.05$       |
| $\pi^+\pi^-3\pi^0$ | 1.55         | $0.347 \pm 0.012$                                       | $26.0 \pm 0.9_{\text{stat}} \pm 3.4_{\text{sys}}$   | -                     |
| $\omega\pi^0\pi^0$ | 1.11         | $0.057 \pm 0.007$                                       | $4.8 \pm 0.6_{\text{stat}} \pm 0.8_{\text{sys}}$    | $3.4 \pm 0.8$         |
| $\eta\pi^+\pi^-$   | 0.66         | $0.0027 \pm 0.0010$                                     | $0.61 \pm 0.23_{\text{stat}} \pm 0.08_{\text{sys}}$ | $0.40 \pm 0.17$       |

The branching fraction  $\psi(3686) \rightarrow \pi^+\pi^-3\pi^0$  is also calculated using Eq. 10.1.2 and fitting the  $\psi(3686)$ -resonance peak with the same function as used for the

$J/\psi$ -resonance. There is a potential background contamination from  $\psi(3686) \rightarrow J/\psi 3\pi^0$ , with  $J/\psi \rightarrow \mu^+\mu^-$  and the muons being misidentified as pions. From the  $M(\pi^+\pi^-)$  distribution in Fig 8.7, it can be concluded that this background is negligible, since events with an invariant mass close to the mass of the  $J/\psi$ -resonance are not observed. Figure 10.3 shows the fit result of the  $\psi(3686)$ -resonance peak in the full  $e^+e^- \rightarrow \pi^+\pi^-3\pi^0\gamma_{ISR}$  channel. For the fit quality  $\chi^2/ndf = 0.38$  is obtained. The fit yields an integrated cross section of  $\sigma_{\psi(3686) \rightarrow \pi^+\pi^-3\pi^0}^{\text{int}} = 0.004 \pm 0.001 \text{ nb GeV}$  for the  $\psi(3686)$ -resonance. The branching fraction is found to be

$$\mathcal{B}(\psi(3686) \rightarrow \pi^+\pi^-3\pi^0) = (0.9 \pm 0.2_{\text{stat}} \pm 0.1_{\text{sys}}) \cdot 10^{-3}. \quad (10.1.3)$$

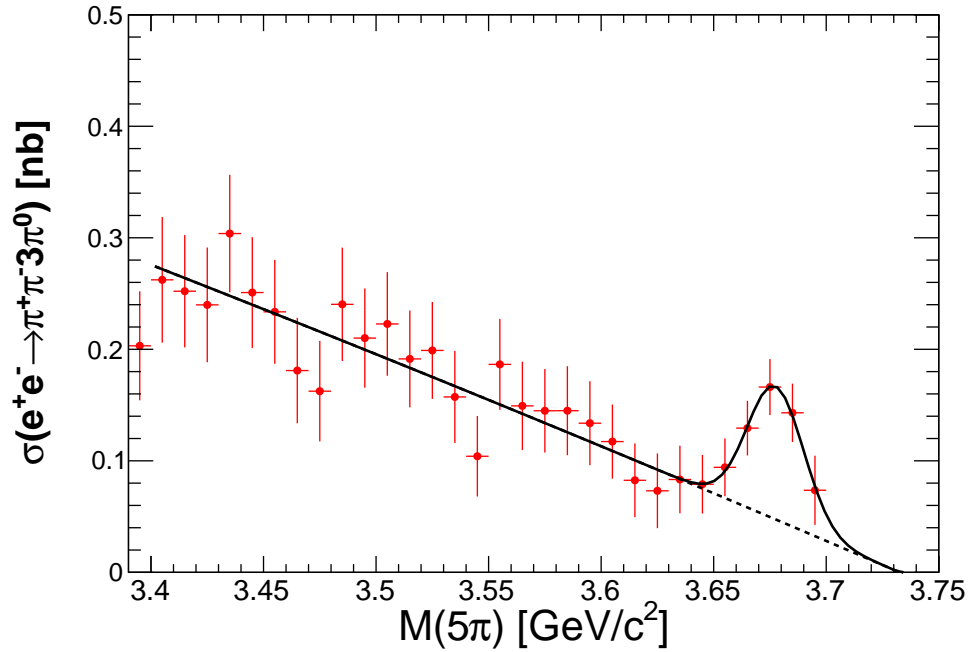


**Figure 10.3.:** Fit to the cross sections of  $e^+e^- \rightarrow \pi^+\pi^-3\pi^0$  in the  $\psi(3686)$  region.

The ratio of the  $J/\psi$  and  $\psi(3686)$  branching fractions to  $\pi^+\pi^-3\pi^0$  is found to be

$$\frac{\mathcal{B}(\psi(3686) \rightarrow \pi^+\pi^-3\pi^0)}{\mathcal{B}(J/\psi \rightarrow \pi^+\pi^-3\pi^0)} = 0.034 \pm 0.005,$$

which does not fulfill the 12% rule [103], which is observed for the ratios of other  $J/\psi$  and  $\psi(3686)$  branching fractions.

# Chapter 11.

## Systematic Uncertainty Estimations

---

*Unlike statistical uncertainties, the systematic uncertainties can shift an entire result towards wrong values. All possible sources of systematic uncertainties of the  $e^+e^- \rightarrow \pi^+\pi^-2\pi^0\gamma_{ISR}$  cross section measurement are explained in this chapter and their impact is estimated. Possible shifts can be tested either by varying all selection criteria or by applying alternative methods, where ever possible, to see how much the result varies. The most important sources for systematic uncertainties are the remaining error of the  $\pi^0$  reconstruction efficiency correction and the subtraction of remaining background contributions from MC simulations. The systematic uncertainties for  $e^+e^- \rightarrow \omega\pi^0\gamma_{ISR}$ , the corresponding fits of the  $\omega$  resonance contributions, as well as the additional uncertainties for the sub-processes of  $e^+e^- \rightarrow \pi^+\pi^-3\pi^0\gamma_{ISR}$  and the branching fractions are discussed in this chapter.*

---

The following uncertainties are taken from external sources. Their contribution to the final result is independent of the conditions applied in the analysis presented in this thesis.

**Luminosity** For the systematic uncertainty due to the scaling to the luminosity of data, the result from Ref. [84] is taken, which is 0.5% for the  $\psi(3770)$  data set. It is determined from the measurement of large angle Bhabha scattering events.

**Tracking Reconstruction Efficiency** The systematic uncertainty stemming from tracking efficiency of charged tracks has been determined in Ref. [105] using the control channel  $e^+e^- \rightarrow \pi^+\pi^-\pi^+\pi^-\gamma_{ISR}$ . The uncertainty was found to be 0.3% per track. For the two charged tracks in this analysis, the linear sum is taken to be conservative. Hence, the total systematic uncertainty due to tracking efficiency is 0.6%.

**ISR Photon Reconstruction Efficiency** The uncertainty of the photon reconstruction efficiency has been determined in Ref. [105]. The control channel  $e^+e^- \rightarrow \pi^+\pi^-2\pi^0$  at a c.m. energy of 3.773 GeV has been used. An uncertainty of 0.3% has been found, which is applied for the ISR photon in the tagged mode.

**VP Correction** The estimated uncertainty of the VP correction from Ref. [99] is 0.1%.

**FSR Correction** The emission of FSR photons from the neutral pions can be neglected compared to the FSR emission of the charged pions. The FSR effects of the final states  $\pi^+\pi^-3\pi^0\gamma_{ISR}$  and the  $\pi^+\pi^-2\pi^0\gamma_{ISR}$  are thus comparable to the final state  $\pi^+\pi^-$ . Therefore, the same uncertainty for the FSR correction as given in Ref. [84] is assumed, which is 0.2%.

**Radiator Function** The PHOKHARA 9.1 generator produces ISR events with a precision of 0.5% [85].

## 11.1. Signal Efficiencies

### 11.1.1. $\pi^0$ Reconstruction

The differences between data and simulation in the  $\pi^0$  reconstruction is determined in chapter 6. The uncertainties of the fit parameters are given in Eq. 6.3.1 and 6.3.2. They correspond to the statistical uncertainty of the  $\pi^0$  efficiency correction. The systematic uncertainty of the  $e^+e^- \rightarrow J/\psi\pi^0\pi^0$  method is 0.68% and the one of

the  $e^+e^- \rightarrow \omega\pi_{tag}^0$  method is 1.05%. The larger one of these two values will be used as the systematic uncertainty of the combined  $\pi^0$  efficiency, which is  $\Delta s = 1.05\%$ . In order to determine the total uncertainty of the  $\pi^0$  efficiency correction, the slope of the  $\pi^0$  correction function Eq. 6.3.4 is shifted by its statistical uncertainty and the offset by the squared sum of its statistical and systematic uncertainties. The function obtained  $\Delta\varepsilon'_{\pi^0}(p)$  reads

$$\begin{aligned} \Delta\varepsilon'_{\pi^0}(p) &= \varepsilon_{\pi^0}(p) \pm \sqrt{p^2\Delta a^2 + \Delta b^2 + 2pw\Delta a\Delta b + \Delta s^2} \\ &= \left(0.06 - 2.41 \text{ GeV}^{-1}c \cdot p \pm \sqrt{0.76 \text{ GeV}^{-2}c^2 \cdot p^2 + 1.15 + 0.39 \text{ GeV}^{-1}c \cdot p}\right) \%, \end{aligned} \quad (11.1.1)$$

where  $w = 0.94$  is the correlation between the parameters  $a$  and  $b$  of the linear fit function. The corresponding correlation matrix has only this one free parameter  $w$ . Figure 11.1 shows the tagged  $e^+e^- \rightarrow \pi^+\pi^-2\pi^0\gamma_{ISR}$  reconstruction efficiency without  $\pi^0$  efficiency correction, with normal  $\pi^0$  correction and with the corrections according to Eq. 11.1.1.

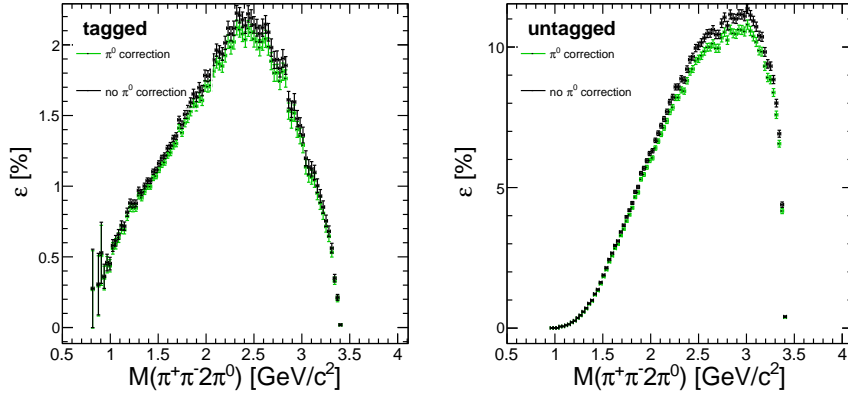


**Figure 11.1.:** Tagged  $e^+e^- \rightarrow \pi^+\pi^-2\pi^0\gamma_{ISR}$  reconstruction efficiency without  $\pi^0$  efficiency correction (blue), with  $\pi^0$  efficiency correction (black), and with the uncertainty shifted one from Eq. 11.1.1 (red).

The relative difference  $\frac{\Delta\varepsilon'_{\pi^0}}{\Delta\varepsilon_{\pi^0}} - 1$  between the nominal  $\pi^0$  efficiency correction function  $\Delta\varepsilon_{\pi^0}$  and the uncertainty shifted one  $\Delta\varepsilon'_{\pi^0}$  can be seen in Fig. 11.1 as the difference between the black and the red dots. The maximum deviation observed over the full mass range is considered as systematic uncertainty. The result is 2.6% and 2.5% for the tagged and the untagged ISR methods, respectively.

### 11.1.2. Intermediate States

The  $e^+e^- \rightarrow \pi^+\pi^-2\pi^0\gamma_{ISR}$  reconstruction efficiency may depend on intermediate structures. If the number of events containing intermediate structures is different in data compared to the simulations, the  $e^+e^- \rightarrow \pi^+\pi^-2\pi^0\gamma_{ISR}$  reconstruction

efficiency may be determined wrongly. In order to estimate the size of this effect and to obtain the corresponding systematic uncertainty, the two sub-processes  $e^+e^- \rightarrow \omega\pi^0\gamma_{ISR}$  and  $e^+e^- \rightarrow \rho^+\rho^-\gamma_{ISR}$  are considered. The event selection of the  $e^+e^- \rightarrow \omega\pi^0\gamma_{ISR}$  sub-process is explained in detail in section 4.1. In order to select  $e^+e^- \rightarrow \rho^+\rho^-\gamma_{ISR}$  events, the best combinations of  $\pi^\pm\pi_{1,2}^0$  for each  $e^+e^- \rightarrow \pi^+\pi^-2\pi^0\gamma_{ISR}$  event are determined, such that non of the  $\pi^0$  is used twice. Events are rejected, if  $|M(\pi^\pm\pi^0) - m_{\rho^\pm}| > 150$  MeV holds. The correlation plot of the two  $\pi^\pm\pi^0$  combinations is shown in Fig. 11.2 for data and signal simulation. The reconstruction efficiencies  $\varepsilon_{\omega\pi^0}$ ,  $\varepsilon_{\rho^+\rho^-}$  and  $\varepsilon_{\text{other}}$  of the corresponding sub-processes and the remaining  $e^+e^- \rightarrow \pi^+\pi^-2\pi^0\gamma_{ISR}$  events need to be determined separately.

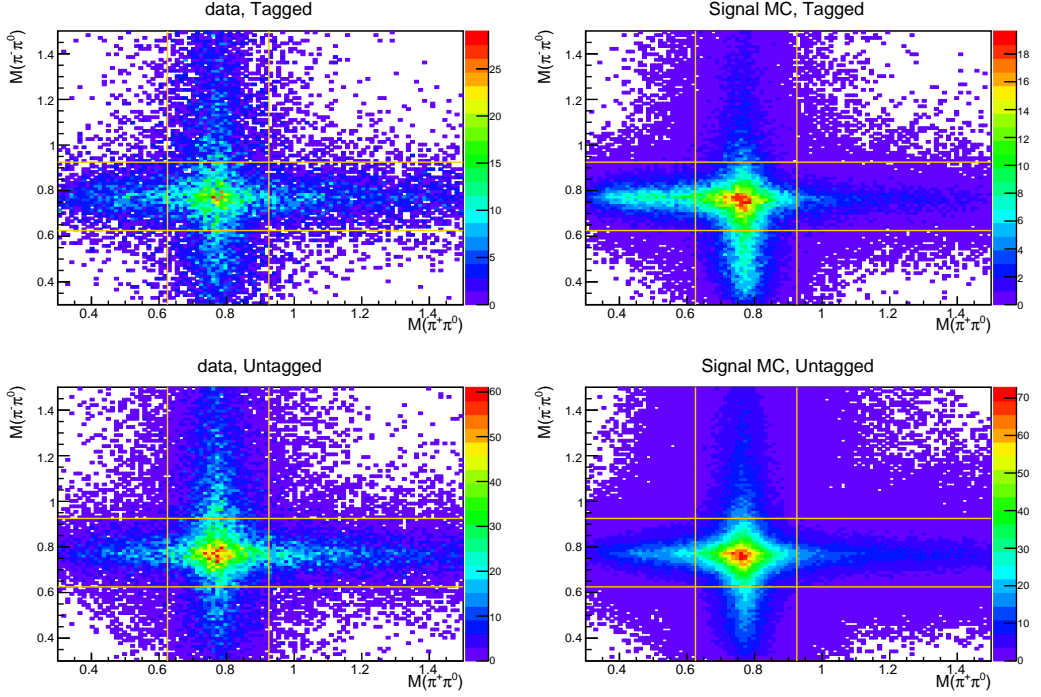


**Figure 11.2.:**  $\rho^\pm$  window in data and signal MC for the  $\rho^+\rho^-\gamma_{ISR}$  selection.

Figure 11.3 shows the reconstruction efficiencies of the individual processes as well as the full  $e^+e^- \rightarrow \pi^+\pi^-2\pi^0\gamma_{ISR}$  final state. In the region  $M(\pi^+\pi^-2\pi^0) \gtrsim 2$  GeV, the reconstruction efficiency  $\varepsilon_{\omega\pi^0}$  differs significantly from the full  $e^+e^- \rightarrow \pi^+\pi^-2\pi^0\gamma_{ISR}$  efficiency. It is found to be lower by approximately 25%. However, the fraction of  $e^+e^- \rightarrow \omega\pi^0\gamma_{ISR}$  events is small compared to the total number of  $e^+e^- \rightarrow \pi^+\pi^-2\pi^0\gamma_{ISR}$  events in that  $M(\pi^+\pi^-2\pi^0)$  region. The  $e^+e^- \rightarrow \rho^+\rho^-\gamma_{ISR}$  efficiency  $\varepsilon_{\rho^+\rho^-}$  does not reveal any significant deviation from the full  $e^+e^- \rightarrow \pi^+\pi^-2\pi^0\gamma_{ISR}$  efficiency. The full  $e^+e^- \rightarrow \pi^+\pi^-2\pi^0\gamma_{ISR}$  reconstruction efficiency  $\varepsilon_{MC}$  obtained from PHOKHARA 9.1 can be decomposed into a  $e^+e^- \rightarrow \omega\pi^0\gamma_{ISR}$  part, a  $e^+e^- \rightarrow \rho^+\rho^-\gamma_{ISR}$  part and a remaining part according to

$$\varepsilon_{MC} = f_1\varepsilon_{\omega\pi^0} + f_2\varepsilon_{\rho^+\rho^-} + (1 - f_1 - f_2)\varepsilon_{\text{other}} ,$$

where  $f_1$  is the fraction of  $e^+e^- \rightarrow \omega\pi^0\gamma_{ISR}$  events and  $f_2$  is the fraction of  $e^+e^- \rightarrow \rho^+\rho^-\gamma_{ISR}$  events in the full amount of  $e^+e^- \rightarrow \pi^+\pi^-2\pi^0\gamma_{ISR}$  process. The values of the individual fractions are taken from the PHOKHARA 9.1 event generator.

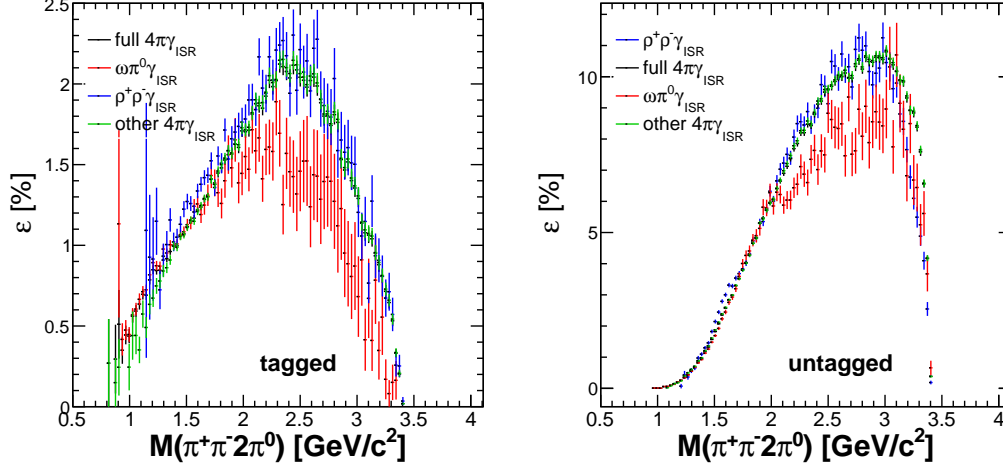


**Figure 11.3.:** The  $e^+e^- \rightarrow \pi^+\pi^-2\pi^0\gamma_{ISR}$  reconstruction efficiency comparison for  $e^+e^- \rightarrow \omega\pi^0\gamma_{ISR}$ ,  $\rho^+\rho^-\gamma_{ISR}$  and other  $e^+e^- \rightarrow \pi^+\pi^-2\pi^0\gamma_{ISR}$  events.

The equivalent fractions  $f'_{1,2}$  are calculated for data and define the corrected efficiency  $\varepsilon_{\text{data}}$  according to

$$\varepsilon_{\text{data}} = f'_1\varepsilon_{\omega\pi^0} + f'_2\varepsilon_{\rho^+\rho^-} + (1 - f'_1 - f'_2)\varepsilon_{\text{other}}.$$

The distributions of  $f'_{1,2}$  for the tagged and untagged methods are shown in Fig. 11.4.

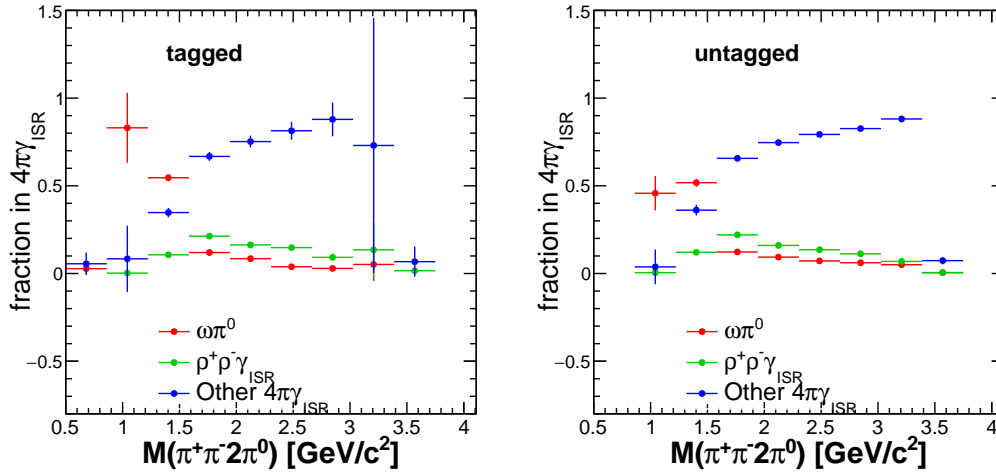


**Figure 11.4.:** Fractions of the  $\omega\pi^0\gamma_{ISR}$ ,  $\rho^+\rho^-\gamma_{ISR}$  and other  $4\pi\gamma_{ISR}$  contributions in the full  $\pi^+\pi^-2\pi^0\gamma_{ISR}$  final state.

The corrected efficiency  $\varepsilon_{\text{data}}$  and the nominal efficiency taken directly from the PHOKHARA 9.1 event generator  $\varepsilon_{MC}$  are shown for comparison in Fig. 11.5.

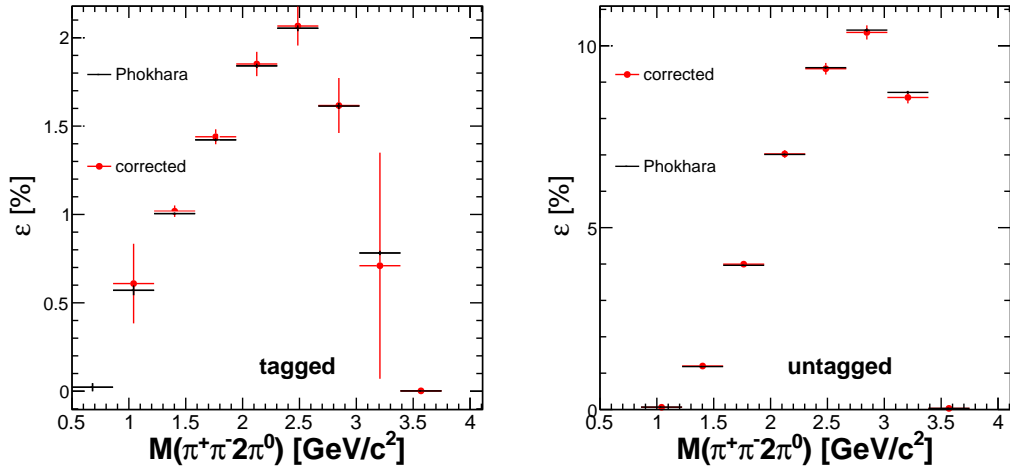


**Figure 11.5.:** Comparison between the efficiency obtained by PHOKHARA 9.1 only and the one corrected for the  $\omega\pi^0$  and  $\rho^+\rho^-$  contributions according to data.

The largest relative deviation  $\Delta\varepsilon = (\varepsilon_{MC} - \varepsilon_{data}) / \varepsilon_{data}$  between efficiencies obtained with the fractions from data or MC is taken as systematic uncertainty. The result is 0.6% for tagged ISR method and 0.6% for untagged one. The nominal efficiency  $\varepsilon_{MC}$  is used to do calculate the cross section.

### 11.1.3. Signal Selection

The systematic uncertainties due to the event selection criteria are determined, except for the  $\chi^2$  selection. The strategy is to vary individual selection requirements. The respective range of variation corresponds to three to five three to five times the resolution of the observable the condition is based on. The relative difference  $\delta(N) = \frac{N}{N_0} - 1$  of the number  $N$  of events in the efficiency corrected  $M(4\pi)$  mass spectra, obtained with the modified event selection, to the number of events  $N_0$  obtained with the nominal event selection, is calculated for every variation of selection criteria. The largest deviation  $\delta(N)$  to zero for each selection requirement is taken as its systematic uncertainty. This method is applied for the following selection criteria:

- Kaon Veto (tagged and untagged)
- Vertex Fit of the two charged tracks (untagged)
- Fake ISR photons  $m_{\gamma\gamma_{ISR}}$  (tagged)
- Minimal angle between the ISR photon and the neutral pions  $\cos\alpha$  (tagged)
- Polar angle of the ISR photon  $\cos\theta_{ISR}$  (untagged)

Their corresponding variation ranges and systematic uncertainties are listed in Table 11.6 of section 11.3.

## 11.2. Background Subtraction

The main background contributions were identified to stem from  $e^+e^- \rightarrow \pi^+\pi^-3\pi^0\gamma_{ISR}$  and  $e^+e^- \rightarrow \pi^+\pi^-3\pi^0$ . Due to a lack of existing measurements of both processes, the cross sections have been determined additionally as a part of this work. The detailed studies of their systematic uncertainties are discussed in the following. Furthermore, the systematic uncertainty introduced by subtracting these background contributions from the  $M(\pi^+\pi^-2\pi^0)$  spectrum is discussed. It is directly related to the systematic uncertainties of the measurement of  $e^+e^- \rightarrow \pi^+\pi^-3\pi^0\gamma_{ISR}$  and  $e^+e^- \rightarrow \pi^+\pi^-3\pi^0$ .

### 11.2.1. Systematic Uncertainty Estimation for

$$e^+e^- \rightarrow \pi^+\pi^-3\pi^0\gamma_{ISR}$$

The uncertainty due to the  $\pi^0$  efficiency correction can be calculated from Eq. 11.1.1, which describes the contribution of a single  $\pi^0$  in the final state. The relative difference  $\frac{\Delta\varepsilon'_{\pi^0}}{\Delta\varepsilon_{\pi^0}} - 1$  between the nominal  $\pi^0$  efficiency correction function  $\Delta\varepsilon_{\pi^0}$  and the function  $\Delta\varepsilon'_{\pi^0}$  shifted by the uncertainty of the  $\pi^0$  reconstruction is shown in Fig. 11.6.

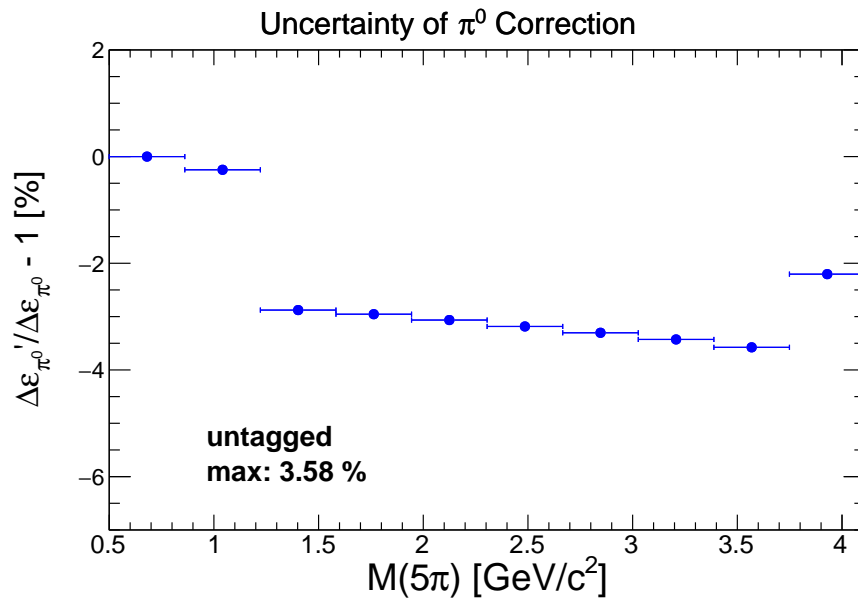


**Figure 11.6.:** Comparison between the normal  $\pi^0$  efficiency correction and the uncertainty shifted one for the  $e^+e^- \rightarrow \pi^+\pi^-3\pi^0$  final state.

For the total systematic uncertainty of the  $\pi^0$  reconstruction efficiency correction the maximum value obtained in Fig. 11.6 is taken, which is 3.58% for the  $e^+e^- \rightarrow \pi^+\pi^-3\pi^0\gamma_{ISR}$  process, where the untagged ISR method is used.

The  $e^+e^- \rightarrow \pi^+\pi^-3\pi^0\gamma_{ISR}$  reconstruction efficiency may depend on intermediate structures. If the fraction of these intermediate structures in the number of all  $e^+e^- \rightarrow \pi^+\pi^-3\pi^0\gamma_{ISR}$  events differs between data and the MC simulations, the full  $\pi^+\pi^-3\pi^0\gamma_{ISR}$  reconstruction efficiency can be wrong. In order to estimate the effect quantitatively, the two sub-processes  $e^+e^- \rightarrow \omega 2\pi^0\gamma_{ISR}$  and  $e^+e^- \rightarrow \eta\pi^+\pi^-\gamma_{ISR}$  are used. Since the  $\omega$  and the  $\eta$  resonances are the most narrow intermediate structures in the  $M(\pi^+\pi^-3\pi^0)$  mass spectrum, they can be easily identified. The reconstruction efficiencies  $\varepsilon_\omega$  of  $e^+e^- \rightarrow \omega 2\pi^0\gamma_{ISR}$  events,  $\varepsilon_\eta$  of  $e^+e^- \rightarrow \eta\pi^+\pi^-\gamma_{ISR}$  events, and the one of the remaining non- $\omega$  and non- $\eta$  events  $\varepsilon_{\text{rest}}$  are determined. Figure 11.7 shows the reconstruction efficiencies of these kind of events along with the full  $e^+e^- \rightarrow \pi^+\pi^-3\pi^0\gamma_{ISR}$  reconstruction efficiency.

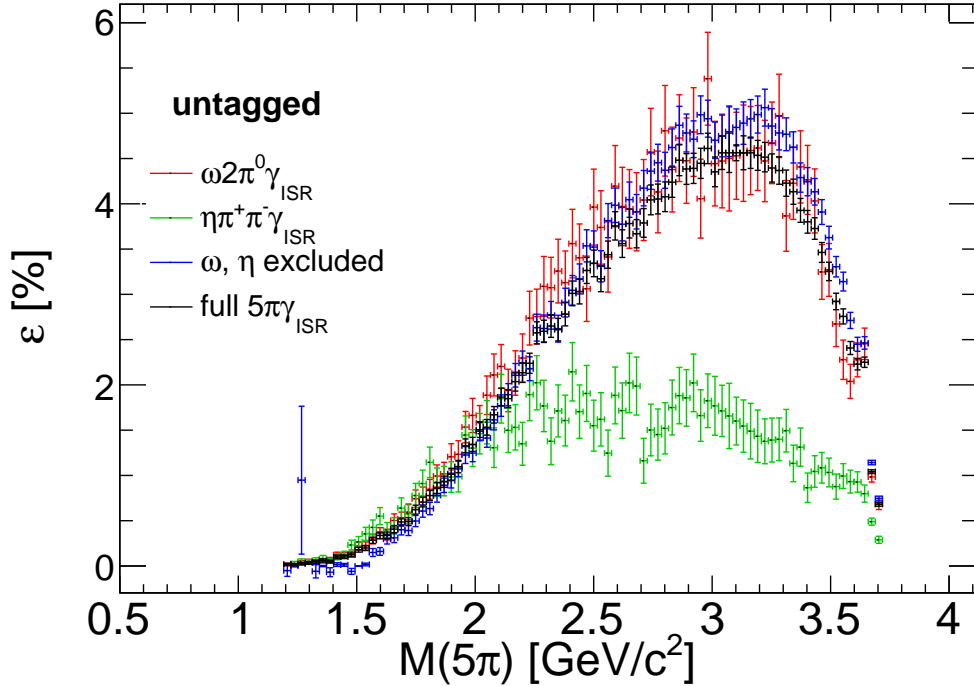


**Figure 11.7.:** Reconstruction efficiency comparison between  $e^+e^- \rightarrow \omega 2\pi^0\gamma_{ISR}$ ,  $e^+e^- \rightarrow \eta\pi^+\pi^-\gamma_{ISR}$ , non- $\omega, \eta$  and the full  $e^+e^- \rightarrow \pi^+\pi^-3\pi^0\gamma_{ISR}$ .

In the region  $M(\pi^+\pi^-3\pi^0) \gtrsim 2 \text{ GeV}$ , the reconstruction efficiency  $\varepsilon_\eta$  of the  $e^+e^- \rightarrow \eta\pi^+\pi^-\gamma_{ISR}$  events differs significantly from the full  $e^+e^- \rightarrow \pi^+\pi^-3\pi^0\gamma_{ISR}$  efficiency. However, the fraction of these events among the total number of  $e^+e^- \rightarrow \pi^+\pi^-3\pi^0\gamma_{ISR}$  events is small. The  $e^+e^- \rightarrow \pi^+\pi^-3\pi^0\gamma_{ISR}$  reconstruction efficiency  $\varepsilon_{MC}$  obtained from Lund- $q\bar{q}$  can be decomposed into a  $e^+e^- \rightarrow \omega 2\pi^0\gamma_{ISR}$  part, an

$e^+e^- \rightarrow \eta\pi^+\pi^-\gamma_{ISR}$  part and a non- $\omega, \eta$  part according to

$$\varepsilon_{MC} = f_1\varepsilon_\omega + f_2\varepsilon_\eta + (1 - f_1 - f_2)\varepsilon_{\text{rest}},$$

where  $f_1$  is the fraction of  $e^+e^- \rightarrow \omega 2\pi^0\gamma_{ISR}$  among the full  $e^+e^- \rightarrow \pi^+\pi^-3\pi^0\gamma_{ISR}$  event sample and  $f_2$  is the according fraction for  $e^+e^- \rightarrow \eta\pi^+\pi^-\gamma_{ISR}$  events. The same fractions  $f'_1$  and  $f'_2$  are calculated for data and the corrected efficiency  $\varepsilon_{\text{data}}$  according to

$$\varepsilon_{\text{data}} = f'_1\varepsilon_\omega + f'_2\varepsilon_\eta + (1 - f'_1 - f'_2)\varepsilon_{\text{rest}}.$$

The distributions of  $f'_1$  and  $f'_2$  are shown in the left panel of Fig. 11.8. The total contributions of  $e^+e^- \rightarrow \omega 2\pi^0\gamma_{ISR}$  and  $e^+e^- \rightarrow \eta\pi^+\pi^-\gamma_{ISR}$  in data are found to be  $(19.6 \pm 0.49)\%$  and  $(2.9 \pm 0.18)\%$ , respectively. The corrected efficiency  $\varepsilon_{\text{data}}$  and the nominal efficiency from Lund- $q\bar{q}$  are shown in the right panel of Fig. 11.8.

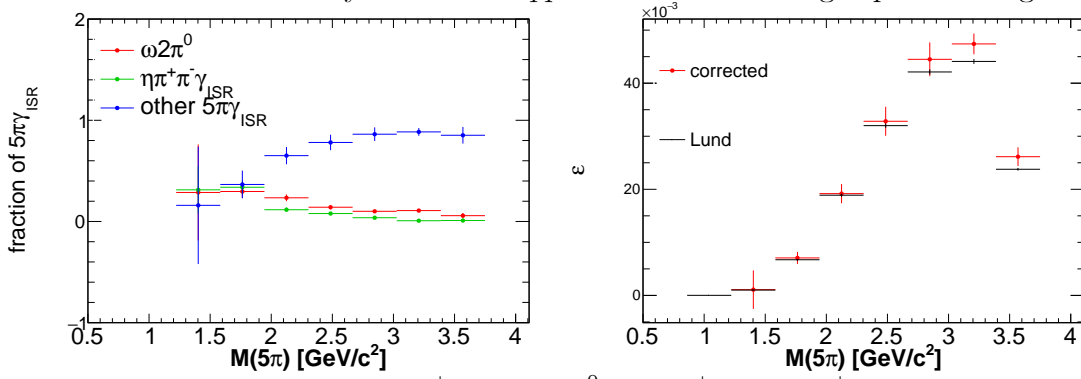


**Figure 11.8.:** Fractions of the  $e^+e^- \rightarrow \omega 2\pi^0\gamma_{ISR}$ ,  $e^+e^- \rightarrow \eta\pi^+\pi^-\gamma_{ISR}$  and non- $\omega, \eta$  contributions in the full  $e^+e^- \rightarrow \pi^+\pi^-3\pi^0\gamma_{ISR}$  final state (left). Comparison between the efficiency obtained by Lund- $q\bar{q}$  only and the one corrected for the  $\omega$  and  $\eta$  contributions according to data (right).

The largest relative deviation  $\Delta\varepsilon = (\varepsilon_{MC} - \varepsilon_{\text{data}}) / \varepsilon_{\text{data}}$  between efficiencies obtained with the fractions from data and MC is found to be 5.5%, which is taken as systematic uncertainty. The nominal efficiency  $\varepsilon_{MC}$  is used to do calculate the cross section.

Another uncertainty to be determined is due to the subtraction of background contributions taken directly from the Lund- $q\bar{q}$  MC simulation. An accuracy of 20% is assumed for the channels listed in Table 5.1, since they are not well known. The scaling of the background contribution is changed by  $\pm 20\%$  and the rescaled background MC is subtracted from data. This results in different event yields in intervals of  $M(\pi^+\pi^-3\pi^0)$ . Figure 11.9 shows the relative deviation between the nominal background contribution and the background contributions scaled by  $\pm 20\%$ . As expected, the deviations of the results with reduced and increased background contributions are symmetric with respect to zero. The largest relative difference is taken as the systematic uncertainty due to background subtraction. A systematic uncertainty of 10.55% is found according to Fig. 11.9.

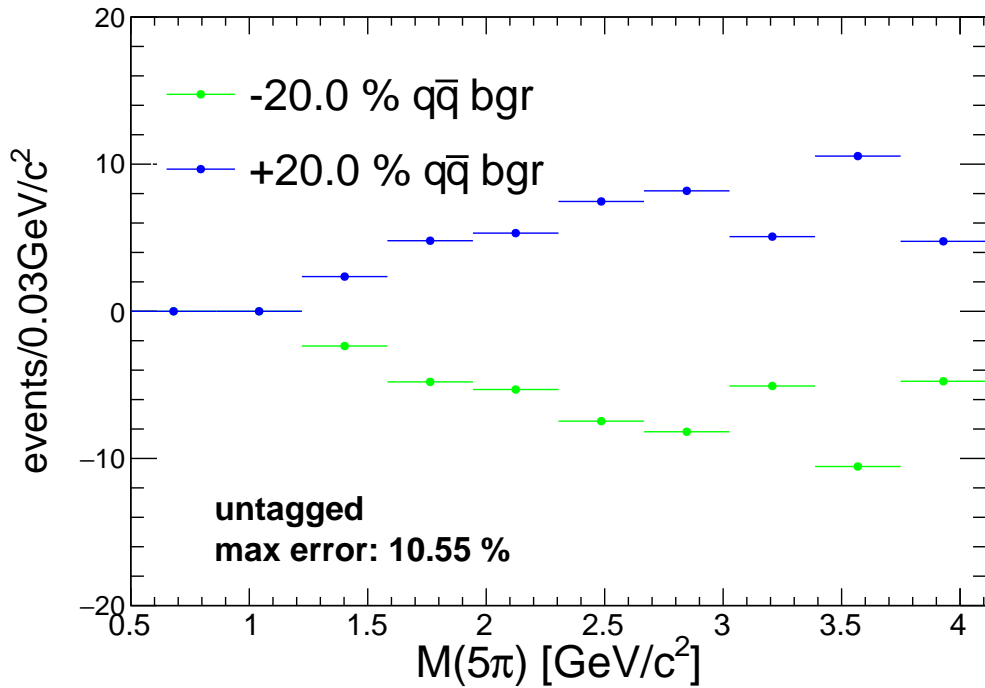


**Figure 11.9.:** Systematic uncertainty from the background subtraction for the  $\pi^+\pi^-3\pi^0$  final state.

The systematic uncertainties of the event selection criteria are also determined with the same strategy used in the four pion analysis. The contributions of the following selection criteria are studied:

- Kinematic fit  $\chi_{4C}^2$
- Kaon Veto
- Vertex Fit of the two charged tracks
- Polar angle of the ISR photon  $\cos\theta_{ISR}$

Their corresponding systematic uncertainties are listed in the summary Table 11.1.

The various sources of systematic uncertainty are assumed to be uncorrelated. Hence, their quadratic sum is taken as total systematic uncertainty. The total systematic uncertainty and the individual contributions are summarized in Table 11.1. The total systematic uncertainty is 13.25%.

**Table 11.1.:** Summary of systematic uncertainties of the  $\pi^+\pi^-3\pi^0\gamma_{ISR}$  final state.

| Source            | Variation                     | Untagged [%] |
|-------------------|-------------------------------|--------------|
| Luminosity        | -                             | 0.50         |
| Tracking          | -                             | 0.60         |
| radiator function | -                             | 0.50         |
| VP correction     | -                             | 0.05         |
| FSR correction    | -                             | 0.20         |
| $\pi^0$ eff.      | -                             | 3.58         |
| rec. eff.         | -                             | 5.50         |
| Bgr. Subrt.       | $\pm 20\%$ Bgr.               | 10.55        |
| $\chi^2$ cut      | $26 < \chi_{4C}^2 < 35$       | 1.09         |
| Vertex cut        | $1.75 < r_{vertex} < 2.25$    | 0.11         |
| Kaon Veto         | on/off                        | 2.52         |
| ISR Angle         | $0.989 < \cos \theta < 0.991$ | 3.57         |
| Total             |                               | 13.81        |

## 11.2.2. Systematic Uncertainty Estimation for

$$e^+e^- \rightarrow \pi^+\pi^-3\pi^0$$

The estimation of systematic uncertainties for the cross section measurement of  $e^+e^- \rightarrow \pi^+\pi^-3\pi^0$  is performed analogously to the procedure described in section 11.2.1. The  $e^+e^- \rightarrow \pi^+\pi^-3\pi^0$  event yield with the  $\pi^0$  efficiency correction function shifted by its uncertainty is calculated for each  $\pi^0$  according to Eq. 11.1.1. The relative difference to the event yield determined with the normal  $\pi^0$  correction is 1.7%.

A systematic uncertainty of the efficiency due to possibly wrong contributions of narrow intermediate structures is not determined, since the  $\omega$  and  $\eta$  intermediate resonances were tuned to match data in the  $e^+e^- \rightarrow \pi^+\pi^-3\pi^0$  MC cocktail.

The uncertainty due to background subtraction is determined. 96% of the background contributions come from the process  $e^+e^- \rightarrow \pi^+\pi^-3\pi^0\gamma_{ISR}$ , where the total uncertainty has been determined as 13.25% in section 11.2.1. The relative difference between the event yield with normal scaling of the background contribution and the one rescaled considering the uncertainty of the  $\pi^+\pi^-3\pi^0\gamma_{ISR}$  final state is taken as systematic uncertainty of the background  $e^+e^- \rightarrow \pi^+\pi^-3\pi^0\gamma_{ISR}$  subtraction. A value of 6.8% is found.

The same procedure is applied for other background contributions, where an uncertainty of 20% is assumed. The corresponding uncertainty is found to be 0.4%.

The systematic uncertainties of the event selection criteria are also determined with the same strategy used for the four pion analysis. The selection criteria of

the kinematic fit and the kaon veto are studied. Their systematic uncertainties are listed in the summary Table 11.2.

The individual sources of systematic uncertainty are assumed to be uncorrelated. Hence, their quadratic sum is taken as total systematic uncertainty for the process  $e^+e^- \rightarrow \pi^+\pi^-3\pi^0$ . All the systematic uncertainties are summarized in Tab. 11.2. The total systematic uncertainty is found to be 7.1%.

**Table 11.2.:** Summary of systematic uncertainties of the  $\pi^+\pi^-3\pi^0$  final state.

| Source                                     | Variation               | Untagged [%] |
|--|-------------------------|--------------|
| Luminosity                                 | -                       | 0.5          |
| Tracking                                   | -                       | 0.6          |
| $\pi^0$ Eff.                               | -                       | 1.7          |
| Bgr. Subrt. $\pi^+\pi^-3\pi^0\gamma_{ISR}$ | $\pm 12\%$ Bgr.         | 6.8          |
| Bgr. Subrt. other                          | $\pm 20\%$ Bgr.         | 0.4          |
| $\chi^2$ cut                               | $45 < \chi_{7C}^2 < 55$ | 0.8          |
| Kaon Veto                                  | on/off                  | 1.0          |
| Total                                      |                         | 7.1          |

### 11.2.3. Subtraction of the Dominating Backgrounds

In the following, the  $M(\pi^+\pi^-2\pi^0)$  spectrum is split in four regions. These four regions are defined in Table 11.3. Systematic uncertainties that depend on  $M(\pi^+\pi^-2\pi^0)$  are studied separately in the four ranges.

**Table 11.3.:** Error regions of the mass spectrum  $M(\pi^+\pi^-2\pi^0)$ .

| Region | Mass range [GeV]                  |
|--------|-----------------------------------|
| R1     | $0.5 < M(\pi^+\pi^-2\pi^0) < 1.5$ |
| R2     | $1.5 < M(\pi^+\pi^-2\pi^0) < 2.0$ |
| R3     | $2.0 < M(\pi^+\pi^-2\pi^0) < 3.0$ |
| R4     | $3.0 < M(\pi^+\pi^-2\pi^0) < 3.8$ |

The final state  $\pi^+\pi^-3\pi^0\gamma_{ISR}$  is measured with a total uncertainty of 13.25%, as shown in section 11.2.1 and the uncertainty of the  $e^+e^- \rightarrow \pi^+\pi^-3\pi^0$  channel is 7.1%, as shown in section 11.2.2. Further, an accuracy of 20% is assumed for the remaining Lund- $q\bar{q}$  background contributions. The scaling of the background contributions is changed according to their uncertainty. The event yields are determined after subtracting the modified background contributions from data. The largest relative difference between the event yields after background subtraction obtained with the default and the modified rescaling factor is used as the systematic uncertainty due to the background subtraction of the specific channel. The corresponding systematic uncertainties from the subtraction of the

$e^+e^- \rightarrow \pi^+\pi^-3\pi^0\gamma_{ISR}$ ,  $e^+e^- \rightarrow \pi^+\pi^-3\pi^0$ , and the remaining Lund- $q\bar{q}$  background contributions are listed in Table 11.4.

**Table 11.4.:** Systematic uncertainties from the background subtractions of the dominating background contributions in four ranges of  $M(\pi^+\pi^-2\pi^0)$  defined in Table 11.3. T stands for the tagged ISR method and U for the untagged one.

| bgr. contr.                    | R1    |       | R2    |       | R3    |       | R4    |       |
|--------------------------------|-------|-------|-------|-------|-------|-------|-------|-------|
|                                | T [%] | U [%] |
| $\pi^+\pi^-3\pi^0$             | 0.0   | 0.0   | 0.1   | 0.0   | 2.5   | 0.1   | 3.2   | 0.2   |
| $\pi^+\pi^-3\pi^0\gamma_{ISR}$ | 0.5   | 0.6   | 0.5   | 0.2   | 7.8   | 0.6   | 10.3  | 0.7   |
| $q\bar{q}$                     | 0.5   | 0.6   | 1.0   | 0.2   | 12.7  | 0.8   | 21.0  | 0.8   |

#### 11.2.4. Subtraction of the Remaining Backgrounds

The same method is performed for the background contributions from the MC samples listed in Table 11.5. An accuracy of 20% is assumed for the non-DD MC sample. The MC samples containing the  $e^+e^- \rightarrow \gamma_{ISR}J/\psi$ ,  $e^+e^- \rightarrow \gamma_{ISR}\psi(3686)$  and  $e^+e^- \rightarrow D\bar{D}$  processes are assumed to have a precision of 10%. The numbers are conservative guesses of the uncertainties of the shapes and scalings of these MC samples and the branching fractions used therein. The resulting uncertainties for subtracting the corresponding background contributions are listed in Table 11.5.

**Table 11.5.:** Systematic uncertainty from the background subtraction of the minor background contributions in the four ranges of  $M(\pi^+\pi^-2\pi^0)$  defined in Table 11.3. T(U) stands for the tagged (untagged) ISR modes.

| MC sample                | R1    |       | R2    |       | R3    |       | R4    |       |
|--------------------------|-------|-------|-------|-------|-------|-------|-------|-------|
|                          | T [%] | U [%] |
| nonDD                    | 0.04  | 0.00  | 0.13  | 0.00  | 2.54  | 0.07  | 5.92  | 0.18  |
| $\gamma_{ISR}J/\psi$     | 0.01  | 0.00  | 0.01  | 0.02  | 0.51  | 0.37  | 0.40  | 0.04  |
| $\gamma_{ISR}\psi(3686)$ | 0.04  | 0.00  | 0.07  | 0.01  | 0.57  | 0.08  | 0.96  | 0.27  |
| $D^+D^-$                 | 0.00  | 0.01  | 0.00  | 0.00  | 0.03  | 0.00  | 0.01  | 0.00  |
| $D^0\bar{D}^0$           | 0.00  | 0.00  | 0.00  | 0.00  | 0.17  | 0.01  | 0.03  | 0.00  |
| total                    | 0.05  | 0.01  | 0.15  | 0.02  | 2.66  | 0.39  | 6.01  | 0.33  |

### 11.3. Summary of the Systematic Uncertainties for

$$e^+e^- \rightarrow \pi^+\pi^-2\pi^0\gamma_{ISR}$$

**Table 11.6.:** Summary of the systematic uncertainties of the  $e^+e^- \rightarrow \pi^+\pi^-2\pi^0\gamma_{ISR}$  final state.

| Source                         | Variation                           | Tagged [%] |     |      |      | Untagged [%] |     |      |     |
|--------------------------------|-------------------------------------|------------|-----|------|------|--------------|-----|------|-----|
|                                |                                     | R1         | R2  | R3   | R4   | R1           | R2  | R3   | R4  |
| Luminosity                     | -                                   |            |     | 0.5  |      |              |     | 0.5  |     |
| Tracking                       | -                                   |            |     | 0.6  |      |              |     | 0.6  |     |
| ISR Photon Eff.                | -                                   |            |     | 0.3  |      |              |     | -    |     |
| radiator function              | -                                   |            |     | 0.5  |      |              |     | 0.5  |     |
| VP correction                  | -                                   |            |     | 0.05 |      |              |     | 0.05 |     |
| FSR correction                 | -                                   |            |     | 0.2  |      |              |     | 0.2  |     |
| $\pi^0$ Eff.                   | -                                   |            |     | 2.6  |      |              |     | 2.5  |     |
| Signal Eff.                    | -                                   |            |     | 0.6  |      |              |     | 0.6  |     |
| Bgr. Subrt. other              | $\pm 10\%$ Bgr.                     | 0.1        | 0.1 | 2.3  | 5.3  | 0.0          | 0.0 | 0.3  | 0.3 |
| Bgr. Subrt. $5\pi$             | $\pm 7.1\%$ Bgr.                    | 0.0        | 0.1 | 2.5  | 3.2  | 0.0          | 0.0 | 0.1  | 0.2 |
| Bgr. Subrt. $5\pi\gamma_{ISR}$ | $\pm 13.8\%$ Bgr.                   | 0.5        | 0.5 | 7.8  | 10.3 | 0.6          | 0.2 | 0.6  | 0.7 |
| Bgr. Subrt. $q\bar{q}$         | $\pm 20\%$ Bgr.                     | 0.5        | 1.0 | 12.7 | 21.0 | 0.6          | 0.2 | 0.8  | 0.8 |
| $\chi^2$ cut                   | Helix cor. on/off                   |            |     | 0.4  |      |              |     | 0.4  |     |
| Vertex cut                     | $1.8 < r_{vertex} < 2.2$            |            |     | -    |      |              |     | 0.2  |     |
| Kaon Veto                      | on/off                              |            |     | 0.1  |      |              |     | 0.1  |     |
| Fake ISR                       | $0.0 < M(\gamma_{ISR}\gamma) < 0.1$ |            |     | 0.4  |      |              |     | -    |     |
| ISR Angle                      | $1.0 < \cos\theta < 1.0$            |            |     | -    |      |              |     | 0.4  |     |
| $\cos\alpha$                   | offset $\pm 2\%$                    |            |     | -    |      |              | 1.3 | -    |     |
| Total                          |                                     | 3.0        | 3.1 | 15.6 | 24.4 | 3.0          | 2.9 | 3.0  | 3.0 |

The various sources of systematic uncertainty are assumed to be uncorrelated. Hence, their quadratic sum is taken as the total systematic uncertainty. All individual sources of systematic uncertainties are summarized in Table 11.6, together with the total systematic uncertainty. For the low mass region, from 920 MeV to 1.8 GeV, which is relevant for  $a_\mu$ , the total systematic uncertainty is found to be between 3.0% and 3.1% for the tagged ISR method depending on the four pion invariant mass  $M(\pi^+\pi^-2\pi^0)$ . For the untagged ISR method the uncertainties are found to be between 3.0% and 2.9%. In the high mass region, above 2 GeV, the systematic uncertainties vary between 15.6% and 24.4% for the tagged method and are found to be 3.0% for the untagged method.

## 11.4. Systematic Uncertainties of the Sub-processes of $e^+e^- \rightarrow \pi^+\pi^-3\pi^0\gamma_{ISR}$

The contributions to the systematic uncertainty of the  $e^+e^- \rightarrow \pi^+\pi^-3\pi^0\gamma_{ISR}$  process have been discussed in section 11.2.1. The total systematic uncertainty is found to be 13.25%.

The systematic uncertainty of the  $\pi^+\pi^-3\pi^0\gamma_{ISR}$  sub-channels  $\omega2\pi^0\gamma_{ISR}$  and  $\eta\pi^+\pi^-\gamma_{ISR}$  are composed of the total systematic uncertainty of the  $\pi^+\pi^-3\pi^0\gamma_{ISR}$  channel, plus an additional uncertainty of the  $\omega$  and  $\eta$  selection criteria, respectively. To estimate the systematic uncertainty of this selection, the size mass window to select the respective resonance is varied. In addition to the nominal mass window of  $720 < M(3\pi) < 850$  MeV to select the  $\omega$  resonance, a tighter window of  $710 < M(3\pi) < 860$  MeV and a less restrictive window of  $730 < M(3\pi) < 840$  MeV are chosen. The sidebands are adjusted accordingly to match the size of the signal region. For the  $\eta$  resonance, here is only an upper bound, which is moved by  $\pm 100$  MeV. For each of the three mass windows, the event yield is determined and corrected for the correspondingly adjusted efficiencies. The maximum change after efficiency correction is taken as systematic uncertainty of the  $\omega$ , or  $\eta$  selection, which is found to be 7.2%. Adding these results in quadrature to the systematic uncertainty of the  $e^+e^- \rightarrow \pi^+\pi^-3\pi^0\gamma_{ISR}$  analysis, a total systematic uncertainty of 14.8% for  $\omega2\pi^0\gamma_{ISR}$  and 14.1% for  $\eta\pi^+\pi^-\gamma_{ISR}$  is obtained.

## 11.5. Systematic Uncertainties for $e^+e^- \rightarrow \omega\pi^0$

The systematic uncertainty of the reaction  $e^+e^- \rightarrow \omega\pi^0\gamma_{ISR}$  is composed of the total systematic uncertainty of the  $e^+e^- \rightarrow \pi^+\pi^-2\pi^0\gamma_{ISR}$  channel, plus an additional uncertainty to consider the  $\omega$  resonance fits. However, the background contribution in the region around the  $\omega$  resonance is different from the background contribution

of the full  $e^+e^- \rightarrow \pi^+\pi^-2\pi^0\gamma_{ISR}$  final state. For the systematic uncertainties from  $e^+e^- \rightarrow \pi^+\pi^-2\pi^0\gamma_{ISR}$  without background subtraction 2.87% is obtained for the tagged ISR method and 2.82% for the untagged one.

In order to determine the systematic uncertainty from the background contributions, the signal to background ratio is calculated under the peaks of the  $\omega$  resonance for each  $M(\omega\pi^0)$  interval. The four kinds of background contributions from  $e^+e^- \rightarrow \pi^+\pi^-3\pi^0$ ,  $e^+e^- \rightarrow \pi^+\pi^-3\pi^0\gamma_{ISR}$ , Lund- $q\bar{q}$  and „other“ sources are investigated separately. Their uncertainties are 7.1%, 13.25%, 20% and 10% respectively. The background contribution in the  $\omega$  resonance region is smaller compared to the rest of the  $M(\pi^+\pi^-\pi^0)$  spectrum. The sum of the signal to background fractions weighted with the uncertainty of the corresponding background channels is listed in Table 11.7 for tagged and untagged ISR methods.

**Table 11.7.:** Systematic uncertainties of the background subtraction for the  $\omega\pi^0$  cross section. The spectrum is not unfolded, so narrow structures appear smeared with the detector resolution.

| Region | Tagged [%] | Untagged [%] |
|--------|------------|--------------|
| R1     | 1.52       | 0.96         |
| R2     | 3.74       | 0.94         |
| R3     | 6.97       | 3.05         |
| R4     | 0.79       | 0.69         |

The  $M(\pi^+\pi^-\pi^0)$  mass distributions used for the fits are filled with only the one  $\pi^0$  candidate, which gives the  $M(\pi^+\pi^-\pi^0)$  mass closest to the PDG omega mass. This choice might introduce a bias. The  $\omega$  resonance peak in the  $M(\pi^+\pi^-\pi^0)$  mass distributions might be enhanced by this choice. In order to estimate the size of this bias, the  $M(\pi^+\pi^-\pi^0)$  mass distributions are constructed again but both  $\pi^0$  candidates are used to calculate  $M(\pi^+\pi^-\pi^0)$ . This means there are two entries per event in the  $M(\pi^+\pi^-\pi^0)$  mass distributions. Comparing the fit results of the two methods yields a difference of 0.004%. Hence, the bias effect is negligible.

To estimate the systematic uncertainty of the  $\omega$  fit, the fit ranges, the binning and the fit model are changed. For the fit range, 10 MeV on the upper and the lower side are cut off the  $M(\pi^+\pi^-\pi^0)$  spectra for the fits of each  $M(\omega\pi^0)$  mass interval. The intervals of the  $M(\pi^+\pi^-\pi^0)$  spectra are changed from 10 MeV to 8 MeV at each  $M(\omega\pi^0)$  interval. For the uncertainty due to the fit model, the PDF of the background is changed to a third order polynomial. These systematic uncertainty tests are applied to the tagged and untagged ISR methods separately. The error weighted mean of the tagged and untagged cross sections is determined with the results of the modified fits. The mean relative deviation between the combined cross sections obtained with the modified fits and the default fits are taken for

the systematic uncertainties for each test case of the fits. The corresponding uncertainties are listed in Table 11.8. The total systematic uncertainty of the  $e^+e^- \rightarrow \omega\pi^0$  cross section is shown in Table 11.9. The uncertainties are added in quadrature, since the sources are uncorrelated.

**Table 11.8.:** Systematic uncertainties of the  $\omega$  fit of the  $\omega\pi^0\gamma_{ISR}$  measurement.

| Source    | Uncertainty [%] |
|-----------|-----------------|
| Fit range | 0.13            |
| Fit model | 0.74            |
| Binning   | 0.35            |
| Total     | 0.82            |

**Table 11.9.:** Total systematic uncertainties for the  $e^+e^- \rightarrow \omega\pi^0$  cross section.

| Region | Tagged [%] | Untagged [%] |
|--------|------------|--------------|
| R1     | 3.16       | 3.30         |
| R2     | 4.38       | 3.04         |
| R3     | 7.42       | 3.94         |
| R4     | 3.08       | 3.02         |

## 11.6. Systematic Uncertainties for the Branching Fractions

The total systematic uncertainty of the branching fractions  $\mathcal{B}(J/\psi \rightarrow \pi^+\pi^-2\pi^0)$ ,  $\mathcal{B}(J/\psi \rightarrow \pi^+\pi^-3\pi^0)$  and  $\mathcal{B}(\psi(3686) \rightarrow \pi^+\pi^-3\pi^0)$  consists of three contributions. The first is the systematic uncertainty of the cross section of the respective final state, which is 3.0% for untagged  $\pi^+\pi^-2\pi^0\gamma_{ISR}$  in the  $J/\psi$  region, and 13.25% for the  $\pi^+\pi^-3\pi^0\gamma_{ISR}$  channel. The second source of uncertainty is the error of the electronic width, which is 2.52% of the  $J/\psi$ , and 7.75% for  $\psi(3686)$ . The third source of uncertainty is the fit to determine the number of events originating from the decay of the charmonium resonances. To estimate the systematic uncertainty of the fit, the fit range, the signal shape, and the background function are varied. For the signal shape, a double Gaussian is used in stead of the single Gaussian. The polynomial describing the background is changed from second order to third order. The uncertainties obtained as the deviations of the variations from the nominal procedures are listed in Table 11.10. The contributions are summed in quadrature to obtain the total uncertainty.

**Table 11.10.:** Systematic uncertainties of the fits for the branching fractions.

| final state                   | fit range [%] | bgr [%] | signal [%] | $\Gamma_{ee}$ [%] | $\sigma$ [%] | Total [%] |
|-------------------------------|---------------|---------|------------|-------------------|--------------|-----------|
| $\pi^+\pi^-2\pi^0$            | 1.35          | 0.53    | 0.26       | 2.52              | 3.0          | 4.14      |
| $\omega\pi^0$                 | 4.22          | 0.41    | 0.13       | 2.52              | 3.0          | 5.74      |
| $\pi^+\pi^-3\pi^0$            | 0.13          | 0.01    | 2.44       | 2.52              | 13.25        | 13.1      |
| $\omega\pi^0\pi^0$            | 0.28          | 0.03    | 7.01       | 2.52              | 13.25        | 16.4      |
| $\eta\pi^+\pi^-$              | 0.56          | 0.22    | 0.17       | 2.52              | 13.25        | 13.3      |
| $\psi(3686) \rightarrow 5\pi$ | 0.02          | 0.24    | 4.12       | 7.75              | 13.25        | 15.6      |

# Appendix A.

## Data-MC Comparison of Kinematic Variables

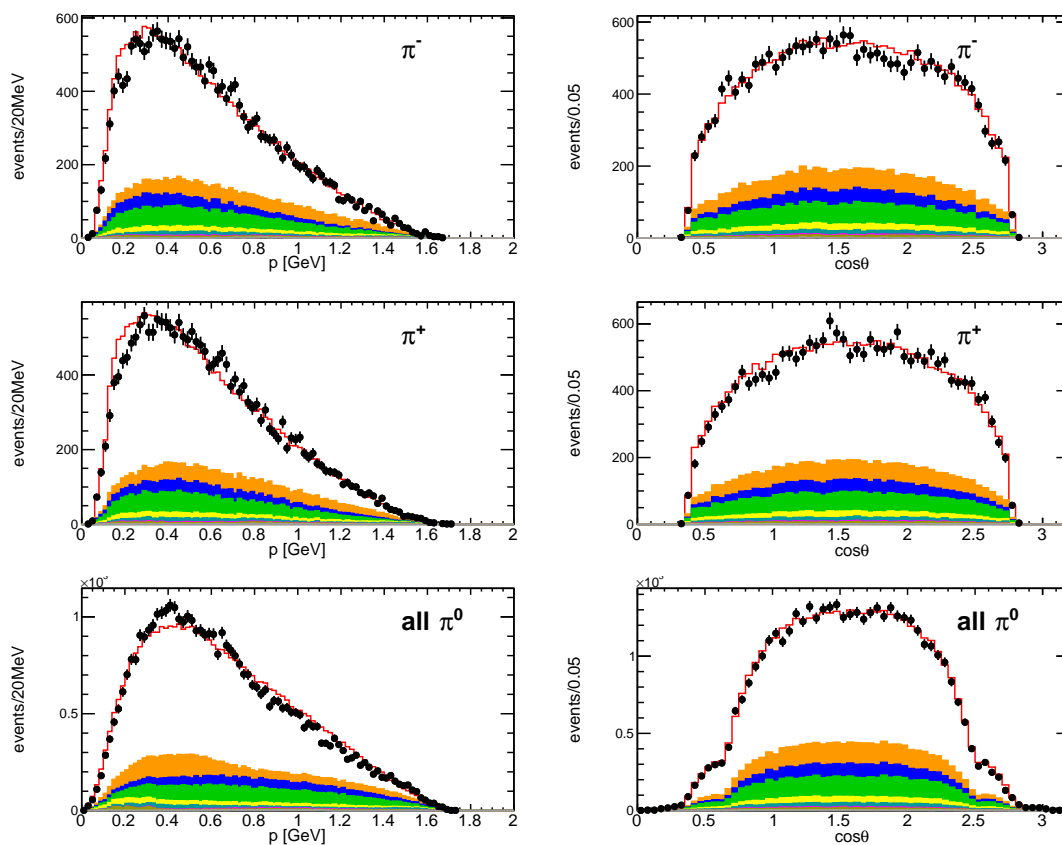


Figure A.1.: Kinematic variables of tagged  $e^+e^- \rightarrow \pi^+\pi^-2\pi^0\gamma_{ISR}$ .

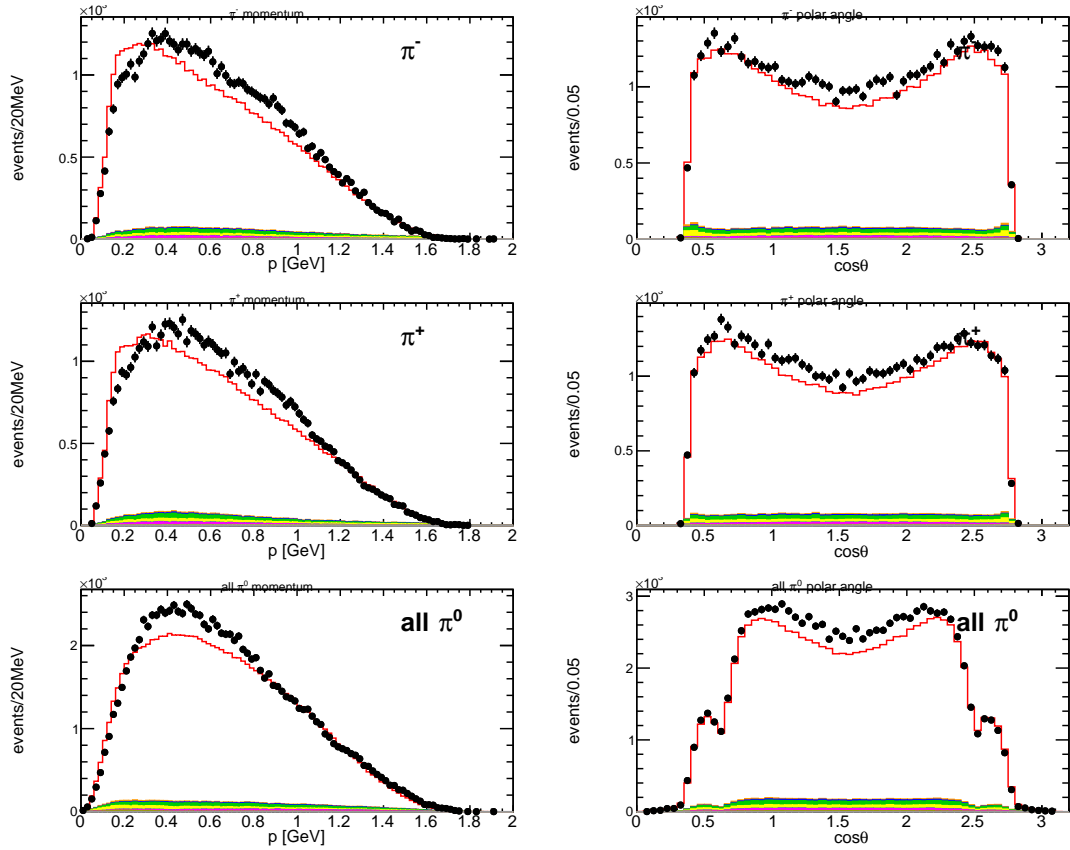


Figure A.2.: Kinematic variables of untagged  $e^+e^- \rightarrow \pi^+\pi^-2\pi^0\gamma_{ISR}$ .

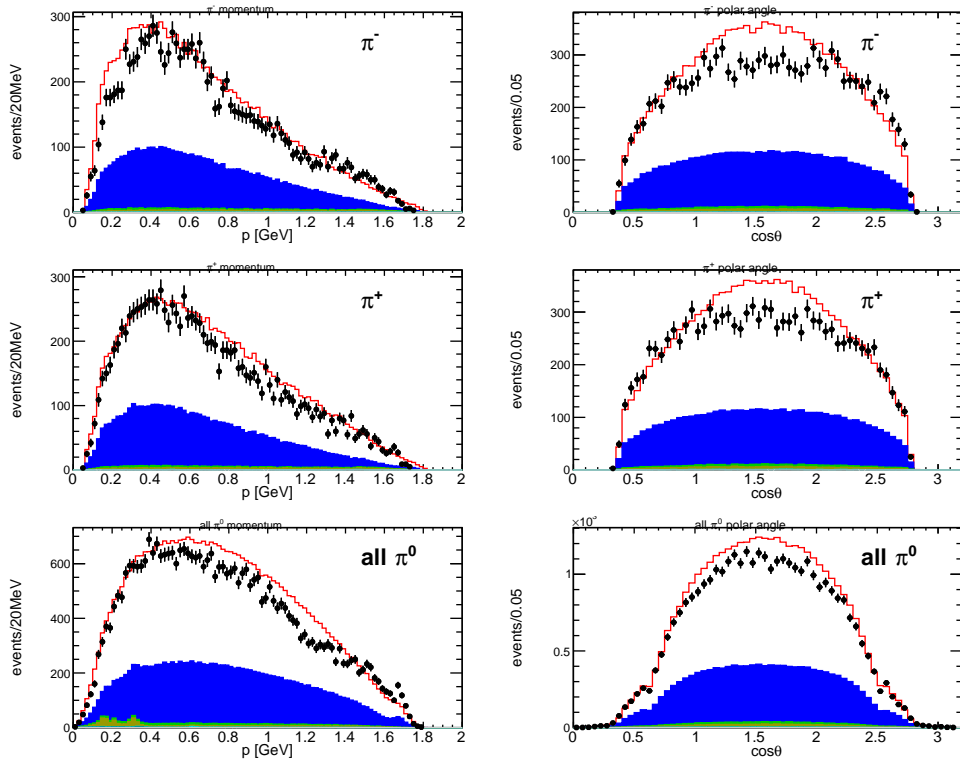


Figure A.3.: Kinematic variables of  $e^+e^- \rightarrow \pi^+\pi^-3\pi^0$ .

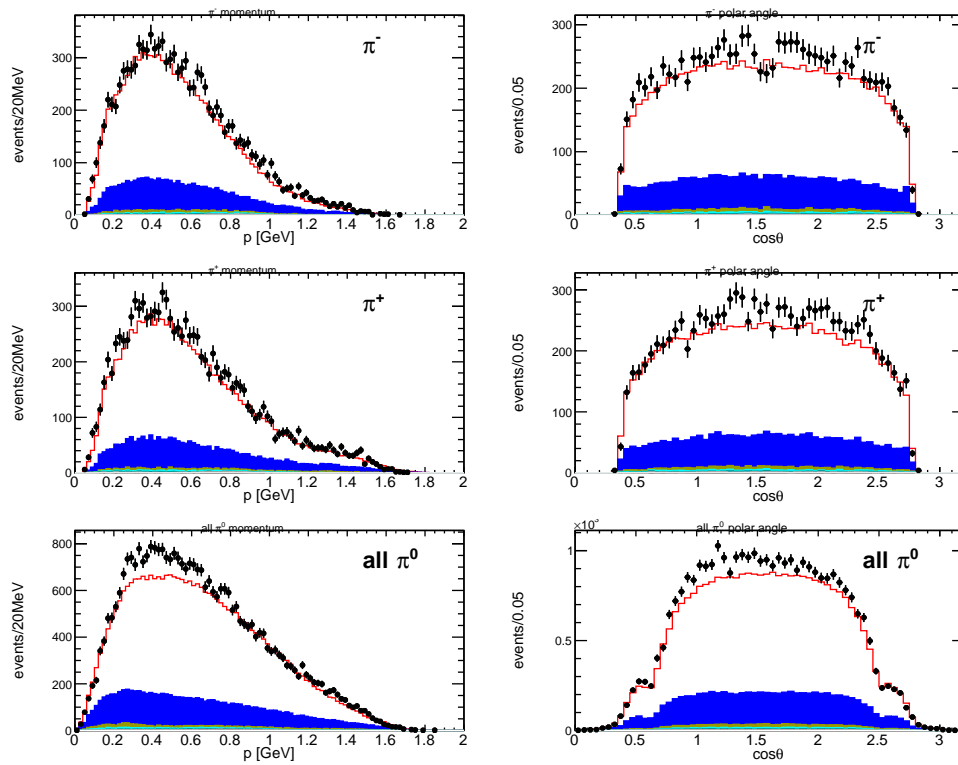


Figure A.4.: Kinematic variables of  $e^+e^- \rightarrow \pi^+\pi^-3\pi^0\gamma_{ISR}$ .



# Appendix B.

## Cross Section Tables

**Table B.1.:** Combined Cross section of  $e^+e^- \rightarrow \pi^+\pi^-2\pi^0$ . FSR and VP corrections are included. No unfolding is performed, narrow structures are smeared with the detector resolution. The first error is statistical, the second is the systematic one. The systematic uncertainty is 3%.

| $\sqrt{s}$<br>[GeV] | $\sigma \pm (\text{stat}) \pm (\text{sys})$<br>[nb] | $\sqrt{s}$<br>[GeV] | $\sigma \pm (\text{stat}) \pm (\text{sys})$<br>[nb] | $\sqrt{s}$<br>[GeV] | $\sigma \pm (\text{stat}) \pm (\text{sys})$<br>[nb] |
|---------------------|---|---------------------|---|---------------------|---|
| 0.93                | $2.96 \pm 1.47 \pm 0.09$                            | 1.75                | $19.12 \pm 0.61 \pm 0.56$                           | 2.55                | $2.28 \pm 0.10 \pm 0.07$                            |
| 0.96                | $3.88 \pm 1.40 \pm 0.11$                            | 1.77                | $17.70 \pm 0.56 \pm 0.52$                           | 2.58                | $2.20 \pm 0.09 \pm 0.07$                            |
| 1.00                | $6.18 \pm 1.77 \pm 0.18$                            | 1.80                | $14.46 \pm 0.49 \pm 0.42$                           | 2.61                | $2.03 \pm 0.09 \pm 0.06$                            |
| 1.02                | $8.82 \pm 1.77 \pm 0.26$                            | 1.83                | $12.57 \pm 0.43 \pm 0.36$                           | 2.64                | $1.95 \pm 0.08 \pm 0.06$                            |
| 1.05                | $8.64 \pm 1.73 \pm 0.26$                            | 1.87                | $11.78 \pm 0.41 \pm 0.34$                           | 2.67                | $1.87 \pm 0.08 \pm 0.06$                            |
| 1.08                | $13.01 \pm 1.91 \pm 0.39$                           | 1.89                | $10.12 \pm 0.36 \pm 0.29$                           | 2.71                | $1.81 \pm 0.08 \pm 0.05$                            |
| 1.11                | $14.39 \pm 1.85 \pm 0.43$                           | 1.92                | $8.71 \pm 0.33 \pm 0.25$                            | 2.74                | $1.54 \pm 0.07 \pm 0.05$                            |
| 1.14                | $17.92 \pm 2.00 \pm 0.53$                           | 1.95                | $8.84 \pm 0.32 \pm 0.26$                            | 2.76                | $1.50 \pm 0.07 \pm 0.05$                            |
| 1.17                | $16.02 \pm 1.68 \pm 0.47$                           | 1.98                | $9.39 \pm 0.32 \pm 0.27$                            | 2.79                | $1.37 \pm 0.07 \pm 0.04$                            |
| 1.21                | $19.07 \pm 1.73 \pm 0.56$                           | 2.01                | $8.46 \pm 0.30 \pm 0.26$                            | 2.82                | $1.38 \pm 0.06 \pm 0.04$                            |
| 1.24                | $19.39 \pm 1.65 \pm 0.57$                           | 2.04                | $8.64 \pm 0.29 \pm 0.26$                            | 2.85                | $1.25 \pm 0.06 \pm 0.04$                            |
| 1.26                | $24.25 \pm 1.74 \pm 0.72$                           | 2.07                | $7.80 \pm 0.26 \pm 0.24$                            | 2.88                | $1.17 \pm 0.06 \pm 0.04$                            |
| 1.29                | $23.39 \pm 1.55 \pm 0.69$                           | 2.10                | $7.17 \pm 0.25 \pm 0.22$                            | 2.91                | $1.10 \pm 0.05 \pm 0.03$                            |
| 1.32                | $26.41 \pm 1.55 \pm 0.78$                           | 2.13                | $6.61 \pm 0.23 \pm 0.20$                            | 2.94                | $1.05 \pm 0.05 \pm 0.03$                            |
| 1.35                | $26.30 \pm 1.44 \pm 0.78$                           | 2.17                | $6.21 \pm 0.22 \pm 0.19$                            | 2.98                | $1.08 \pm 0.05 \pm 0.03$                            |
| 1.39                | $32.38 \pm 1.51 \pm 0.96$                           | 2.19                | $5.20 \pm 0.19 \pm 0.16$                            | 3.01                | $1.00 \pm 0.05 \pm 0.03$                            |
| 1.41                | $32.50 \pm 1.39 \pm 0.96$                           | 2.23                | $5.02 \pm 0.18 \pm 0.15$                            | 3.03                | $1.30 \pm 0.05 \pm 0.04$                            |
| 1.45                | $32.78 \pm 1.31 \pm 0.97$                           | 2.26                | $4.53 \pm 0.17 \pm 0.14$                            | 3.06                | $1.85 \pm 0.06 \pm 0.06$                            |
| 1.48                | $33.07 \pm 1.24 \pm 0.98$                           | 2.28                | $4.15 \pm 0.16 \pm 0.13$                            | 3.09                | $2.07 \pm 0.07 \pm 0.06$                            |
| 1.51                | $32.41 \pm 1.16 \pm 0.96$                           | 2.31                | $4.00 \pm 0.15 \pm 0.12$                            | 3.12                | $0.90 \pm 0.04 \pm 0.03$                            |
| 1.53                | $29.61 \pm 1.03 \pm 0.87$                           | 2.34                | $3.85 \pm 0.15 \pm 0.12$                            | 3.15                | $0.66 \pm 0.03 \pm 0.02$                            |
| 1.56                | $28.35 \pm 0.96 \pm 0.83$                           | 2.38                | $3.54 \pm 0.14 \pm 0.11$                            | 3.18                | $0.68 \pm 0.03 \pm 0.02$                            |
| 1.59                | $27.00 \pm 0.89 \pm 0.79$                           | 2.40                | $3.29 \pm 0.13 \pm 0.10$                            | 3.22                | $0.65 \pm 0.03 \pm 0.02$                            |
| 1.63                | $25.06 \pm 0.82 \pm 0.73$                           | 2.44                | $3.11 \pm 0.12 \pm 0.09$                            | 3.25                | $0.60 \pm 0.03 \pm 0.02$                            |
| 1.65                | $26.16 \pm 0.81 \pm 0.76$                           | 2.46                | $2.67 \pm 0.11 \pm 0.08$                            | 3.27                | $0.57 \pm 0.03 \pm 0.02$                            |
| 1.68                | $23.73 \pm 0.74 \pm 0.69$                           | 2.50                | $2.61 \pm 0.11 \pm 0.08$                            | 3.30                | $0.57 \pm 0.03 \pm 0.02$                            |
| 1.71                | $21.34 \pm 0.67 \pm 0.62$                           | 2.52                | $2.55 \pm 0.10 \pm 0.08$                            | 3.33                | $0.56 \pm 0.03 \pm 0.02$                            |

**Table B.2.:** Combined Cross section of  $e^+e^- \rightarrow \omega\pi^0$ . FSR and VP corrections are included. No unfolding is performed, narrow structures are smeared with the detector resolution.

| $\sqrt{s}$<br>[GeV] | $\sigma \pm (\text{stat}) \pm (\text{sys})$<br>[nb] | $\sqrt{s}$<br>[GeV] | $\sigma \pm (\text{stat}) \pm (\text{sys})$<br>[nb] | $\sqrt{s}$<br>[GeV] | $\sigma \pm (\text{stat}) \pm (\text{sys})$<br>[nb] |
|---------------------|---|---------------------|---|---------------------|---|
| 1.01                | $8.14 \pm 1.80 \pm 0.27$                            | 1.79                | $0.92 \pm 0.25 \pm 0.03$                            | 2.58                | $0.20 \pm 0.05 \pm 0.01$                            |
| 1.07                | $12.55 \pm 2.12 \pm 0.42$                           | 1.85                | $0.93 \pm 0.22 \pm 0.04$                            | 2.64                | $0.21 \pm 0.05 \pm 0.01$                            |
| 1.13                | $15.68 \pm 2.36 \pm 0.52$                           | 1.91                | $0.50 \pm 0.10 \pm 0.02$                            | 2.70                | $0.15 \pm 0.05 \pm 0.01$                            |
| 1.19                | $17.07 \pm 2.40 \pm 0.57$                           | 1.97                | $0.82 \pm 0.11 \pm 0.03$                            | 2.76                | $0.08 \pm 0.05 \pm 0.00$                            |
| 1.25                | $15.58 \pm 1.94 \pm 0.51$                           | 2.03                | $0.79 \pm 0.12 \pm 0.03$                            | 2.82                | $0.14 \pm 0.05 \pm 0.01$                            |
| 1.31                | $15.41 \pm 1.73 \pm 0.51$                           | 2.09                | $1.10 \pm 0.15 \pm 0.06$                            | 2.88                | $0.09 \pm 0.05 \pm 0.00$                            |
| 1.37                | $19.38 \pm 1.54 \pm 0.62$                           | 2.15                | $0.87 \pm 0.13 \pm 0.04$                            | 2.94                | $0.09 \pm 0.04 \pm 0.00$                            |
| 1.43                | $19.41 \pm 3.14 \pm 0.61$                           | 2.21                | $0.69 \pm 0.09 \pm 0.03$                            | 3.00                | $0.08 \pm 0.05 \pm 0.00$                            |
| 1.49                | $13.94 \pm 1.36 \pm 0.44$                           | 2.27                | $0.44 \pm 0.08 \pm 0.02$                            | 3.06                | $0.14 \pm 0.04 \pm 0.00$                            |
| 1.55                | $11.18 \pm 1.13 \pm 0.45$                           | 2.34                | $0.29 \pm 0.08 \pm 0.02$                            | 3.12                | $0.09 \pm 0.03 \pm 0.00$                            |
| 1.61                | $6.56 \pm 0.73 \pm 0.24$                            | 2.40                | $0.31 \pm 0.06 \pm 0.01$                            | 3.18                | $0.04 \pm 0.03 \pm 0.00$                            |
| 1.67                | $4.64 \pm 0.45 \pm 0.19$                            | 2.46                | $0.26 \pm 0.07 \pm 0.01$                            | 3.24                | $0.04 \pm 0.03 \pm 0.00$                            |
| 1.73                | $1.80 \pm 0.33 \pm 0.07$                            | 2.52                | $0.22 \pm 0.05 \pm 0.01$                            | 3.30                | $0.03 \pm 0.03 \pm 0.00$                            |

**Table B.3.:** Cross section of  $e^+e^- \rightarrow \pi^+\pi^-3\pi^0$ . FSR and VP corrections are included. No unfolding is performed, narrow structures are smeared with the detector resolution.

| $\sqrt{s}$<br>[GeV] | $\sigma \pm (\text{stat}) \pm (\text{sys})$<br>[nb] | $\sqrt{s}$<br>[GeV] | $\sigma \pm (\text{stat}) \pm (\text{sys})$<br>[nb] | $\sqrt{s}$<br>[GeV] | $\sigma \pm (\text{stat}) \pm (\text{sys})$<br>[nb] |
|---------------------|---|---------------------|---|---------------------|---|
| 1.51                | $1.85 \pm 1.24 \pm 0.26$                            | 2.23                | $0.93 \pm 0.18 \pm 0.13$                            | 2.94                | $0.30 \pm 0.05 \pm 0.04$                            |
| 1.53                | $1.50 \pm 1.08 \pm 0.21$                            | 2.26                | $0.71 \pm 0.15 \pm 0.10$                            | 2.98                | $0.32 \pm 0.05 \pm 0.04$                            |
| 1.56                | $1.78 \pm 0.98 \pm 0.25$                            | 2.28                | $0.58 \pm 0.13 \pm 0.08$                            | 3.01                | $0.36 \pm 0.05 \pm 0.05$                            |
| 1.59                | $2.08 \pm 0.88 \pm 0.29$                            | 2.31                | $0.76 \pm 0.14 \pm 0.11$                            | 3.03                | $0.87 \pm 0.07 \pm 0.12$                            |
| 1.63                | $2.67 \pm 1.00 \pm 0.37$                            | 2.34                | $0.72 \pm 0.14 \pm 0.10$                            | 3.06                | $3.99 \pm 0.23 \pm 0.55$                            |
| 1.65                | $2.04 \pm 0.81 \pm 0.28$                            | 2.38                | $0.44 \pm 0.12 \pm 0.06$                            | 3.09                | $6.87 \pm 0.22 \pm 0.95$                            |
| 1.68                | $1.61 \pm 0.63 \pm 0.22$                            | 2.40                | $0.63 \pm 0.12 \pm 0.09$                            | 3.12                | $1.08 \pm 0.07 \pm 0.15$                            |
| 1.71                | $1.43 \pm 0.60 \pm 0.20$                            | 2.44                | $0.57 \pm 0.12 \pm 0.08$                            | 3.15                | $0.35 \pm 0.04 \pm 0.05$                            |
| 1.75                | $2.43 \pm 0.67 \pm 0.34$                            | 2.46                | $0.52 \pm 0.10 \pm 0.07$                            | 3.18                | $0.36 \pm 0.04 \pm 0.05$                            |
| 1.77                | $1.14 \pm 0.43 \pm 0.16$                            | 2.50                | $0.51 \pm 0.10 \pm 0.07$                            | 3.22                | $0.30 \pm 0.04 \pm 0.04$                            |
| 1.80                | $1.20 \pm 0.42 \pm 0.17$                            | 2.52                | $0.53 \pm 0.10 \pm 0.07$                            | 3.25                | $0.29 \pm 0.04 \pm 0.04$                            |
| 1.83                | $1.16 \pm 0.39 \pm 0.16$                            | 2.55                | $0.51 \pm 0.10 \pm 0.07$                            | 3.27                | $0.28 \pm 0.03 \pm 0.04$                            |
| 1.87                | $1.30 \pm 0.41 \pm 0.18$                            | 2.58                | $0.45 \pm 0.08 \pm 0.06$                            | 3.30                | $0.28 \pm 0.03 \pm 0.04$                            |
| 1.89                | $0.61 \pm 0.30 \pm 0.08$                            | 2.61                | $0.36 \pm 0.08 \pm 0.05$                            | 3.33                | $0.31 \pm 0.03 \pm 0.04$                            |
| 1.92                | $1.28 \pm 0.36 \pm 0.18$                            | 2.64                | $0.48 \pm 0.08 \pm 0.07$                            | 3.36                | $0.25 \pm 0.03 \pm 0.03$                            |
| 1.95                | $1.43 \pm 0.31 \pm 0.20$                            | 2.67                | $0.40 \pm 0.08 \pm 0.05$                            | 3.39                | $0.23 \pm 0.03 \pm 0.03$                            |
| 1.98                | $1.04 \pm 0.29 \pm 0.14$                            | 2.71                | $0.36 \pm 0.07 \pm 0.05$                            | 3.42                | $0.26 \pm 0.03 \pm 0.04$                            |
| 2.01                | $1.31 \pm 0.29 \pm 0.18$                            | 2.74                | $0.41 \pm 0.07 \pm 0.06$                            | 3.45                | $0.19 \pm 0.03 \pm 0.03$                            |
| 2.04                | $0.83 \pm 0.23 \pm 0.11$                            | 2.76                | $0.42 \pm 0.07 \pm 0.06$                            | 3.49                | $0.22 \pm 0.03 \pm 0.03$                            |
| 2.07                | $1.08 \pm 0.24 \pm 0.15$                            | 2.79                | $0.33 \pm 0.06 \pm 0.05$                            | 3.51                | $0.18 \pm 0.02 \pm 0.02$                            |
| 2.10                | $0.91 \pm 0.21 \pm 0.13$                            | 2.82                | $0.45 \pm 0.07 \pm 0.06$                            | 3.54                | $0.15 \pm 0.02 \pm 0.02$                            |
| 2.13                | $0.84 \pm 0.20 \pm 0.12$                            | 2.85                | $0.34 \pm 0.06 \pm 0.05$                            | 3.57                | $0.16 \pm 0.02 \pm 0.02$                            |
| 2.17                | $0.88 \pm 0.19 \pm 0.12$                            | 2.88                | $0.35 \pm 0.06 \pm 0.05$                            | 3.60                | $0.11 \pm 0.02 \pm 0.01$                            |
| 2.19                | $0.82 \pm 0.18 \pm 0.11$                            | 2.91                | $0.25 \pm 0.05 \pm 0.03$                            | 3.63                | $0.10 \pm 0.02 \pm 0.01$                            |

# Bibliography

- 
- [1] S. L. Glashow and S. Weinberg, Phys. Rev. D **15**, 1958 (1977).
- [2] G. 't Hooft, Nucl. Phys. B **61**, 455 (1973).
- [3] D. J. Gross and F. Wilczek, Phys. Rev. D **8**, 3633 (1973).
- [4] D. J. Gross and F. Wilczek, Phys. Rev. D **9**, 980 (1974).
- [5] G. Arnison *et al.* [UA1 Collaboration], Phys. Lett. B **122**, 103 (1983).
- [6] G. Arnison *et al.* [UA1 Collaboration], Phys. Lett. B **126**, 398 (1983).
- [7] F. Abe *et al.* [CDF Collaboration], Phys. Rev. Lett. **74**, 2626 (1995)  
doi:10.1103/PhysRevLett.74.2626 [hep-ex/9503002].
- [8] J. E. Augustin *et al.*, Phys. Rev. Lett. **33**, 1406 (1974)
- [9] F. Englert and R. Brout, Phys. Rev. Lett. **13**, 321 (1964).
- [10] P. W. Higgs, Phys. Lett. **12**, 132 (1964).
- [11] P. W. Higgs, Phys. Rev. Lett. **13**, 508 (1964).
- [12] P. W. Higgs, Phys. Rev. **145**, 1156 (1966).
- [13] Atlas Collaboration, Physics Letters **B** 716 1-29 (2012).
- [14] CMS Collaboration, Physics Letters **B** 716 30-61 (2012).
- [15] M. Kobayashi and T. Maskawa, Prog. Theor. Phys. **49**, 652 (1973).
- [16] P. Langacker and M. x. Luo, Phys. Rev. D **44**, 817 (1991).
- [17] F. Jegerlehner, Acta Phys. Polon. B **38**, 3021 (2007).
- [18] P. A. M. Dirac, Proc. Roy. Soc. **A** 117 (1928) 610; **A** 118 351 (1928).
- [19] H. M. Foley and P. Kusch, Phys. Rev. **73** 412 (1948).
- [20] J. S. Schwinger, Phys. Rev. **73** 416 (1948).
- [21] R. L. Garwin, D. P. Hutchinson, S. Penman and G. Shapiro, Phys. Rev. **118**  
271 (1960).
- [22] G. Charpak, F. J. M. Farley and R. L. Garwin, Phys. Lett. **1** 16 (1962).
- [23] J. Bailey, W. Bartl, G. von Bochmann, R. C. A. Brown, F. J. M. Farley,  
M. Giesch, H. Jostlein and S. van der Meer *et al.*, Nuovo Cim. A **9** 369 (1972).
- [24] J. Bailey *et al.*, Nucl. Phys. B **150** 1 (1979).
- [25] R. M. Carey, W. Earle, E. Efstathiadis, M. F. Hare, E. S. Hazen, B. J. Hughes,  
F. Krienen and J. P. Miller *et al.*, Phys. Rev. Lett. **82** 1632 (1999).

- 
- [26] H. N. Brown *et al.* [Muon (g-2) Collaboration], Phys. Rev. D **62** 091101 (2000).
- [27] H. N. Brown *et al.* [Muon g-2 Collaboration], Phys. Rev. Lett. **86** 2227 (2001).
- [28] G. W. Bennett *et al.* [Muon g-2 Collaboration], Phys. Rev. Lett. **89**, 101804 (2002); [Erratum-ibid. **89**, 129903 (2002)].
- [29] G. W. Bennett *et al.* [Muon g-2 Collaboration], Phys. Rev. Lett. **92** 161802 (2004).
- [30] G. W. Bennett *et al.* [Muon g-2 Collaboration], Phys. Rev. D **73** 072003 (2006).
- [31] C. Patrignani *et al.* [Particle Data Group], Chin. Phys. C **40**, no. 10, 100001 (2016).
- [32] B. L. Roberts, Chin. Phys. C **34**, 741 (2010).
- [33] T. Mibe [J-PARC g-2 Collaboration], Nucl. Phys. Proc. Suppl. **218**, 242 (2011).
- [34] T. Aoyama, M. Hayakawa, T. Kinoshita and M. Nio, Phys. Rev. Lett. **109**, 111808 (2012).
- [35] A. Kurz, T. Liu, P. Marquard, A. V. Smirnov, V. A. Smirnov and M. Steinhauser, PoS LL **2016**, 009 (2016) [arXiv:1607.01399 [hep-ph]].
- [36] C. Gnendiger, D. Stöckinger *et al.* Phys. Rev. D **88**, 053005 (2013).
- [37] F. Jegerlehner and A. Nyffeler, Phys. Rept. **477** 1 (2009).
- [38] J. Burmester *et al.* [PLUTO Collaboration], Phys. Lett. **66B**, 395 (1977).
- [39] Z. Jakubowski *et al.* [Crystal Ball Collaboration], Z. Phys. C **40**, 49 (1988); Crystal Ball Collaboration (C. Edwards *et al.*), SLAC-PUB-5160 (1990).
- [40] J. Z. Bai *et al.* [BES Collaboration], Phys. Rev. Lett. **84** 594 (2000); J. Z. Bai *et al.* [BES Collaboration], Phys. Rev. Lett. **88** 101802 (2002).
- [41] K. Hagiwara, A. Keshavarzi, A. D. Martin, D. Nomura and T. Teubner, Nucl. Part. Phys. Proc. **287-288**, 33 (2017).
- [42] M. Davier, Nucl. Part. Phys. Proc. **287-288**, 70 (2017).
- [43] T. Blum, A. Denig, I. Logashenko, E. de Rafael, B. Lee Roberts, T. Teubner and G. Venanzoni, arXiv:1311.2198 [hep-ph].
- [44] I. B. Vasserman, P. M. Ivanov, G. Y. Kezerashvili, I. A. Koop, A. P. Lysenko, Y. N. Pestov, A. N. Skrinsky and G. V. Fedotovitch *et al.*, Sov. J. Nucl. Phys. **33** 368 (1981).

- [45] L. M. Barkov, A. G. Chilingarov, S. I. Eidelman, B. I. Khazin, M. Y. Lelchuk, V. S. Okhapkin, E. V. Pakhtusova and S. I. Redin *et al.*, Nucl. Phys. B **256** 365 (1985).
- [46] I. B. Vasserman, L. M. Kurdadze, V. A. Sidorov, A. N. Skrinsky, A. G. Khabakhpashev, Y. M. Shatunov and B. A. Shvarts, Sov. J. Nucl. Phys. **30** 519 (1979).
- [47] R. R. Akhmetshin *et al.* [CMD-2 Collaboration], Phys. Lett. B **527** 161 (2002).
- [48] R. R. Akhmetshin *et al.* [CMD-2 Collaboration], Phys. Lett. B **578** 285 (2004).
- [49] V. M. Aulchenko *et al.* [CMD-2 Collaboration], JETP Lett. **82** (2005) 743; [Pisma Zh. Eksp. Teor. Fiz. **82** (2005) 841];
- [50] R. R. Akhmetshin, V. M. Aulchenko, V. S. Banzarov, L. M. Barkov, N. S. Bashtovoy, A. E. Bondar, D. V. Bondarev and A. V. Bragin *et al.*,
- [51] JETP Lett. **84** 413 (2006); [Pisma Zh. Eksp. Teor. Fiz. **84** (2006) 491]; R. R. Akhmetshin *et al.* [CMD-2 Collaboration], Phys. Lett. B **648** 28 (2007).
- [52] M. N. Achasov, K. I. Beloborodov, A. V. Berdyugin, A. G. Bogdanchikov, A. V. Bozhenok, A. D. Bukin, D. A. Bukin and T. V. Dimova *et al.*, J. Exp. Theor. Phys. **103** 380 (2006).
- [53] A. Quenzer, M. Ribes, F. Rumpf, J. L. Bertrand, J. C. Bizot, R. L. Chase, A. Cordier and B. Delcourt *et al.*, Phys. Lett. B **76** 512 (1978).
- [54] D. Bisello *et al.* [DM2 Collaboration], Phys. Lett. B **220** 321 (1989).
- [55] A. Aloisio *et al.* [KLOE Collaboration], Phys. Lett. B **606** 12 (2005).
- [56] F. Ambrosino *et al.* [KLOE Collaboration], Phys. Lett. B **670** 285 (2009).
- [57] F. Ambrosino *et al.* [KLOE Collaboration], Phys. Lett. B **700** 102 (2011).
- [58] D. Babusci *et al.* [KLOE Collaboration], Phys. Lett. B **720**, 336 (2013).
- [59] B. Aubert *et al.* [BaBar Collaboration], Phys. Rev. Lett. **103** 231801 (2009).
- [60] M. Ablikim *et al.* [BESIII Collaboration], Phys. Lett. B **753**, 629 (2016)
- [61] G. Cosme *et al.*, Phys. Lett. B **63**, 349 (1976).
- [62] G. Cosme *et al.*, Nucl. Phys. B **152**, 215 (1979).
- [63] B. Esposito *et al.*, Lett. Nuovo Cim. **31**, 445 (1981).
- [64] C. Bacci *et al.*, Nucl. Phys. B **184**, 31 (1981).
- [65] L. M. Kurdadze *et al.*, J. Exp. Theor. Phys. Lett. **43** 643 (1986).
- [66] D. Bisello *et al.*, Preprint LAL-90-35 (Orsay, 1990).

- [67] S. I. Dolinsky *et al.*, Phys. Rept. **202**, 99 (1991).
- [68] R. R. Akhmetshin *et al.* [CMD-2 Collaboration], Phys. Lett. B **466**, 392 (1999).
- [69] M. N. Achasov *et al.*, Preprint BUDKER-INP-2001-34 (Novosibirsk, 2001).
- [70] [The BaBar Collaboration], arXiv:1709.01171 [hep-ex].
- [71] [http://pic.cas.cn/pic\\_eihep\\_cas/tpk/msf/](http://pic.cas.cn/pic_eihep_cas/tpk/msf/)
- [72] M. Ablikim *et al.* [BESIII Collaboration], Nucl. Instrum. Meth. A **614** 345 (2010).
- [73] <http://tdc.web.cern.ch/TDC/hptdc/hptdc.htm>
- [74] Shu-Jun Wei *et al.*, Nucl. Instrum. Meth. A **598**, 323-327 (2009).
- [75] N. Berger *et al.*, Chinese Physics C34(12), 1779-1784 (2010).
- [76] S. Agostinelli *et al.* [GEANT4 Collaboration], Nucl. Instrum. Meth. A **506**, 250 (2003).
- [77] J. Allison, *et al.*, IEEE Trans. Nucl. Sci. **53**, 270 (2006).
- [78] Yutie Liang *et al.*, Nucl. Instrum. Meth. A **603**, 325 (2009).
- [79] Rene Brun and Fons Rademakers, Nucl. Instrum. Meth. A **389**, 81-86 (1997).
- [80] Barrand, G. *et al.*, Comput. Phys. Commun. **140**, 45 (2001).
- [81] M. Ablikim *et al.*, Phys. Rev. Lett. **110**, 252001 (2013).
- [82] K. Nakamura *et al.* (Particle Data Group), G **37** 075021 (2010).
- [83] M. Ablikim [BESIII Collaboration], Chin. Phys. C **37** 123001 (2013).
- [84] M. Ablikim *et al.*, Phys. Lett. B **753**, 629 (2016).
- [85] H. Czyz, A. Grzelinska and J. H. Kuhn, Phys. Rev. D **81** 094014 (2010).
- [86] R. G. Ping, Chin. Phys. C **38** 083001 (2014).
- [87] B. Andersson, S. Mohanty, F Soderberg, Eur. Phys. J. C **21** 631-647 (2001).
- [88] R. L. Yang, R. G. Ping and H. Chen, Chin. Phys. Lett. **31** 061301 (2014).
- [89] Phys. Rev. D **78** 074027 (2008).
- [90] V. P. Druzhinin, S. I. Eidelman, S. I. Serednyakov and E. P. Solodov, Rev. Mod. Phys. **83**, 1545 (2011).
- [91] S. Actis *et al.* [Working Group on Radiative Corrections and Monte Carlo Generators for Low Energies Collaboration], Eur. Phys. J. C **66** 585 (2010).
- [92] Z. Was, P. Golonka and G. Nanava, Nucl. Phys. Proc. Suppl. **181-182**, 269 (2008).

- 
- [93] M. Ablikim *et al.* [BESIII Collaboration], Phys. Rev. D **87**, 1, 012002 (2013).
- [94] B. Aubert *et al.* [BaBar Collaboration], Phys. Rev. D **73**, 052003 (2006).
- [95] M. Ablikim *et al.* [BESIII Collaboration], Phys. Rev. Lett. **104** 132002 (2010).
- [96] M. Ablikim *et al.* [BESIII Collaboration], BESIII DocDB-doc-446-v1
- [97] J. S. Schwinger, Particles, Sources and Fields, Vol. 3, Redwood City, USA Addison-Wesley 99 (1989).
- [98] A. Hofer, J. Gluza and F. Jegerlehner, Eur. Phys. J. C **24**, 51 (2002).
- [99] S. Actis *et al.* [arXiv:0912.0749 [hep-ph]].  
F. Ignatov, <http://cmd.inp.nsk.su/~ignatov/vpl>.
- [100] M. N. Achasov *et al.*, Phys. Lett. B **486**, 29 (2000).
- [101] M. N. Achasov *et al.*, arXiv:1610.00235 [hep-ex].
- [102] F. Ambrosino *et al.* [KLOE Collaboration], Phys. Lett. B **669**, 223 (2008).
- [103] X. H. Mo, C. Z. Yuan and P. Wang, hep-ph/0611214.
- [104] S. Eidelman and F. Jegerlehner, Z. Phys. C **67**, 585 (1995).
- [105] M. Ablikim *et al.* [BESIII Collaboration], Measurement of  $e^+e^- \rightarrow \gamma_{ISR}3\pi$  cross section via initial state radiation, [(to be published)].